THESIS

HYDRODYNAMICS IN MEANDERING COMPOUND CHANNELS WITH VARIED EMERGENT FLOODPLAIN VEGETATION DENSITIES: A 3D NUMERICAL MODELING STUDY

Submitted by

Nicolas P. Brouillard

Department of Civil and Environmental Engineering

In partial fulfillment of the requirements

For the Degree of Master of Science

Colorado State University

Fort Collins, Colorado

Summer 2021

Master's Committee:

Advisor: Ryan Morrison
Co-Advisor: Peter Nelson

Ellen Wohl

ABSTRACT

HYDRODYNAMICS IN MEANDERING COMPOUND CHANNELS WITH VARIED EMERGENT FLOODPLAIN VEGETATION DENSITIES: A 3D NUMERICAL MODELING STUDY

Emergent floodplain vegetation can influence the hydrodynamic interactions between floodplain and main channel flows during floods in meandering compound channels. These interactions impact the flow and boundary shear stress fields in the main channel, which govern sediment transport, channel morphodynamics, and the capacity to convey flood flows. These processes are important to sustaining aquatic habitats, understanding geomorphic change, and predicting flood severity. However, the effects of emergent floodplain vegetation density on flow phenomena in meandering compound channels are poorly understood. Therefore, this study had three objectives: 1) accurately numerically model three-dimensional (3D) flows at different relative depths (ratio of floodplain to main channel flow depths) in a meandering compound channel with a fixed rectangular main channel cross section and a smooth floodplain using data from published physical experiments, 2) use the numerical model to simulate varied emergent floodplain vegetation density conditions, and 3) analyze the effects of different emergent floodplain vegetation densities on the main channel and floodplain hydrodynamics. Specifically, the effects of floodplain vegetation conditions on primary flows, secondary flows, and boundary shear stresses in the main channel were explored. This study also looked at how floodplain vegetation density affected total discharge capacity as well as inbank and overbank layer-averaged flow patterns. Smooth floodplain, low floodplain vegetation density, and high

floodplain vegetation density scenarios were modeled with uniform arrays of emergent cylinders with non-dimensional vegetation densities (portion of the control volume occupied by vegetation) of 0, 0.00946, and 0.0368, respectively, based on natural floodplain forests. These scenarios were modeled for eleven relative depths ranging from 0 to 0.80. Previous research in meandering compound channels with smooth and roughened floodplains has shown that minimum average streamwise velocities and boundary shear stresses in the main channel occur at a given threshold value of overbank relative depth. Therefore, a major focus of this research was to examine the relationships between vegetation densities, overbank relative depths, and minima in average main channel streamwise velocities and boundary shear stresses. The 3D numerical model accurately replicated the results of previously published physical experiments (objective 1) based on calibrated error metrics comparing free surface elevations and main channel streamwise velocities. Results from the calibrated numerical model show that as floodplain vegetation density increased, the initial minimum values of average main channel streamwise velocities and boundary shear stresses were lower in magnitude and occurred at greater relative depths and discharges (objectives 2 and 3). Unlike in the smooth and low vegetation density floodplain scenarios, these average main channel values generally did not increase with relative depth and discharge above the initial minimum case for the high vegetation density scenario. Furthermore, the main channel boundary shear stress field had strong gradients and had greater variations in magnitude in the vegetated floodplain scenarios compared with the smooth floodplain scenario. Additionally, increasing floodplain vegetation density greatly reduced the discharge capacity as well as the average main channel streamwise velocities and boundary shear stresses above the lowest relative depths. Finally, the character of the main channel primary and secondary flow structures as well as the inbank and overbank layer-averaged flows were also affected by floodplain vegetation density. As vegetation density increased, floodplain flows deviated further from the valley-wise direction and plunged more steeply into the main channel below the bankfull level, thus increasing interactions between inbank and overbank flow layers. The strength of separation between inbank and overbank flow layers at an imaginary bankfull level horizontal plane is believed to influence energy losses in the flow, which helps to explain trends in the flow velocity and boundary shear stress fields. In conclusion, this study illustrates why river scientists and engineers should consider the effects of floodplain vegetation density on main channel hydrodynamic processes in similar meandering compound channel systems.

ACKNOWLEDGEMENTS

I want to thank my advisors, Ryan Morrison and Peter Nelson for sharing their wellsprings of knowledge, wisdom, and guidance with me throughout my graduate studies at Colorado State University. I would also like to thank them for providing me with this amazing opportunity to perform research on such a fruitful and interesting project, which was funded by the National Science Foundation, Award 1916780. Thank you, Ellen Wohl for providing your well-informed input as a committee member for my thesis.

Thank you to my family, friends, and educators who have helped me get where I am. To my parents and brother, thank you for always being a phone call away when I needed your support. To my colleague and friend, Danny White, thank you for sharing in the creative spirit and for being available to talk about nearly any topic we thought was interesting. Thank you to my fellow graduate students including David Cortese, Liz Byron, Matt Lurtz, Ben Tyner, Joey Sinclair, Joe Pugh, and others for sharing in the ups and downs of graduate school in good spirit. Thank you, Toni Saleen, for believing in me many years ago and for helping me cultivate a curious mind. Finally, I would like to thank my friend and roommate, Adara Creasman, whose support and encouragement could not have come at a better time for the completion of my thesis.

TABLE OF CONTENTS

LIST OF TABLES

LIST OF FIGURES

1 INTRODUCTION

1.1 Background

Vegetation on the floodplains of compound channels has commonly been understood to perform functions primarily on the floodplain; yet their roles in shaping flow phenomena including that in the main channel may prove to be significant as well. In classical views, riparian and floodplain vegetation performs functions such as providing habitats for wildlife on the floodplain (Bottorff, 1974; Decamps et al., 1987) as well improving bank stabilization and local sedimentation (Hickin, 1984). In response to floodplain afforestation, stream channel narrowing has been observed (Liébault & Piégay, 2002).The removal of riparian vegetation has also been linked to channel widening in rivers (Kondolf & Curry, 1986). These and similar studies often attribute geomorphic responses to bank strengthening and local sedimentation effects due to vegetation rather than any greater influences of vegetation as elements which interact with the flow field during overbank flows. Floodplain vegetation, however, may play greater roles in shaping flow and morphodynamic phenomena beyond bank stabilization and local sedimentation.

In their 2007 modeling study, Wiel and Darby found that effects of woody riparian vegetation on the geotechnical stability of riverbanks is relatively small compared with unvegetated scenarios. They suggest that “well documented effects of vegetation on channel morphology” may be primarily caused by mechanisms such as vegetation-flow interactions rather than by the mechanical bank stabilization effects of woody vegetation (Wiel & Darby, 2007). Researchers such as Bywater-Reyes et al. (2017) have pointed out that riparian vegetation especially woody vegetation such as trees have significant effects on channel morphology observed in natural systems. Gurnell and Petts (2006) refer to trees as "riparian engineers" which may drive island formation in river corridors. Yet there are insufficient field and laboratory results to explain the connections between vegetation, hydraulics, and channel evolution (Bywater-Reyes et al., 2017).

In addition to likely effects on channel morphology, floodplain vegetation may provide ecological benefits related to flow-vegetation interactions. Floodplain flow resistance due to floodplain vegetation may affect fluxes in and out of the main channel onto the floodplain, which can play roles in controlling the fate of seeds, larvae, nutrients, and pollutants (Farzadkhoo et al., 2019; Nepf & Vivoni, 2000; Sullivan et al., 2020). Pollutants and nutrients such as dissolved organic carbon can be removed from the flow through biogeochemical processes on the floodplain which depend on floodplain fluxes and residence times (Helton et al., 2015; Sullivan et al., 2020). Floodplain roughness and vegetation conditions may also affect the stage-discharge relationships in meandering compound channels (James & Wark, 1992; Liu et al., 2016), thus impacting aquatic habitat availability during overbank flow events.

Numerous studies have focused solely on vegetation in open channel flow fields showing that vegetation has significant impacts on hydrodynamic and morphodynamic phenomena including flow resistance, vortex shedding, wake interactions, turbulence, and sediment transport (Aberle & Järvelä, 2013; Klopstra et al., 1997; Nepf, 1999; Nepf & Vivoni, 2000; Tanino & Nepf, 2008; Wang et al., 2018). Within these studies, the vegetation which occupies a flow field is often categorized as either submerged or emergent depending on whether the vegetation height is lower or greater than the flow depth, respectively (Nepf & Vivoni, 2000). Further, vegetation is also typically distinguished as flexible or rigid based on how the vegetation stems are able or unable to bend and move under the influence of the flow field (Aberle & Järvelä, 2013). These characteristics of vegetation have been shown to strongly influence flow-vegetation interactions (Aberle & Järvelä, 2013; Nepf & Vivoni, 2000). Emergent woody vegetation such as trees, often linked to geomorphic change in natural stream systems, are typically modeled effectively as rigid, vertical cylinders (Vargas-Luna et al., 2016). In compound channels, the effects of floodplain vegetation on flood flows will also influence and be influenced by the meandering nature of flows, which in themselves can be complex.

Because the main channel of most streams in nature meander to some degree (Sellin et al., 1993), flume studies in meandering compound channels have been a major focus in river science research for years (James & Wark, 1992; Shiono & Muto, 1998; Toebes & Sooky, 1967). Floodplain flows in meandering compound channels influence the main channel flow field, particularly the character and strength of secondary currents as well as momentum exchanges between the inbank and overbank flow layers (Moncho-Esteve et al., 2018; Shiono & Muto, 1998; Toebes & Sooky, 1967). A phenomenon observed in many studies is the reversal of the rotating main channel secondary flow cell direction at the bend apexes as the flow depth is increased above bankfull in meandering compound channels with straight floodplain walls. This phenomena is likely due to the shift from centrifugal steering in inbank flow cases to exchanges of momentum between the overbank and inbank flow layers in flows above bankfull (Toebes & Sooky, 1967). These secondary currents and momentum exchanges affect the distribution of the main channel flow velocities and thus boundary shear stresses as well. Secondary and primary flow structures and boundary shear stresses affect sediment motion on the bed which affects channel morphology and sediment transport.

As most floodplains are roughened to some degree by vegetation or other obstacles, there have been some flume experiments with floodplain roughness elements in straight (Dupuis et al., 2017; Thornton et al., 2000; Yang et al., 2012) and meandering compound channels (Chan, 2003; Farzadkhoo et al., 2019; Loveless et al., 2000; Sellin et al., 1993; Shiono et al., 2008, 2009; Spooner, 2001). Dupuis et al. (2017) used homogenous arrays of emergent cylinders to represent large woody floodplain vegetation and submerged artificial grass to represent floodplain meadows in their straight compound channel flume experiments. Their results showed that the floodplain mixing layer width stabilized and was homogenized in the vertical direction to the greatest degree for their emergent wooded floodplain scenarios in addition to producing the strongest secondary currents compared with their other floodplain roughness scenarios (Dupuis et al., 2017). Sellin et al. (1993) and Loveless et al. (2000) describe the same set of meandering compound channel experiments at the UK Flood Channel Facility (FCF), which had floodplain roughness elements resembling porous corrugations perpendicular to the valley-wise direction. They found a drop in sediment transport rates in their wide roughened floodplain scenario at low overbank flows compared with their bankfull case. They suggested that these findings support the idea of bankfull conditions as the 'dominant' channel forming conditions (Loveless et al., 2000; Sellin et al., 1993). The Shiono et al. group's work at Loughborough University sheds light on flow and sediment transport phenomena influenced by uniform distributions of submerged and emergent floodplain roughness elements in a meandering compound channel (Chan, 2003; Shiono et al., 2008, 2009; Spooner, 2001). Their findings showed that increasing floodplain roughness greatly reduced main channel velocities, boundary shear stresses, and sediment transport. However, the emergent floodplain roughness elements in their experiments were scaled and shaped to resemble houses on the floodplain rather than emergent vegetation. In the artificially grassed floodplain meandering compound channel experiments of Liu et al. (2016), the submerged, flexible grass cases were shown to increase the strength of secondary flow cells within the bend sections (curved portion of the meandering main channel) and weaken secondary flows at the crossover section (straight portion of the meandering main channel) during overbank flows. Farzadkoo et al. (2018) performed longitudinal dispersion experiments using dye with random and tandem arrangements of emergent rigid, cylindrical vegetation stems at different floodplain vegetation densities in a meandering compound channel with a one-sided meandering floodplain. They showed that increasing floodplain vegetation density reduced and homogenized the floodplain velocities (Farzadkhoo et al., 2018). The experiments of James et al. (2001) in compound meandering channels with marginal floodplain vegetation showed that marginal floodplain vegetation introduced resistance to the flow through increased drag but reduced flow resistance by dampening flow separation at tight bends. Overall, these studies show how floodplain roughness conditions have significant impacts on compound channel hydrodynamics.

In many meandering compound channel experiments with and without floodplain roughness elements, there is a common trend where main channel inbank flow characteristics drop in magnitude below those of the bankfull conditions until a threshold relative depth (ratio of floodplain to main channel flow depths). There have been observed decreases in main channel inbank discharges (James & Wark, 1992; Liu et al., 2016; Waterways Experiment Station (U.S.) & United States., 1956), streamwise velocities (Chan, 2003; Lyness et al., 1998; Shiono & Muto, 1998), boundary shear stresses (Chan, 2003; Loveless et al., 2000; Sellin et al., 1993; Shiono et al., 2009), and sediment transport rates (Chan, 2003; Karamisheva et al., 2006; Loveless et al., 2000; Lyness et al., 1998; Sellin et al., 1993; Shiono et al., 2009) at a threshold relative depth above the bankfull level. In these studies, values of these flow variables would decrease as relative depth initially increased above bankfull up to a threshold value typically at low overbank relative depths. At relative depths above these threshold overbank relative depths, the values would usually begin to increase with relative depth. Toebes and Sooky (1967) concluded that energy losses in meandering compound channels increased as flows became greater than the bankfull condition until a threshold depth was achieved, and above this threshold depth, the energy losses decreased. Understanding how the presence and absence of floodplain vegetation affects the appearance of minima in main streamwise velocities and boundary shear stresses would be of interest to river scientists and engineers for predicting geomorphic change and aquatic habitat suitability among other applications.

James and Wark (1992) recommended the use of 2D and 3D models to better understand flows in meandering compound channels. Three-dimensional models were preferred as these may better capture the complex three-dimensional nature of the flows in meandering compound channels (James & Wark, 1992). One-dimensional, two-dimensional, and three-dimensional (1D, 2D, and 3D) numerical models have been employed to better understand vegetation-flow interactions (W. X. Huai et al., 2009; López & García, 1998; Raupach & Shaw, 1982), flows in meandering channels, compound channels (Pezzinga, 1994), and combinations of these (Abril & Knight, 2004; Crosato & Saleh, 2011; Ervine et al., 2000; Fischer-Antze et al., 2001; Ghani et al., 2010; Helmiö, 2002; W. Huai et al., 2008, 2009; Jing et al., 2009; Li & Millar, 2011; Martín-Vide, 2001; Naot et al., 1996; Rameshwaran & Shiono, 2007; Shan et al., 2017; Shukla & Shiono, 2008; Wormleaton & Ewunetu, 2006a; Zen et al., 2016). Of the numerical studies in meandering compound channels with floodplain roughness elements, Ervine et al. (2000) used a 2D model to simulate flows from the SERC-C experiments at the U.K. Flood Channel Facility (FCF) at HR Wallingford which had “rod” or cylinder roughened floodplains in a meandering compound channel. However, this model did not directly account for the cylinder-flow interactions. Wormleaton and Ewunteu (2006) used 3D numerical modeling to replicate the experiments described by Sellin et al. (1993) and Loveless et al. (2000), which had varied submerged floodplain roughness elements in a meandering compound channel (Wormleaton & Ewunetu, 2006b). However, the roughness elements in their study were not representative of rigid, emergent vegetation such as floodplain trees. The review of the available literature indicates that no 3D numerical hydrodynamic modeling studies have been undertaken with homogeneously distributed arrays of rigid emergent cylindrical floodplain elements representing floodplain forests at different vegetation densities in a meandering compound channel.

This study explores how emergent floodplain vegetation density in a meandering compound channel affects various features of the flow using a 3D numerical hydrodynamic model. These features of the flow include stage-discharge relationships, primary and secondary flow structures, and boundary shear stresses which are important to the natural and built environment. Our results provide additional views on the overall flow field as well as main channel primary and secondary flow structures and boundary shear stresses in meandering compound channels with and without emergent floodplain vegetation at different vegetation densities.

1.2 Objectives

The following three objectives guided the research work of the current study.

<u>Objective 1</u>: Accurately reproduce the flow conditions of meandering compound channel flume experiments with smooth floodplains from published works in a 3D numerical flow model.

<u>Objective 2</u>: Use the 3D numerical flow model setups from Objective 1 as base conditions for simulating flows in meandering compound channels with varied emergent floodplain vegetation density conditions.

Objective 3: Explore how changes in emergent floodplain vegetation density affect main channel and floodplain hydrodynamics in a meandering compound channel with emergent, cylindrical floodplain roughness elements at various relative depths. Focus was placed on determining if minima in the average main channel streamwise velocities and boundary shear stresses would occur for the vegetated floodplain cases. If these minima did occur, determine how emergent floodplain vegetation density affects their appearance and offer explanations for these results in the context of observed patterns in the 3D flow field.

2 METHODS

2.1 Model Scenarios

This study compared three model scenarios based on differences in the dimensionless vegetation population density or the portion of the flow control volume occupied by vegetation. These included (a) “smooth (unvegetated)”, (b) “low vegetation density”, and (c) “high vegetation density” floodplain scenarios with dimensionless floodplain vegetation population densities of (a) 0, (b) 0.00946, and (c) 0.0368, respectively. The non-zero dimensionless floodplain vegetation population density scenarios are collectively referred to as the “vegetated” floodplain scenarios. The three scenarios are described in the following sections.

2.1.1 Smooth Floodplain Scenario

The smooth floodplain numerical models are based on physical flume experiments performed by the Shiono research group at Loughborough University with data provided in Spooner (2001), Chan (2003), Shiono et al. (2008), and Shiono et al. (2009) which will subsequently be referred to as the “Shiono et al.” experiments. Shiono et al. performed experiments in a meandering compound channel with varied relative depths and floodplain roughness types as well as fixed flat and mobile sand beds with vertical main channel walls (Chan, 2003; Shiono et al., 2008; Spooner, 2001). The fixed flat bed experiments were completed with smooth floodplain conditions, whereas the mobile bed experiments included smooth, artificially grassed, and a combination of artificial grassed and block roughened floodplain scenarios. Their fixed flat bed experiments were run until uniform flow conditions were met. For their natural bed experiments, equilibrium bed and uniform flow conditions were met through the manipulation of three tailgates and a sediment recycling pump, respectively (Chan, 2003).

The Shiono et al. group collected and analyzed data regarding the flow velocity field, flow depth, bed topography, sediment transport, and boundary shear stresses with detailed analysis especially for their 0, 0.20, 0.29, and 0.46 relative depth cases. The fixed flat bed experiments were selected as the physical basis for the current numerical modeling study rather than their mobile bed experiments because the focus of the current study was on hydrodynamics rather than morphodynamics. Further descriptions of these Shiono et al. experimental setups are provided in sections 2.2.1 Smooth Floodplain Base Geometry and 2.2.2 Relative Depths and Flow Rates. These studies were an ideal physical basis for the 3D numerical experiments of the current study because the researchers ran numerous scenarios and collected a great amount of data with which model comparisons could be made. The current study could also indirectly compare the vegetated floodplain model results with the roughened floodplain results in the Shiono et al. experiments. Analysis of their roughened floodplain cases is not included in this current study as both of their roughened floodplain cases incorporated submerged flexible vegetation which was outside the scope of this study.

2.1.2 Vegetated Floodplain Scenarios

Using the smooth floodplain model discussed in section 2.1.1 Smooth Floodplain Scenario as a base scenario, two vegetated floodplain scenarios with emergent cylindrical roughness elements on the floodplain were developed as described in the following scenarios:

- Low density arrangement with cylindrical vegetation elements to represent low density mature floodplain forests with a dimensionless vegetation density of 0.00946 shown in Figure 1

- High density arrangement with cylindrical vegetation elements to represent high density mature floodplain forests with a dimensionless vegetation density of 0.0368 shown in Figure 2

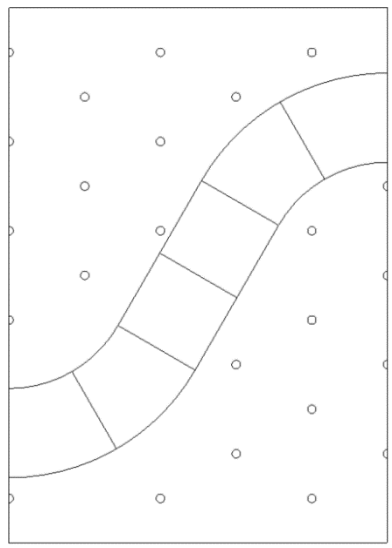

Figure 1. Low vegetation density setup

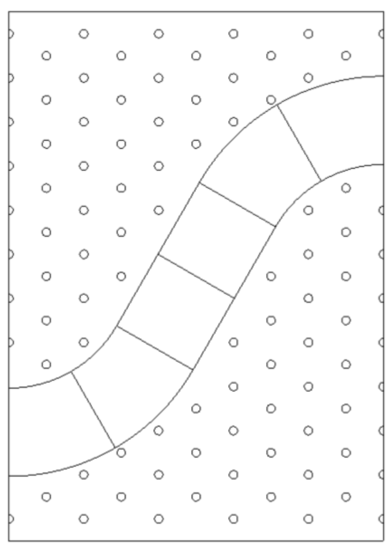

Figure 2. High vegetation density setup

The cylinder diameter and average spacing for the low and high vegetation density cylinder arrays were selected based on field data for floodplain and riparian forests, computed dimensionless vegetation population densities, experimental setups, and the geometric and grid limitations of the base smooth floodplain model. The selected average cylinder spacings were 0.3963 m and 0.1981 m for the low and high vegetation density cases, respectively. The cylinder diameters were 0.038 m for both floodplain vegetation density cases. The following section describes how the spacings and diameter were chosen.

In the current study, vegetation cylinders were arranged in a staggered array similar to the methods of Lyness et al. (1998) and Stone and Shen (2002). Spacing between rows of stems in the lateral direction were 0.4 and 0.2 m for the low and high floodplain vegetation density scenarios, respectively. Staggered columns in the longitudinal direction were spaced at 0.34 and 0.17 m for the low and high floodplain vegetation density scenarios, respectively. The selected spacings were chosen so that cylinder centers would align with the mesh grid nodes in the numerical models to ensure that all the cylinders were resolved in the same manner by the computational mesh described in section 2.2.3 Grid and Mesh Conditions. The spacing were also selected that cylinder arrangements would be symmetrical along the meanders on the left and right floodplains. For the low vegetation density case, the vegetation array from the left floodplain was mirrored and translated to the right floodplain to prevent vegetation stem overlap with free surface probe locations described in section 2.2.2 Relative Depths and Flowrates. Between the valley walls and the closest cylinder centers a minimum gap of one half the row spacing was maintained. Between the head of the valley and the closest cylinder centers at the furthest upstream column of cylinders, a gap of one column spacing was added. The cylinder arrays occupied the floodplain from the valley head to the valley tail. The average spacing between stems was computed as the average spacing between one vegetation stem and the nearest six surrounding stems. Using this method for the low floodplain vegetation density scenario, four stems had a spacing of 0.3944 m and two stems had a spacing of 0.4 m for an average stem spacing of 0.3963 m. For the high floodplain vegetation density scenario, four stems had a spacing of 0.1972 m and two stems had a spacing of 0.2 m for an average stem spacing of 0.1981 m.

To choose a vegetation stem diameter for the numerical experiments, the dimensionless vegetation population densities were computed for field and laboratory observations of floodplain vegetation arrays. Vegetation density and dimensionless vegetation population density as defined in Nepf (1999) are helpful for characterizing arrays of rigid cylindrical vegetation elements. Vegetation density, *a*, represents the "projected plant area per unit volume" (Nepf, 1999) defined by Equation (1) where *n* is the number of stems per unit area, *d* is the stem diameter, *h* is the flow depth, and ΔS is the average stem spacing. The dimensionless (vegetation) population density, *ad*, from Nepf (1999) represents the "fractional volume of the flow domain occupied by plants" (Nepf, 1999) and is shown in Equation (2).

$$a = nd = \frac{dh}{\Delta S^2 h} = \frac{d}{\Delta S^2} \qquad (1)$$

$$ad = \frac{d^2}{\Delta S^2} \qquad (2)$$

Values of the dimensionless vegetation population density were compared across field and laboratory observations to determine an appropriate range from which a modeled stem diameter could be computed. The average number of floodplain cottonwood tree stems per unit area on the South Platte River near Denver, Colorado was 0.022 stems per square meter with a range of 0.0136 to 0.073 stems per square meter (Bottorff, 1974). The average stem diameter was 0.36 m, and the maximum stem diameter was 1.02 m. Using the reported average stem diameter and minimum number of cottonwood stems per unit area, the minimum dimensionless vegetation population density was 0.00176. The computed average dimensionless vegetation population density was 0.00285. Using the reported average stem diameter and maximum number of stems per area, the maximum dimensionless vegetation population density was 0.00946. Using the reported maximum stem diameter and maximum number of stems per area, the maximum dimensionless vegetation density was 0.0759. In laboratory experiments, Dupuis et al. (2016) studied a straight compound channel with various floodplain roughness scenarios including wooded floodplains represented by staggered arrays of emergent cylinders. For these wooded floodplain scenarios, the cylinder diameters were 1:100 scale of 1 meter diameter trees with mean separation distances of 11.3 meters based on descriptions of a typical riparian forest in the lower reaches of the River Rhône in France as described by Terrier (2010). The computed dimensionless vegetation population density for these riparian forests was 0.00783 which is within the range computed for floodplain forests on the South Platte River.

Lyness et al. (1998), O'Sullivan (1999), and Karimsheva et al. (2006) performed experiments in a meandering compound channel with "rod roughened" floodplains. These experiments had rod (cylinder) densities of 90, 180, and 270 rods per square meter with 25 mm diameter rods (Karamisheva et al., 2006; Lyness et al., 1998; O'Sullivan et al., 2003). These rod densities and diameter correspond with dimensionless vegetation population densities of 0.0562, 0.112, and 0.169 which were fairly high compared with the riparian forests on the River Rhône and South Platte River. Stone and Shen (2002) also performed laboratory vegetation flow studies with emergent and submerged rigid cylinders with corresponding dimensionless vegetation population densities of 0.00698, 0.00700, 0.0279, and 0.0762 which were reasonable compared with the River Rhône and South Platte River riparian forests.

For the current study, a vegetation diameter of 0.038 m was selected to reproduce the dimensionless vegetation population density for the maximum field dimensionless vegetation density of 0.00946 using the average field stem diameter of 0.36 m based on the data from the South Platte River with the stem spacing for the low vegetation density scenario in the current numerical experiments. The ratio of the selected vegetation diameter to the highest average stem spacing (low floodplain vegetation density scenario) was about 0.96, which was similar to ratio of vegetation diameter to stem spacing on the River Rhône which was 0.88. If the lowest vegetation spacing scenario (high floodplain vegetation density) had been used to determine the vegetation diameter, the diameter would have been too small to be properly resolved by the mesh grid described in section 2.2.3 Grid and Mesh Conditions. The resulting dimensionless vegetation population density for the high vegetation density scenario was 0.0368 which was lower than the highest computed value for the South Platte riparian forests and the experiments of Stone and Shen (2002). Using stem diameter as a length scaling factor between the current numerical model stem diameter of 0.038 m and the floodplain cottonwood stem diameter values from Bottorff (1974), the main channel width of an equivalent river would be between 3.8 m and 11 m based on the average and maximum field vegetation diameters (width scales of approximately 1:9.5 and 1:27) which is within reason for smaller rivers and streams with large woody floodplain vegetation. The experiments of Spooner (2001), Chan (2003), and Shiono et al. (2008, 2009) had a main channel width scaling of 1:322.5 (2:645) compared with the average width of major rivers in the U.K. (Chan, 2003) which would be substantially larger rivers than those represented by the current study's width scaling.

2.2 Three-Dimensional Numerical Model

Simulations were run in the 3D computational fluid modeling (CFD) software FLOW-3D® HYDRO (Version 12.1.1.05; 2021; https://www.flow3d.com; Flow Science, Inc.). The following sections describe the inputs, setup, and solver methods of the models in FLOW-3D® HYDRO.

2.2.1 Smooth Floodplain Base Geometry

We digitally produced the 3D geometry with a smooth floodplain and fixed flat rectangular main channel in AutoCAD 2019 based on descriptions of the experimental setups used by Shiono et al. The meandering channel form was composed of curved "bend" sections and straight "crossover" sections shown in Figure 3 and Figure 4. The curved bend sections were formed from concentric circles with radii of 0.0565 and 0.0965 m. The circle centers were laterally offset from the valley centerline by 0.0577 m. The Shiono et al. experiments specify a lateral offset of 0.0573 m. However, to reproduce the lateral offset of the Shiono et al. experiments, the crossover section length would need to be increased to approximately 0.7509 m which would increase the sinuosity to 1.3841. The lateral offset of 0.0577 m was selected to avoid these changes in crossover length and sinuosity.

The inlet geometry was not fully described in Spooner (2001), Chan (2003), Shiono et al. (2008), nor Shiono et al. (2009). It was assumed that the inlet geometry consisted of a rectangular basin with a width equal to the valley width and a longitudinal length equal to two main channel widths, 0.08 m. The bed of this upstream basin was set at the same elevation as the main channel bed. At the outlet at the downstream end of the meandering channel, the geometry was also not fully discussed in the publications. Based on flume setup schematics from Chan (2003), there appeared to be an additional 60° crossing angle section of the main channel attached to the downstream end of the final quarter meander shown in Figure 3 for the current model. This additional 60° section aligned the outlet of the main channel with the valley centerline. Key model geometry parameters based on the Shiono et al. descriptions are summarized in Table 1.

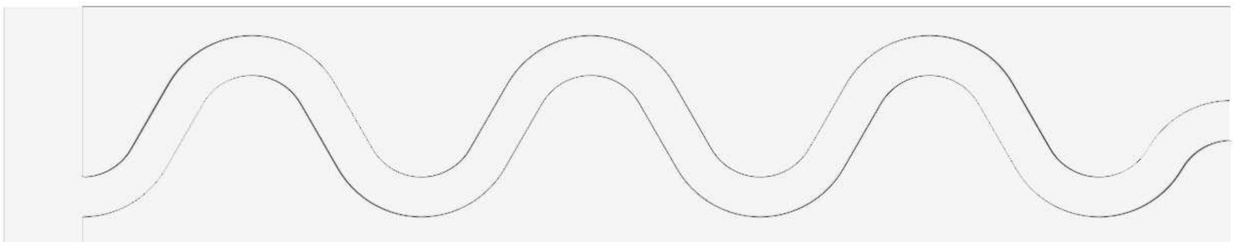

Figure 3. Smooth floodplain plan form geometry in FLOW-3D® HYDRO

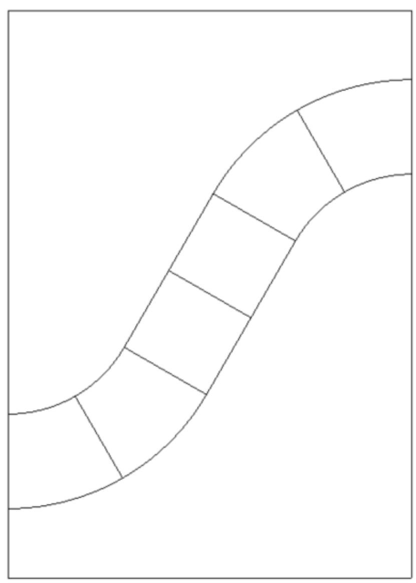

Figure 4. Study half meander geometry with cross section lines

At the lateral and longitudinal minima and maxima as well as the vertical minima, the 3D geometry was extended beyond the desired ranges. This overextension of the geometry ensured that the FLOW-3D® HYDRO mesh grid overlapped the geometry to improve its resolution. The 3D smooth floodplain fixed bed geometry was exported from AutoCAD 2019 as a stereolithographic (.stl) file. The .stl file was imported into FLOW-3D® HYDRO. Within

FLOW-3D® HYDRO, the geometry was translated in the X direction by -2.5 m, Y by -0.1 m, and Z by -0.21 m. The roughness height of the solid geometry was set to 0.001 m as described in section 2.2.6 Model Calibration and Validation.

Table 1. Model geometry parameters

Parameter	Value	Units
Sinuosity	1.3837	m
Meander wavelength, λ	3.4	m
Crossover angle, ω	60	°
Cross-over length	0.75	m
Radius of curvature to channel centerline	0.765	m
Lateral offset of center of curvature from valley centerline?	0.0577	m
Meandering section valley length	11.05	m
Headbox valley length	0.80	m
Main channel width	0.40	m
Valley basin width	2.4	m
Meander belt width	1.815	m
Main channel side slope	90	°
Bed slope represented in gravity components	0.002	-

The Shiono et al. experiments were conducted in a tilted flume with a valley slope of 1/500 (0.2%). In the current models, rather than tilt the geometry to represent the 0.2% valley slope, the components of gravity in the down-valley (x) and vertical (z) directions were adjusted in FLOW-3D® HYDRO to account for the bed slope without tilting the geometry. The geometry was kept with a zero percent down-valley slope; i.e., the bed and floodplain surface elevations were kept constant at 0 m and 0.04 m, respectively. Having the bed and floodplain geometry maintain a zero percent slope helped resolve the .stl geometry in more uniform detail across the length of the flume without requiring increased grid resolution.

In the Shiono et al. experiments, the flow was reported to be approximately uniform. With uniform flow in the numerical model, horizontal layers taken at points along the vertical axis could be assumed to be of approximately constant depth and constant distance above the bed. This assumption increased the ease of data post-processing by allowing sections to be cut at vertical planes parallel with the bed and the computational mesh grid. A limitation of the modified gravity slope representation was that the vertical direction was slightly off from the true vertical direction by approximately 0.229°. Therefore, the location of measurements along vertical planes were slightly different from those expected in reality. However, the differences in measurement location are assumed to be negligible.

2.2.2 Relative Depths and Flowrates

Relative depth, *dr*, is a dimensionless parameter representing the ratio of the flow depth on the floodplain, h_{fp}, to total flow depth in the main channel, h_t. Various formulations of relative depth are provided in Equation (3) where h_{bf} is the bankfull depth.

$$dr = \frac{h_{fp}}{h_t} = \frac{h_{fp}}{h_{fp} + h} = \frac{h_t - h_{bf}}{h_t} \tag{3}$$

The location of free surface elevation measurements for computing the relative depth were based on the descriptions of measurement locations provided in Spooner (2001) and Chan (2003). For overbank flows in the numerical model, the free surface elevation was taken at six nodes along the valley centerline aligned with the meander apexes. For the bankfull case, the free surface elevation was taken at the six nodes at the centers of the crossover sections along the centerline of the main channel. Within the main channel, there was superelevation which influenced the lateral and streamwise free surface elevations main channel and the floodplain free surface elevation varied as well. However, the variations across free surface due to superelevation were assumed to be negligible in the calculation of relative depth. Therefore, the Equation (4) was used to approximate relative depth:

$$dr = \frac{h_{fp}}{h_{fp} + h_{bf}} \tag{4}$$

Bankfull depth was constant at 0.04 m because it was a fixed feature of the rigid geometry. The floodplain depth based on the free surface elevation on the floodplain for overbank flows was averaged over the six meander apexes and the bankfull case was averaged over the six crossover section centerline points. Parameters including tailwater free surface elevation, roughness height, and discharge were calibrated to maintain a percent error in the average free surface elevation equal to or less than +/-5%. Further explanation of these methods is provided in section 2.2.6 Model Calibration and Validation section.

Relative depths of approximately 0, 0.13, 0.20, 0.25, 0.29, 0.35, 0.40, 0.46, and 0.50, were selected based on the available experimental data from Spooner (2001) and Chan (2003) along with supplemental relative depths of 0.60 and 0.80, which were not tested by the Shiono et al. group. The measured free surface elevations for the smooth floodplain scenario provided in Chan (2003) were used as input values for the vegetated floodplain scenarios to remain consistent between floodplain scenarios. The flowrates for the smooth cases at each relative depth case were provided in Spooner (2001) and Chan (2003). However, the bankfull flowrates were adjusted from the described values to prevent significant overbank flows from occurring.

The flowrates for the vegetated floodplain relative depth cases below a relative depth of 0.60 were solved for in an iterative process described in section 2.2.6 Model Calibration and Validation. The flowrates for the 0.60 and 0.80 relative depth cases were computed using best fit curves as described in section 2.2.6 Model Calibration and Validation. Table 2 provides the computed relative depths based on the average free surface elevations as well as the total flowrates (Q) as described in sections 2.2.6 and 3.1 Model Calibration and Validation. The first column of Table 2 denotes the relative depth case names based on nomenclature used by the Shiono et al. group, which are used to subsequently refer to the experimental cases across each row. Note that the actual computed relative depths differ slightly from the relative depth case names. The second column contains the computed relative depths based on the free surface elevations provided in Chan (2003).

Table 2: Relative depths and volumetric flow rates for each floodplain scenario and relative depth case

Relative Depth	Shiono et al.	Smooth		Low Vegetation Density		High Vegetation Density	
Case	Smooth dr	dr	Q (m^3/s)	dr	Q (m^3/s)	dr	Q (m^3/s)
0.00	-0.002	-0.005	0.00451	-	-	-	-
0.13	0.128	0.142	0.00595	0.131	0.00525	0.129	0.00484
0.20	0.205	0.205	0.00793	0.204	0.00718	0.206	0.00605
0.25	0.248	0.244	0.00991	0.249	0.00886	0.247	0.00688
0.29	0.295	0.293	0.01348	0.293	0.01116	0.293	0.008051
0.35	0.353	0.354	0.01982	0.352	0.01506	0.352	0.009935
0.40	0.403	0.403	0.0253	0.402	0.01901	0.402	0.01194
0.46	0.457	0.455	0.03312	0.457	0.02420	0.457	0.01460
0.50	0.497	0.497	0.04246	0.495	0.02820	0.495	0.01671
0.60	-	0.599	0.07657	0.603	0.04720	0.595	0.02356
0.80	-	0.796	0.2365	0.799	0.1210	0.798	0.04682

This range of relative depth cases is reasonable compared with observed relative depths in meandering compound stream systems in the real world. For instance, Fukuoka reports floods in meandering compound rivers in Japan with relative depths up to 0.76 (Fukuoka, n.d.). Finally, as an alternative to relative depth, relative flow area between overbank and inbank flows at the meander apex was also computing as shown in Equation (5) where Ar is the relative flow area, b_v is the valley width, and b_{mc} is the meandering main channel width. This formulation accounts for the widths of the main channel and floodplain which relative depth neglects.

$$Ar = \frac{h_{fp} \cdot b_v}{h_{fp} \cdot b_v + h_{bf} \cdot b_{mc}} \tag{5}$$

2.2.3 Grid and Mesh Conditions

The solver mesh was built on a Cartesian structured grid. Cartesian structured grids provide control over how the mesh is resolved. Within FLOW-3D® HYDRO, users can specify mesh planes with desired grid refinements along the X, Y, and Z directions. The meshing algorithm produces a gradient of grid refinement between mesh planes along the specified axis based on the values set at each mesh plane. The mesh grid was set at 0.01 m grid refinement in the longitudinal (X) and lateral (Y) directions to produce equal resolution of the input geometry along horizontal planes for all floodplain scenarios. In the vertical direction for the smooth floodplain models, mesh planes along the Z-axis with grid refinements of 0.01 m were specified at 0.01 m below the main channel bed elevation, at bankfull elevation (h_{bf}), and at the upper vertical limit (Z_{max}) at a distance above the desired free surface elevation (Z_{fs}) equal to the distance between Z_{fs} and h_{bf} as described in Equation (6).

$$Z_{max} = Z_{max} = 2Z_{fs} - h_{bf} \tag{6}$$

Preliminary model sensitivity to the mesh refinement revealed that increasing the grid refinement at the desired free surface elevation reduced temporal fluctuations in the free surface elevation as the flow developed. Therefore, a mesh plane with a grid refinement of 0.005 m was specified at the desired free surface elevation. For the vegetated floodplain cases, the same vertical grid refinements were used as described for the smooth scenario except an additional maximum plane with 0.01 m grid refinement was set at an elevation of 0.1 m for relative depths of 0.13 to 0.50. For relative depth cases of 0.60 and 0.80, the additional maximum plane was set at an elevation equal to Z_{fs} plus h_{bf}. This added mesh headroom ensured that the mesh resolution of the cylinders at the desired free surfaces was similar between relative depth cases.

2.2.4 Initial and Boundary Conditions

Within the FLOW-3D® HYDRO models, initial and boundary conditions represent the fluid conditions within the domain at the start of each simulation and the fluid conditions at the bounds of the fluid domain while the simulations are running, respectively. The solver requires the specification of these conditions, which are either known explicitly or assumed, to solve for the unknown values of the flow field across the domain and through time.

The initial conditions were set as a constant fluid free surface elevation based on the desired free surface elevations. Boundary conditions for the flow field were set at the vertical, longitudinal, and lateral minima and maxima. A symmetry condition was set at the vertical minimum. The vertical maximum was set to a pressure boundary condition with fluid fraction set to zero to represent a boundary open to the atmosphere. The lateral minimum and maximum were set as wall boundary conditions to represent the walls of the flume basin. At the upstream boundary, a volumetric flowrate boundary condition with a maximum free surface elevation represented the inflow condition at the head of the flume. A pressure boundary condition at the downstream boundary represented the free surface elevation at the tail of the flume. This downstream boundary condition free surface elevation was calibrated to be 102.5% of the desired free surface elevation for the overbank cases barring the bankfull case, which was set at 100% of the desired free surface elevation as discussed in 2.2.6 Model Calibration and Validation. Other than the volumetric flowrates at the upstream boundary conditions, the boundary conditions for each given relative depth case were the same between the smooth and vegetated floodplain scenarios. The input flowrates for the upstream boundary condition are summarized in Table 2. The input free surface elevations from Chan (2003) and from the model calibration for the initial and upstream boundary conditions as well as the adjusted values for the downstream boundary condition ($Z_{fs\ ds}$) are summarized in

Table 3.

Table 3. Initial, upstream boundary, and downstream boundary free surface elevation conditions

Relative Depth Case	Initial and Upstream Boundary Condition Z_{fs} (m)	Downstream Boundary Condition $Z_{fs\ ds}$ (m)
0.00	0.03991	0.03991
0.13	0.04587	0.04702
0.20	0.0503	0.05156
0.25	0.05319	0.05452
0.29	0.05670	0.05812
0.35	0.06180	0.06334
0.40	0.06696	0.06863
0.46	0.07373	0.07557
0.50	0.079528	0.081516
0.60	0.1	0.1025
0.80	0.2	0.2050

2.2.5 Model Solver

Once the mesh and initial conditions were set, the FAVORize tool in FLOW-3D® HYDRO was used to assign solid and fluid properties in the mesh domain based on the input solid information from the .stl files and the initial fluid height conditions. The FAVORize tool computes the area fractions of the fluid and solid geometry at the six planes bounding each grid cell as well as the volume fractions within the cell's control volume. The FAVORized geometries are shown in Figure 5 (a), (b), and (c) for the smooth, low vegetation density, and high vegetation density floodplain scenarios, respectively.

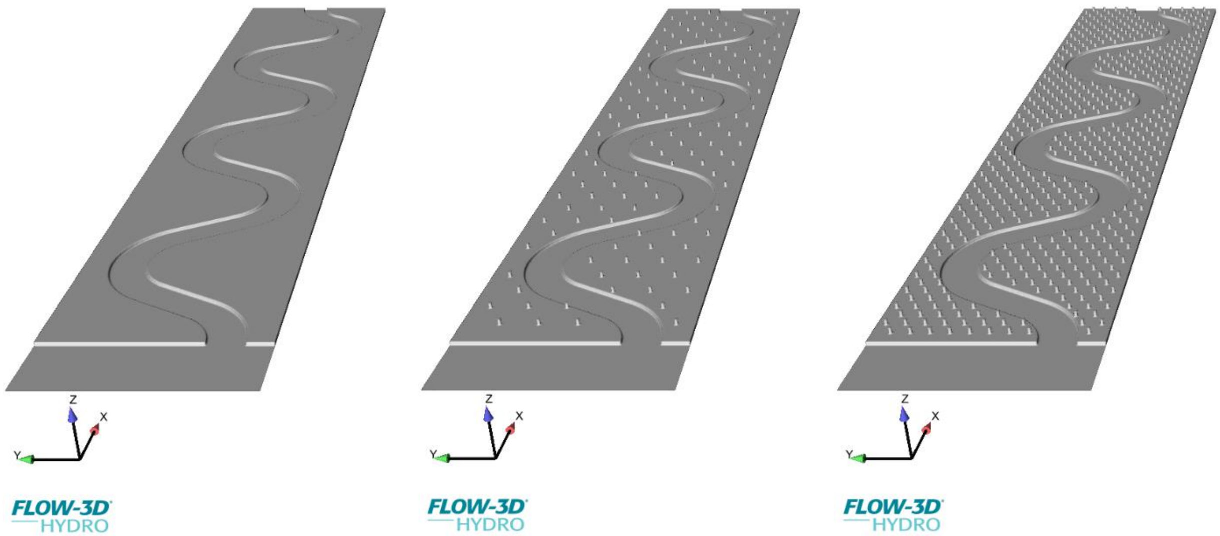

(a) (b) (c)

Figure 5. (a) Smooth, (b) low vegetation density, and (c) high vegetation density floodplain scenarios rendering in FLOW-3D® HYDRO

The renormalization group (RNG) k-epsilon model was selected as the turbulence model. Flow Science, Inc. considers this model to be one of their fastest and most robust turbulent models. The RNG k-epsilon turbulence model has been shown to be more effective than the standard k-epsilon turbulence model for representing flow separation and vortex shedding phenomena (Choudhury, 1993), which are expected to occur in meandering compound channels and flows around cylindrical elements, respectively. The RNG k-epsilon turbulence model used a rigorous statistical approach to arrive at the k-epsilon equations for the Reynolds-Averaged Navier Stokes (RANS) continuity and momentum equations (Yakhot & Orszag, 1986). The RNG k-epsilon turbulence model differs from the standard k-epsilon turbulence model in that it resolves multiple turbulent length scales rather than using a constant turbulent length scale (Smith & Woodruff, 1997). In the standard k-epsilon turbulence model, the constants are empirically derived, whereas in the RNG k-epsilon model these constants are arrived at explicitly.

The methodology of resolving the flow field near walls using a given turbulence model is of high importance in hydrodynamic modeling in flows bounded by a solid geometry such as the meandering compound channel and cylinder vegetation elements in the current study. In FLOW-3D® HYDRO at mesh cells where at least one face intersects the solid geometry, i.e., it is "partially or wholly blocked by a solid wall" (Flow Science, Inc., 2021), the turbulent kinetic energy, k_T, and dissipation of turbulent kinetic energy, ε_T, transport equations are formulated to consider the shear velocity, u_*, within these cells. These specific formulations of k_T and ε_T are shown in Equations (7) and (8), where *CNU* is a constant equal to 0.085 under the RNG k-epsilon formulation, κ is the von Karman constant taken as 0.4, and d is the normal distance from the wall. FLOW-3D® HYDRO computes shear velocity, u_*, with the logarithmic law of the wall equation shown in Equation (9) where u is the freestream velocity, ρ is the fluid density, and μ is the dynamic viscosity of the fluid. The fluid density, ρ, was set at 1,000 kg/m^3 and the dynamic viscosity was 0.001 kg/m/s based on the properties of water at 20° C. As a final note on the turbulence model selection, because the RNG k-epsilon model is a Reynolds-Averaged Navier Stokes (RANS) method, the Reynolds stresses are assumed to be isotropic and the flow field is smoothed out through time in the averaging processes.

$$k_T = \frac{u_*^2}{\sqrt{CNU}} \tag{7}$$

$$\varepsilon_T = \frac{u_*^3}{\kappa d} \tag{8}$$

$$u = u_* \left[\frac{1}{\kappa} \ln\left(\frac{\rho u_* d}{\mu}\right) + 5.0\right] \tag{9}$$

The 2nd order monotonicity-preserving momentum advection solver was selected as it is recommended for highly swirled flows which are assumed to occur in meandering compound channels and around vegetation stems. The total duration of model runs was 90 seconds with a solver time-step, which was dynamically computed within the model to optimize run time while preventing numerical instabilities, and a data output time step of 0.5 seconds.

2.2.6 Model Calibration and Validation

Numerical model parameters including roughness height and free surface elevation for the downstream boundary condition were calibrated to produce minimum errors in the predicted free surface elevations and average main channel streamwise velocities. Percent relative error and trends in the predicted free surface elevations and average main channel streamwise velocities were used to validate the numerical model results in comparison with the Shiono et al. physical experiment results for the smooth floodplain scenario base model. These calibrations and validations were performed on relative depth cases of 0, 0.20, 0.29, and 0.46 for the smooth floodplain scenario as these were the cases with reported cross sectional averaged streamwise velocities in the Shiono et al. results. Additionally, qualitative comparisons between the primary and secondary flow structures were used to validate the numerical model against physical model results. Average free surface elevations were also used to calibrate the discharges for the vegetated floodplain cases and the bankfull case.

Free Surface Elevation

The free surface elevation was measured at the six meander apexes in the valley center for the overbank cases and at the center of the main channel at the six crossover sections for the bankfull case. The free surface elevations, sampled at each probe every 0.5 seconds from t = 80 seconds to t = 90 seconds, were temporally averaged and compared to the experimental observations. The free surface elevations were averaged across the six probes. These final averaged free surface elevations were also used to compute the relative depths used later in this study.

Quantitative Comparisons of Main Channel Streamwise Velocities

Cross-section and region-averaged streamwise velocities in the main channel below the bankfull level were used as a secondary basis for calibrating model parameters and validating model results. Based on the methods of the Shiono et al. group, inbank flow velocities were observed up to the bankfull level at seven cross sections along the main channel at the fifth downstream half meander shown in Figure 6.

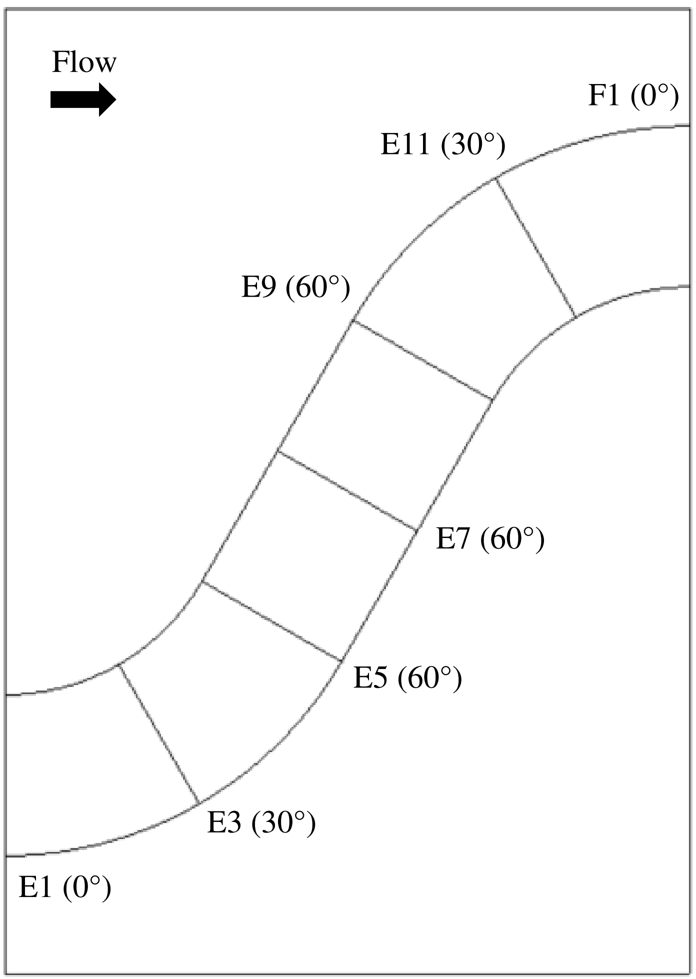

Figure 6: Study half meander with study cross sections E1 through F1 with crossing angles after Chan (2003)

The region of the main channel between E1 and E5 is referred to as the “upstream bend”, between E5 and and E9 as the “crossover”, and between E9 and F1 as the “downstream bend”. The cross sections E1 and F1 are referred to as “apex sections” with 0° crossing angles, E3 and E11 are “bend sections” with a 30° crossing angles, and E5, E7, and E9 are the “crossover sections” with 60° crossing angles. The X and Y-components of the flow velocity were spatially averaged over the-cross-section planes. The section averaged velocity normal to the cross sections was computed using the X and Y-components of the section-averaged velocities and the crossing angle of the given cross section to produce cross section averaged streamwise velocities. The Shiono et al. experimental results for cross section averaged streamwise velocities for relative depths of 0, 0.20, 0.29, and 0.46 were extracted from Figure 5.33 in Chan (2003) using the Engauge Digitizer program. The predicted numerical model cross section averaged streamwise velocity results were plotted against the digitized Chan (2003) experimental results.

For each calibration and validation case, the section averaged streamwise velocities were then averaged together to produce average main channel streamwise velocities. The Shiono et al. experiment’s average main channel streamwise velocities are provided in Table 4.1 of Spooner (2001). The percent relative error in the numerically predicted section and region-averaged streamwise velocities versus the Shiono et al. model results were computed.

It should be noted that in the Shiono et al. experiments, the velocity field was measured at points along the cross-sectional planes with a vertical spacing of 0.005 m and horizontal spacings of 0.02 m except near the main channel walls where the horizontal spacing was 0.01 m. The locations of computed velocity values in the current numerical study were defined by the mesh grid refinement of the numerical model. In the Shiono et al. experiments, there were vertical gaps of 0.005 m between the bed and the lowest elevation measurements above the bed as well as lateral gaps of 0.01 m between the main channel walls and the measurements. These physical boundary gaps in the measurements were reflected in the numerical modeling post-processing methods for model calibration and validation. The full main channel extents were considered for subsequent analyses.

Roughness Height Calibration

The roughness height of the solid geometry was calibrated to produce average free surface elevations and uniform free surface slopes measured by the Shiono et al. group for their smooth floodplain scenarios (Spooner, 2001). Roughness heights of 0, 0.001, and 0.002 m were run for the relative depth cases of 0.20, 0.29 and 0.46 smooth floodplain scenario. The relative error in average free surface elevation and main channel section-averaged streamwise velocity were compared between the roughness height scenarios to inform the roughness height chosen for the model.

A roughness height of 0.002 m reduced the relative error in the average free surface elevation and a roughness height of 0 m reduced the relative error the sectional averaged streamwise velocities. The final selected roughness height was 0.001 m to minimize both the errors in both the average free surface elevation and the sectional-averaged streamwise velocities. This final roughness height is reasonable considering the conditions of the Shiono et al. smooth floodplain physical experiments. In the Shiono et al. experiments, the sand grain size composing the fixed, flat bed was 0.000855 m which is approximately equal to a roughness height of 0.001 m. The bed was fixed with cement, the floodplain was formed of painted foam, and the valley walls were formed of Perspex (Chan, 2003; Spooner, 2001). The main channel and floodplain were noted to have a “homogenous surface roughness” for the smooth floodplain cases (Chan, 2003). Unnoted obstacles and imperfections in the main channel, floodplain, and valley walls may have introduced roughness into the Shiono et al. experimental setups.

Tailwater Boundary Conditions

The tailwater or downstream boundary conditions were set as a pressure boundary as discussed in Section 2.2.4 Initial and Boundary Conditions. The model was first run with the pressure boundary set at the desired uniform free-surface elevation. The free surface elevation at the downstream boundary was then altered to reduce the error in free-surface elevation in subsequent iterations of the model so that the longitudinal free surface was approximately parallel with the bed and floodplain surfaces. Increasing the free surface elevation at the downstream boundary condition by 2.5% for the overbank cases was found to reduce the error in free surface elevation predictions and flatten the free surface slope. The downstream free surface elevation for the bankfull case was kept at the desired free surface elevation.

Cylinder Scenario and Bankfull Volumetric Flowrate Calibration

The volumetric flow rates for the vegetated floodplain cases were assumed to be lower than those in the smooth cases for the same relative depths. The volumetric flow rate for each relative depth below 0.60 for each floodplain vegetation density case was calibrated to minimize percent relative error in the desired average free surface elevation. The final volumetric flowrates (discharges) were estimated using a bracketing root-finding technique that used two initial guess flowrates that produce free surface elevations above and below the desired value. Initially, two guess flowrates were set at 25% increments of the smooth floodplain flowrates at the same relative depth, i.e., either 25, 50, 75, or 100% of the smooth floodplain flowrates. If one of the percent relative errors was negative and the other was positive, the two guess discharges were assumed to bracket the desired flowrate. If both percent relative errors were negative, then the greater flowrate became the new low flowrate and a new model was run with a higher increment of the smooth floodplain flowrate. The opposite was performed if both percent errors were positive. Once the bracketing flowrates were found, the final flowrate was solved for by linearly interpolating between the bracketing flowrates and percent relative errors to produce a desired percent error of 0%. The newly interpolated flowrate was then run in the model. The percent relative error in free surface elevation was computed for the final interpolated flowrate models to verify that they were in acceptable bounds.

A similar bracketing technique was used to calibrate the near bankfull discharge because the free surface elevations produced using the designated flowrate from Chan (2003) produced flows that significantly spilled onto the floodplain for the smooth model. It was assumed that relative errors in flowrate measurements were likely higher for low flows so the adjustment in bankfull discharge is assumed to be reasonable.

High Relative Depth Discharge Calibration

Once the flowrates for the overbank relative depth cases of approximately 0.13, 0.20, 0.25, 0.29, 0.35, 0.40, 0.46, and 0.50 had been calibrated and run for all floodplain roughness scenarios, exponential curves were fit to the overbank relative depth-discharge data. Equations describing these fit curves are provided in section 3.2 Stage-Discharge and were used to compute the discharges for the relative depth cases of 0.60 and 0.80 for each floodplain scenario.

Quantitative Validation

The final base smooth floodplain numerical model results were validated against results described in Spooner (2001), Chan (2003), and Shiono et al. (2008). The average free surface elevation percent relative errors were computed along with the linearly regressed free surface slope for the relative depth cases of 0, 0.20, 0.29, and 0.46. Because the linearly regressed free surface slope was computed under the altered gravity conditions with a zero-slope bed, a corrected free surface slope was computed to represent what the free surface slope would be in reality with a bed slope of 0.002 and a normal vertical gravity term. The pointer probe used in the Shiono et al. experiments had a reported error margin of 0.1 mm (Shiono et al., 2008). In their experiments, the longitudinal free surface slope was controlled by three tail gates to produce a uniform free surface elevation at the meander apexes along the valley centerline. The longitudinal free surface slope for the experiments was reported to be within +/- 2% of the valley slope. The cross section and region averaged main channel streamwise velocities were compared with results of Spooner (2001) and Chan (2003) for relative depth cases of 0, 0.20, 0.29, and 0.46. The mean point velocities calculated from laser Doppler anemometer (LDA) data by the Shiono et al. group were reported to have an error of +/-3% (Spooner, 2001).

To our knowledge, error in the volumetric discharge in the Shiono et al. experiments was not reported by the previous researchers in the available publications. For the final overbank smooth floodplain scenario validation model setups, the model was run with the specified volumetric flowrate as well as with flowrates equal to +/- 5% of the specified flowrate to provide error estimates for the free surface elevations, sectional averaged main channel streamwise velocities, and region averaged main channel streamwise velocities. Error estimates were also produced for the measured data from the Shiono et al. models based on the reported errors associated with each value. Where no measures of uncertainty were reported in the Shiono et al. experiments, +/-5% error was applied to the measured data from these physical experiments. The current numerical and Shiono et al. experiment results with error estimates were compared to validate the numerical model's ability to predict the observed values.

Qualitative Validation

In Figures 6(a), 7(a), and 8(a) from Shiono et al. (2008) plots of the streamwise velocity contours (primary flows) at cross sections E1 through F1 of the Shiono et al. experiments are shown. They also provided plots of the resultant vectors parallel to the same cross sections (secondary flows) in their Figures 9(a), 10(a), and 11(a). Chan (2003) provides streamwise velocity contours and streamwise at cross sections E1, E7, and F1 same relative depths as Shiono with the addition of plots for the 0.20 relative depth case in their Figures 5.14 and 5.24. These figures from Shiono et al. (2008) and Chan (2003) were compared with combined streamwise velocity contour and parallel resultant velocity vector plots from the current numerical model results. The methodology for producing the contour and vector plots is described in Section 2.3 Primary and Secondary Main Channel Flows. Note that for the plots in Shiono et al. (2008) and Chan (2003) are viewed from the downstream perspective looking upstream whereas the plots in the current study are viewed from the upstream perspective looking downstream. Therefore, the cross-section plots for Shiono et al. experiment and current numerical experiments should be mirror images of each other along the vertical centerline.

2.3 Data Post-Processing

Results data were exported from FLOW-3D® HYDRO to be post-processed in MATLAB scripts and FlowSight®. Probes at single points in space, 2D clips along surfaces, and 3D clips in volumes were used to extract and visualize output data from FLOW-3D® HYDRO at defined locations. The built-in calculator tool in FlowSight® was used to compute additional various scalar and vector quantities from the model outputs.

Temporal averaging over the last 10 seconds of the model was used for free surface elevation measurements. The majority of the results analysis other than the free surface elevation measurements was performed on instantaneous data at the final model time of 90 seconds at the fifth downstream half meander where the Shiono et al. group collected much of their reported data in their flume experiments (Chan, 2003).

For consistency, outer bend refers to the main channel bank that curves outward within the main channel at the apex section E1 up to the central crossover section, E7. Inner bend refers to the bank that curves inward at the apex section up to the central crossover section. At the central crossover section at E7, banks are simply referred to as left and right bank. Downstream and upstream of the central crossover section, the bends are referred to as the downstream bends and upstream bends, respectively. Outer and inner half of the channel refer to the flow regions on either side of the channel centerline. Overbank and inbank refer to the flow regions above and below bankfull elevation at 0.04 m as indicated by the dashed red line in the figures. Interior cross section refers to cross sections E3, E5, E7, E9, and E11 which lie between apex sections E1 and F1. For the interior cross sections, the left and right banks are adjacent to the upstream and downstream floodplains, respectively.

2.3.1 Stage-Discharge

Total volumetric flowrate was plotted versus relative depth as a representation of the stage-discharge relationships for each of the floodplain roughness scenarios. Exponential curves were fit to the overbank discharge data versus relative depth data for the overbank flow cases. Volumetric flowrate was also plotted versus relative area to capture information about the main channel and floodplain widths that is not captured by relative depth.

The characteristic velocity, U_s, was defined as the total discharge (Q) divided by the total cross-sectional flow area (A) shown in Equation (10). The average free surface elevations computed in the section 2.2.6 Model Calibration and Validation were used to compute the cross-sectional flow area, which was taken across the valley width at the bend apex assuming a constant, uniform free surface shown in using Equation (11) where B_V is the valley width, Z_{FS} is the computed average free surface elevation, Z_{BF} is the bankfull elevation, B_{MC} is the main channel width, and h_{BF} is the bankfull depth. For the vegetated floodplain models, the vegetation stems which intersect the meander apex were not considered in the cross-sectional area approximations.

$$U_s = \frac{Q}{A} \tag{10}$$

$$A = B_V * (Z_{FS} - Z_{BF}) + B_{MC} * h_{BF} \tag{11}$$

2.3.2 Main Channel Streamwise Velocities

As in the Model Calibration and Validation section, the channel streamwise cross section and region averaged velocities were analyzed at the same cross sections along the same half meander described previously. Near bed and near wall velocities were included in the further analyses as opposed to the calibration and validation methodology which excluded velocity values near the walls and bed.

2.3.3 Boundary Shear Stress

Using MATLAB and the calculator tool in FlowSight, the boundary shear stress magnitude, τ, was computed in the main channel from the shear velocity at the cell centers of first layer of grid cells centers above the main channel bed, Z = 0.005 m, with Equation (12). The main channel boundary shear stresses were spatially averaged over the study section half meander in FlowSight as well as visualized in contour plots in MATLAB and in line plots along each of the seven study cross sections. The “distance from the wall measured in viscous lengths” (Pope, 2000), y^+, was computed in FLOW-3D® HYDRO with the absolute distance from the wall, *y*, the shear velocity, u_*, and the kinematic fluid viscosity, *v*, in Equation (13). The values of y^+ were checked to ensure that they were generally within the log law region typically assumed to be between $30 < y^+ < 300$. The average main channel boundary shear stresses were also made non-dimensional with the fluid density and the square of the characteristic velocity, U_s, described in section 2.3.2 Main Channel Streamwise Velocities to produce non-dimensional average main channel boundary shear stresses, τ_*, as shown in Equation (14).

$$\tau = \rho u_*^2 \tag{12}$$

$$y^+ = \frac{y u_*}{\nu} \tag{13}$$

$$\tau_* = \frac{\tau}{\rho U_s^2} \tag{14}$$

2.3.4 Primary and Secondary Main Channel Flows

Primary flows in the main channel including the overbank layer were analyzed using contour plots of the streamwise velocity normalized by the character velocity at the seven cross sections. The resultant vectors of the lateral and vertical components of the normalized velocity were plotted on top of the streamwise velocity contour plots so the secondary flow structures could be analyzed as well.

To produce the normalized streamwise contour and cross stream vector plots, the 3D velocity field values were extracted from the seven cross sections using FlowSight. In MATLAB, velocity components were interpolated along a uniform grid at the cross sections from the extracted 3D velocity field. The horizontal components of velocity were corrected to produce the resultant streamwise velocity component normal to the cross sections. The resultant vectors parallel to the cross sections were computed from the horizontal velocity components which were corrected to be parallel to the cross-sectional surfaces and from the vertical component of velocity.

The velocities normal and parallel to the cross-sectional velocities were normalized by a characteristic velocity described in section 2.3.2 Main Channel Streamwise Velocities for each case, similar to the methods presented by Shiono and Muto (1998). The velocity vectors were then scaled by 0.04 for the overbank cases and 0.3 for the bankfull cases to improve plot legibility. The horizontal and vertical axes representing the vertical and lateral coordinates within the main channel were normalized with the bankfull depth (h) of 0.04 m which is reflected in the final velocity vector scaling.

2.3.5 Layer-Averaged Flow Velocity Field

The 3D velocity field data were exported from FLOW-3D® HYDRO. The X and Y-direction velocity data were interpolated on a structured grid. The interpolated horizontal velocity component data were then vertically averaged at each horizontal coordinate along the structured grid separately in the lower flow layer below bankfull level and the upper layer above the bankfull level. The partitioning of flow regions at the bankfull level and subsequent layer-averaging has been employed by other researchers (Shiono and Muto, 1998, Chan 2003, Sellin et al. 1993). Researchers have reported that at high overbank flow depth, the lower and upper flow layers followed the main channel and floodplain flow velocity angles respectively thus a horizontal shear layer likely forms separating the two layers (Sellin et al., 1993). However, Shiono and Muto (1998) note that at low relative depths this upper- and lower-layer sectioning may not always be adequate because the two layers are more interdependent at low relative depths compared with at high relative depths. Note that in describing the physical regions within the flow field, the floodplain adjacent to the left bank of the main channel will be referred to as the 'upstream' floodplain and the floodplain adjacent to the right bank will be referred to as the 'downstream' floodplain.

3 RESULTS

3.1 Model Calibration and Validation

Free Surface Elevation Validation

The predicted free surface elevations percent relative errors for the smooth floodplain validation cases are shown for the bankfull case in Figure 7 and Figure 8 for the overbank cases with relative depths of 0.20, 0.29, and 0.46. The percent relative error in the free surface elevation predictions were within +/-7% for the bankfull case and within +/-1% of the measured values for the overbank cases. The percent relative error in the free surface elevation generally decreased as longitudinal distance along the valley increased for the 0.29 and 0.46. The computed relative depths, average free surface elevation percent relative error, linearly fit free surface slopes from the model results under the modified gravity term conditions, and linearly fit free surface slope corrected for a bed slope of 0.002 and normal vertical gravity conditions are summarized in Table 4. Note that positive slopes indicate that the free surface elevation is decreasing moving down-valley.

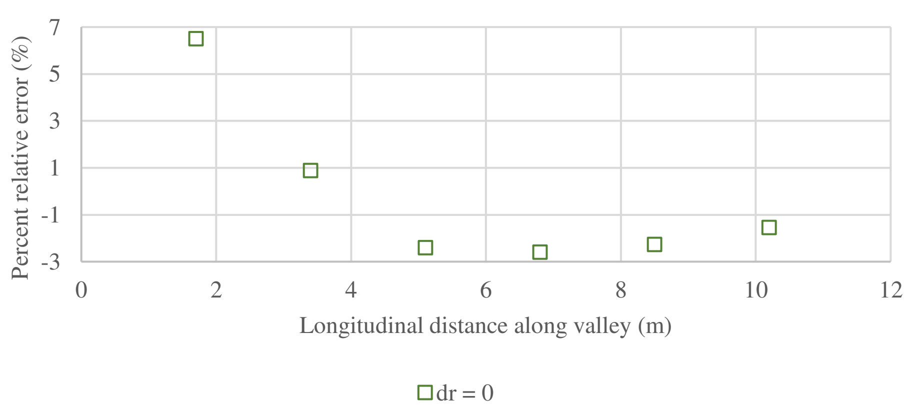

Figure 7. Percent error in free surface elevation for the smooth floodplain bankfull validation case

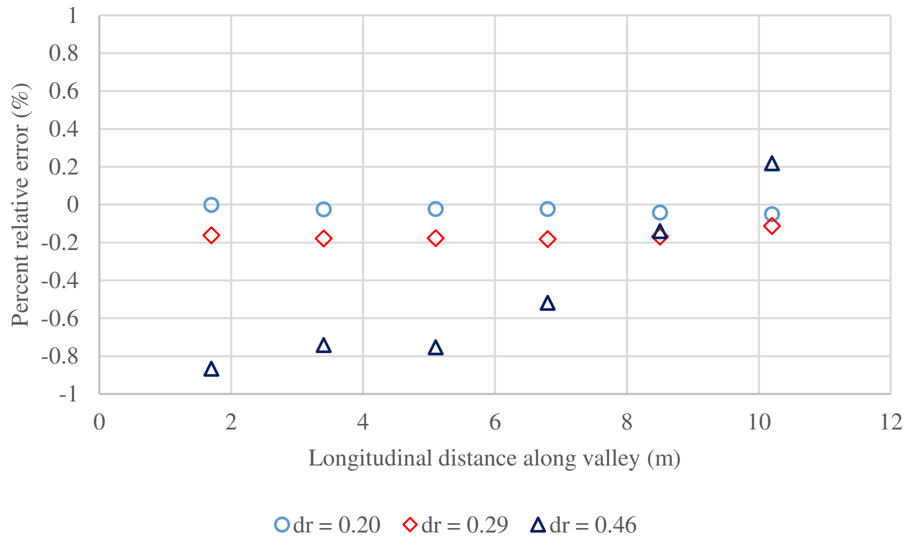

Figure 8: Percent error in free surface elevation for the smooth floodplain overbank validation cases

Table 4: Free surface slopes values from linear regression

Relative Depth Case	Computed dr	Average Free Surface Elevation Relative Error (%)	Free Surface Slope with Adjusted Gravity	Corrected Free Surface Slope
0	-0.005	-0.23	3.34E-04	0.00167
0.20	0.205	-0.03	2.48E-06	0.00200
0.29	0.293	-0.16	-2.58E-06	0.00200
0.46	0.455	-0.47	-9.26E-05	0.00191

The average free surface elevation for all the validation cases was computed. The linearly fit free surface slopes under the altered gravity component were on the of on the order of 10^{-4} and 10^{-6} which is relatively close to zero. The free surface slope corrected to represent conditions with a sloped bed and gravity only in the vertical direction was close to the bed slope of the Shiono et al. experiments (0.002) indicating that uniform flow conditions were approximated well in the numerical models.

Main Channel Velocity Validation

The main channel region averaged velocities for the smooth floodplain validation cases are plotted in Figure 9. For the overbank cases, the agreement between modeled and measured velocities increased with relative depth. The predicted main channel averaged streamwise velocities are lower for the overbank cases and greater for the bankfull case. The minimum in main channel averaged streamwise velocity is important to note as this is a key feature of interest in this study. The reported main channel averaged streamwise velocity for the Shiono et al. experiments was greater in magnitude and occurred at a higher relative depth than in numerically modeled results. Also note that for the bankfull case, the error bars for the 95% and 105% discharge were both positive so the greater of the two is displayed. The main channel section averaged velocities for the Shiono et al. smooth floodplain experiments and for the current numerical experiments are plotted with error bars in Figure 10 for relative depth cases of (a) 0, (b) 0.20, (c) 0.29, and (d) 0.46. Note that the "Section ID" is modeled after the plot style of Chan (2003). Sections IDs 1 through 11 correspond cross sections E1 through E11, and Section ID 13 corresponds with cross section F1. The closest agreement between modeled and measured data was seen for dr = 0.29 and 0.46 with error bars not intersecting at sections E1 and E7 for dr = 0.29 and E1 and E9 for dr = 0.46. There are no intersecting error bars for the low overbank relative depth case, dr = 0.20. However, the general trends in the section averaged streamwise velocity were predicted well for all relative depths.

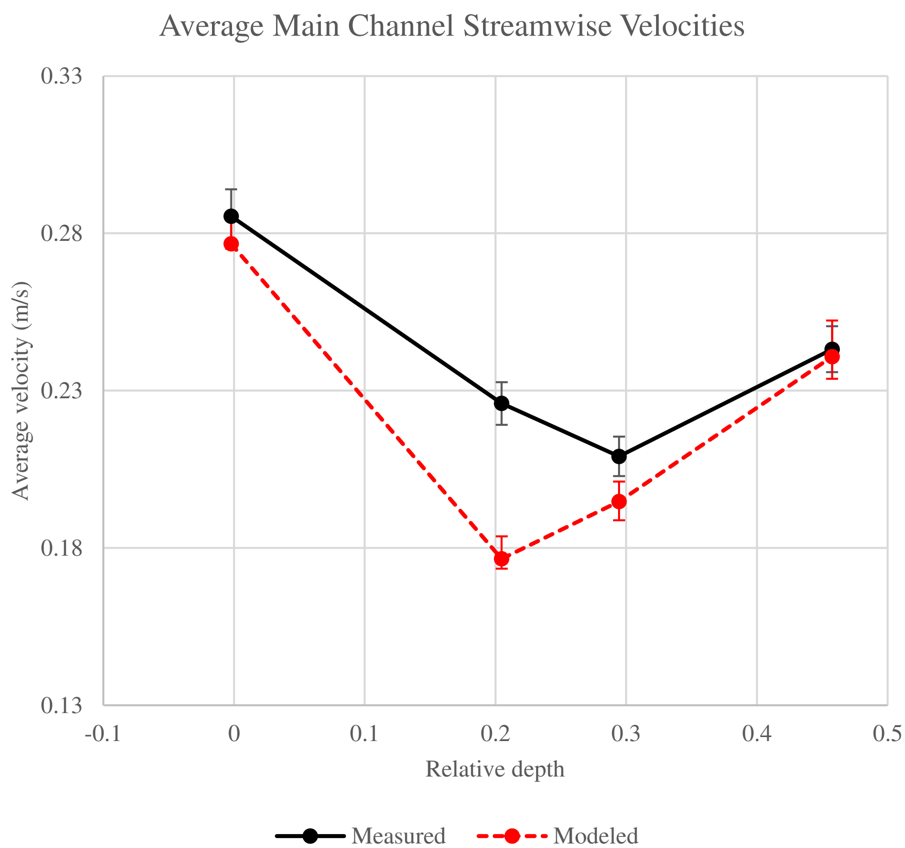

Figure 9: Average main channel streamwise velocities measured from Shiono et al. and numerically modeled in current study

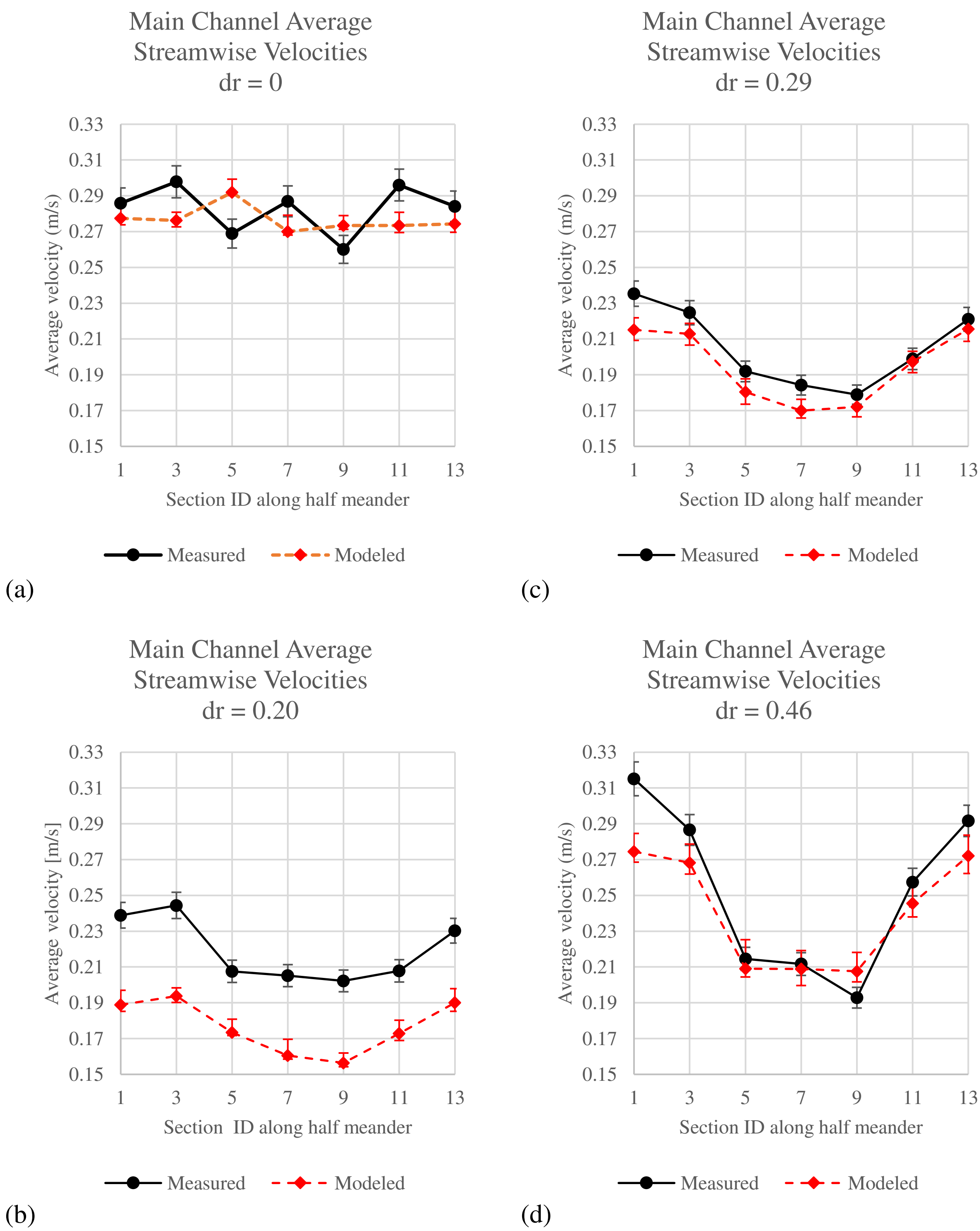

Figure 10. Main channel cross section averaged velocities along study half meander measured from Shiono et al. and numerically modeled in current study for relative depth scenarios of (a) 0, (b) 0.20, (c) 0.29, and (d) 0.46

Qualitative Validation of Primary and Secondary Flow Structures

In general, the numerical models reproduced the primary and secondary flow structures provided in Chan (2003) and Shiono (2008) are shown for the validation cases in Figure 11, through Figure 14 for primary flow structures and Figure 15 through Figure 18 for secondary flow structures for relative depth cases of 0, 0.20, 0.29, and 0.46, respectively. The current numerical model results for the normalized streamwise velocity contours (primary flow structures) and resultant vectors parallel (secondary flow structures) to each study cross section for relative depth cases of 0, 0.20, 0.29, and 0.46 are shown in Figure 19 through Figure 22, respectively. Particular focus for the primary flow structure comparisons was placed on identifying the character of the high streamwise velocity 'filament' or the somewhat continuous region of high velocities through the half meander as well as the 'lobes' or localized regions of low streamwise velocity. For the secondary flow structure analysis, the character of rotational flow secondary flow cells and cross stream currents were compared. Note that the plots from Chan (2003) and Shiono (2008) were plotted with the left bank on the right side and the current study plots were plotted with the left bank on the left; therefore, the figures are mirror representations of each other. Also note that the axes of the current study plots are normalized by the bankfull depth. The following section describes the agreement between the Shiono et al. results and those of the current study.

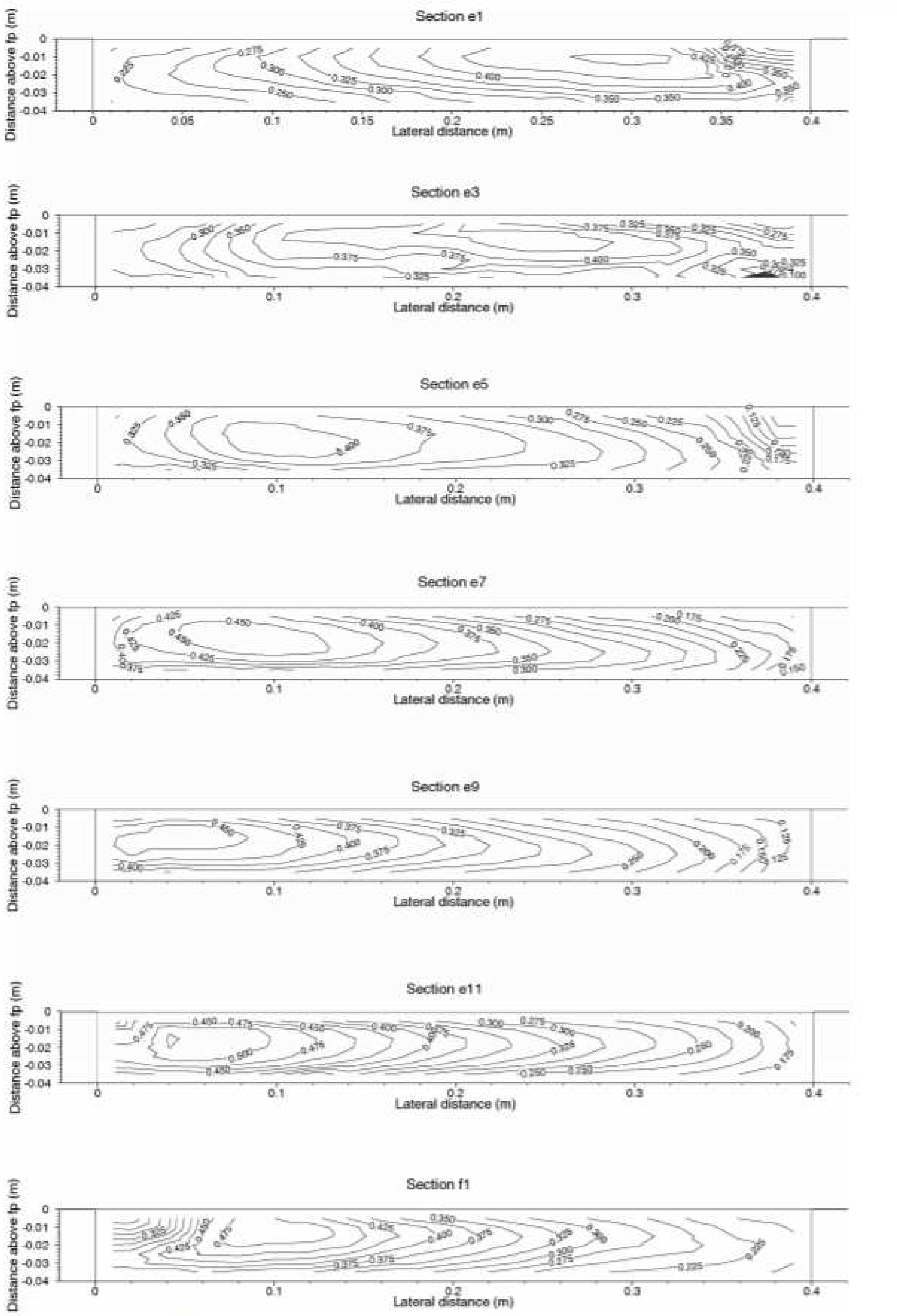

Figure 6(a) Longitudinal velocity (U) for the non-mobile bed case, $DR = 0.0$.

Figure 11. Primary flow structure plots for dr = 0 (bankfull) case from Figure 6(a) of Shiono et al. (2008)

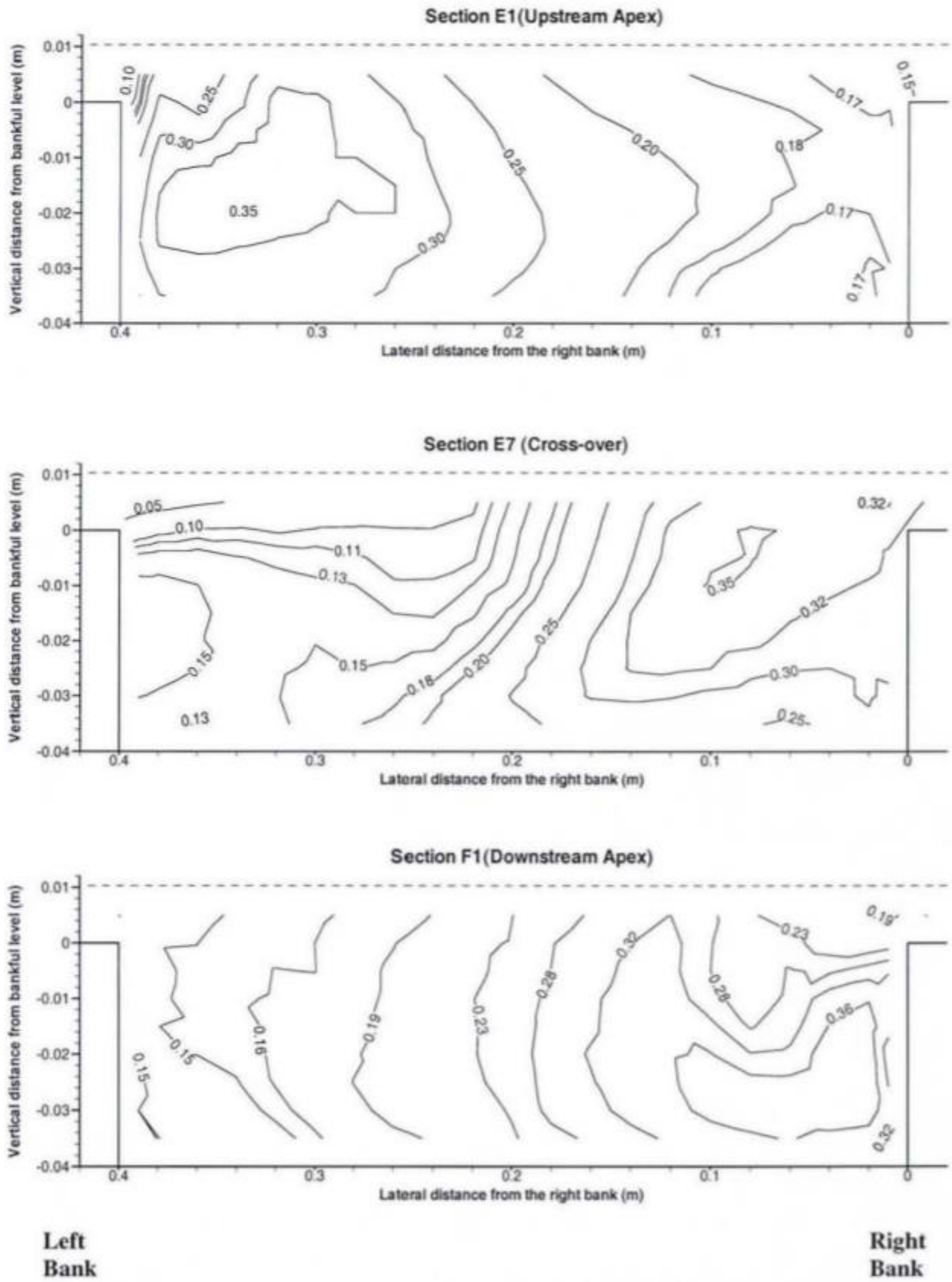

Figure 5.14: Longitudinal velocity distribution at Dr=0.20 for G4 case

Figure 12. Primary flow structure plots for dr = 0.20 case from Figure 5.14 of Chan (2003)

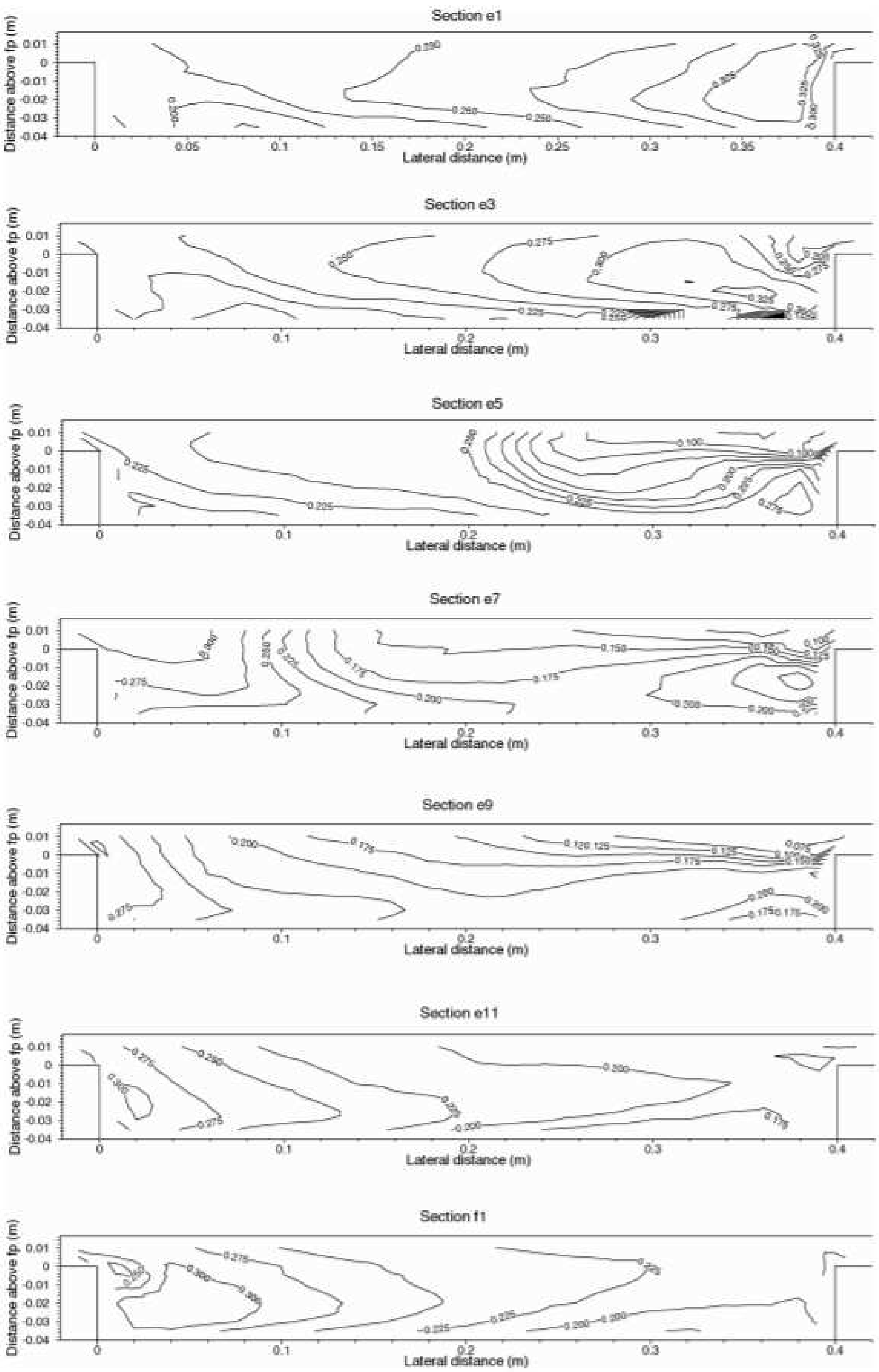

Figure 7(a) Longitudinal velocity (U) for the non-mobile bed case, $DR = 0.3$.

Figure 13. Primary flow structure plots for dr = 0.29 case from Figure 7(a) of Shiono et al. (2008)

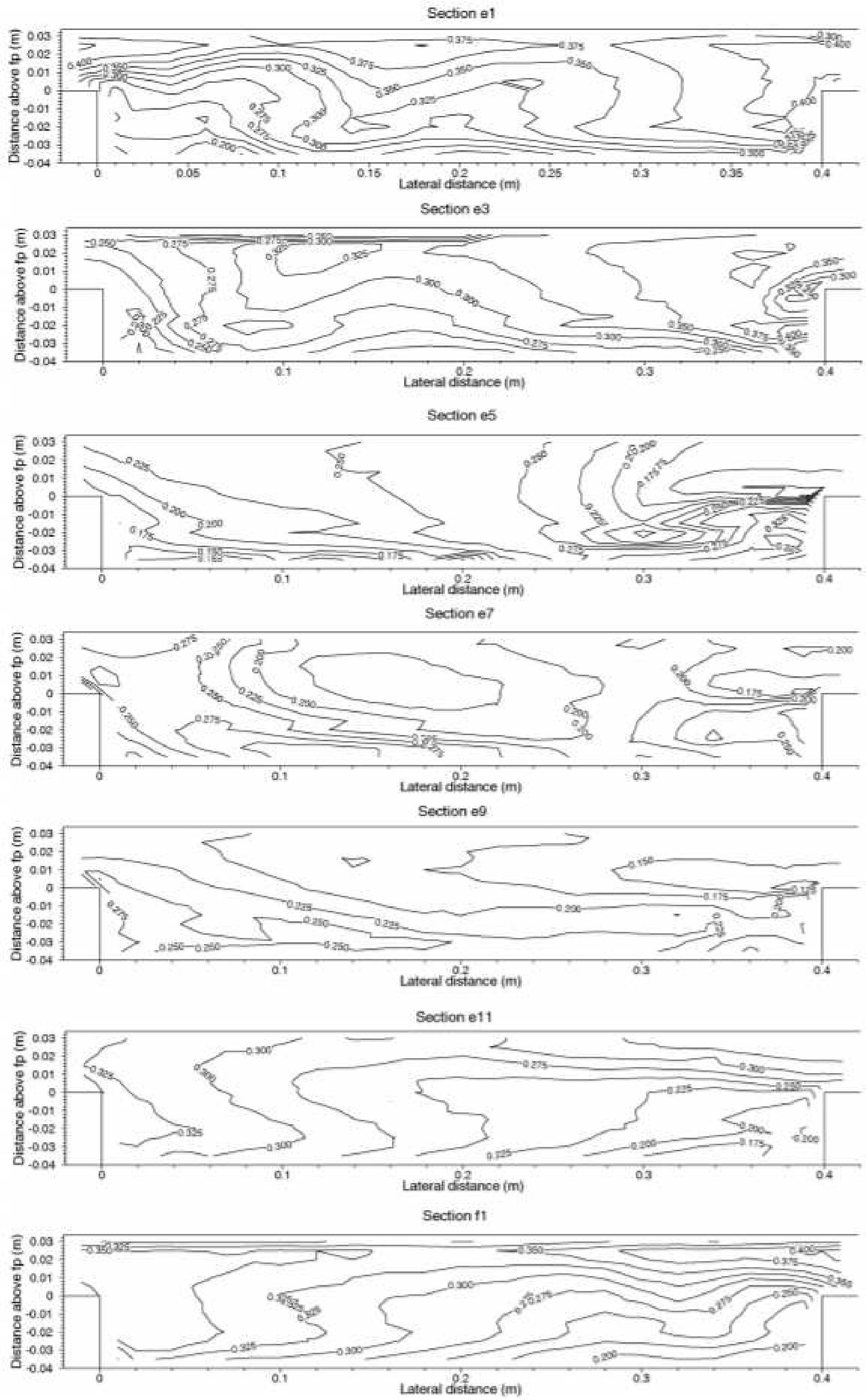

Figure 8(a) Longitudinal velocity (U) for the non-mobile bed case, $DR = 0.45$.

Figure 14. Primary flow structure plots for dr = 0.46 case from Figure 8(a) of Shiono et al. (2008)

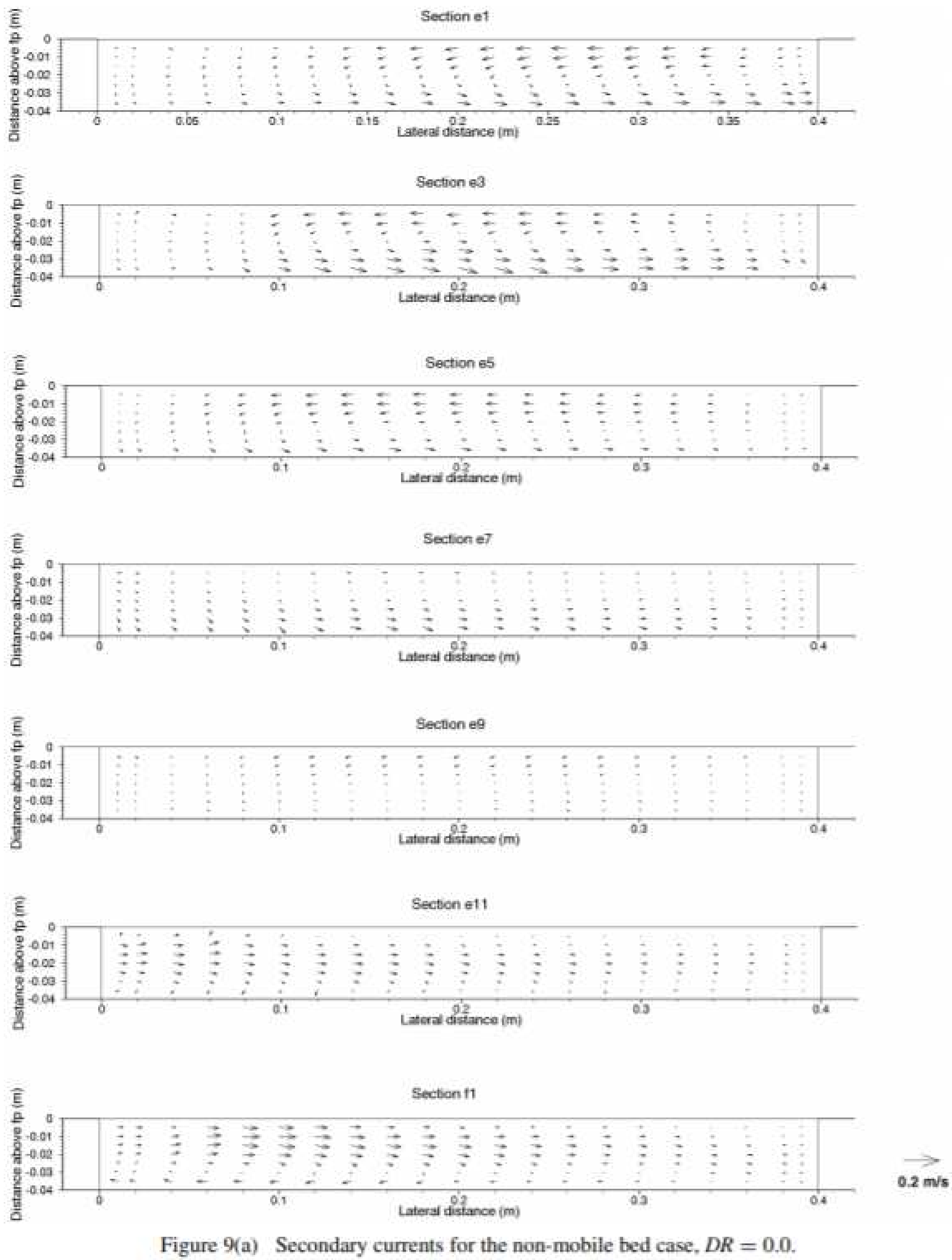

Figure 15. Secondary flow structure plots for dr = 0 (bankfull) case from Figure 9(a) of Shiono et al. (2008)

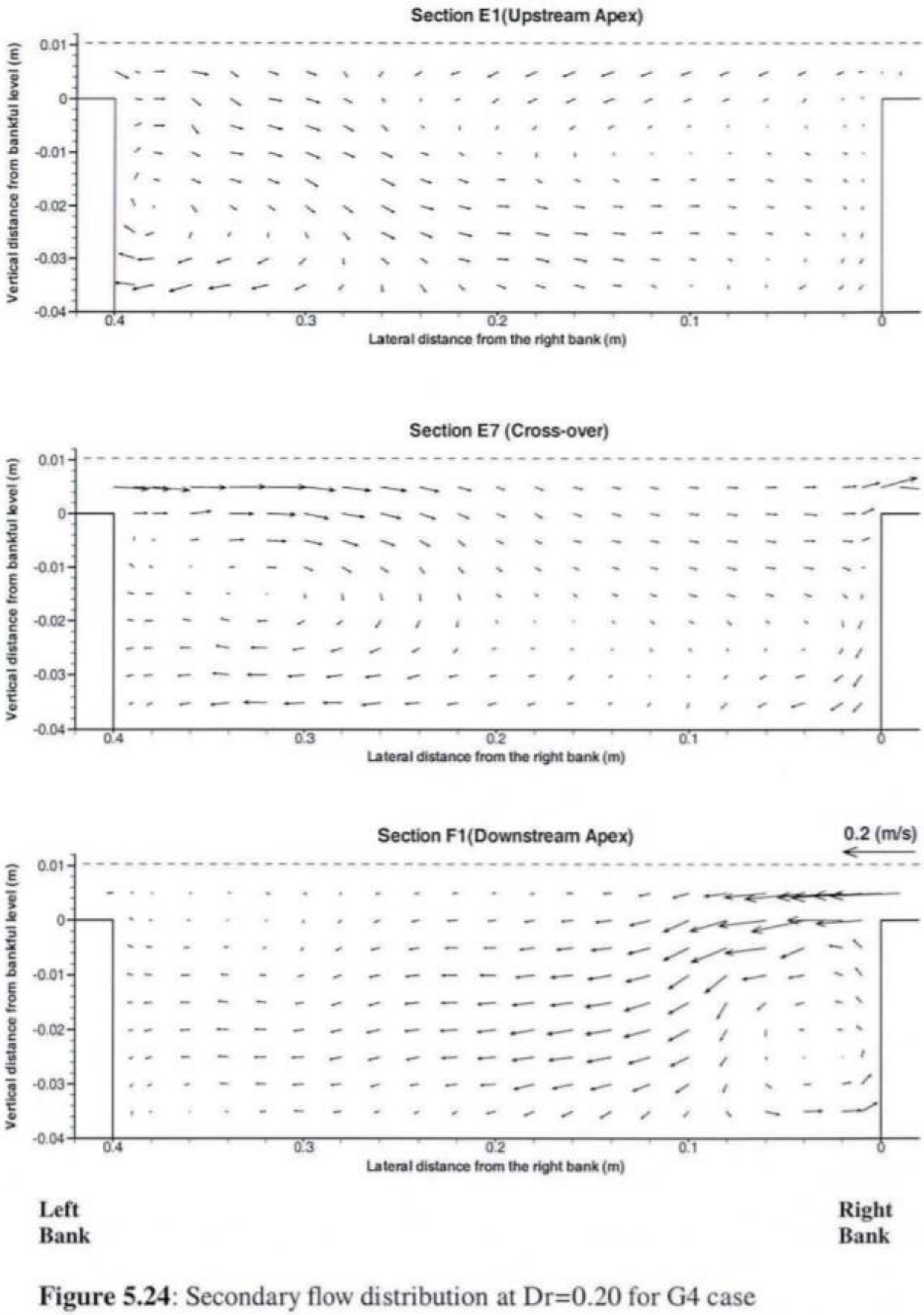

Figure 16. Secondary flow structure plots for dr = 0.20 case from Figure 5.24 of Chan (2003)

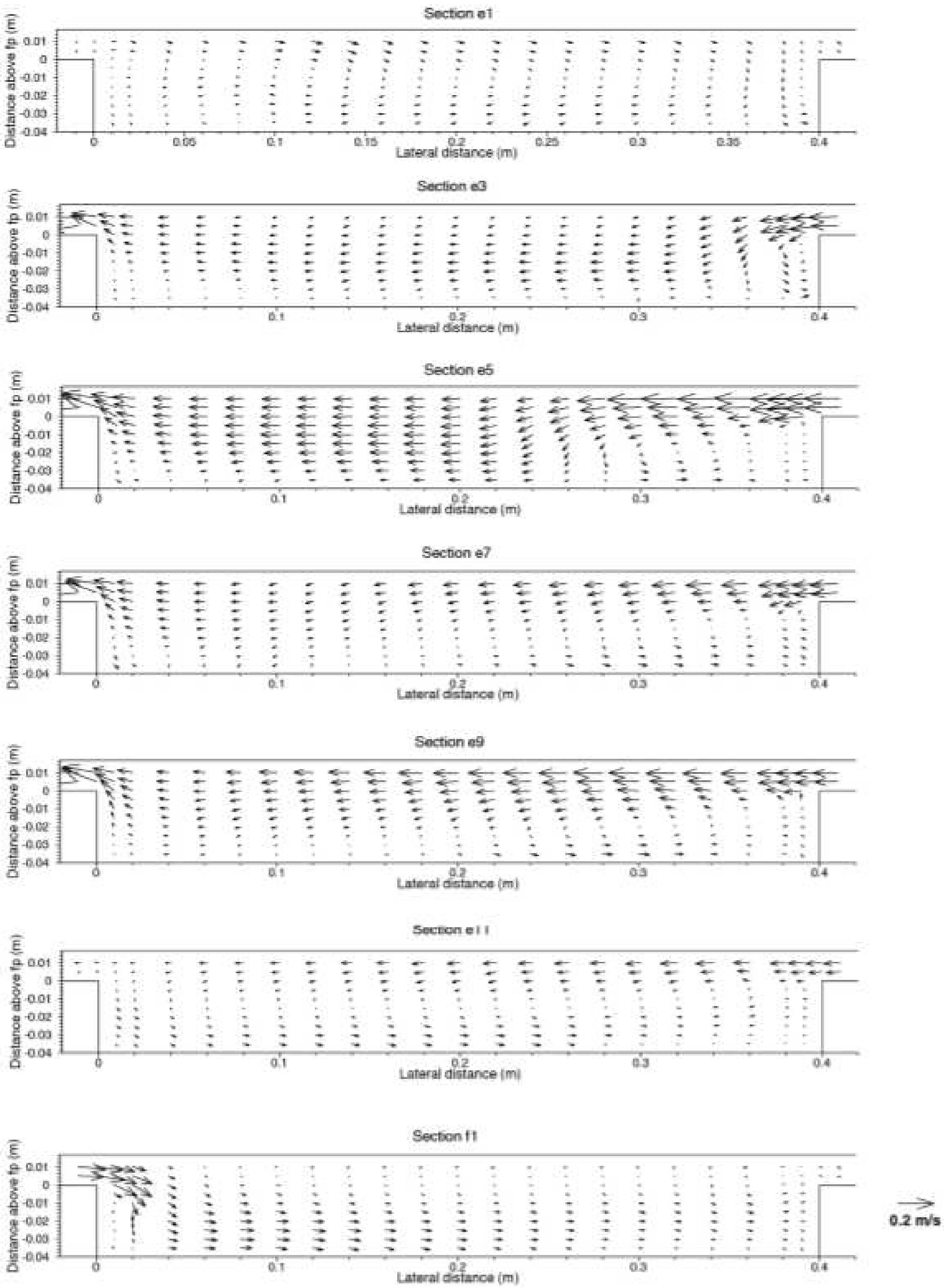

Figure 10(a) Secondary currents for the non-mobile bed case $DR = 0.3$.

Figure 17. Secondary flow structure plots for dr = 0.30 case from Figure 10(a) of Shiono et al. (2008)

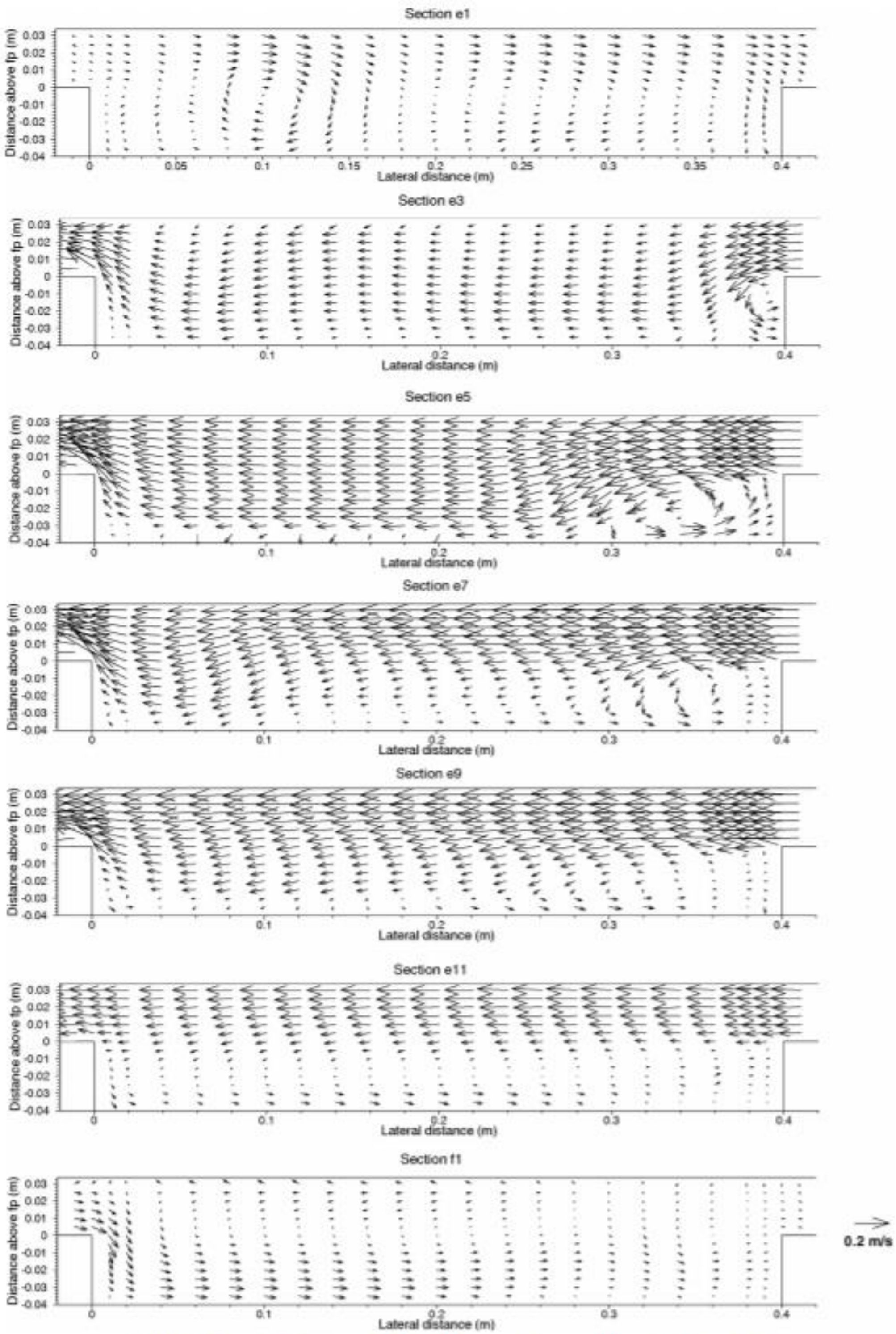

Figure 11 Secondary currents for the non-mobile bed case, $DR = 0.45$.

Figure 18. Secondary flow structure plots for dr = 0.46 case from Figure 11 of Shiono et al. (2008)

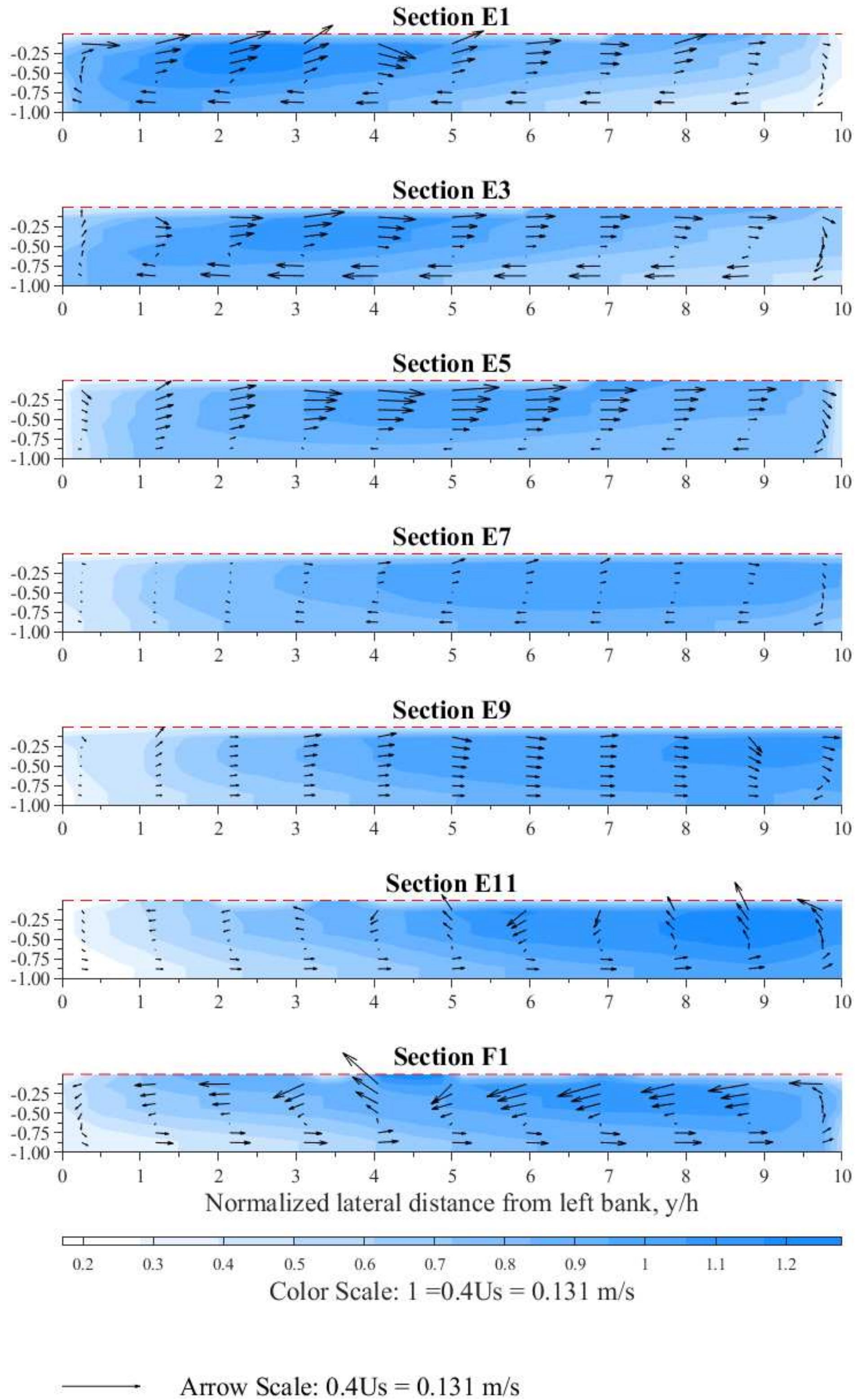

Figure 19. Primary and secondary flows for smooth floodplain dr = 0 (bankfull)

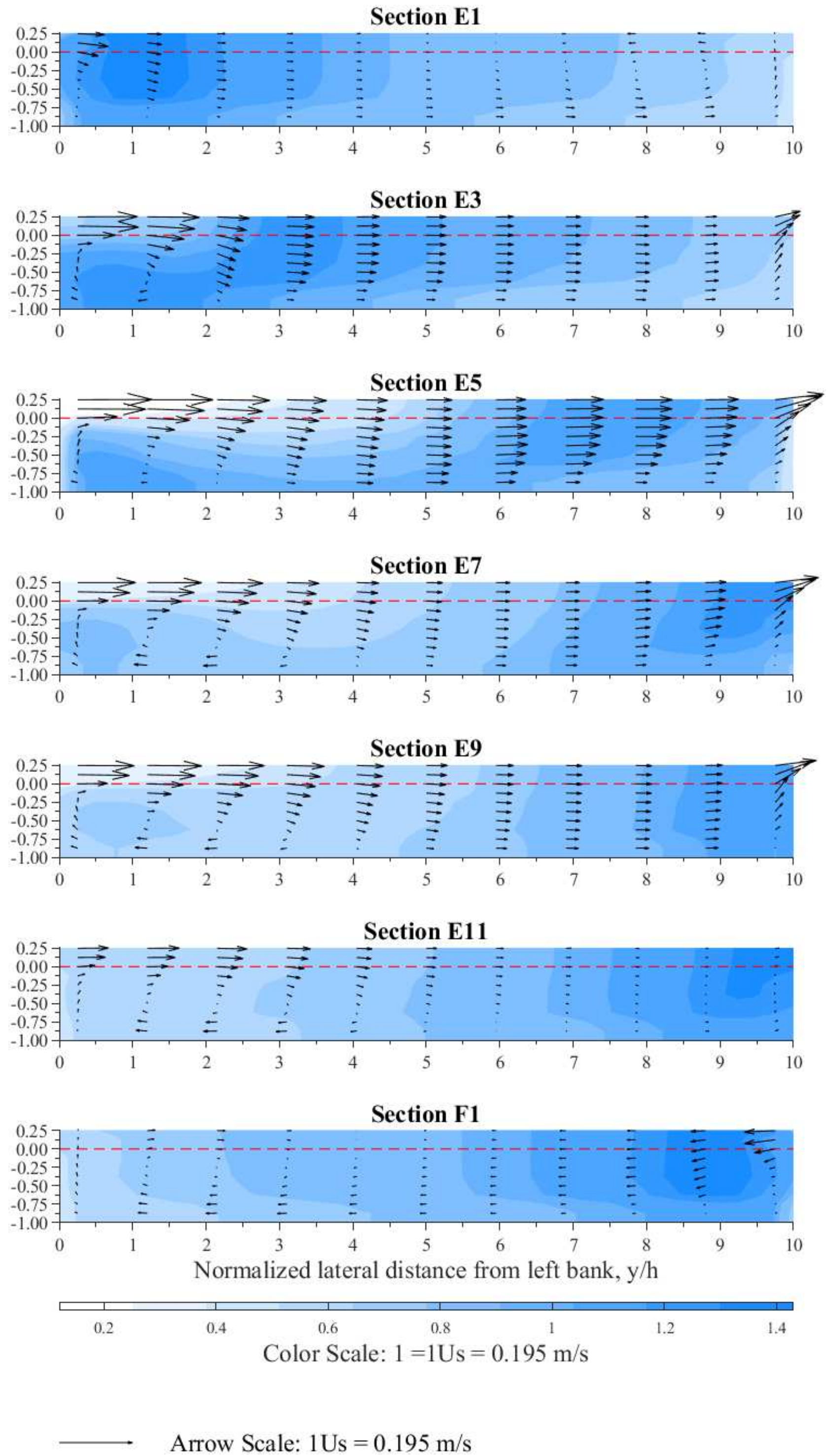

Figure 20. Primary and secondary flows for smooth floodplain dr = 0.20

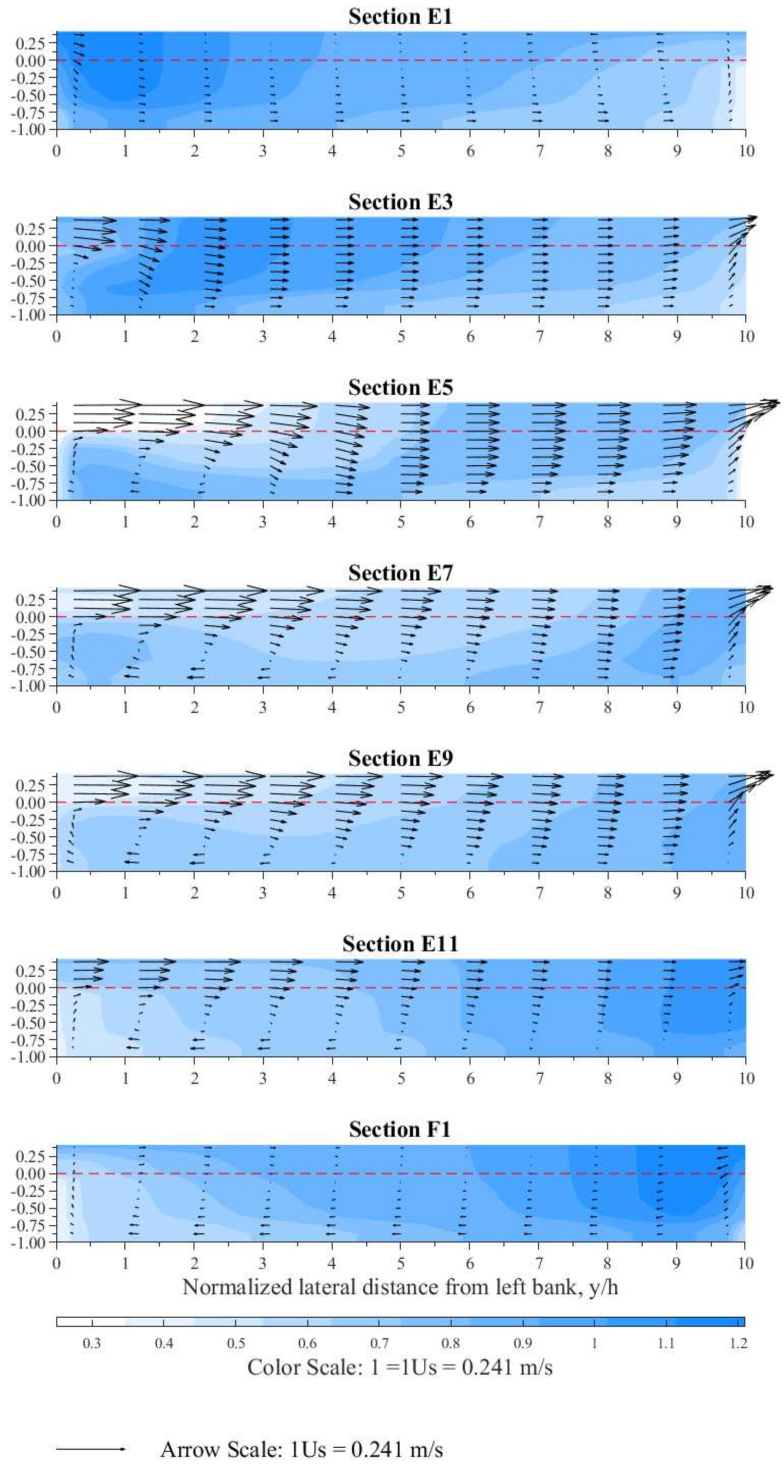

Figure 21. Primary and secondary flows for smooth floodplain dr = 0.29

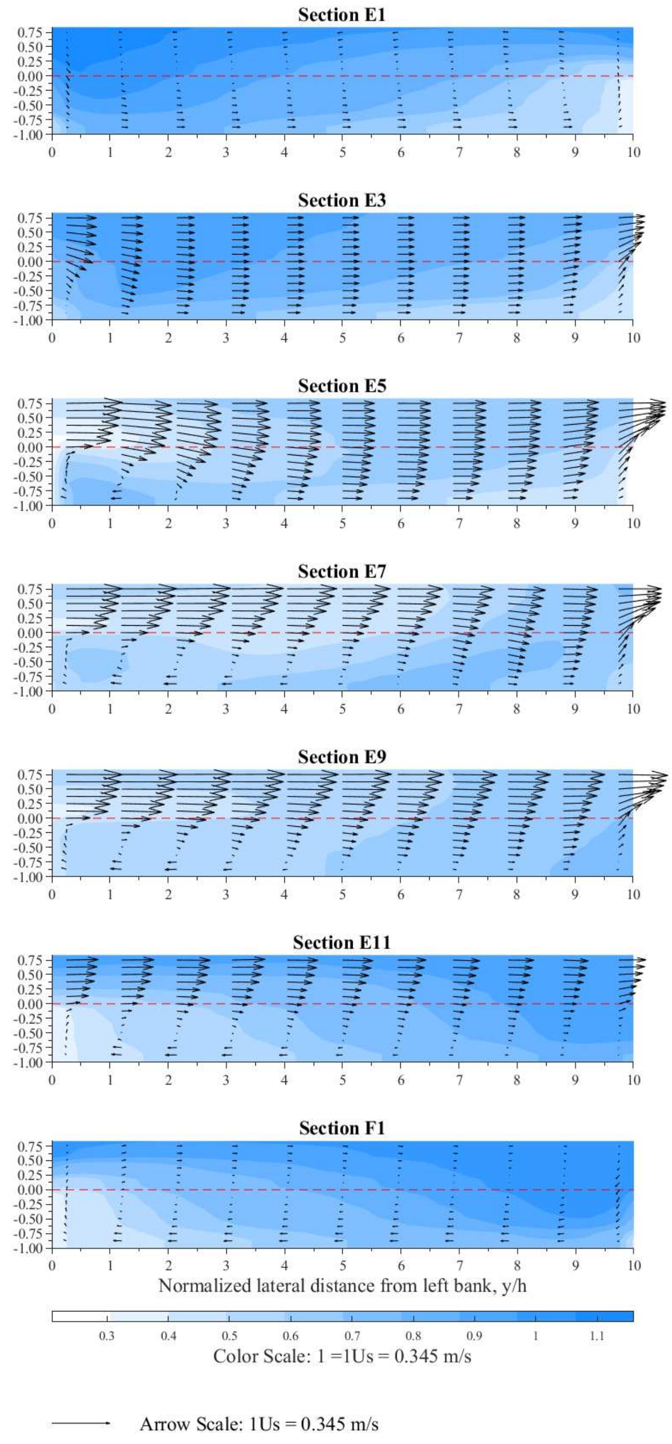

Figure 22. Primary and secondary flows for smooth floodplain dr = 0.46

Bankfull, Relative Depth of 0

For both physical numerical results for the bankfull case (dr = 0), the high velocity filament starts at the upstream apex near the surface slightly away from the channel walls at the inner bend (left bank). The maximum velocity filament migrates toward the opposite bank (right bank) until it is at closest to the left bank at section E11. At section F1, the maximum velocity filament moves slightly away from the left bank. The clockwise and counterclockwise secondary flow cell observed at the inner bends of the upstream and downstream meander apexes, respectively, seen in the physical experiments were observed in the current numerical models. These flow cells in the numerical experiments do not extend across the channel to the extent that they do in the physical experiment results. For both apex sections, the flow near the surface moves toward the inner bend. The flow near the bed generally moves toward the outer bend. At the cross-section, high velocity flows above the banks move from left to right. The velocity magnitude below the banks generally increases moving from left to right. There is a clockwise flow cell below the bank centered near the left bank in the crossover section. The clockwise flow cells seen at section E5 in the physical experiments was not observed in the numerical model results. The bulk cross stream flows at section E11 were seen in both physical and numerical model results although the numerical model also had strong near bed flows in the opposite direction. Overall, the flows in the numerical model match expected patterns for inbank flows in a meandering compound channel.

Relative Depth of 0.20

For the relative depth of 0.20, the location of the maximum velocity filament was predicted at the upstream apex section E1 and the crossover section E7. At section E1, the maximum velocity filament is near the surface adjacent to the inner bend. At section E7, the high velocity filament near the surface at the right bank and the lower magnitude high velocity lobe near the bed at the left bank are captured in the current numerical model. However, the high velocity filament at section F1 in the Shiono et al. model results is near the bed at the inner bend whereas it is located near the surface in the numerical model results. For the cross stream and vertical components of velocity, there are clockwise and counterclockwise flow cells centered near the inner bend at the upstream and downstream apex sections, respectively. Relatively high velocity flows originate from the inner bends at the apex sections and flows downward on a diagonal path toward the bed in the center of the channel. The relative magnitude of these diagonal flows at the apex sections is greater in the Shiono et al. experiment results than in the numerical results. At the cross-over section, the clockwise flow cell centered in the left half of the channel was captured by the numerical models. The high velocity flows that enter the cross-over section at the left bank and exit at the right bank are also present in the current numerical model results.

Relative Depth of 0.29

The current numerical model replicated the streamwise flow patterns for the relative depth of 0.29 case. In both the numerical and physical model results, the high velocity the maximum velocity filament begins at the inner bend of the upstream meander apex. Moving downstream to sections E3 and E5, the maximum velocity filament remains near the right bank yet it was more concentrated near the bed. At section E7, the high velocity filament was now near the surface at the left bank. A lower magnitude high velocity lobe remains at the right bank near the bed at section E7. Moving further downstream, the patterns of high and low velocity contours are similar between the numerical and physical model results. However, the high velocity filament near the right bank is closer to surface in the numerical models compared with that in the Shiono et al. experiments. The cross stream and vertical velocities were also predicted for the 0.30 relative depth case. At the upstream apex section E1, there is a counterclockwise flow cell centered in the outer half of the channel that spans nearly the entire channel width. At sections E3 through E9, high velocity flows enter the main channel from the floodplain at the left bank and slightly lower magnitude flows exit onto the floodplain at the right bank. For E3 and E5, the bulk flow direction is generally from left bank to right bank with section E5 having the greatest cross stream velocities in the main channel below the bankfull level. For sections E7 through E11, most of the high cross stream flows are near and above the bankfull level. There is a clockwise flow cell that develops near the left bank section E3 that grows in width moving downstream up to section E11. At section F1, the clockwise flow cell persists with the lower portion of the channel near the bed having a large region of high cross stream velocities relative to the low magnitude cross stream velocities near the surface.

Relative Depth of 0.46

The current numerical model results are similar to the Shiono et al. model results for relative depth of 0.46 although there appears to be more disorder in the order physical model results compared with the numerical model results. At the upstream apex section in the Shiono et al. model, there are two regions of high velocity: one at the right bank near the surface and the other at the left bank near the surface and extending downward into the main channel. The high velocity regions were observed in the current numerical model results however they appeared closer to the free surface. At section E3, the high velocity region near the left bank moved closer to the bed in both physical and numerical model results. However, the secondary high velocity region near the surface in the right half of the channel in the physical experiment results was not present in the numerical model results. The high velocity filaments that occurred at the bed near the left bank at section E5 and E7 in the physical experiment were observed in the numerical model. Also at section E7, the wide high velocity filament in the right side of the channel along the bed was predicted in the current numerical model. At section E9, the maximum velocity filament shifts to the right corner of the channel mostly below the bankfull level. At section E11 and F1, the high velocity filament is above the bed and high velocities are observed on the left side of the channel near the free surface.

For the velocity vector plots, there were nearly channel spanning counterclockwise flow cells with high near-bed cross stream velocities for the numerical model cases at the upstream and downstream apexes, respectively. For the Shiono et al. experiments, they observed two counterclockwise flow cells which nearly form a larger continuous flow cells. The numerical model predicted the same general cross stream flow structures observed for the interior cross sections E3 through E11. A large portion of the main channel flows below bankfull in sections E3 and E5 are in the rightward direction with the greatest below bankfull cross stream vectors occurring in section E5. A counterclockwise flow cell forms near the bed at the left bank at section E5 in the numerical model and at E3 in the Shiono et al. experiments. This flow cell increased in height and width moving downstream to section E11. Sections E7, E9, and E11 were dominated by high rightward moving cross stream flows above the bankfull level whereas at the apexes, the near bed velocities were relatively more significant.

In summary, the current numerical model predicted the flow structures observed in the Shiono et al. experiments. These flow structures included high velocity filaments and lobes which migrated through the half meander for each case. Secondary flow cells and regions of high and low cross stream velocities were also found to match between the current numerical model results and the results of the Shiono et al. experiments.

3.2 Stage-Discharge

The relative depth-discharge curves for the smooth and vegetated floodplain are shown in Figure 23. The discharges for the overbank cases followed logarithmic trends which were approximated by the best fit Equations (15), (16), and (17) for the smooth, low vegetation density, and high vegetation density floodplain cases, respectively. Equations (15), (16), and (17) had R^2 values of 0.9995, 0.9997, and 0.9993, respectively.

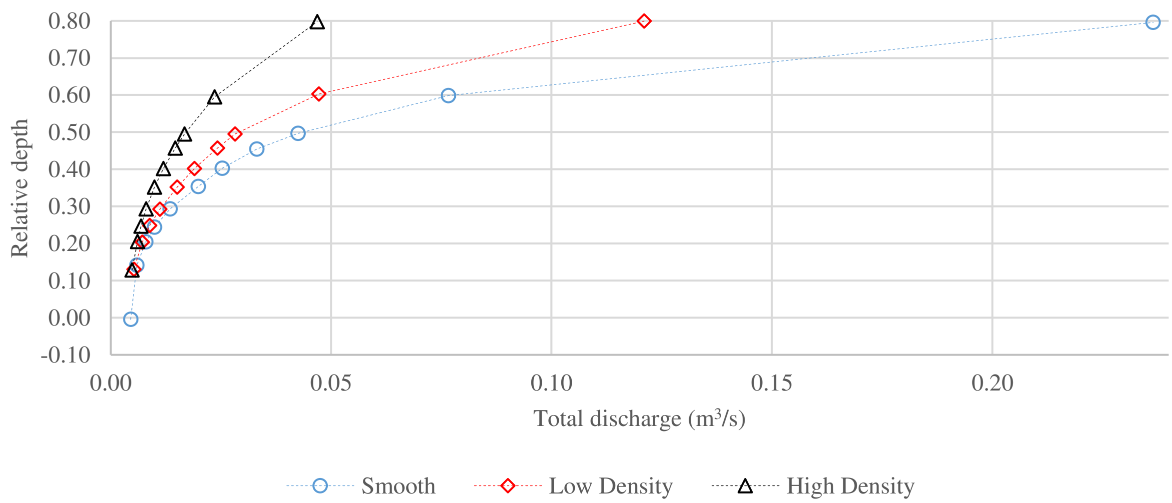

Figure 23: Relative depth versus total discharge (flowrate) for smooth, low vegetation density, and high vegetation density floodplain scenarios

$$dr = 0.176ln(Q) + 1.0512 \quad (15)$$

$$dr = 0.2126ln(Q) + 1.2495 \quad (16)$$

$$dr = 0.2897ln(Q) + 1.6837 \quad (17)$$

To better see how floodplain vegetation density affects the stage-discharge relationship, Figure 24 shows the relative depth versus the percent reduction in total flow from the smooth floodplain case to each vegetated floodplain case. Discharge capacity was reduced as relative depth and vegetation density were increased compared with the smooth scenario discharges. For relative depth cases of 0.80, the discharge capacity decreased up to approximately 50 and 80% for the low and high vegetation density scenarios, respectively.

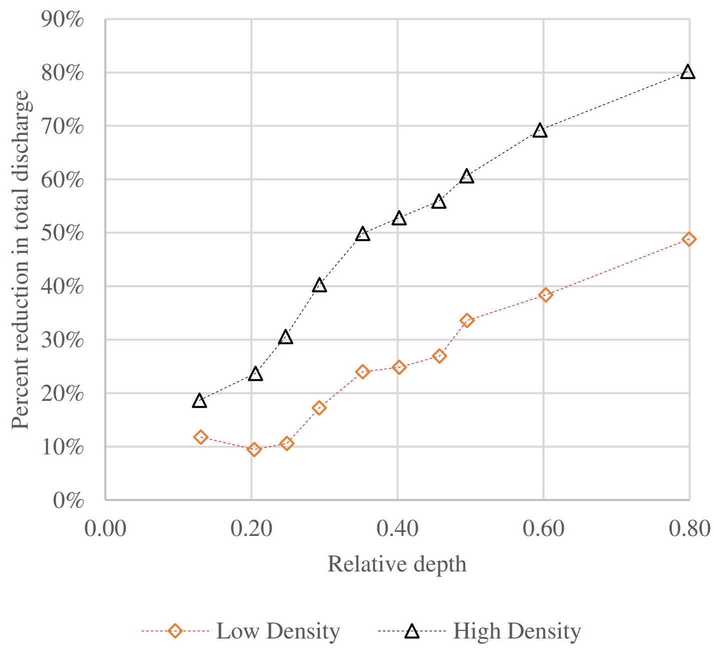

Figure 24. Reduction in total discharge capacity for the low and high floodplain vegetation density cases versus relative depth

The characteristic velocities computed from the total discharges and average flow depths are plotted versus relative in Figure 25 as an alternative representation of the stage discharge relationship. For the smooth, low vegetation density, and high vegetation density cases, there are initial minima in the characteristic velocity at relative depths of 0.14, 0.20, and 0.29, respectively. For the smooth floodplain cases, the characteristic velocity increases linearly after an initial plateau as relative depth increases and exponentially as relative area increases. As relative depth and relative area increase above bankfull for the smooth and vegetation density cases, there is an initial plateau in characteristic velocity followed by a linear increase, and then a final plateau high relative depth. A similar trend is observed in the relative area plot for the low vegetation density floodplain cases. For the high vegetation density case, the characteristic velocity is generally constant at low and moderate relative depths. There is a gradual reduction at low relative depths up to a relative depth of 0.30. The characteristic velocity then increases gradually up to a relative depth of 0.50 before decreasing again down to its lowest value at a relative depth of 0.80.

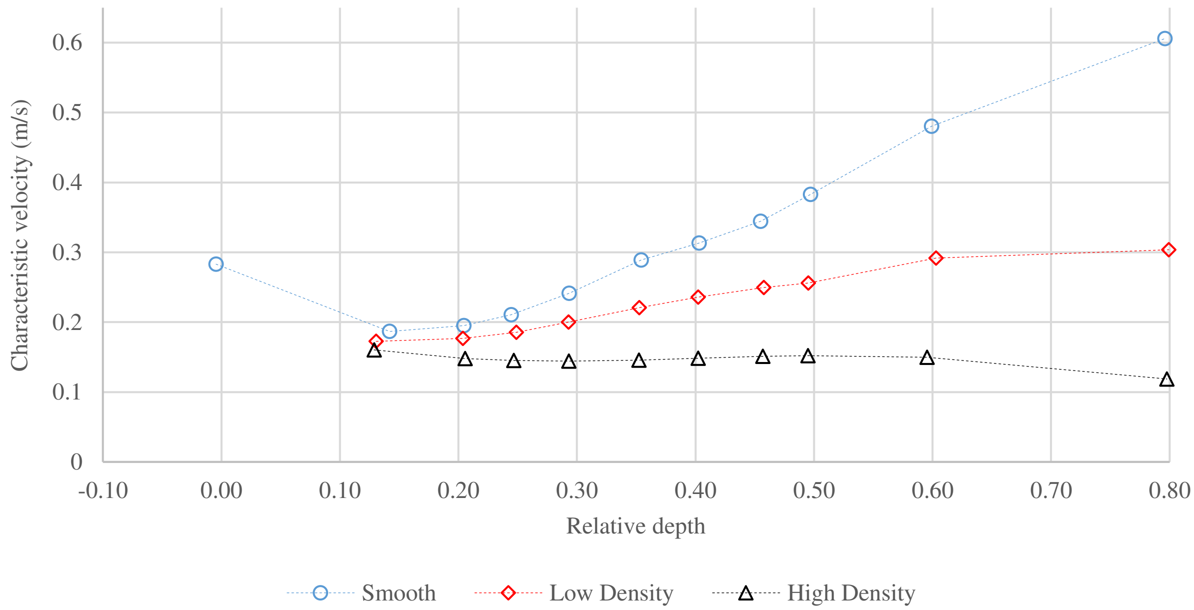

Figure 25. Characteristic velocity versus relative depth for the smooth, low vegetation density, and high vegetation density floodplain scenarios

3.3 Main Channel Streamwise Velocities

Main channel velocities are shown in relation to relative depth and total discharge in Figure 26 and Figure 27, respectively. At the lowest overbank relative depths of 0.13 and 0.20, the average main channel streamwise velocities were greatest for the high vegetation density case. For the 0.13 relative depth cases, the average main channel streamwise velocity was slightly higher for the low vegetation density case than the smooth. The opposite was found at relative depth of 0.20. At each relative depth greater than 0.20, the average main channel streamwise velocity was lower as vegetation density increased.

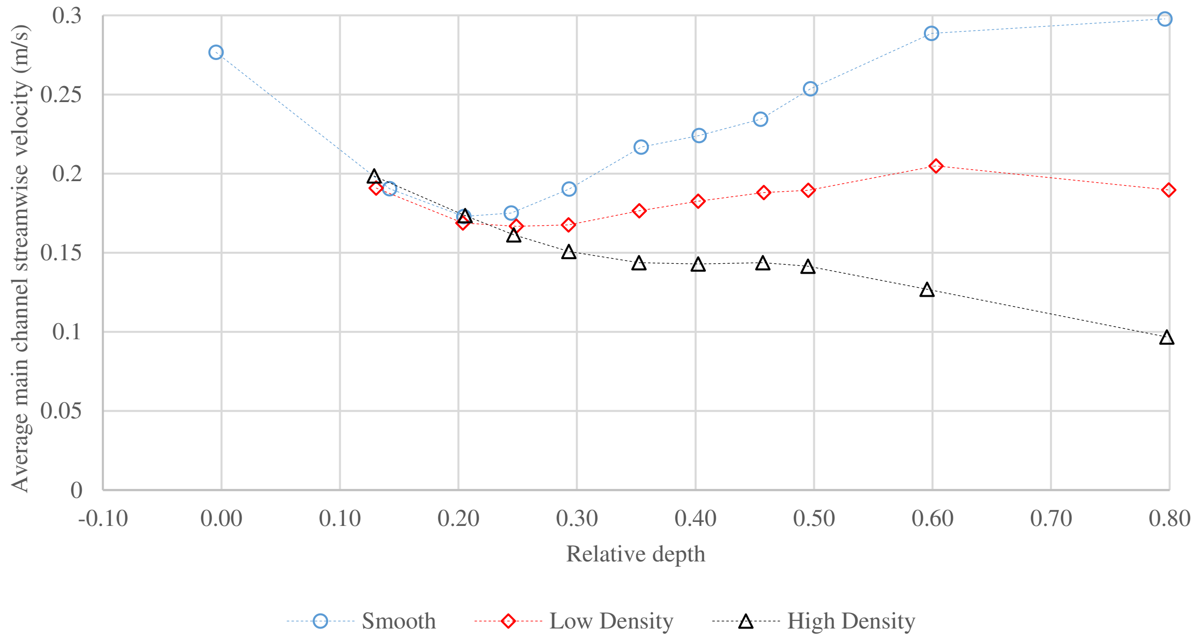

Figure 26. Average main channel streamwise velocity plotted versus relative depth

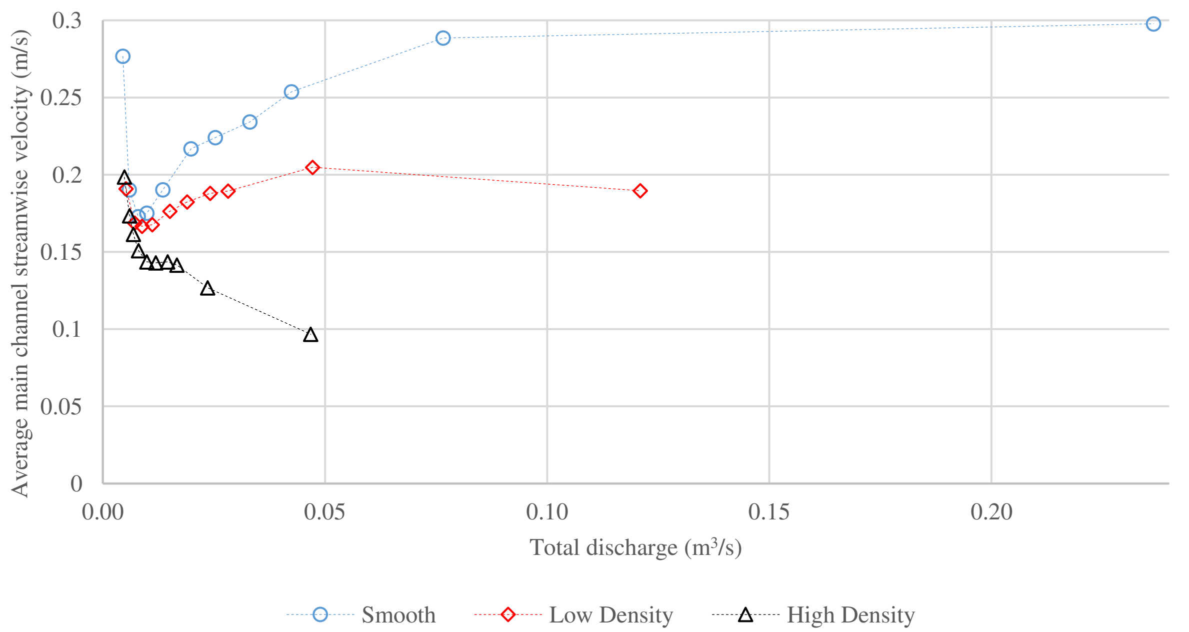

Figure 27. Average main channel streamwise velocity plotted versus total discharge

For all roughness scenarios, minimum channel streamwise velocity was observed at relative depths of 0.20 and 0.25 or discharges of 0.00793 and 0.00866 m^3/s for the smooth and low vegetation density floodplain cases, respectively. The relative depth at which these initial minima were observed will subsequently be referred to as the ‘threshold’ relative depth. As relative depth and discharge increased, the streamwise velocity increased in the smooth and low density vegetated floodplain cases. For the low vegetation density case, there is a second local minimum in average main channel streamwise velocity at the highest relative depth of 0.80. For the high vegetation density case, an initial low point in average main channel streamwise velocity compared with that at lower relative depths occurs at a relative depth of 0.35 or a discharge of 0.00994 m^3/s. This initial drop in average main channel streamwise velocities was followed by a general plateau in velocities with increasing relative depth. The average main channel streamwise velocity again dropped at a relative depth of 0.80 or a discharge of 0.02356 m^3/s. For the smooth case, the average main channel streamwise velocities generally plateaued between relative depth cases of 0.60 and 0.80. The percent of the total flow in the main channel is also plotted against the total flow and relative depth in Figure 28 and Figure 29, respectively. As relative depth and discharge increased, the percent of the total flow conveyed in the main channel below the bankfull level decreased. This decrease indicates that as the total flow increases, the relative portion of that flow in the main channel decreases even as the average main channel streamwise velocities increase for the smooth and low vegetation density scenarios. The percent of the total flow in the main channel was greater at each given relative depth as floodplain vegetation density increased. At low relative depths, this difference between the percent of total flow in the floodplain roughness scenarios was greater. As relative depth increased, the percent of the total flow in the main channel between floodplain roughness scenarios converged. Opposite trends were seen for the percent of the total flow in the main channel versus total flow. The percent of total flow in the main channel was generally lower for a given flow rate as vegetation density increased. At low flowrates, the differences between percent of the total flow in the main channel were close in value between the floodplain roughness scenarios. As total flow increased, the percent of the total flow values diverged.

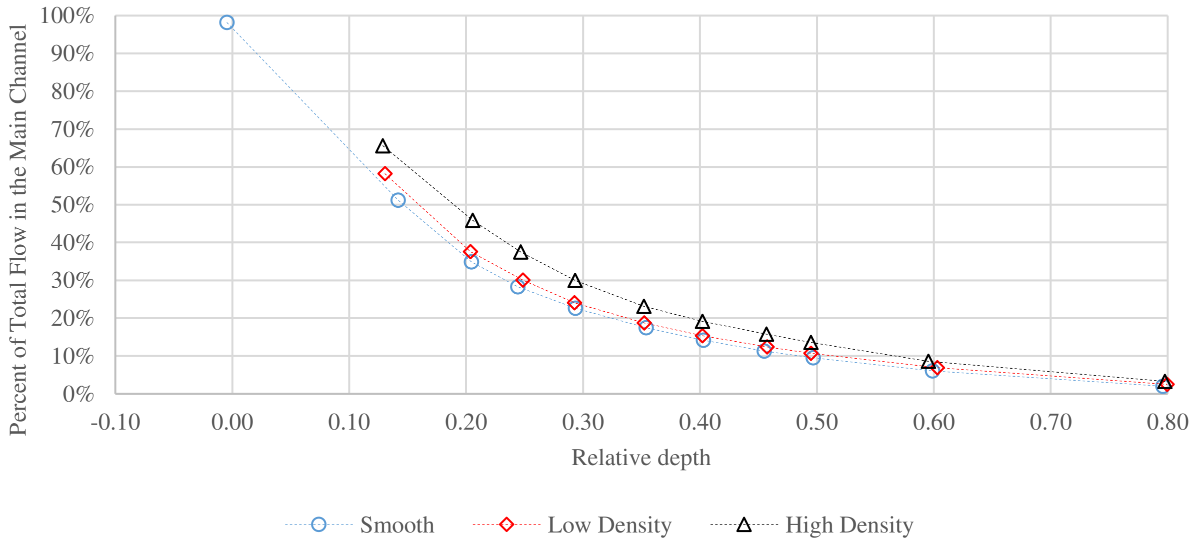

Figure 28. Percent of the total flow in the main channel plotted versus relative depth

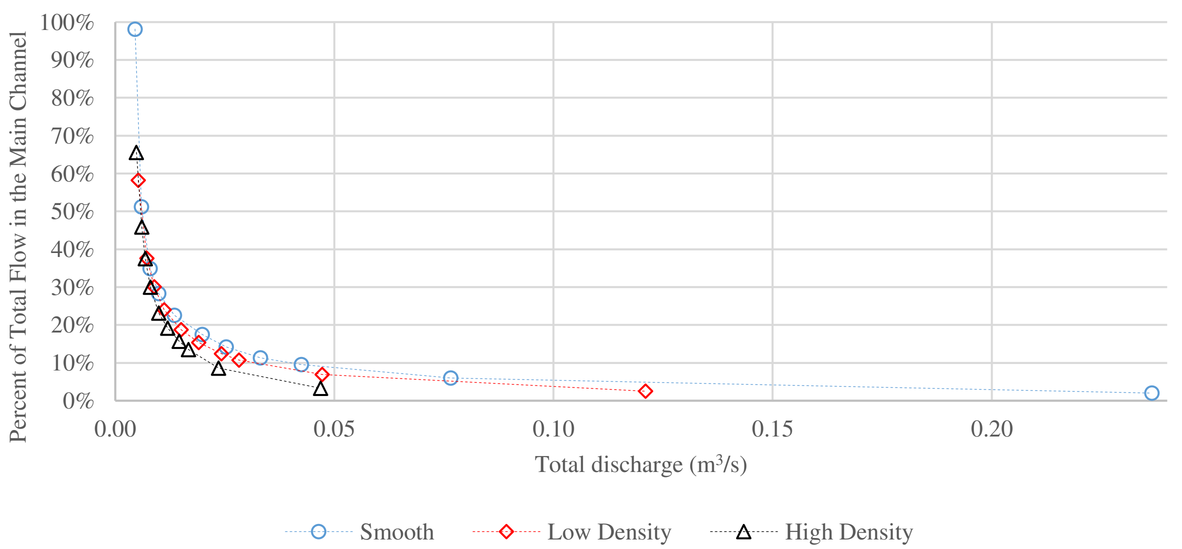

Figure 29. Percent of the total flow in the main channel plotted versus total discharge

The average main channel streamwise velocities were also made non-dimensional dividing by the characteristic velocity for each case. The resulting non-dimensional average main channel streamwise velocities were plotted versus relative depth and total flow in Figure 30 and Figure 31, respectively. As vegetation density increased for a given relative depth or discharge, the non-dimensional velocity was greater. Between the floodplain roughness scenarios, the non-dimensional average main channel streamwise velocities followed nearly the same decreasing trend with minor divergences as relative depth was increased. The non-dimensional average main channel streamwise velocities were similar between floodplain roughness scenarios at low total flowrates. As flowrate increased, the non-dimensional average main channel streamwise velocities diverged.

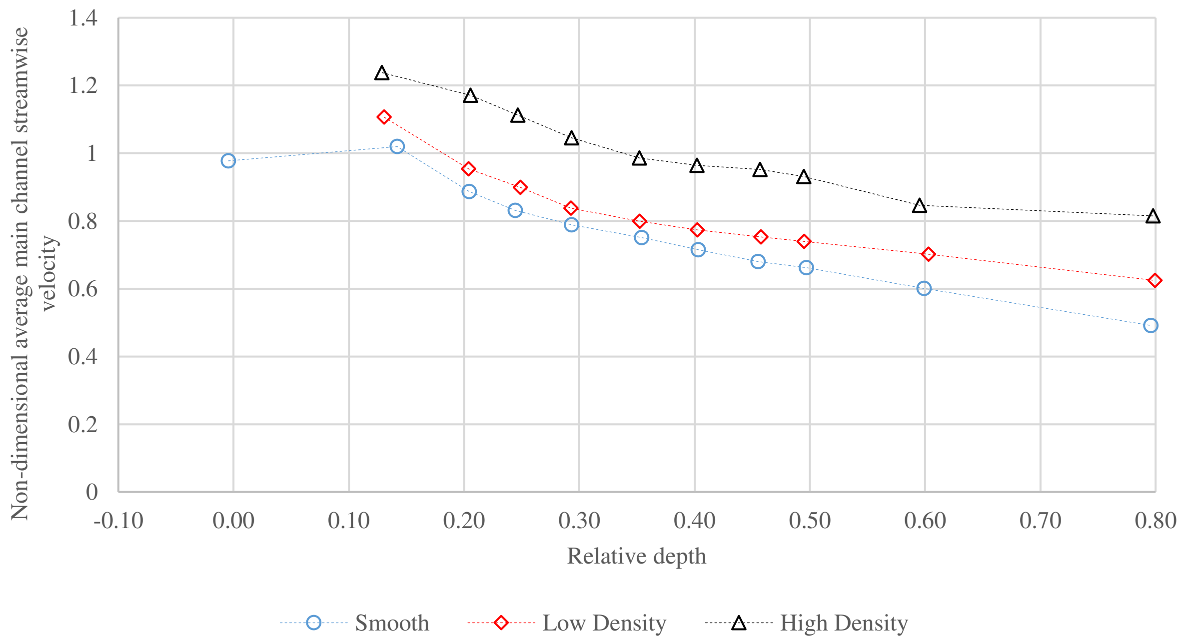

Figure 30. Non-dimensional average main channel streamwise velocity plotted versus relative depth

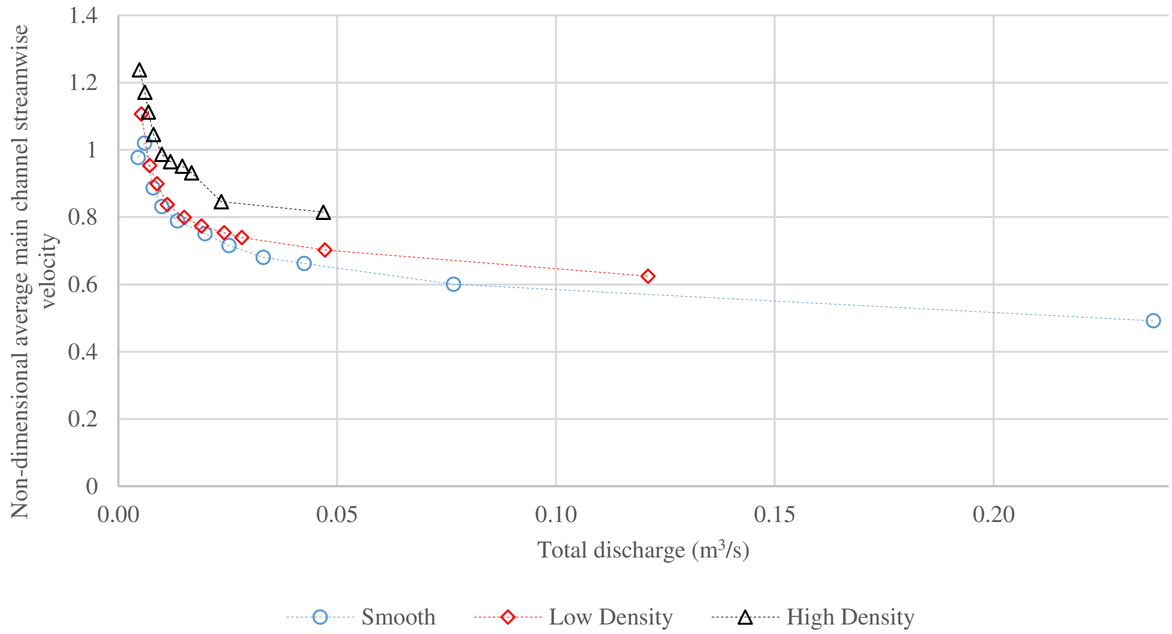

Figure 31. Non-dimensional average main channel streamwise velocity plotted versus total discharge

3.4 Boundary Shear Stresses

The average main channel boundary shear stress versus relative depth and versus volumetric discharge for each roughness scenario are shown in Figure 32 and Figure 33, respectively. The trends in average main channel boundary shear stress versus relative depth and discharge are virtually the same as those in the average main channel streamwise velocity plots. The locations of the reductions, plateaus, and increases in average main channel boundary shear stress versus relative depth and discharge are the same as those in the average main channel streamwise velocities.

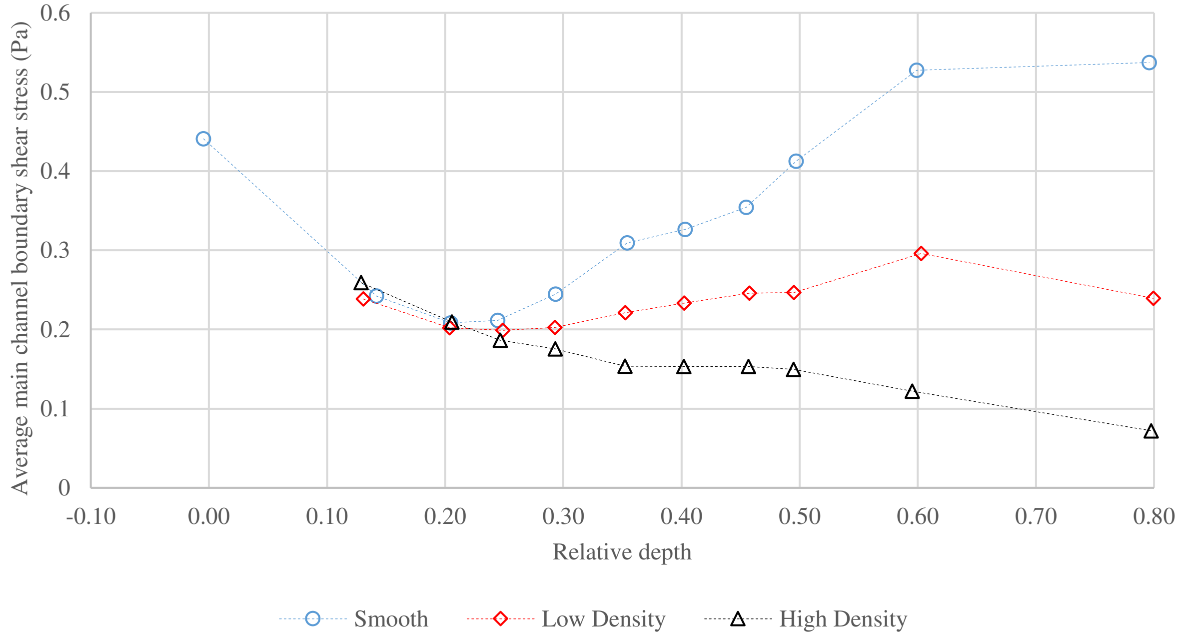

Figure 32: Average main channel boundary shear stress plotted versus relative depth

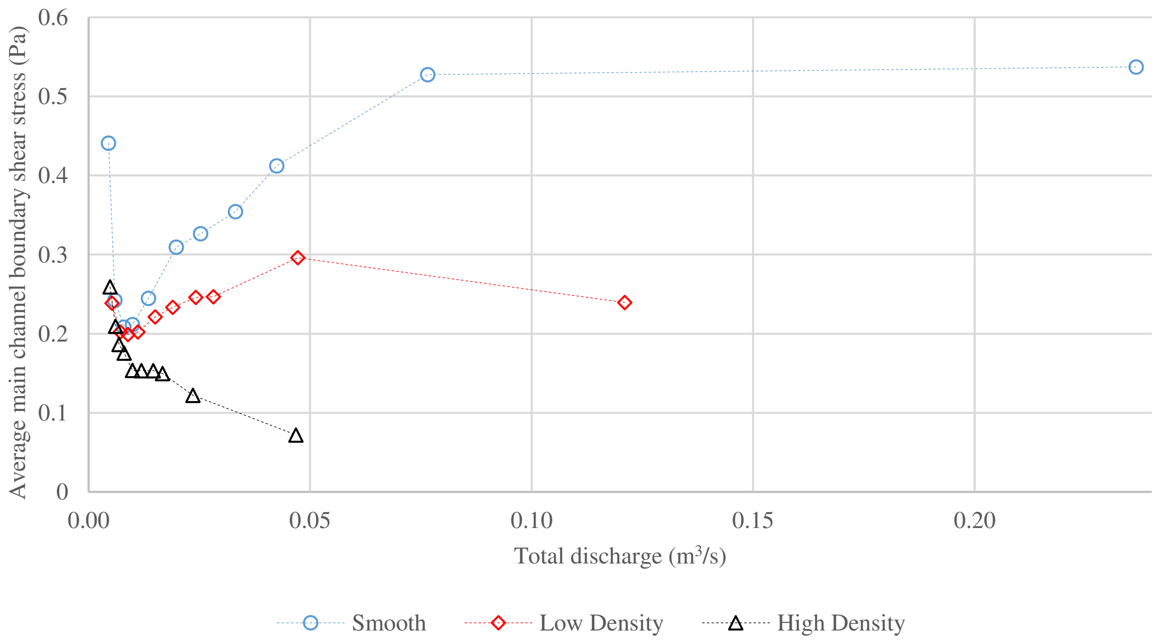

Figure 33. Average main channel boundary shear stress plotted versus total discharge

The non-dimensional main channel boundary shear stresses are also shown in relation to relative depth and total discharge in Figure 34 and Figure 35, respectively. As with the dimensional average main channel boundary shear stresses, the trends in the non-dimensional average main channel boundary shear stress versus relative depth and discharge are also very similar to those for the non-dimensional average main channel streamwise velocities.

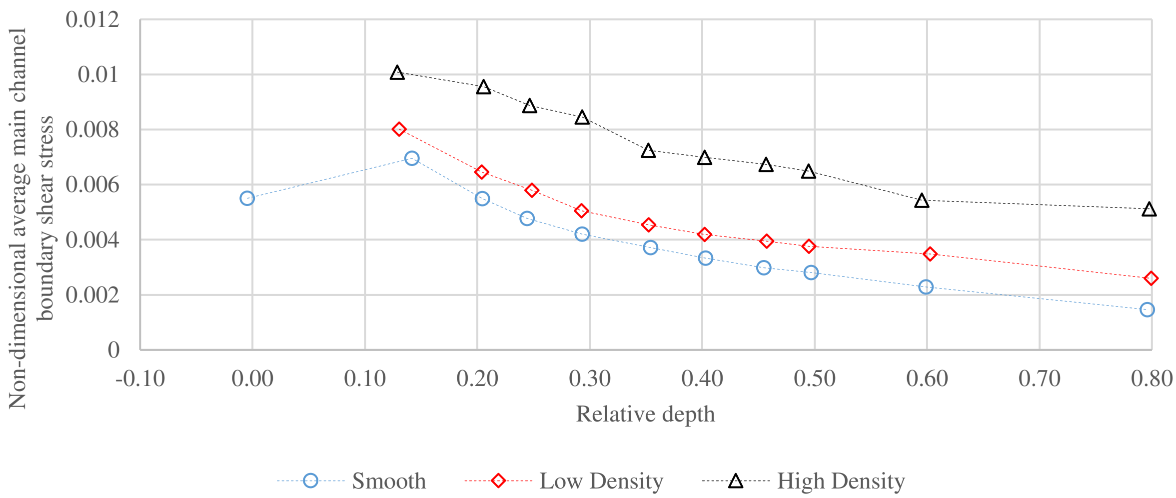

Figure 34. Non-dimensional average main channel boundary shear stress plotted versus relative depth

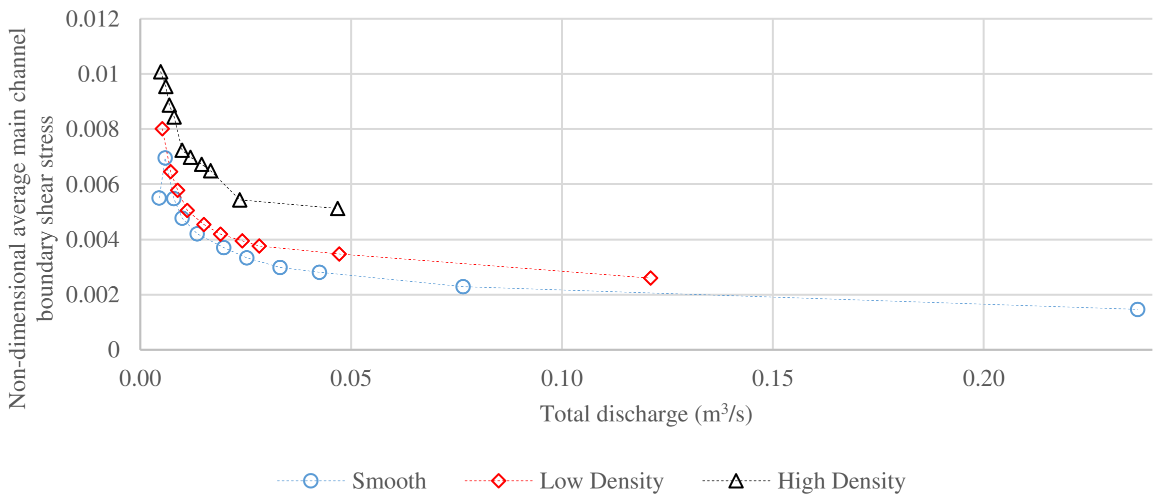

Figure 35. Non-dimensional average main channel boundary shear stress plotted versus total discharge

To provide more detail about the boundary shear stress field, the main channel boundary shear stresses were analyzed in plan view as contour plots and at each study cross section as line plots for all floodplain roughness and relative depth cases, which are provided in B. Focus was placed on the contour plot cases where there were minima and other transitions in the trends of average main channel streamwise velocities and boundary shear stresses. The contour plots for these cases are shown in Figure 36 through Figure 41. Note that the color scale varies between cases with the upper limit representing the maximum observed boundary shear stress for the given case. In general, as vegetation density increased, high and low boundary shear stress regions were patchier and more dispersed throughout the main channel compared with the more continuous regions in the smooth cases. For cases with overall low average main channel boundary shear stresses, the high boundary shear stresses were more concentrated near the inner bends. The high boundary shear stress regions crossed the main channel just upstream of the crossover section for cases with overall low average main channel boundary shear stresses. For cases with overall high main channel boundary shear stresses, regions of high boundary shear stress regions typically crossed the main channel within the crossover section similar to the boundary shear stress patterns observed in the bankfull case. The trends in main channel boundary shear stresses are described in further detail in the following section.

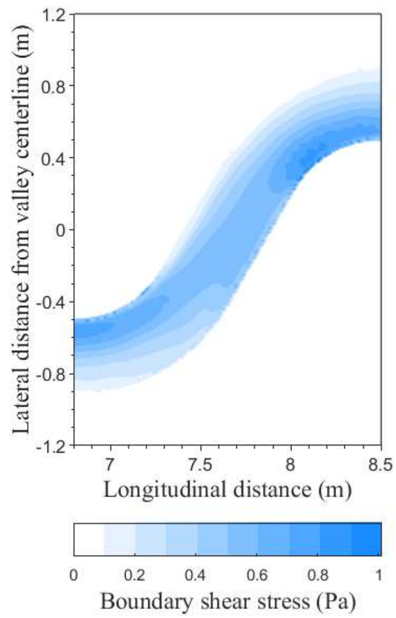

Figure 36. Planform main channel boundary shear stress contour plot for bankfull case (dr = 0, Q = 0.00451 m^3/s)

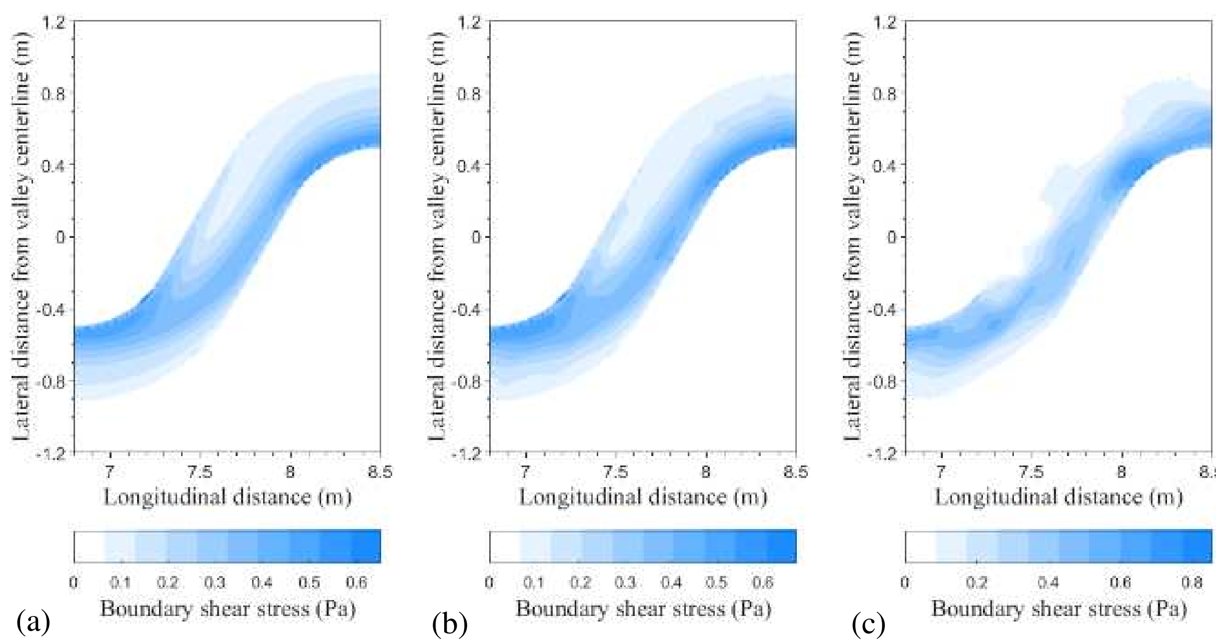

Figure 37. Planform main channel boundary shear stress contour plots of low overbank relative depth (dr = 0.13) cases for (a) smooth (Q = 0.00595 m^3/s), (b) low vegetation density (Q = 0.00525 m^3/s), and (c) high vegetation density (Q = 0.00484 m^3/s) floodplain scenarios

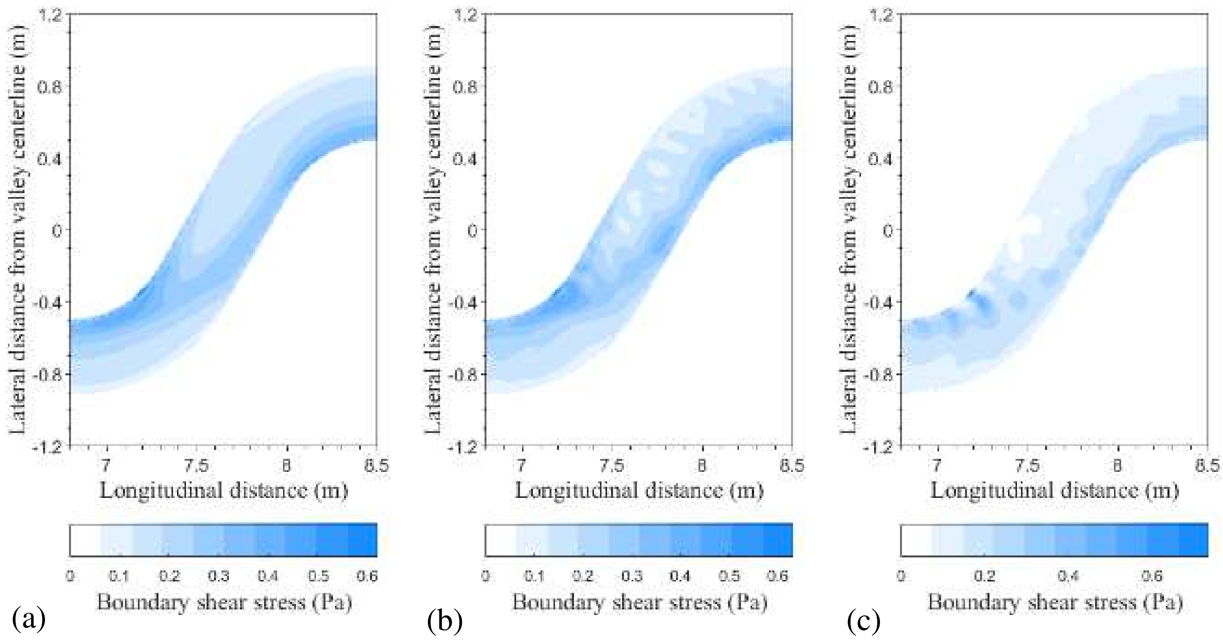

Figure 38. Planform main channel boundary shear stress contour plots of initial drop in average main channel boundary shear stress cases for (a) smooth (dr = 0.20, Q = 0.00793 m^3/s), (b) low vegetation density (dr = 0.25, Q = 0.00886 m^3/s), and (c) high vegetation density (dr = 0.35, Q = 0.009935 m^3/s) floodplain scenarios

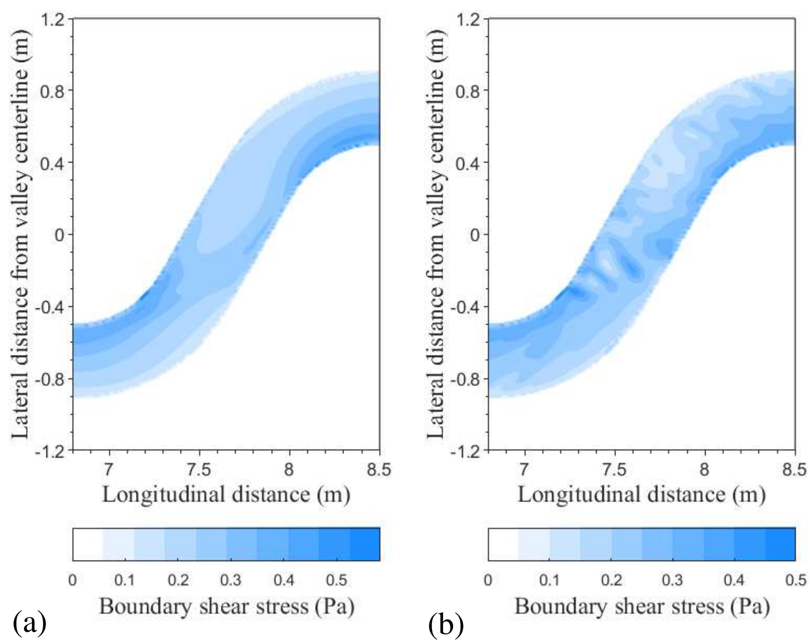

Figure 39. Planform main channel boundary shear stress contour plots of first steep rise in average main channel boundary shear stress cases for (a) smooth (dr = 0.29, Q = 0.1348 m^3/s) and (b) low vegetation density (dr = 0.35, Q = 0.01506 m^3/s) floodplain scenarios

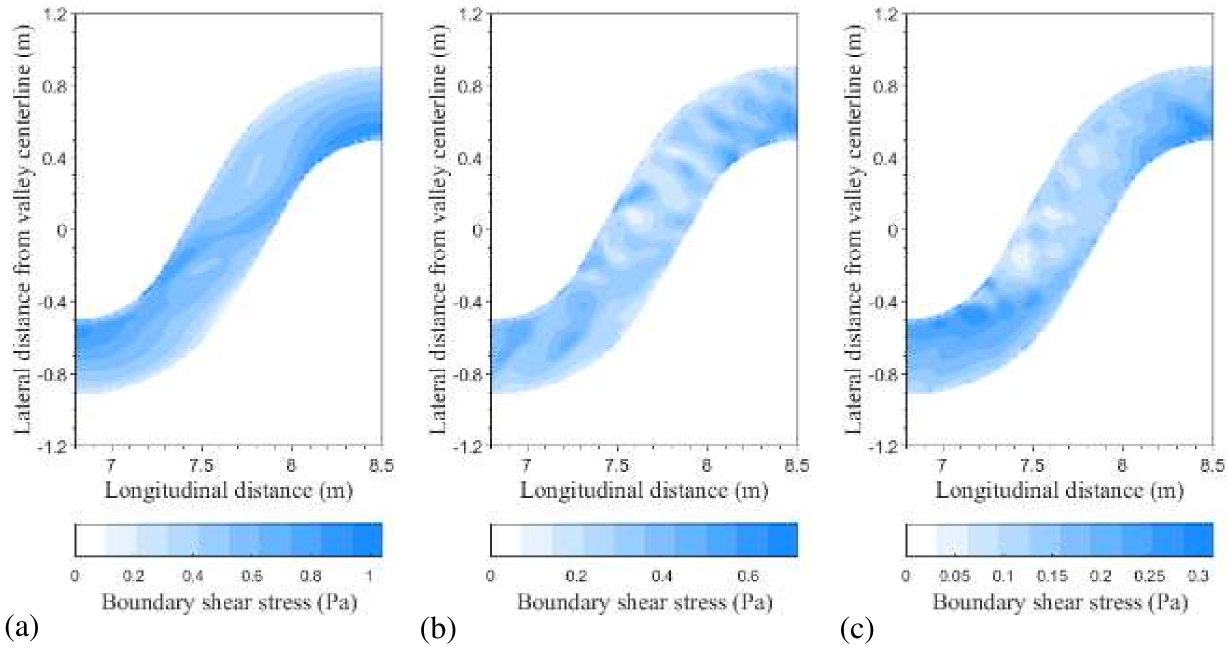

Figure 40. Planform main channel boundary shear stress contour plots before plateau in average main channel boundary shear stress for the (a) smooth case (dr = 0.60, Q = 0.07657 m^3/s), (b) at high average boundary shear stress before second reduction for the low vegetation density (dr = 0.60, Q = 0.04720 m^3/s), and (c) at the last value in the average boundary shear stress plateau before the second reduction for the high vegetation density (dr = 0.50, Q = 0.01671 m^3/s) floodplain scenarios

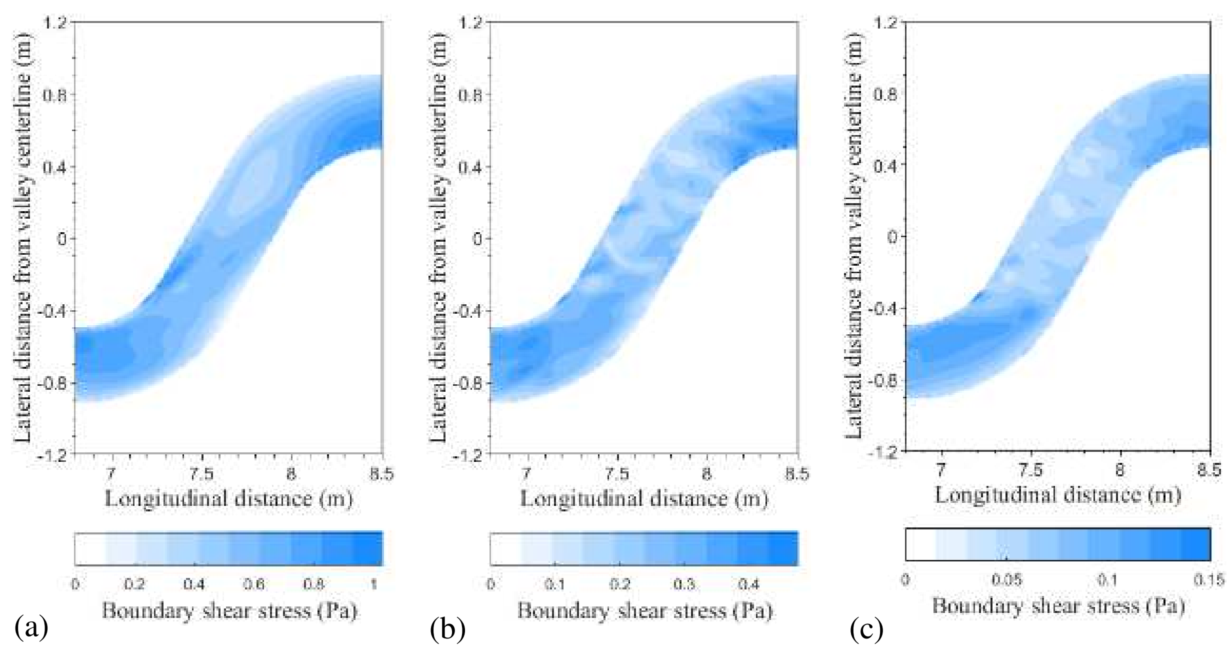

Figure 41. Planform main channel boundary shear stress contour plots of highest relative depth (dr = 0.80) cases for (a) smooth (Q = 0.2365 m^3/s), (b) low vegetation density, (Q = 0.1210 m^3/s), and (c) high vegetation density (Q = 0.04682 m^3/s) floodplain scenarios

For the bankfull condition, the greatest boundary shear stresses occur near the inner bends in the bend regions of the channel upstream and downstream of crossover region. In the crossover region, there were moderately high boundary shear stresses adjacent to the right bank which span a large portion of the channel width. Low boundary shear stresses are concentrated near the left bank of channel upstream of the downstream bend region. In the region downstream of the crossover section, low boundary shear stresses are concentrated near the right bank.

As relative depth increased just above bankfull (dr = 0.13), the high boundary shear stress regions became much more concentrated as the low velocity regions grew in area. The greatest relief in boundary shear stresses were observed in the high vegetation density case. The regions of high and low boundary shear stress for this high vegetation density case were less continuous or patchier than in the smooth and low vegetation density cases. The lowest boundary shear stresses for the high vegetation case occur along the outer bend (left bank) just downstream of the meander apex extending to the upstream side of the crossover section. The lowest boundary shear stresses for this case also occur along the outer bend of the upstream bend sections. Moderately low boundary shear stresses for the high vegetation density case occurred along the upstream portion of the inner bend (left bank) of the upstream bend section where they are not present in the smooth and low vegetation density cases. The boundary shear stress fields for the smooth and low vegetation density floodplain cases were similar in the locations and extent of high and low boundary shear stress regions. Compared with the bankfull case, the bands of high boundary shear stress for smooth and low vegetation density cases were concentrated into smaller regions along the inner bends that crossed the main channel ~~at~~ near the upstream side of the crossover section. There were also portions of the high boundary shear stress region that stayed along the left bank within the crossover section. Because the high boundary shear stress regions were more concentrated, the low boundary shear stress regions covered more area within the main channel than in the bankfull case. For the smooth and low vegetation density cases, a continuous low boundary shear stress region that spanned about half the channel width was present in the crossover section and the downstream bend section. There were also low boundary shear stress regions concentrated along the outer bend of the upstream bend section. Some patchiness in the boundary shear stress was observed in the low floodplain vegetation density case that was not present in the smooth case yet not to the extent observed for the high vegetation density case.

At the first initial reductions in the average main channel boundary shear stress, the high boundary shear stress regions were concentrated into smaller areas as vegetation density increased compared with the low overbank flow cases. The regions of high and low boundary shear stress became patchier for the vegetated floodplain cases. In these vegetated cases, ridgelike patterns of low and high boundary shear stress nearly perpendicular to the main channel streamwise direction following the meander. These patterns appear in bands along the left bank of the channel. For the low vegetation density case, this band of ridges is narrowest near the downstream end of the upstream bend section. Moving downstream, the band of ridges widened. For the high vegetation density case, the band of ridges started just upstream of the bend apex along the inner bend (left bank) Just upstream of the crossover section, the band of ridges crosses the main channel to the right bank. Between vegetated cases, the relief in the magnitude of the ridges was greater in the high vegetation density case.

At the first steep increase in average main channel boundary shear stress, the relief in the boundary shear stress ridges for the low vegetation density cases increased compared with the reduced average main channel boundary shear stress case. For the low vegetation density case, the high boundary shear stress ridges occupy more of the upstream portion of the crossover section. Due to the presence of these ridges, high boundary shear stress regions were found near the outer bend (left bank) of the downstream bend section where a continuous low boundary shear stress region is located for the smooth case. There was a somewhat continuous region of low boundary shear stresses at the transition between the crossover region and the downstream bend section for the low vegetation density case, but it was not as large as the continuous low velocity regions for the smooth cases.

At the relative depth of 0.60 before the plateau in average boundary shear stresses for the smooth case, high boundary shear stress regions form at the inner bends of the bend sections as was observed at lower relative depths. However, the section of the high boundary shear region that crosses the channel from the left bank to the right bank has a higher relative magnitude and crosses further upstream at the middle of the crossover section compared with the low relative depth cases. Just upstream and downstream of this crossover high boundary shear stress region, there are small, discrete regions of low boundary shear stress. Low boundary shear stress regions also border the outer bends of the upstream and downstream bend sections.

At the relative depth cases just before the second drops in average main channel boundary shear stress for the vegetated floodplain cases, the patterns of high and low boundary shear stress were still discontinuous similar to the lower relative depth cases. For the low vegetation density case, regions of low boundary shear stress are prominent in the crossover section. Moderately low boundary shear stress regions occupy the downstream bend section adjacent to the outer bend and are separated by high boundary shear stress regions near the outer bend. At the upstream bend section, there are two regions of high boundary shear stress which nearly span the entire channel. Along the left bank of the crossover section, there are lobes of high boundary shear stress. For the high vegetation density case, lobes of low boundary shear stress filled a band starting at the downstream side of the upstream bend apex. This band of low boundary shear stress lobes grew in width moving downstream into the crossover region. High boundary shear stress regions were located along the inner bends of upstream and downstream within the bend regions as opposed to being within the crossover regions as observed at lower relative depth. At the downstream inner bend, a high boundary shear stress ridge appeared that nearly spans the channel width.

For the highest relative depth of 0.80 in the smooth case, as there were lobes of low boundary shear stress for the 0.60 relative depth case. However, the high boundary shear stresses dominated a large portion of the main channel. For the vegetated cases, the high boundary shear stresses tended to be in the inner bends of the bend section. Low boundary shear stress regions occupied the crossover section especially for the high vegetation density case. Greater patchiness in the high and low boundary shear stresses was observed for the low vegetation density.

3.5 Primary and Secondary Main Channel Flows

The figures in the following section show the primary flows (streamwise) into the page in contour plots. The secondary flows (cross stream and vertical) are shown as resultant velocity vectors. The bankfull level is indicated as a dashed red line.

<u>Primary Main Channel Flows</u>

As vegetation density increased, the primary flow field generally had greater variations and discontinuities in the distribution of high and low velocity regions especially as relative depth increased. In nearly all floodplain scenarios, as relative depth increased, the streamwise velocities became stronger at the apex sections (E1 and F1) and at the 30° bend sections (E3 and Ell), but became weaker in the crossover section (E5, E7, and E9). The strengthening of the streamwise velocities in the bend sections and weakening in the crossover sections as relative depth increased can be seen in Figure 43 and Figure 46 comparing the low relative depth case of 0.13 and high relative depth case of 0.80 for the high floodplain vegetation scenario. In the bankfull case on the other hand, the high velocity filament in the main channel is maintained throughout the entire main channel cross sections, as shown in Figure 42. As relative depth increased, the width of the low magnitude streamwise velocity regions near the surface increases in the crossover section.

At low relative depths for the smooth case, the high streamwise velocity filament crosses the main channel further upstream as vegetation density increases. For the vegetated cases, the low velocity filament near the surface split into two lobes at section E7 at relative depth of 0.25 for the low vegetation density scenarios shown in Figure 44 and at relative depth of 0.46 shown in Figure 45. Generally, this split pattern was observed at subsequently higher relative depths where it also appeared in section E9. The high velocity filaments were separated into multiple lobes especially at the high relative depths for the vegetated cases. In the smooth cases, multiple lobes of high and low velocities were observed as well. However, the high and low velocity regions for the smooth floodplain cases appeared more continuous than in the vegetated floodplain cases.

The high streamwise velocity filament in the crossover region, particularly at section E7, moved toward the bed as relative depth increased up to and including 0.60 for the smooth case, 0.50 for the low vegetation density case, and 0.35 for the high vegetation density case. The near-bed high streamwise velocity region in the crossover region became less prominent as relative depth increased above these relative depths.

In the smooth floodplain cases, the lowest streamwise velocities were found in section E5. In the low floodplain vegetation density cases, the lowest streamwise velocity regions were found in sections E5, E7, and occasionally in E9. For the high vegetation cases, the lowest streamwise velocity regions typically appeared in sections E3, E5, E7, and occasionally E9 with the largest regions of low velocity flow generally in section E5. These results show that as vegetation density increases, the lowest velocity regions may be found further downstream and over a longer extent of the main channel streamwise direction as shown in Figure 45 which compares the profiles for all floodplain scenarios.

The lateral and vertical area that these low velocity regions occupied also grew as vegetation density was increased. At the high relative depth of 0.80 for high vegetation density case, the streamwise velocity was reduced significantly in the crossover section shown in Figure 46. The crossover section for this case is also where the lowest main channel boundary shear stresses were observed and where the highest below bank main channel cross stream velocities occurred for the given case.

Secondary Main Channel Flows

Various secondary flow structures were observed. At the apex sections for low overbank relative depths, there was a small, low magnitude rotating secondary flow cell with low near bed velocities located near the inner bends. At the upstream apex, this flow cell rotated in the clockwise direction, and at the downstream apex it was counterclockwise. There was also a larger flow cell at the outer bend that rotated in the opposite direction from the smaller inner bend flow cell.

For the bankfull case, there are two counter rotating flow cells at the meander apexes with the same flow directions as was seen in the low overbank cases. However, in the bankfull case the rotating flow cells at the inner bends are greater in magnitude and area than the rotating cell at the inner bend. As relative depth increased to the relative depths where the minima in the average main channel streamwise velocity occurred (dr = 0.20 for smooth, dr = 0.25 for low vegetation density, and dr = 0.35 for high vegetation density), the small inner bend secondary flow cell at the apex sections virtually disappeared shown in Figure 44. For the main channel streamwise velocity minimum in the smooth case, the large flow cell which rotates toward the outer bend near the bed and toward the inner bends at the apex sections spans nearly the entire channel width. For the vegetated cases where the average main channel streamwise velocity minima occurred, these channel-spanning rotating flow cells were not present at the apex sections. This channel-spanning rotating flow cell persisted to higher relative depths in the smooth case. As relative depth increased for the smooth cases, the near surface portion of the cross-stream flow decreased in relative magnitude and the near bed relative velocity magnitudes remained approximately constant.

At the apex sections for the vegetated cases above the average main channel streamwise velocity minima, similar rotating flow cells with surface flows toward the inner bend and near-bed flows toward the outer bend, appeared in the outer half of the channel at relative depths of 0.35 for the low vegetation density scenario and at 0.40 for the high vegetation case. As relative depth increased above these values, these apex section rotating flow cells grew in width and strength especially for the high vegetation density cases near the bed. At a relative depth of 0.46 for the low vegetation density case, two flow cells rotating in the same direction were observed at the apex sections. For this case, the flow cell in the inner half of the channel was larger than one in the outer half. The two flow cell pattern at the apexes of the low density cases persisted until a relative depth of 0.50 after which only one flow cell appeared for higher relative depths.

For the high density vegetation case, the one flow cell at the apex sections. For most cases, the secondary flow velocities at the apex sections were weaker compared with those in the interior sections E3 through E11. As vegetation density was increased however, the relative magnitude of the near bed cross stream velocities generally increased in the apex sections.

In the interior sections for nearly all cases, there is a clockwise flow cell that forms between the bed and the bankfull level at section E3. Moving downstream, the flow cell increases in lateral extent along the bed of the channel. In the high vegetation density scenario, the secondary flow cell at section E3 was not apparent until a relative depth of 0.29 and higher. For the high vegetation density scenarios moving downstream from section E3 to section E11, the clockwise flow cell along the left bank did not laterally grow to the extent of those in the smooth and low vegetation density cases. For the smooth cases, the lateral extent of the inbank clockwise flow cell did not vary greatly with relative depth for a given interior cross sections. For the vegetated cases, this inbank clockwise flow cell varies in lateral extent, relative strength, and central location for given cross sections at different relative depths.

The major patterns of secondary flows for overbank also included high magnitude cross stream flows, which entered into the main channel from the floodplain on the left bank between sections E1 and E11 and the right bank at section F1. Within the internal section E3 to E11, the cross-stream flows exit the main channel onto the floodplain. Therefore, inflows from the floodplain into the main channel occur at the upstream floodplain interface and exit onto the downstream floodplain. The greatest inflow and outflow magnitudes occurred in the crossover sections E5, E7, and E9. At section E5, the inflows were weaker than the outflows whereas in section E7 inflows and outflows were generally equal and at section E9 inflows were stronger than outflows. Section E5 typically had the greatest inbank cross stream velocities of all sections and the lowest vertical velocity gradients in the crossover region. As vegetation density increased, the cross stream velocities at section E5 increased especially near the bed.

The area of the near surface low streamwise velocity filament along the left bank in the crossover section increased as the entering cross stream flows from the upstream floodplain increased in magnitude and extent. As vegetation density increased, the flows returning to the main channel from the upstream floodplain at the left bank appeared to plunge into the inbank portion of the channel more steeply for the vegetated cases compared with smooth case. Where flows plunged into the main channel steeply toward the bed, the boundary shear stresses tended to be lower, and where the secondary flows welled upward, boundary shear stresses were higher as can be seen at section E7 in Figure 45. For the smooth cases, the returning flows from the left floodplain in the crossover section remained mostly in the horizontal direction and high in magnitude across the width of the main channel above the bankfull level especially at higher relative depths. As relative depth increased for the low vegetation density cases above the minimum average main channel streamwise velocity case (dr = 0.25), the cross-stream flows returning to the main channel from the upstream floodplain in the crossover section became more horizontal and plunged less into the inbank portion of the main channel except at the highest relative depth of 0.80.

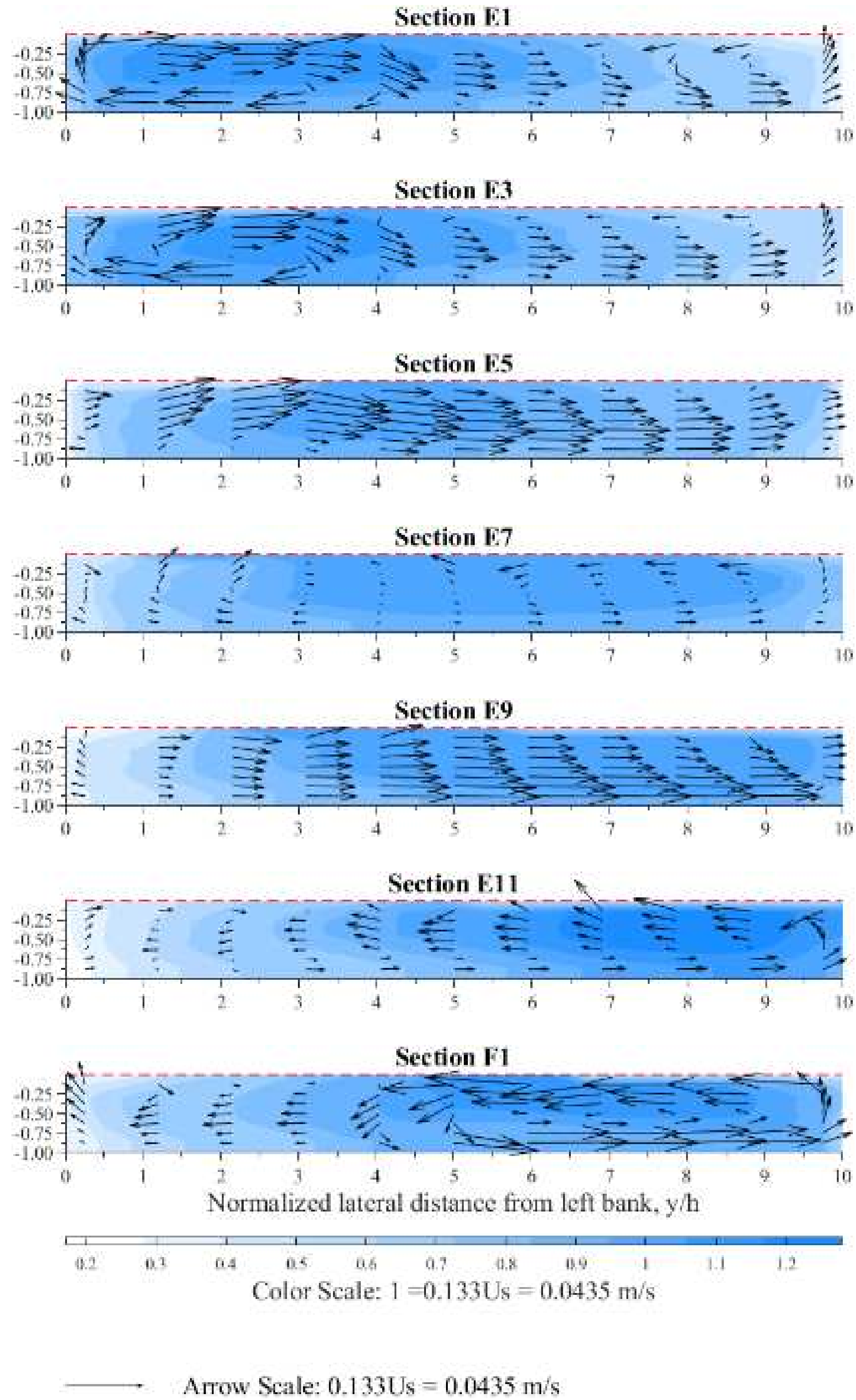

Figure 42. Primary and secondary flows for bankfull case (dr = 0)

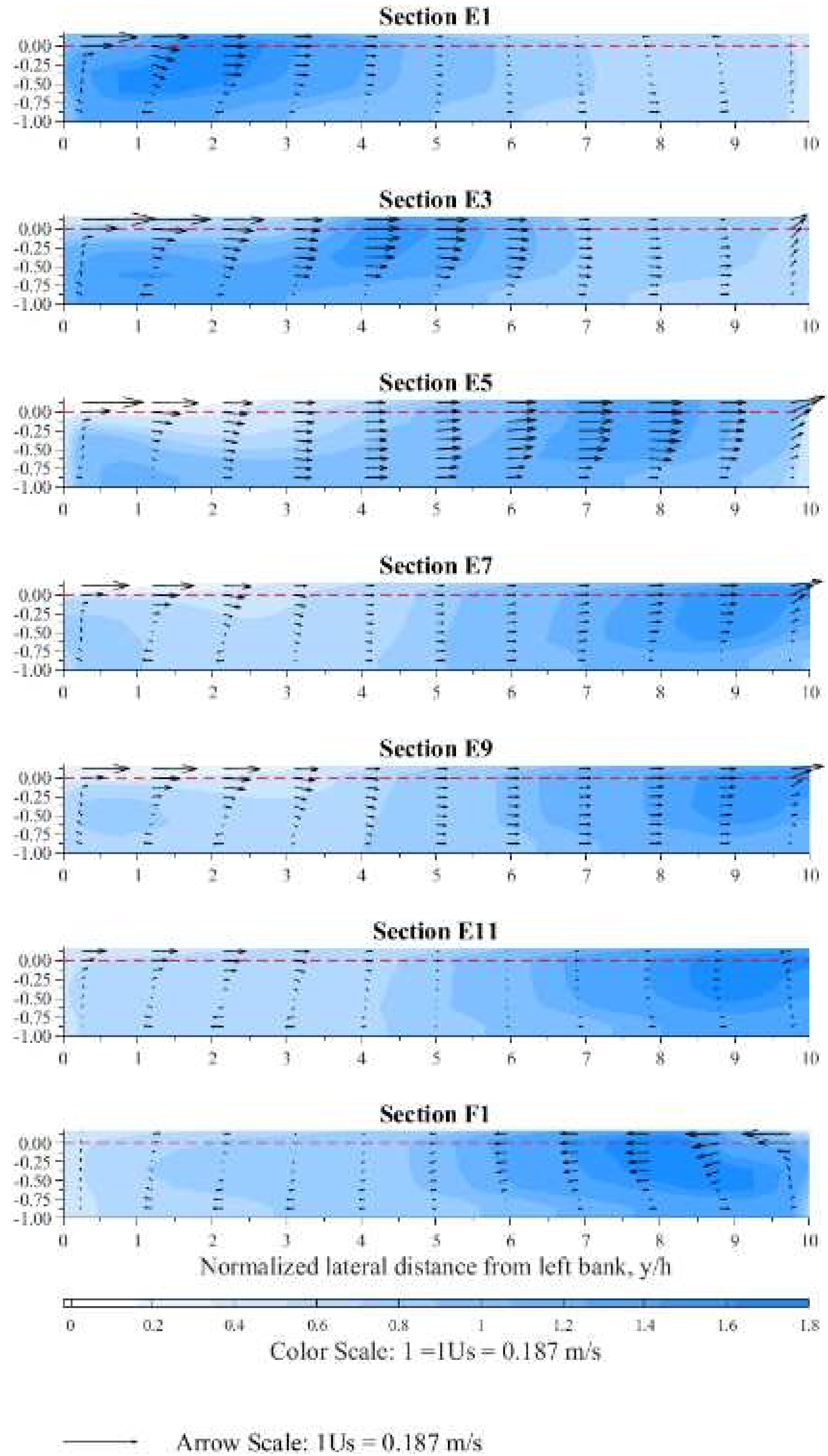

(a)

Figure 43. Primary and secondary flows for relative depth of 0.13 for (a) smooth floodplain, (b) low floodplain vegetation density, and (c) high floodplain vegetation density scenarios

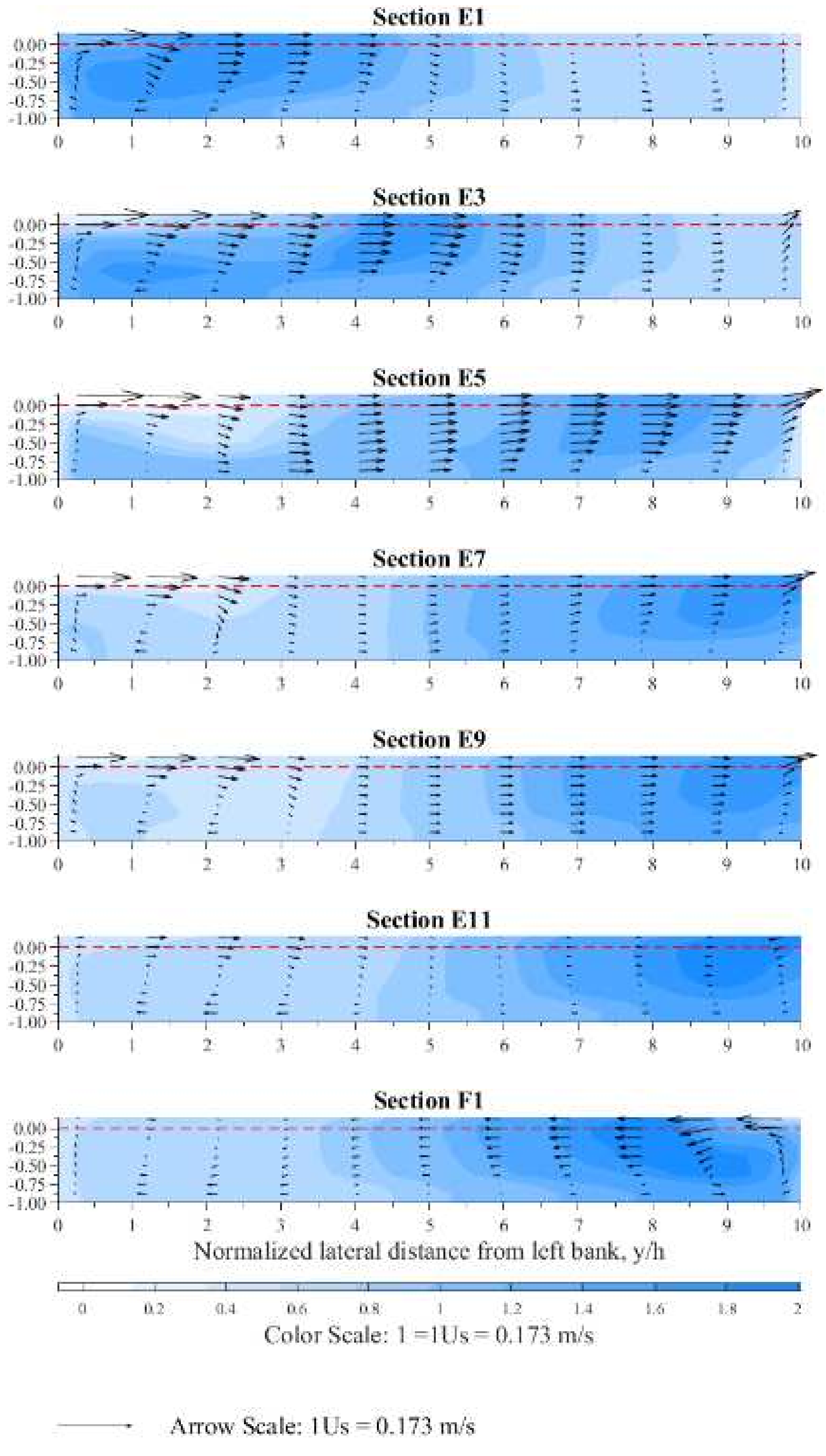

(b)

Figure 43. Primary and secondary flows for relative depth of 0.13 for (a) smooth floodplain, (b) low floodplain vegetation density, and (c) high floodplain vegetation density scenarios

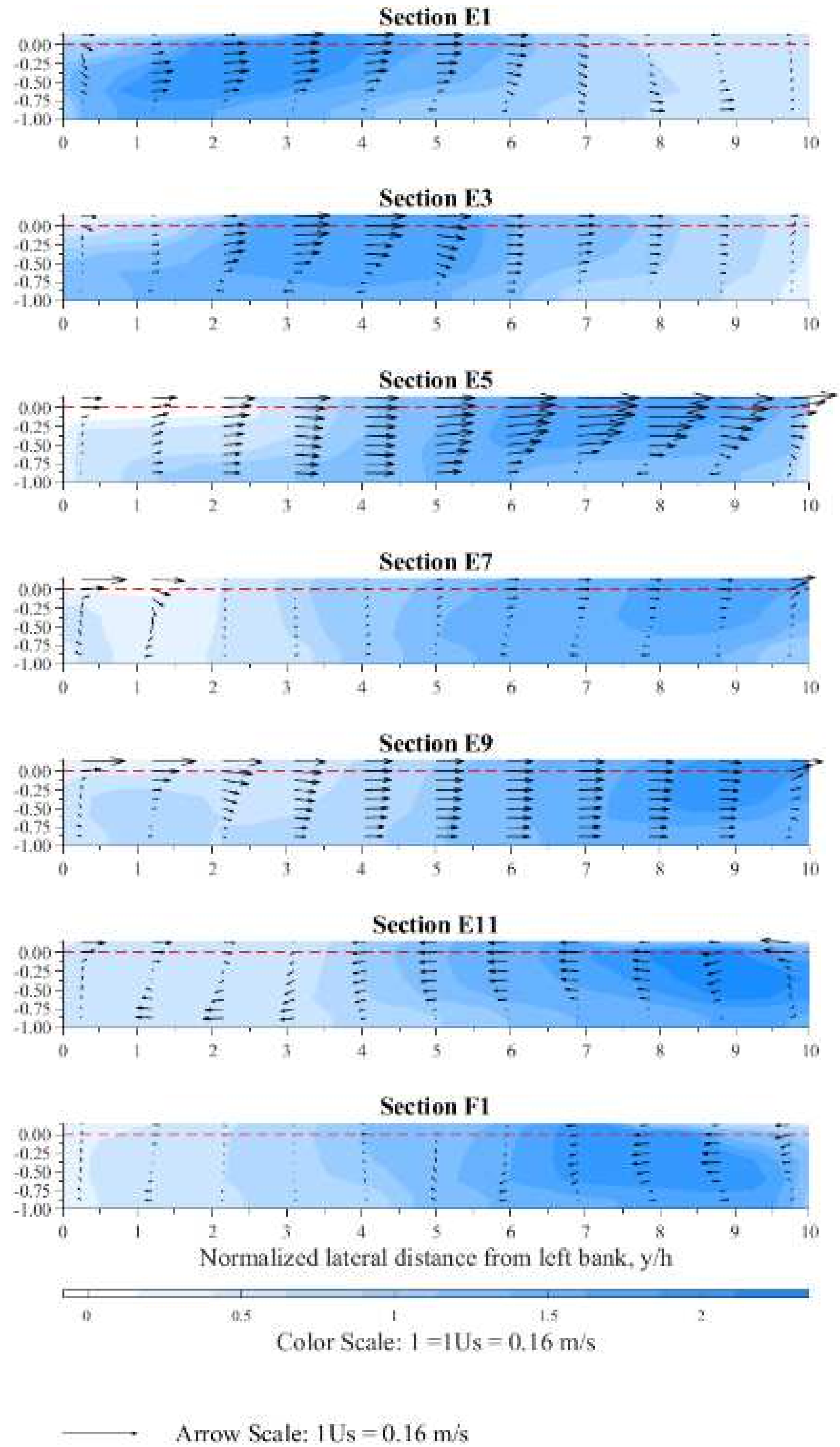

(c)

Figure 43. Primary and secondary flows for relative depth of 0.13 for (a) smooth floodplain, (b) low floodplain vegetation density, and (c) high floodplain vegetation density scenarios

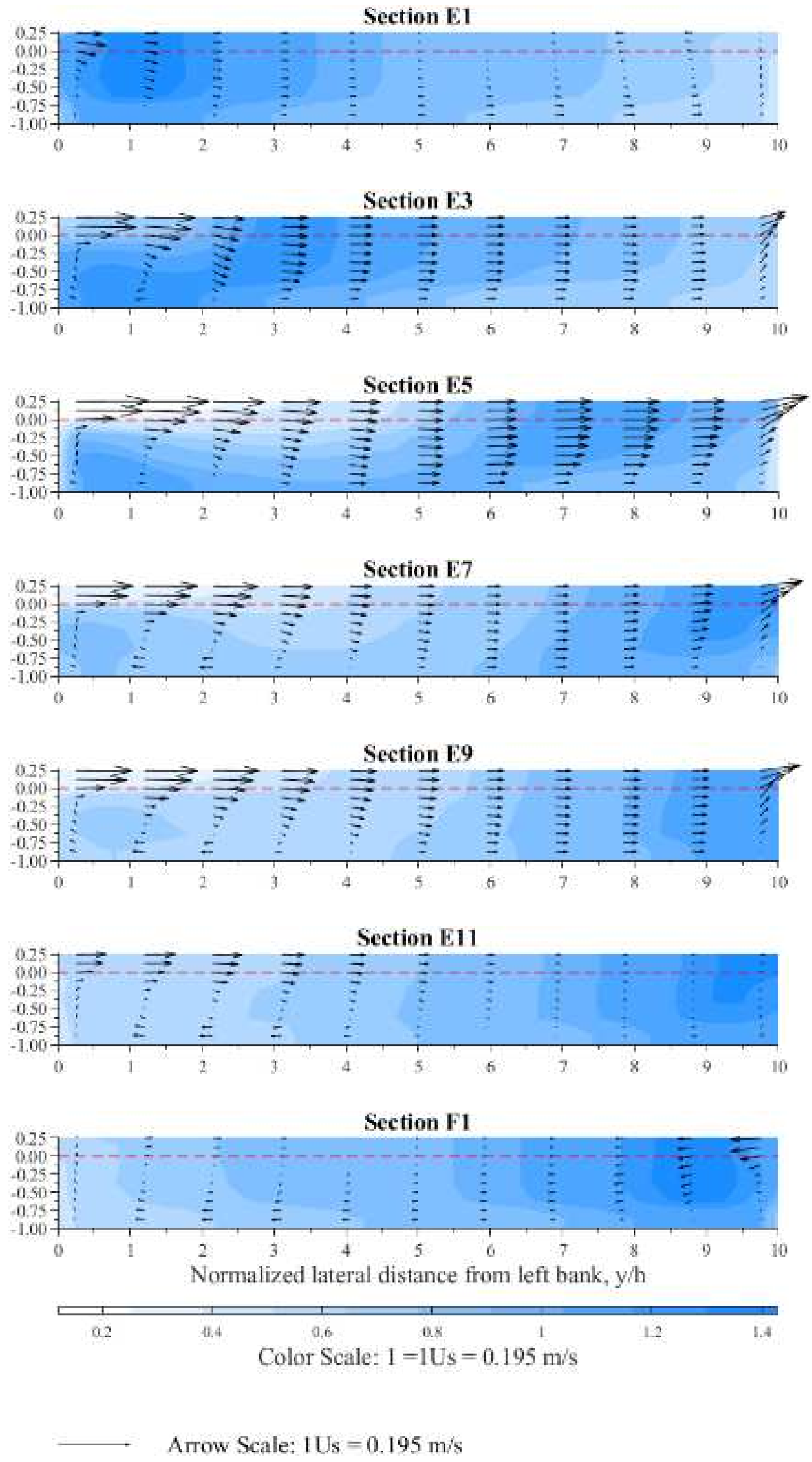

(a)

Figure 44. Primary and secondary flows for relative depth cases for average main channel minima in (a) smooth floodplain (dr = 0.20), (b) low floodplain vegetation density (dr = 0.25), and (c) high floodplain vegetation density (dr = 0.35) scenarios

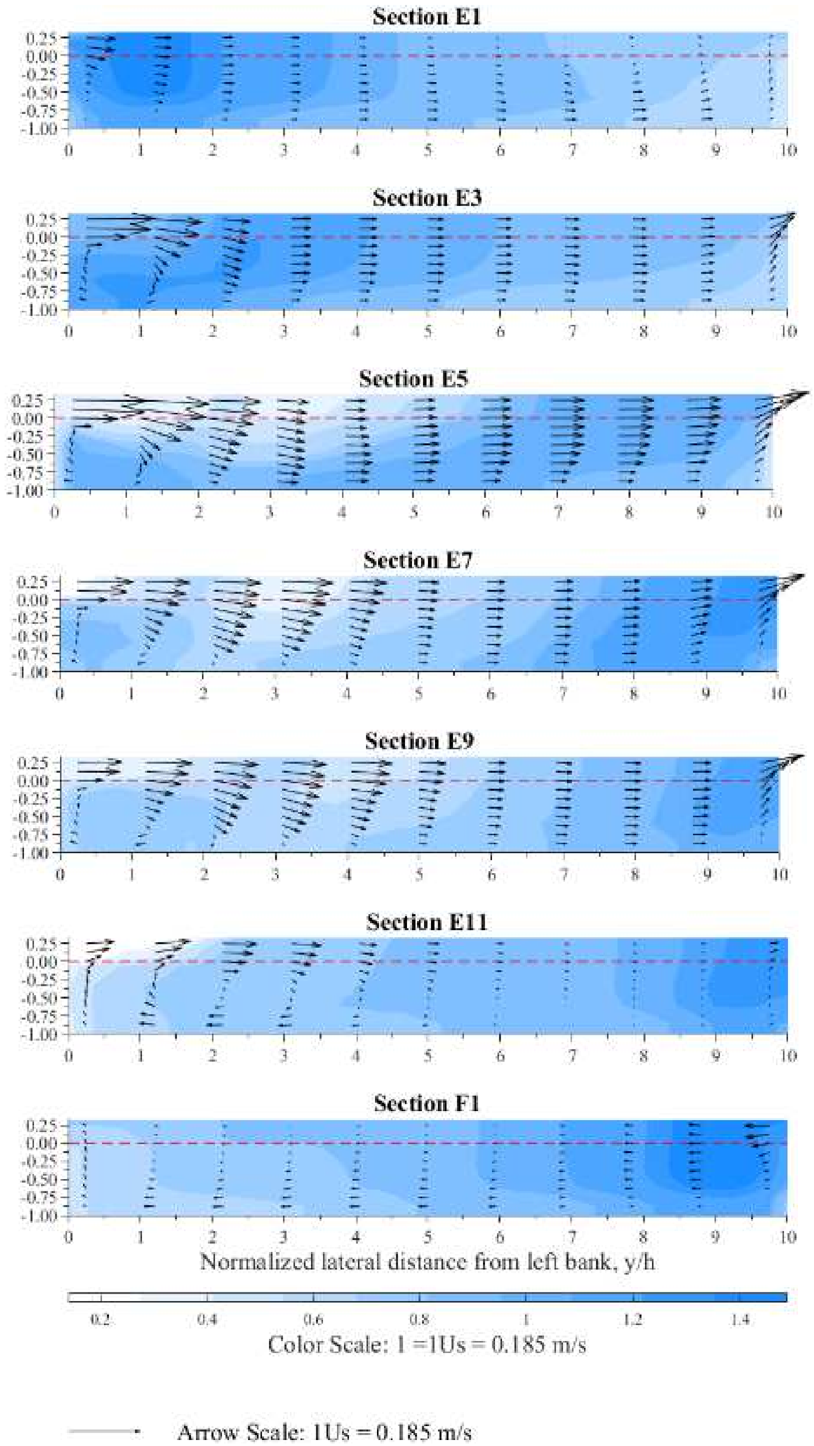

(b)

Figure 44. Primary and secondary flows for relative depth cases for average main channel minima in (a) smooth floodplain (dr = 0.20), (b) low floodplain vegetation density (dr = 0.25), and (c) high floodplain vegetation density (dr = 0.35) scenarios

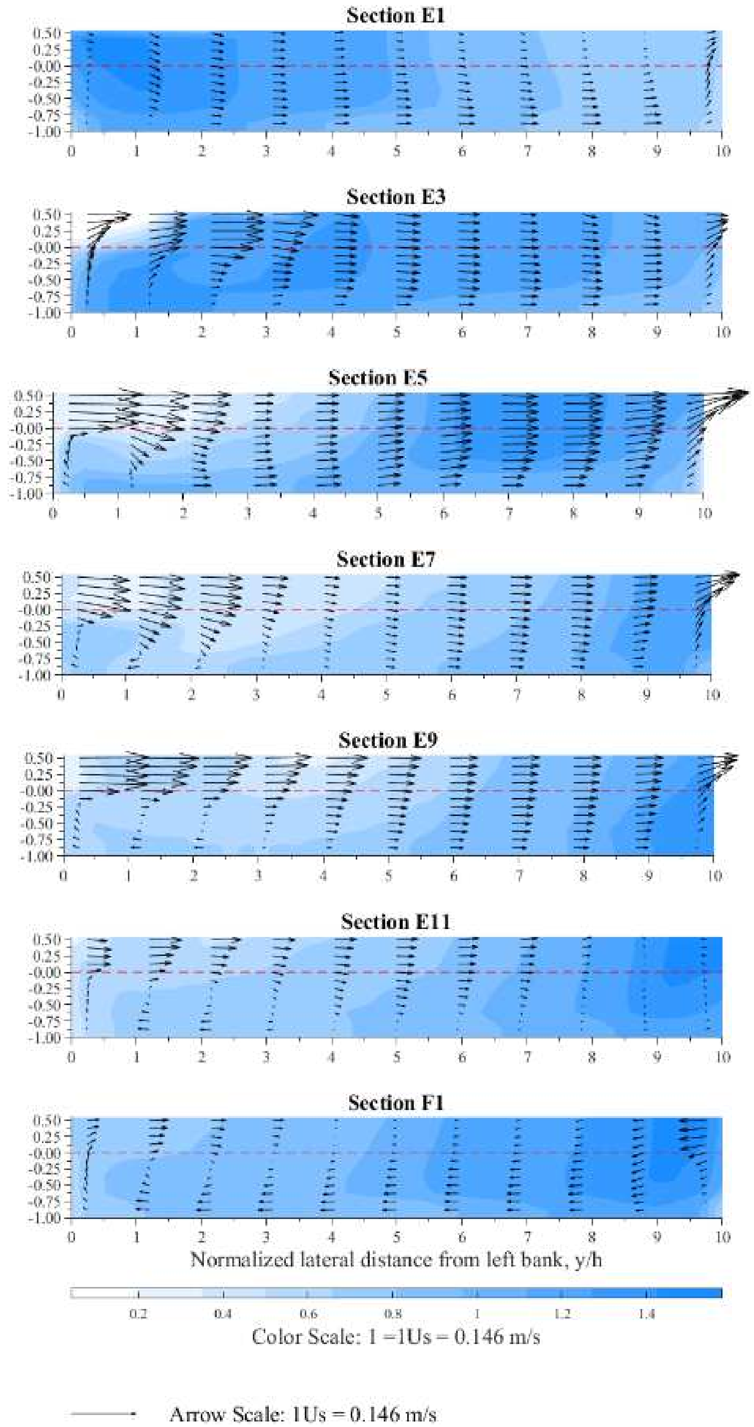

(c)

Figure 44. Primary and secondary flows for relative depth cases for average main channel minima in (a) smooth floodplain (dr = 0.20), (b) low floodplain vegetation density (dr = 0.25), and (c) high floodplain vegetation density (dr = 0.35) scenarios

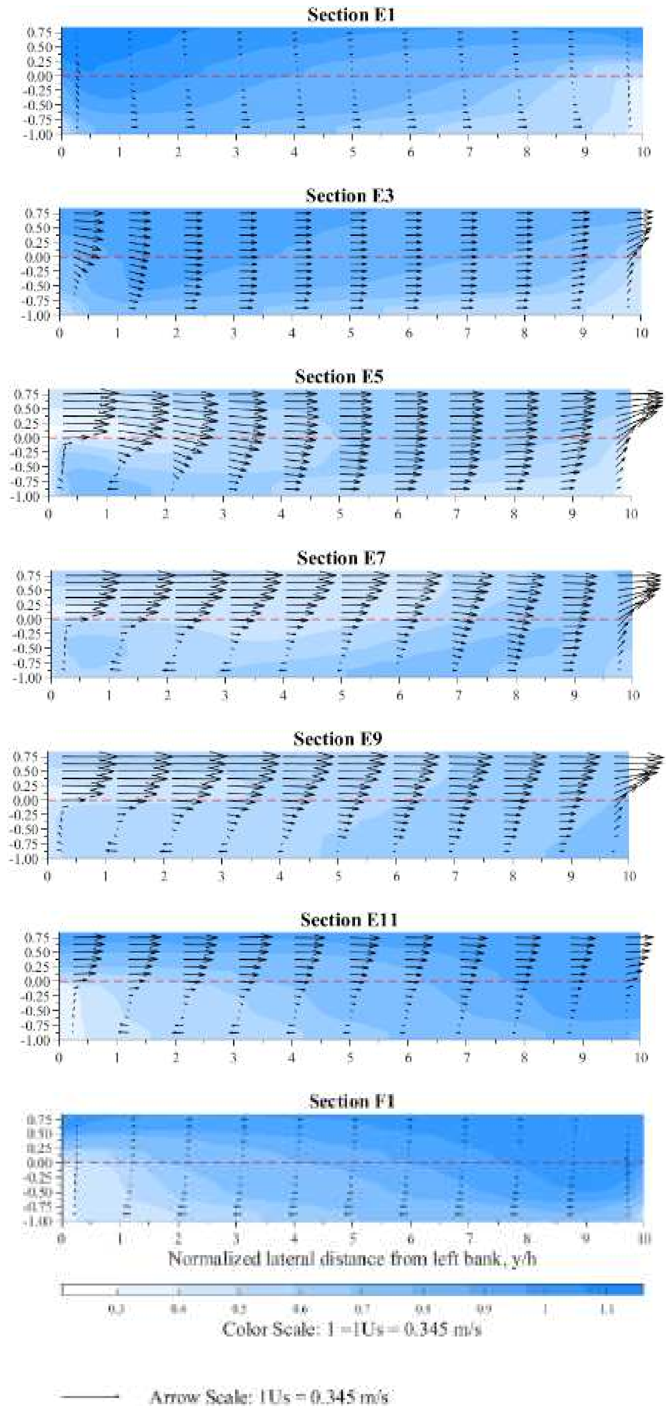

(a)

Figure 45. Primary and secondary flows for relative depth cases of 0.46 for for (a) smooth floodplain, (b) low floodplain vegetation density, and (c) high floodplain vegetation density scenarios

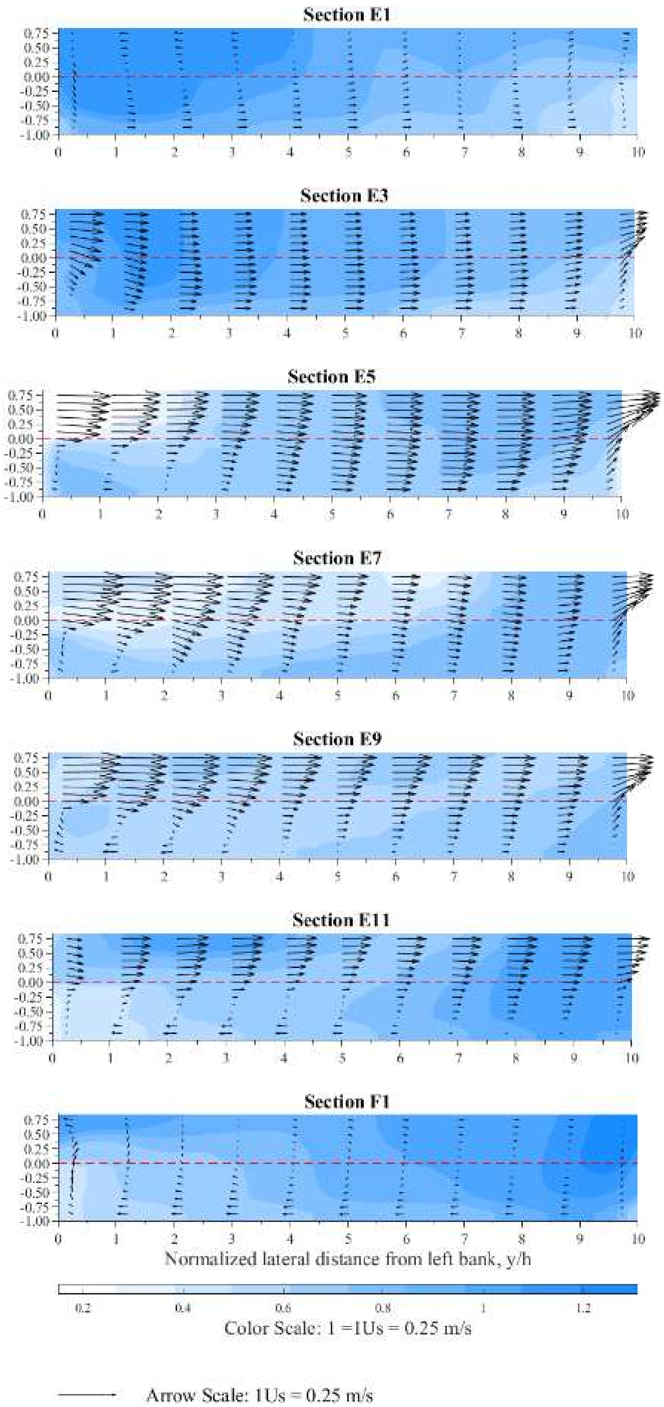

(b)

Figure 45. Primary and secondary flows for relative depth cases of 0.46 for for (a) smooth floodplain, (b) low floodplain vegetation density, and (c) high floodplain vegetation density scenarios

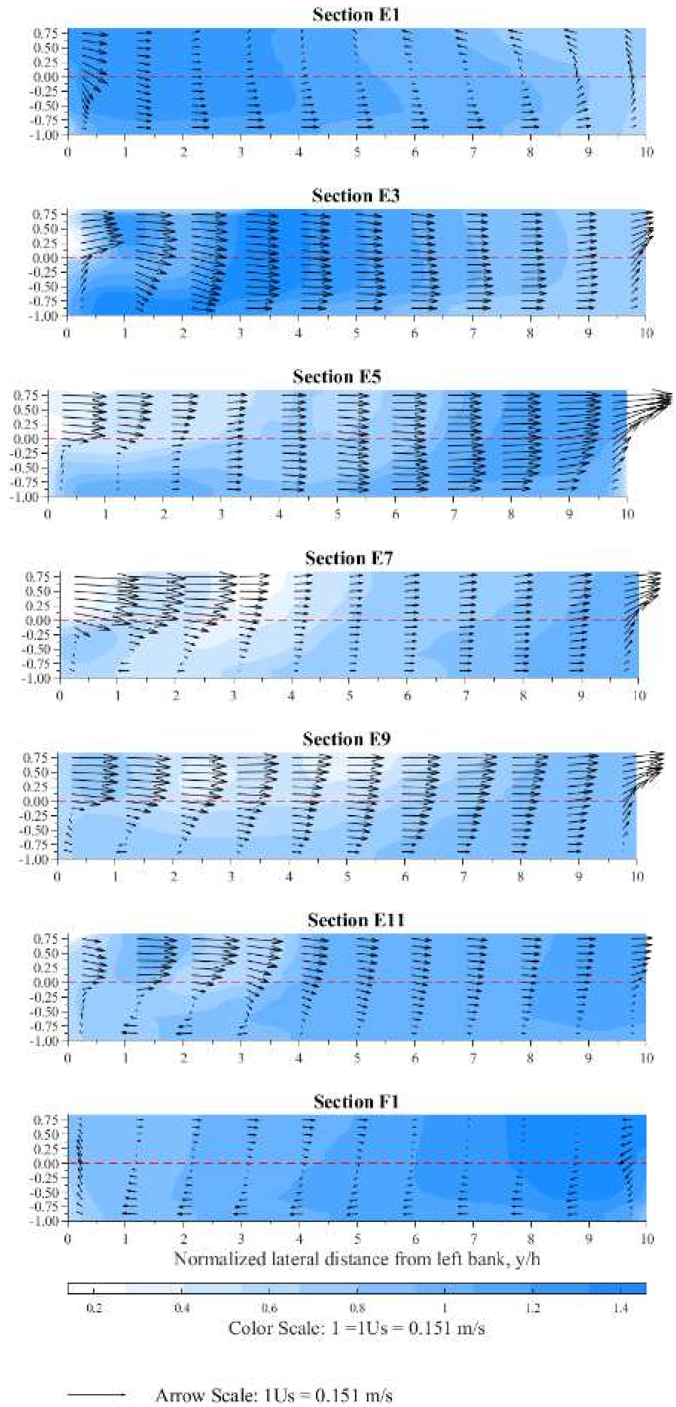

(c)

Figure 45. Primary and secondary flows for relative depth cases of 0.46 for for (a) smooth floodplain, (b) low floodplain vegetation density, and (c) high floodplain vegetation density scenarios

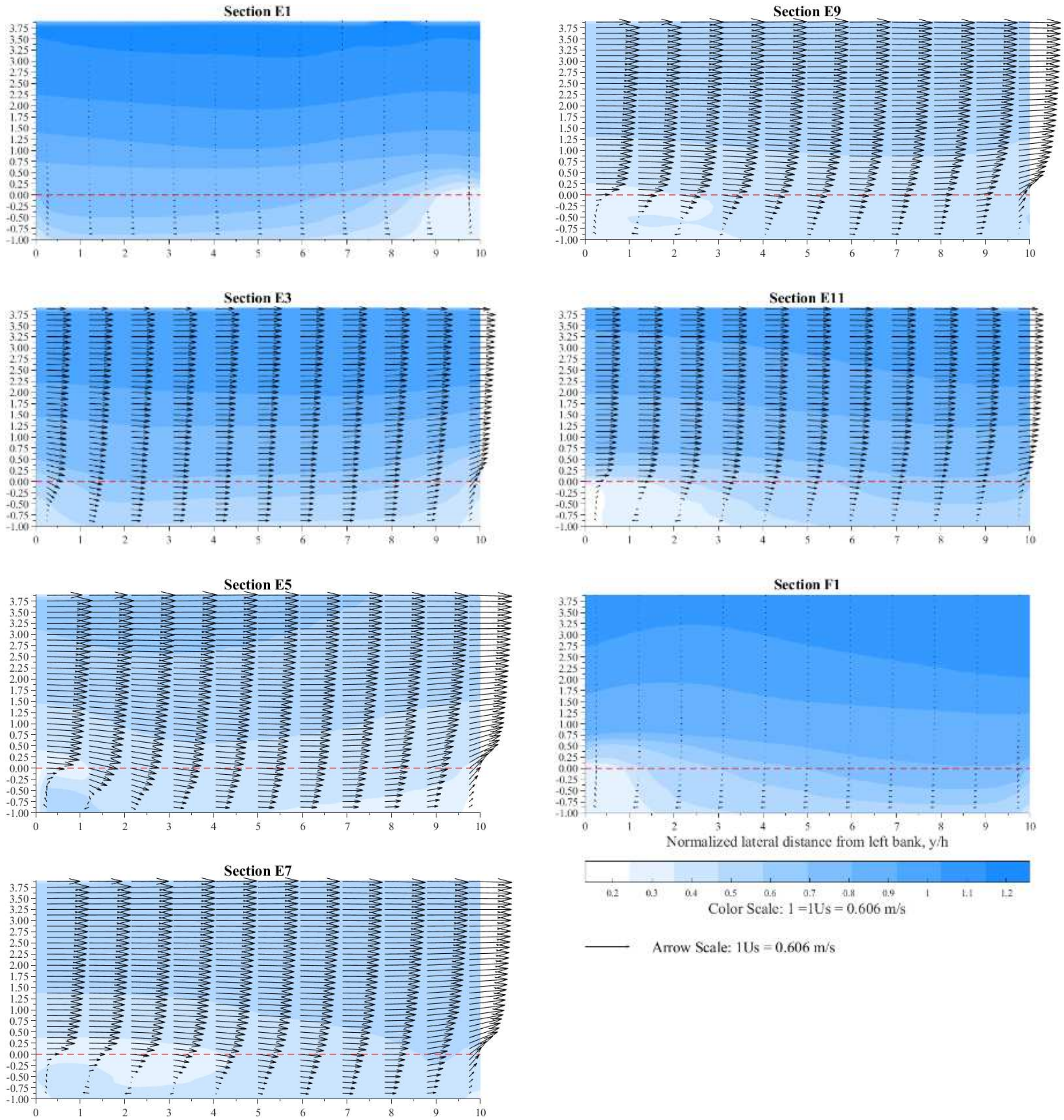

(a)

Figure 46. Primary and secondary flows for highest relative depth cases of 0.80 for (a) smooth floodplain, (b) low floodplain vegetation density, and (c) high floodplain vegetation density scenarios

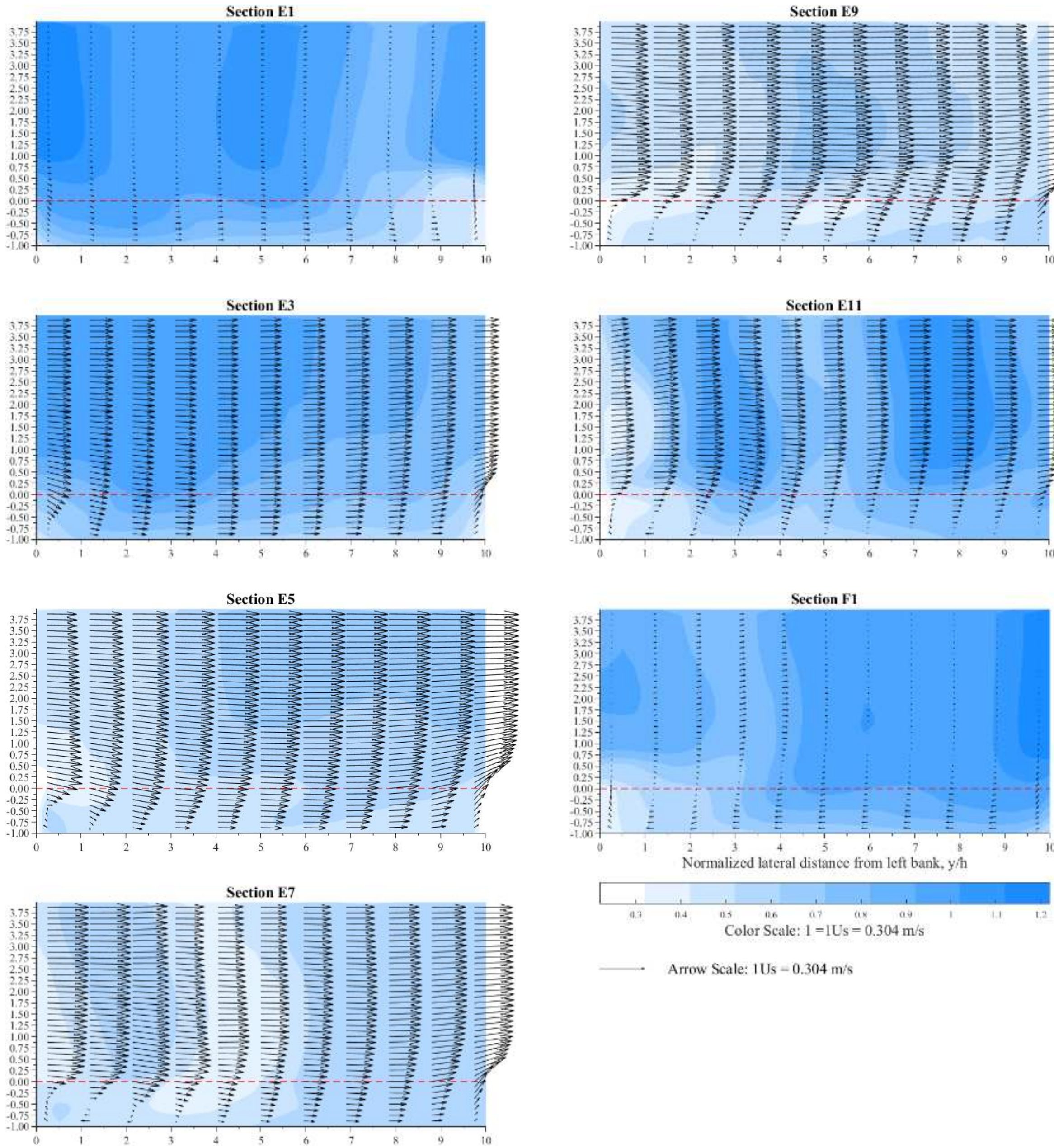

(b)

Figure 46. Primary and secondary flows for highest relative depth cases of 0.80 for (a) smooth floodplain, (b) low floodplain vegetation density, and (c) high floodplain vegetation density scenarios

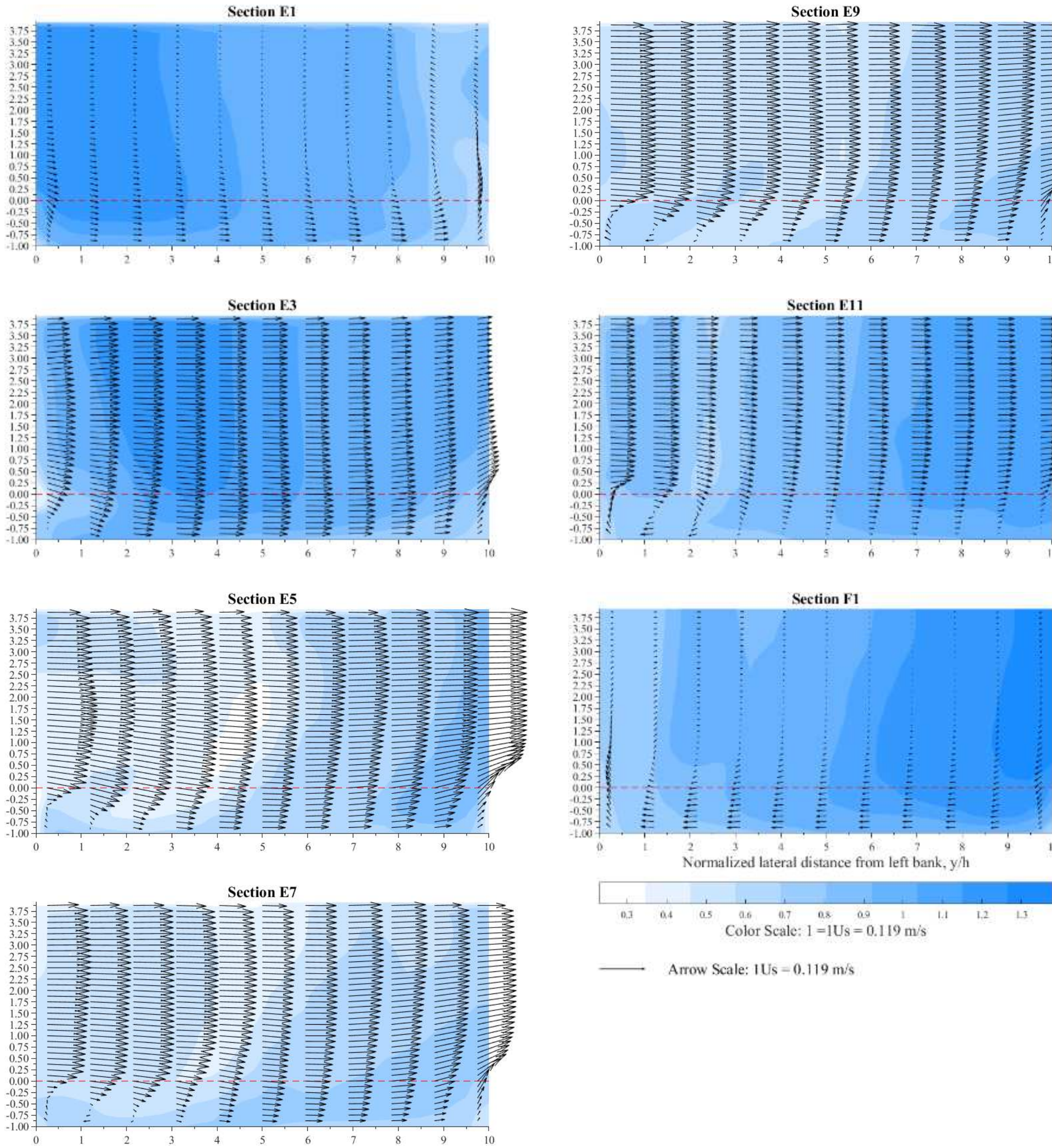

(c)

Figure 46. Primary and secondary flows for highest relative depth cases of 0.80 for (a) smooth floodplain, (b) low floodplain vegetation density, and (c) high floodplain vegetation density scenarios

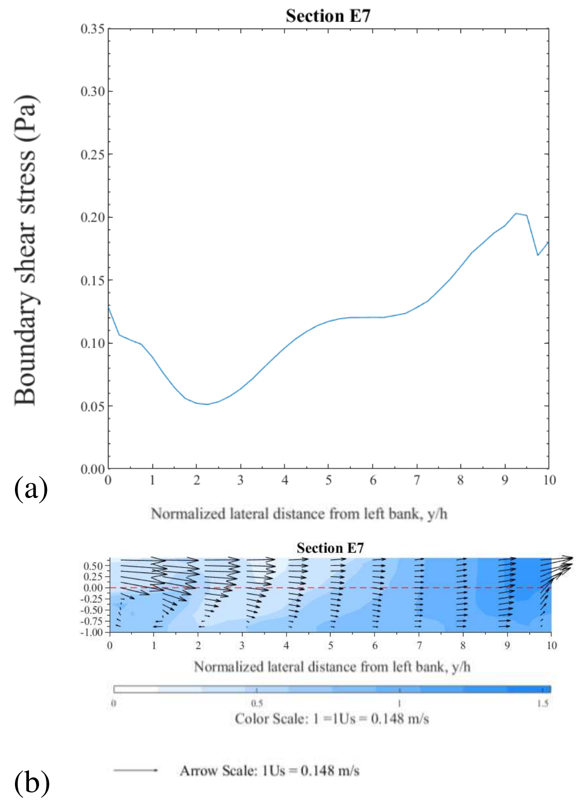

Figure 47. (a) Main channel boundary shear stress plot and (b) primary and secondary flow plot at section E7 for the high vegetation density relative depth of 0.40 scenario showing where regions of downward and upward secondary flows correlate with regions of low

3.6 Layer-Averaged Flow Velocity Fields

In analyzing the planform layer-averaged flow fields, particular focus was placed on regions of diverging and converging inbank and overbank flow vectors within the main channel region. In other words, observations were made in regions where the inbank and overbank flow directions were similar and dissimilar. Additionally, regional flow angles were noted, and comparisons between regional velocity vector magnitudes were made.

At low overbank relative depths, the floodplain flows were generally aligned with the main channel streamwise direction as shown in Figure 48 for the low overbank relative depth cases of 0.13. As vegetation density increased at the low relative depth, the inbank and overbank velocity vectors in the main increased in magnitude compared with the velocities on the floodplain. The regions of high inbank and overbank velocities in the main channel became more aligned and increased in span across the main channel as vegetation density was increased. At the apex section this high velocity region shifted toward the centerline of the main channel with increased floodplain vegetation density.

As relative depth increased, the main channel and floodplain flow vectors in the upstream bend section became more aligned with the valley-wise direction and flow velocity magnitudes on the floodplain increased in relation to the inbank flows as shown in Figure 49 and Figure 50 for high relative depth cases (dr = 0.60). As vegetation density increased for these high relative depth cases, overbank flows aligned more with the meandering streamwise flow paths and the magnitude of the inbank velocities relative to the overbank flow velocities decreased. The flows exiting onto the floodplain maintained more influence from the meandering main channel flow paths as floodplain vegetation density was increased. In the smooth cases at high relative depths, the flow directions of the overbank flows were predominately in the valley-wise direction.

At the relative depths where initial main channel streamwise velocity and boundary shear stress minima were observed, the regions of converging and diverging velocity vectors tended to occupy similar locations for the smooth, low vegetation density, and high vegetation density cases as shown in Figure 51.

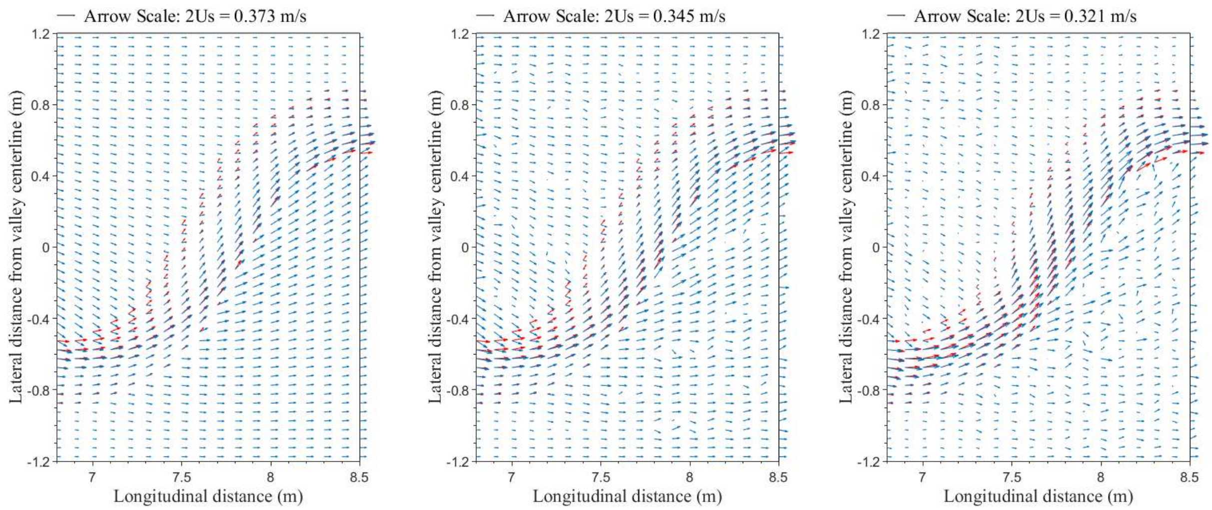

(a.) (b.) (c.)

Figure 48. Layer-averaged flow fields for relative depth cases of 0.13 for (a) smooth (Q = 0.00595 m^3/s), (b) low vegetation density (Q = 0.00525 m^3/s), and (c) high vegetation density (Q = 0.00484 m^3/s) floodplain scenarios

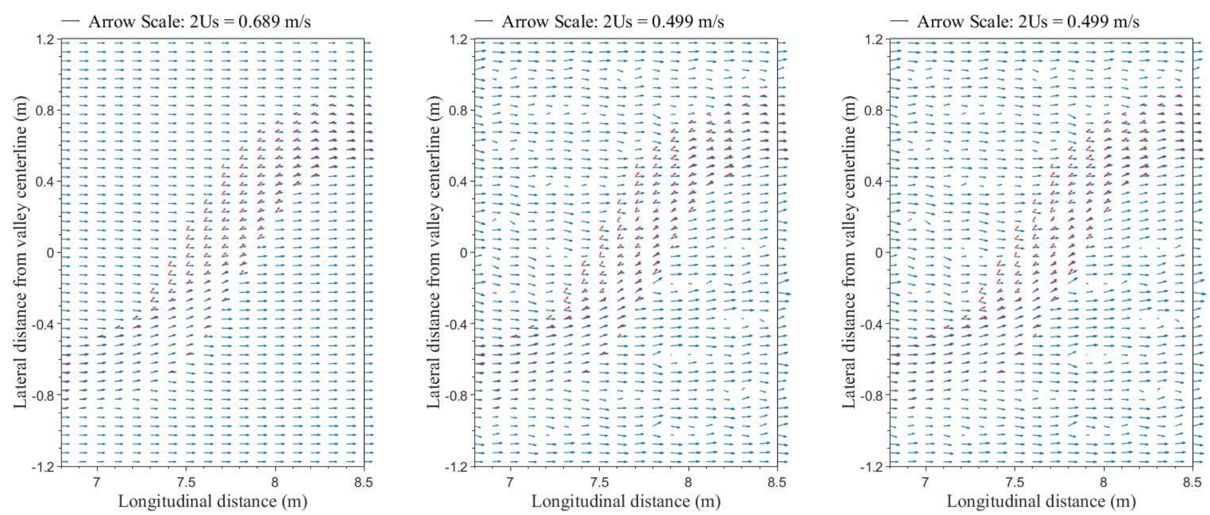

(a.) (b.) (c.)

Figure 49. Layer-averaged flow fields for relative depth cases of 0.46 for (a) smooth (Q = 0.03312 m^3/s), (b) low vegetation density (Q = 0.02420 m^3/s), and (c) high vegetation density (Q = 0.01460 m^3/s) floodplain scenarios

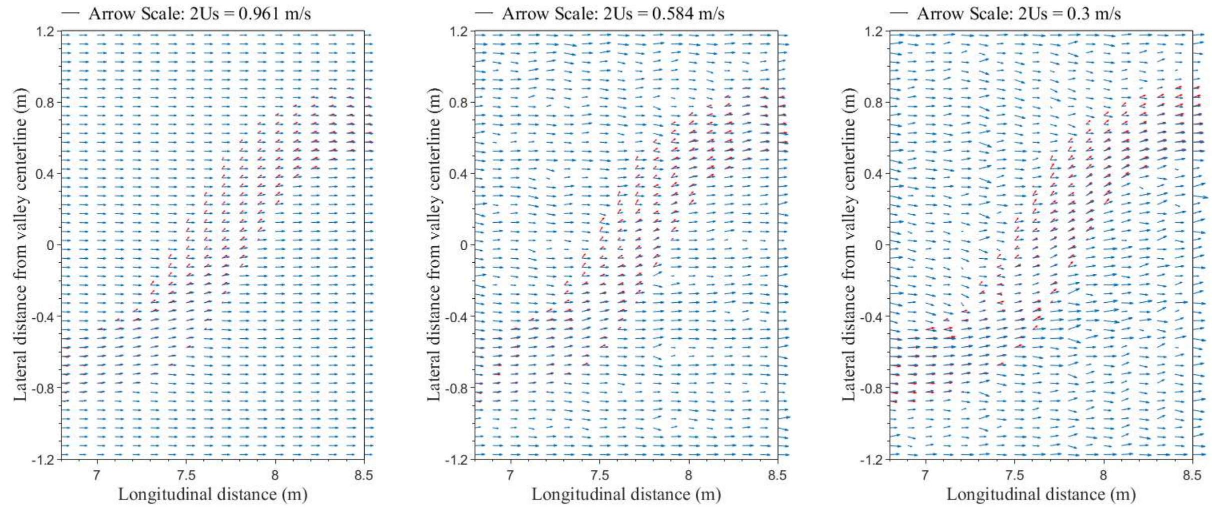

(a.) (b.) (c.)

Figure 50. Layer-averaged flow fields for high relative depth case relative depth cases of 0.60 for (a) smooth (Q = 0.07657 m^3/s), (b) low vegetation density (Q = 0.04720 m^3/s), and (c) vegetation density (Q = 0.02356 m^3/s) floodplain scenarios

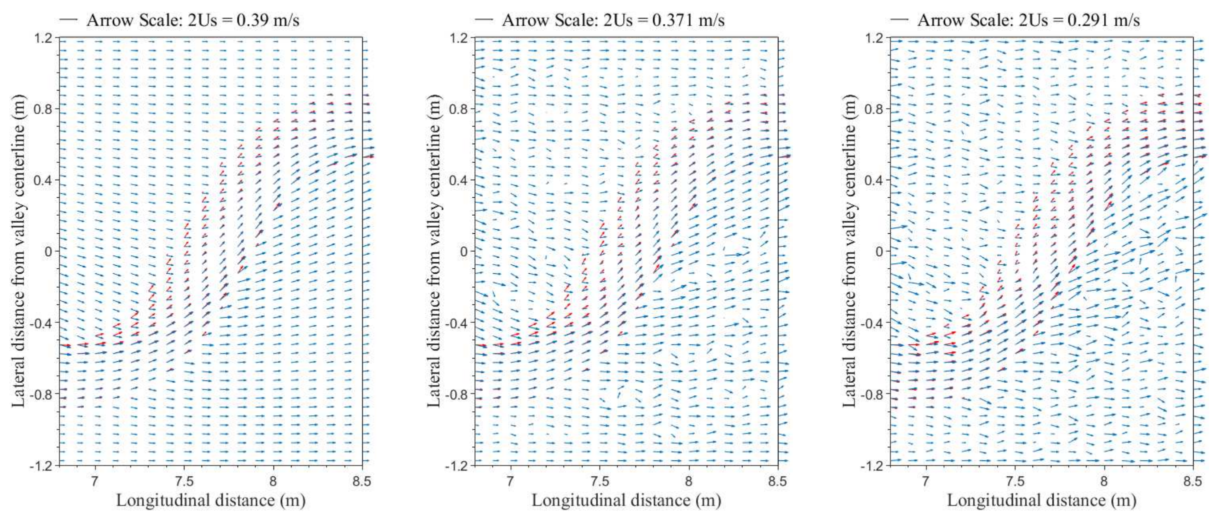

(a.) (b.) (c.)

Figure 51. Layer-averaged flow fields for initial drop in average main channel boundary shear stress cases for (a) smooth (dr = 0.20, Q = 0.00793 m^3/s), (b) low vegetation density (dr = 0.25, Q = 0.00886 m^3/s), and (c) high vegetation density (dr = 0.35, Q = 0.009935 m^3/s) floodplain scenarios

4 DISCUSSION

4.1 Stage-Discharge

Floodplain vegetation density was shown to significantly affect the stage-discharge relationships in the meandering compound channel. As floodplain vegetation density increased, the stage-discharge relationships also increased. Therefore, small increases in discharge would result in greater increases in stage with increased floodplain vegetation density. One would expect the stage to be greater for a given total flowrate as floodplain vegetation density is increased. For the low floodplain vegetation density scenario, the discharge capacity was reduced up to nearly 50%, and for the high floodplain vegetation density scenario, it was reduced by 80% compared with the smooth floodplain scenario. These reductions in discharge capacity are consistent with those of other researchers who studied flows in meandering compound channels with roughened floodplains. The US Army Corps of Engineers (1956) found that as floodplain roughness was increased, the discharge capacity in meandering compound channels was reduced. For the mobile bed experiments of Chan (2003), the discharge capacity for their smooth case scenarios was approximately 50% greater than that of their roughened floodplain scenarios. Liu et al. (2016) reported the discharge capacity in their smooth floodplain scenario was 30% greater than that in their artificial grass roughened floodplain scenario.

4.2 Main Channel Streamwise Velocities and Boundary Shear Stresses

Floodplain vegetation density had notable influences on the average main channel streamwise velocities and boundary shear stresses as can be seen in the average main channel value plots Figure 26, Figure 27, Figure 32, and Figure 33. At the lowest relative depth of 0.13 and 0.20, the high floodplain vegetation density scenario had the greatest average main channel streamwise velocities and boundary shear stresses. However, the values were similar between all floodplain scenarios indicating that at the lowest relative depths, the effects of floodplain vegetation density on the average main channel streamwise velocities and boundary shear stresses were not appreciable.

At higher relative depths and vegetation densities, the average main channel streamwise velocities and boundary shear stresses were lower. James and Wark (1992) concluded that during overbank flows, boundary shear stresses were expected to decrease compared with those under bankfull conditions. This conclusion was seen at low relative depths for all floodplain scenarios. However, this was not observed at high relative depths for the smooth floodplain scenario, where the average main channel streamwise velocities and boundary shear stresses exceeded those of the bankfull case. For the smooth floodplain scenario at these high relative depths, the average main channel streamwise velocities and boundary shear stresses did not change much between relative depth cases of 0.60 and 0.80 even though the total discharge increased by over 200% between the two cases. This indicates that for the smooth floodplain cases at the highest relative depths, the main channel flow field may be less likely to be affected by further increases in total flowrate and flow depth compared with lower relative depths and flowrates; however, more data points at high relative depths are required to strengthen or weaken this hypothesis. Between floodplain scenarios, the percent of the total flow in the main channel converged between floodplain roughness scenarios at high relative depths and low discharges. Therefore, at high relative depths and low discharges, one would expect there to be little difference in the percent of the total flow conveyed in the main channel between floodplain roughness scenarios. One should note that although the percent of the total flows in the main channel would be similar at these relative depths and total flows, the actual inbank flowrates would vary drastically between floodplain scenarios.

The decreasing trends in non-dimensional average main channel streamwise velocities and boundary shear stresses had nearly the same slope across all of the floodplain roughness scenarios, as seen in Figure 30, Figure 31, Figure 34, and Figure 35. This similarity indicates that as relative depth was increased for all floodplain roughness scenarios, the average main channel velocity changed at a lower rate than the characteristic velocity increased, the average main channel velocity decreased at a greater rate when the characteristic velocity did not increase greatly, or both. Shiono et al. (1999) also showed that the non-dimensional boundary shear stress decreased with increasing flow depth as well in their meandering compound channel experiments.

The planform main channel boundary shear stress analysis revealed that as floodplain vegetation density was increased, the heterogeneity or patchiness of the boundary shear stress field also increased, as can be seen in Figure 36 through Figure 41. At the lowest overbank relative depth (dr = 0.13) shown in Figure 37, discontinuities or patchiness and a larger range in the main channel boundary shear stresses were observed for the high floodplain vegetation density scenario. At the same relative depth, the regions of low and high main channel boundary shear stresses for the low floodplain vegetation density scenario were only slightly discontinuous, and for the smooth floodplain scenario, the regions were continuous. Therefore, at low relative depths, having high density vegetation on the floodplain appeared to increase the heterogeneity and discontinuity of boundary shear stress magnitude in the main channel, whereas low floodplain vegetation densities may not produce much difference in the main channel boundary shear stress field when compared with that in a smooth floodplain system.

At high relative depths for the vegetated floodplain scenarios, strong gradients of boundary shear stresses perpendicular to the meandering main channel walls began to appear at the threshold relative depths where the initial minima in main channel boundary shear stresses occurred, as can be seen in Figure 38. These strong gradient boundary shear stress patterns in the vegetated scenarios indicate that even for flows where the average main channel boundary shear stress is minimized, there are still regions of relatively high boundary shear stress present, especially for the high floodplain vegetation density scenario. These results also show that low and high boundary shear stress regions were distributed across the main channel in the vegetated floodplain scenarios where they would not be found in the smooth floodplain scenario.

Increasing floodplain vegetation density and increasing relative depth appeared to concentrate the regions of high boundary shear stresses within tighter bands inside the main channel, as can be seen in Figure 39 and Figure 40. The low vegetation density scenarios had larger regions of high boundary shear stress than in the high vegetation density cases. The bands of low and high boundary shear stress, which were aligned with the valley-wise direction for the vegetated floodplain scenarios, are reminiscent of the valley-wise aligned bedforms observed by Chan (2003) in their block roughened floodplain cases. In the study of Chan (2003) and the current study, the three-dimensional elements on the floodplain may have constricted the flow causing local accelerations between rows of elements as well as produce local decelerations. These high and low velocity regions on the floodplain may have helped produce the bands of low and high boundary shear stresses in the main channel which could drive similar patterns in the bed topography.

The plots of average main channel velocities, boundary shear stresses, and characteristic velocities versus relative depth have similar trends. Therefore, there may be a link between the processes which form each. What may be happening is that as the total amount of flow which can be passed through a given total area (i.e., characteristic velocity) increased, the amount of flow passing through the main channel also increased. As the flow being passed through the main channel increased in the streamwise direction, the average main channel streamwise velocities and boundary shear stresses increased. As vegetation density increased, the total amount of flow which could be passed through a given total area decreased; thus, the average main channel streamwise velocities and boundary shear stresses also decreased.

4.3 Primary Flows, Secondary Flows, and Layer-Averaged Velocity Fields

Primary Flows

Relative depth and floodplain vegetation density were seen to affect the relative strength and patterns of the primary streamwise flow in and above the meandering compound channel across the studied half meander. As flows increased above bankfull for all floodplain roughness scenarios, the width of the near-surface low streamwise velocity region increased in area, as can be seen when comparing Figure 43 and Figure 45. In addition, the high streamwise velocities tended to be concentrated into smaller regions at the bend sections and became weaker in relative magnitude at the crossover sections. Comparatively for the bankfull case, the main channel high streamwise velocity filament maintained high magnitudes through the crossover region. This indicates that overbank flows may either exert a dampening force on the streamwise velocities in the crossover section, an amplifying force on the streamwise velocities in the bend sections, or perhaps both. The strength of these dampening and amplifying forces appears to be dependent on the floodplain vegetation density. At high relative depths for the vegetated floodplain scenarios, the high and low regions of streamwise velocity were split into more regions than in the smooth floodplain scenarios. Therefore, it appears that floodplain vegetation also influences the discontinuity of low and high streamwise velocity regions in the main channel.

The continuity of the main channel streamwise high velocity filament across the half meander appeared to be dependent on relative depth and floodplain vegetation density. Willets and Rameshwaran (1996), Ishigaki (1997), and Shiono and Muto (1998) show that the maximum streamwise velocity filament moves from the inner bank of the main channel at the upstream apex to the inner bank at the downstream apex, which is what was observed at low relative depths for all floodplain scenarios, as can be seen in Figure 43. However, at high relative depths especially for the vegetated floodplain cases, the high streamwise velocity filament in the main channel appeared to be 'washed out' in the crossover region, as can be seen in Figure 46. The high streamwise velocity filament in the crossover section tended to move toward the bed as relative depth increased up to a given value. Above the threshold relative depth of 0.35 for the high floodplain vegetation density scenario, the near bed high streamwise velocity filament in the crossover section became relatively less significant, as can be seen in Figure 45 at section E7. These trends in the near-bed high streamwise velocity region may be related to why the average main channel streamwise velocity increased with relative depths above the minima threshold for the smooth and low vegetation density floodplain scenarios; yet for the high floodplain vegetation density scenarios, the average main channel streamwise velocities continued to decrease as relative depth increases.

<u>Secondary Flows</u>

The presence, extent, relative strength, and character of the apex section secondary flow cells appeared to be influenced by the floodplain vegetation density. For the vegetated cases, the size, strength, and location of the inbank clockwise flow cell in the interior sections varied greatly, as can be seen in Figure 43(b)(c) and Figure 45(b)(c). These variations in the secondary flow field indicates that the flow field may have been discontinuous or patchy for the vegetated floodplain scenarios similar to the observed boundary shear stress field for the same scenarios. This similarity between the patchy primary flow, secondary flow, and boundary shear stress fields can be seen in Figure 47, which compares the boundary shear stress and secondary flows at section E7 for a relative depth of 0.40. These patterns indicate that the discontinuities in the primary and secondary flow fields guide the redistribution and patchiness of low and high boundary shear stresses, which are dependent on the relative depth and total flowrate for the vegetated floodplain cases. On the other hand, the lack of change in character of the interior section secondary flow cells with relative depth in the smooth floodplain scenarios indicates that either its formation is somewhat independent of the flow depth and total flowrate, only the dimensional strength of the flow cell is dependent on the flow depth and total flowrate, or both.

As floodplain vegetation density increased, the inbank cross stream velocities also increased, which appeared to be related to how overbank flows returned to the main channel from the floodplain. The greatest inbank cross stream velocities typically occurred at section E5 at the upstream end of the crossover section, as can be seen in Figure 43 through Figure 46. These high cross stream velocities at section E5 increased with vegetation density, particularly near the bed. The cause of this increase in inbank and near-bed cross stream velocities appeared to be the flows returning to the main channel that plunged below the bankfull level from the upstream floodplain in the crossover regions. For the high vegetation density cases, the flows returning from the upstream floodplain tended to plunge more steeply into the inbank portion of the main channel within the crossover section than in the smooth and low vegetation density scenarios, as seen in Figure 45 when comparing the flows at the left bank near the free surface of section E7 between floodplain vegetation scenarios. As relative depth increased beyond dr = 0.25, where the average main channel streamwise velocity was minimized for the low vegetation density case, the returning flows from the upstream floodplain became more horizontal and thus plunged less steeply into the main channel if at all. For the smooth case above dr = 0.20, flows from the upstream floodplain tended to maintain a horizontal path over the bankfull level of the main channel. It appears that for the smooth and low vegetation density cases above the threshold relative depth, the cross-stream flow returning to the main channel from the floodplain at the crossover region separates more fully along the bankfull level compared with the high vegetation density case. The degree of overbank and inbank flow separation may influence exchanges of momentum between overbank and inbank flow layers. The smooth floodplain cases showed flow phenomena observed in flume studies in compound in which a horizontal shear layer formed over the main channel (Ervine & Jasem, 1995).

At the highest relative depth of 0.80, the flow separation at the crossover section weakens and the below bank main channel cross stream flows increase in strength. At this relative depth, the rate of increase in main channel averaged velocity and boundary shear stress decreases versus relative depth compared with the lower relative depth for all of the floodplain roughness cases. This indicates that at very high relative depths, the intrusion of the valley-wise floodplain flows into the inbank main channel region extracts momentum from the main channel flows. In addition, the influence of the overbank flow layer on the inbank flow field appears to be at its greatest in the high vegetation density cases.

There are likely relationships between the location of high and low boundary shear stresses and secondary and primary flow patterns. Chan (2003) notes the findings of Shiono et al. (1999) and Nezu and Onitsuka (1999) which showed that boundary shear stresses were higher where downward secondary flows were present and lower where upward secondary flows were present. Figure 47 shows the opposite trend occurring in the current study where downward secondary flows correlated with lower boundary shear stresses and upward secondary flows correlated with higher boundary shear stresses. These results are more consistent with those reported by Lorena (1992) who observed high boundary shear stresses occurring on the floodplain where the main channel flows upwelled onto the floodplain.

Layer-Averaged Flow Velocity Fields

The layer-averaged velocity fields appeared to be strongly dependent on relative depth and floodplain vegetation conditions. The area of inbank flow aligned with the valley-wise direction increased, and these inbank velocities decreased in magnitude relative to the overbank velocities as relative depth and vegetation density increased. At low relative depths, the layer-averaged velocity vectors in and over the main channel were generally aligned with the meandering walls of the main channel. As the flows spilled onto the down-valley floodplain at the crossover section, the overbank flow layer maintained a deviated path set by the exiting meandering flows until they re-entered the main channel downstream. The deviated angle in the floodplain flows away from the valley-wise direction may also introduce strong cross stream flows within the bend section. At low relative depths, a vertical shear layer likely forms in the main channel between the slow deviated floodplain flows returning to the faster main channel at a large angle of attack. These results indicate that at low overbank relative depths, the inbank flow layer exerted a strong influence on the overbank flow direction. In cases where the angle of the floodplain flows strongly deviated from the valley-wise direction, secondary flows appeared to plunge at steeper angles into the inbank portion of the main channel.

As relative depth increased, the overbank flow layer became more aligned with the straight valley walls. The valley-wise overbank flow layer appeared to exert a greater influence on the main channel flow direction at these higher relative depths. The inbank and overbank velocity vectors diverge where the floodplain flows return to the main channel on the up-valley side of the main channel. The opposite tends to occur at the down-valley side of the main channel where flows re-enter the floodplain. These results are consistent with the finding of Shiono and Muto (1998) who observed that at low overbank flow depths, the main channel flows appeared to 'dominate' the flow even up to the free surface. They saw that at these low overbank depths, the floodplain flow angles deviated from the valley-wise direction due to the influences of the main channel flows. Shiono and Muto (1998) also saw that at high overbank flow depths, the overbank flow layer was primary aligned with the straight valley walls.

The regions of converging velocity vectors tended to appear at approximately the same locations as the high streamwise velocity filaments and high boundary shear stress regions, particularly in the bend sections. The rotating secondary flow cells and regions of low main channel boundary shear stress were observed in the region where the flow vectors diverged, particularly in the crossover region where floodplain flows entered the main channel region. Shiono and Knight (1996) reported that the overbank flow that crosses over the main channel drives the formation of secondary currents in the main channel whereas for inbank flows centrifugal forces are primarily responsible for secondary current genesis. These connections can be seen in comparing planform boundary shear stresses, the cross-sectional plots of primary and secondary flows, and planform layer-averaged velocities in Figure 37, Figure 43, and Figure 48. Shiono and Muto (1998) observed that areas with large differences in flow angles between layers corresponds with eddy trains and indicated that a large amount of turbulent kinetic energy should be generated in this region. These results suggest that inbank main channel flow phenomena are influenced by interactions with the overbank flow layer. At the relative depths where the initial minima in average main channel streamwise velocities and boundary shear stresses occurred, the patterns of diverging and converging flow regions were nearly the same implying that the mechanisms for producing these minima might be similar for all of the floodplain scenarios.

4.4 Minima in Average Main Channel Streamwise Velocity and Boundary Shear Stress

A key point of interest for the current study was to see whether drops or minima in the average main channel streamwise velocity and boundary shear stresses would occur at some threshold overbank relative depth, as have been reported in meandering compound channels by other researchers. If these minima did occur, how would floodplain vegetation density affect their appearance? In the current study, the average main channel streamwise velocities and boundary shear stresses initially decreased at low overbank relative depths compared with the values for the bankfull case for all floodplain vegetation scenarios. As vegetation density increased, the initial minima in the average main channel streamwise velocities and boundary shear stresses occurred at greater threshold relative depths or total flowrates and were lower in magnitude. For the smooth and low floodplain vegetation density scenarios, at relative depths above the threshold values for the minima in the average main channel streamwise velocities and boundary shear stress, the average main channel values began to increase with relative depth. Interestingly, the main channel values did not increase with relative depth for the high vegetation density scenario. At high relative depths for both vegetated floodplain scenarios, secondary drops in the main channel values occurred. These results indicate that during overbank flows, floodplain vegetation density has a strong influence on the average streamwise velocities and boundary shear stresses in the main channel of meandering compound channels above the lowest overbank relative depths and discharges.

At the lowest relative depths, floodplain flows were relatively slow compared with those in the main channel for all floodplain scenarios, as can be seen in the layer-averaged flow plots in Figure 48 and Figure 51. These relatively slow floodplain flows may contribute to or be products of energy losses at the floodplain-main channel interface where floodplain flows enter and exit the main channel in the crossover sections of the primary and secondary flow plots in Figure 43 and Figure 44. Stein and Rouve (1988 and 1989) explained that the flows in the main channel ‘well’ out onto the floodplain, which dampens the floodplain flows in compound meandering channels, as can be seen in the crossover sections of the threshold relative depth cases . In their dye injection experiments in a meandering compound channel, Smith (1978) also found that flows exited the main channel and spilled onto the floodplain. James and Wark (1992) concluded that additional dampening of the flow results from these exchanges of fast and slow flows between the floodplain and main channel. Kiely et al. (1989 and 1990) observed that floodplain flows cross over and enter the main channel at the crossover section from the upstream floodplain and exit onto the downstream floodplain. They explained that energy losses due to the expansions and contractions of the flow occur as the flow depth changes from the shallow floodplain to the deeper main channel then back the shallow floodplain as floodplain flows cross the main channel.

At the threshold minima in average main channel streamwise velocities and boundary shear stresses, the cross-channel flows from the floodplain appeared to plunge more steeply at the upstream floodplain along the left bank as can be seen in Figure 44 near the left banks of the crossover section especially at section E7. This suggests that when the floodplain flows are slow enough, they are not able to achieve significant flow separation along the bankfull level at the crossover sections, but rather dip in and out of the main channel. Chan (2003) also noted the presence of “floodplain flow plunging into the main channel” at the crossover sections in their reduced main channel boundary shear stress case. Chan (2003) explained that the main channel boundary shear stress reduction was due to energy losses as a result of these plunging crossover flows producing contraction and expansion effects. When these slower floodplain flows return to the main channel, these may add low momentum fluid to the main channel which promotes a further dampening of the main channel flow. The combined dampening effects of the contraction-expansion losses and addition of low momentum fluid into the main channel at low relative depths are believed to cause the initial drops in the average main channel streamwise velocities and boundary shear stresses. As floodplain vegetation density increased, these potential drivers of the initial minima in average main channel streamwise velocities and shear stresses became more significant thus the minima were lower in magnitude. The floodplain velocities relative to the flows in and over the main channel were lower in magnitude, floodplain flows plunged more severely into the main channel, and the average main channel minima were lower in magnitude as floodplain vegetation density was increased.

As relative depth increased above the threshold value for the average main channel minimum for the smooth and low vegetation density scenarios, the flow velocities on the floodplain increased magnitude in valley-wise direction relative to flows in the main channel region as can be seen in Figure 49(a)(b) and Figure 50(a)(b). When these faster, valley-wise floodplain flows return to the main channel at the apex section, they add high momentum fluid that helps drive the main channel streamwise flow. When these faster floodplain flows return to the main channel at the crossover section, they separate at the floodplain main channel-floodplain interface at the bankfull level as can be seen in Figure 45(a) at section E7. Where this flow separation occurs, a horizontal shear layer separating the inbank and overbank flow layers. Kiely et al. (1989 and 1990) also performed experiments in a meander compound channel with a rectangular main channel cross section and noted that the main channel flows follow the paths set by the meandering channel form while the overbank flows are generally guided by the floodplain walls. Kiely explains that this difference in the flow directions may be evidence for horizontal shear layer between inbank and overbank flows. Stein and Rouve (1988 and 1989) and James and Wark (1992) also support the existence of a horizontal shear layer at the bankfull level in meandering compound channels. The horizontal shear layer may prevent the inbank and overbank flows from interacting significantly thus less energy is pulled from the main channel flows. When less energy is pulled out of the main channel flows, the average main channel streamwise velocities and boundary shear stresses should rise with relative depths above the minima thresholds.

As vegetation density increased at relative depths above the minima threshold, the floodplain flows were low in magnitude relative to the inbank flows and deviated more from the valley-wise direction. For the low vegetation density scenario, the floodplain flows appear to be just fast enough to generally be aligned with the valley-wise direction and have relatively strong horizontal separation at the bankfull level. Thus, as floodplain vegetation density was increased to the highest value, the vertical shear layer appears to have prevailed over the horizontal shear layer thus producing greater energy losses. In their mobile bed experiments, Chan (2003) found that the crossover flows were great enough to bring sediment from the main channel onto the down-valley floodplain and then deposit it back into the main channel down-valley for the roughened floodplain cases but not the smooth floodplain cases. Their results indicate that the overbank crossover section flows likely plunged into and welled out the main channel more significantly in the roughened floodplain than in the smooth floodplain cases. This result supports the current study's claim that increasing floodplain vegetation density decreases the strength of the horizontal flow separation at the bankfull level thus causes greater plunging of floodplain flows into the main channel at the crossover section. This plunging results in greater energy losses in the main channel and floodplain flows due to the contraction-expansion effects. These losses compound as they promote the slowing and deviation of floodplain flows which continue to produce a vertical shear layer where the floodplain flows return to the main channel at higher relative depths. Thus, for the vegetated floodplain scenarios, the main channel energy losses are greater than in the smooth floodplain due to the weakening of the horizontal shear layer at the bankfull level and the strengthening of the vertical shear layer at the floodplain-main channel interface. These increased energy losses help explain why the average main channel streamwise velocities are generally lower as floodplain vegetation density increased. For the low vegetation density scenarios, the horizontal separation appeared to be strong enough due to strong enough as the floodplain that the average main channel streamwise velocities and boundary shear stresses could rise with increased relative depth above the threshold for the minimum. For the high floodplain vegetation density scenarios, the horizontal shear layer appeared to be weakened enough that significant exchanges between inbank and overbank flow layers occurred. These exchanges resulted in high energy losses that prevented the average main channel streamwise velocities and boundary shear stresses from rising with relative depth.

For channel region partitioning in meandering compound channels used in discharge approximations and for 2D numerical models with compound channel cross sections, the bankfull level is typically assumed to form a horizontal boundary between inbank and overbank flows due to the presence of the horizontal shear layer (Sellin et al., 1993; Shiono & Muto, 1998). Shiono and Muto (1998) concluded that the partitioning method at the bankfull level may be appropriate for high relative depth cases because the difference in flow angles between the inbank and overbank flow layers became constant at high flow depths. Thus, the inbank and overbank layers did not appear to interact across the bankfull level where a horizontal shear layer was assumed to form. Shiono and Muto (1998) also concluded that this partitioning method may not be appropriate at low relative depths because the inbank and overbank flow layers appear to be dependent. The results of the current study support the assertion that flows may be partitioned at an imaginary plane at the bankfull level at high relative depths but not low relative depths for meandering compound channels with smooth floodplains. Importantly, the results of the current study indicate that the partitioning at the bankfull level horizontal plane may also not be appropriate for vegetated and roughened floodplain cases.

4.6 Implications for Geomorphology

The results of the current study support Wiel and Darby's (2007) suggestion that woody riparian vegetation may play a more significant role in channel forming processes through vegetation-flow interactions rather than solely through mechanical bank stabilization. In the numerical model, increasing emergent vegetation density generally decreased streamwise velocities and boundary shear stresses in the main channel, especially in the crossover region. If similar processes occurred in nature, the drops in average main channel streamwise velocities and boundary shear stresses may promote the deposition of sediments and other materials such as large wood in the main channel. For the smooth floodplain scenario, the main channel boundary shear stresses increased at relative depths above the minimum threshold values up to approximately the same values seen in the bankfull case. Therefore, compound meandering channels with smooth floodplains may see higher sediment erosion and transport at high relative depths in natural settings.

Chan (2003) saw that the reductions in main channel streamwise velocities and boundary shear stresses resulted in drops in sediment transport for their mobile bed experiments with the same meandering compound channel geometry used in the current study. They observed drops in sediment transport for their smooth, artificially grassed, and artificially grassed plus large block roughened floodplain scenarios. They observed that as floodplain roughness was increased for the same channel configuration, the minima in sediment transport were lower, occurred at greater relative depths, and occurred over a greater range of relative depths. For the roughened floodplain scenarios, the bedforms were described as having ‘irregular and variable patterns’ (Chan, 2003). These trends are consistent with the trends in the main channel streamwise velocities and boundary shear stresses observed in the current study as floodplain vegetation density increased. In the current study, the patchiness in the boundary shear stress field, observed especially in the crossover region that occurred in the vegetated floodplain scenarios, may be expected to produce similarly patchy or irregular bedforms if the bed were mobile. Because increasing floodplain vegetation density was seen to redistribute regions of high and low boundary shear stress throughout the main channel, one might expect deposition and erosion to occur in locations where these do not typically occur during flows below bankfull. This redistribution of depositional and erosional regions may increase the heterogeneity of bedforms during overbank flows in meandering compound channels with vegetated floodplains. High and low regions of boundary shear stress nearly perpendicular to the streamwise meandering direction may amplify ripple or dune formation in sand bed systems. The formation of such bedforms would likely increase the hydraulic resistance in the main thus compounding the reductions in total sediment transport and total discharge capacity.

Gurnell and Petts (2006) observed increased island formation in river corridors where large wood could be mobilized during floods and deposited in the channel to assist in island formation by accumulating sediments and providing habitats for new plant growth. The current study indicates that standing woody vegetation could aid in this island formation process. An alternative or supplemental explanation for the promotion of island formation where large wood is available and floods occur, is that where large wood is available, live woody floodplain vegetation is also likely present. During floods like the overbank flows in the current study, this large standing woody vegetation may reduce the main channel streamwise velocities and boundary shear stresses thus promoting deposition of sediment and large wood as well as protecting pioneer vegetation on nascent islands from being removed by scouring in the flood flows.

Brooks and Brierley (2002) noted that riparian vegetation may have a role in the preservation of river forms, specifically in the Thurra River in Australia, which has seen little change in the past 16 ka. They explain that factors including riparian vegetation have helped the channel reach a “mediated equilibrium” by increasing floodplain roughness thus reducing the conveyance in main channel during overbank flow events common to this river. Their results suggested that these equilibrium conditions are likely independent of a “dominant discharge” (Brooks & Brierley, 2002). The current study’s results appear to bolster the idea that floodplain vegetation increases main channel resilience to geomorphic change during overbank flows. In the current study, the maintained low average main channel streamwise velocities and boundary shear stresses at high relative depths in the vegetated floodplain cases indicate that meandering compound channels with floodplain vegetation may be more resilient to scouring and geomorphic change than those with smooth floodplains for overbank flows especially at high flows. Reductions in average main channel boundary shear stresses due to increased floodplain vegetation density may result in bed aggradation and thus changes in main channel slope and main channel width to depth ratio. Loveless et al. (2000) posited that the large drops in total bedload transport at low overbank flows in their wide, roughened floodplain scenarios in a meandering compound channel supported the idea of bankfull discharge as the dominant channel forming discharge. The results of the vegetated floodplain scenarios support the position that bankfull flow is the primary channel forming flow (Wolman & Miller, 1960). For these vegetated floodplain scenarios, the average main channel streamwise velocities and boundary shear stresses values did not rise above those in the bankfull case. However, in the smooth floodplain scenarios at very high relative depths and flowrates, the average main channel streamwise velocities and boundary shear stresses exceeded those in the bankfull case. These results indicate that the channel form in meandering channels with smooth floodplains may experience similar or greater change during extremely high flow events compared with changes under bankfull flow conditions.

Unvegetated meandering fluvial channels, such as those in arid regions, early Earth before plants evolved, and even on ancient Mars have been shown to have migrated at much greater rates than similar vegetated channels (Ielpi & Lapôtre, 2020). These increased rates of migration in unvegetated meandering channels are reported to be due to the lack of bank strengthening provided by vegetation (Ielpi & Lapôtre, 2020); however, there may be additional hydrodynamic effects at play as well as indicated by Wiel and Darby (2007). The current study indicates that the main channels of meandering compound channels with unvegetated floodplains would likely experience greater flow velocities and boundary shear stresses for given flowrates compared with vegetated cases which could aid in increasing the rates of meander migration in unvegetated environments. The results of the current study may give clues to channel formation and the past presence or lack of floodplain vegetation when studying fluvial geomorphic records.

4.7 Implications for River Restoration and Management

Geomorphologic and Habitat Sustainability Implications for River Restoration

Floodplain vegetation density is a parameter that humans often change through planting and removal practices with limited understanding of how these actions might affect the main channel flow and boundary shear stress fields. Practitioners may need more information to better predict how floodplain vegetation conditions might affect main channel hydrodynamics, which have important influences on geomorphic change and aquatic habitat sustainability. Therefore, the results of the current study may be of importance in guiding future planting and removal practices on the floodplains of meandering compound channels. Increasing floodplain vegetation density was seen to increase the discontinuity and heterogeneity of the main channel flow and boundary shear stress fields. These heterogeneous flow and boundary shear stress fields would likely result in similarly heterogeneous patterns of sediment transport and deposition; thus, increasing habitat heterogeneity. At high overbank flows, highly vegetated floodplains would likely decrease the main channel velocities and boundary shear stresses in the crossover regions which would aid in local deposition of sediments and materials such as large wood in the main channel compared with scenarios with unvegetated floodplains. However, practitioners should note as Jaeger and Wohl (2011) noted, channel responses due to anthropogenic activities that alter riparian vegetation conditions, such as the removal of invasive riparian plants, may be highly dependent on site-specific conditions, particularly observed flow regimes. Practitioners should take care in recognizing that in natural river systems, floodplain vegetation conditions may have effects on hydrogeomorphology that extend beyond defined local spatial and temporal borders (Gurnell et al., 2016).

The floodplain vegetation conditions may aid in promoting various other ecological benefits. Increasing vegetation density was seen to weaken the horizontal flow separation at the bankfull level which would increase the plunging of overbank flows into the inbank main channel region and the upwelling of inbank main channel flows back onto the floodplain. This increased plunging and upwelling may aid in transferring materials between the inbank main channel flows and the overbank flows on the floodplain, which would affect the fate of sediment, pollutants, nutrients, larvae, and seeds (Sullivan et al., 2020). Finally, the flow depth on the floodplain is expected to be greater for a given overbank discharge in vegetated floodplain scenarios compared with unvegetated, "smooth" floodplain scenarios. This increased flow depth would increase the coverage of flood flows across the floodplain and therefore, increase aquatic habitat availability.

Stage Discharge Implications for River Management Practitioners

From an infrastructure and human safety standpoint, increasing the discharge capacity is often viewed as paramount for preventing damaging overbank flows from occurring. Increasing floodplain vegetation density in the current study was seen to decrease discharge capacity; yet may also offer increased geomorphic and ecological benefits. One possible geomorphic benefit of increasing floodplain vegetation density, which may be of interest to river management practitioners, is the potential protection of the main channel form due to reductions in average main channel streamwise velocities and boundary shear stresses during high overbank flow events. In channels where discharge is controlled, high floodplain vegetation densities could be used strategically to reduce scour and meander migration potential in the main channel for desired flows. River management practitioners should also take note of the partitioning methods chosen for discharge estimation in meandering compound channels. The results of the current study support the conclusions of Shiono and Muto (1998) which stated that the horizontal partition at the bankfull level may be appropriate for high relative depths for discharge estimation techniques and 2D modeling but may not be appropriate at low relative depths due to increased flow interactions across the bankfull level. Importantly, the current study's results indicate that the bankfull level horizontal partition technique may not be appropriate in channels with floodplain vegetation because the overbank and inbank flow layers are assumed to interact across the bankfull level.

4.8 Limitations

This study was limited in areas including the data from physical experiments available to validate the numerical models, model setup, data processing, and numerical model result agreeance with those of physical experiments. The descriptions of the Shiono et al. experimental setup and results did not contain all desired details for the current study. Information about the geometry and conditions at the head and tail of their flume experimental setups could not be located. In the current study assumptions on the geometry and conditions at the head and tail of the flume were based on schematic drawings and photographs in the publications. The error in total discharges measured by flow meters were also not found. It was assumed that the error for the flow measurements was around +/- 5%. Finally, the vegetated floodplain experiments were purely numerical and not validated against physical models with floodplain vegetation. However, the vegetation cylinders were added to the floodplains of the already calibrated and validated smooth floodplain models, and modeling techniques from the validated cases were used for the vegetated floodplain cases.

For the model setup, limitations included the choice of grid resolution and choice of turbulence model, both of which were influenced by the need to reduce computational costs. The grid resolution was selected as to effectively model the validation cases while minimizing computational costs. Further refinement of the grid would have better resolved the geometry of the channel and vegetation but would have significantly increased computational costs. The RNG k-epsilon turbulence closure method is a Reynold-Averaged Navier-Stokes (RANS) method. RANS methods smooth out the flow field which causes them to lose detail. Large eddy simulations (LES) may provide a better representation of the flow; however, for this study computational cost limited the use of LES. Stoesser et al., (2010) report that LES models are better than RANS models at predicting secondary flow structures, as RANS tends to overestimate the size and magnitude of secondary flows in meandering compound channel. This overestimation of secondary flows may have resulted in some of the discrepancies in the appearance and magnitude of the average main channel minimum values for the current study compared with the physical validation study from the Shiono et al. research group. LES is also recommended for modeling flows around cylinder arrays for capturing vortex shedding phenomena and wake interactions. However, the high computational expenses of LES modeling were a limiting factor for the choice of turbulence model, and the validation results showed that the RNG k-epsilon model performed well for the validation cases.

In processing all results other than the free surface elevation, the instantaneous values were selected rather than time averaging the results over a study period. Because the selected model was RANS-based, fluctuations in velocity were treated as isotropic. Thus, it was assumed that the temporally dependent fluctuations in velocity would already be dampened, and time averaging would therefore be redundant. In the boundary shear stress analysis, there were small regions of the field that were not in the expected range of y+ for the logarithmic law of the wall to be valid. This indicates that for limited regions, the grid refinement near the bed was either too high or too low. These regions were not significant in size and therefore were assumed to be negligible.

Three-dimensional fluid dynamics models may be too computationally expensive for many river science and engineering practices. Therefore, practitioners using simpler, less computationally expensive numerical models at lower dimensions may want to consider the results of the current and similar studies to inform modeling choices and the interpretation of results. However, these practitioners should note that the current study represents a simplification of much more complex channel systems which occur in reality. Due to these simplifications, the results of the current study should not be used for making definitive assumptions but rather be used for providing a better fundamental understanding of general trends that may occur in the real world.

Lastly, flows around vegetation and in meandering compound channels are extremely complex even in simplified representations such as those used in the current study. This complexity makes it difficult to untangle mutual influences of different flow mechanisms. Further rigorous investigations of these flows mechanisms are required to better understand flows in meandering compound channels with varied emergent floodplain vegetation densities.

4.9 Future Research

Opportunities for expanding upon this study are vast. The following variations in the meandering compound channel and vegetation setups are recommended for future studies.

Meandering Compound Channel Variations:

- Channel morphology including natural main channel cross section geometries and floodplain topographies
- Main channel and floodplain valley wall sinuosities
- Width-to-depth ratio
- Bed slopes
- Mobile bed experiments

Vegetation Variations:

- Arrangements, e.g., random arrays, regions of varied vegetation density, etc.
- Vegetation densities
- Vegetation morphology
- Stem diameters
- Submergence
- Stem flexibility

Future researchers may want to expand on the choices made in the numerical models of the current study. Where computational costs are not a limiting factor, researchers may choose to explore LES and higher grid resolutions when modeling flows in meandering compound channels with varied emergent floodplain vegetation densities. Physical flume experiments and field studies in meandering compound channels with varied emergent floodplain vegetation densities should be performed and compared with the results of the current numerical modeling study.

5 CONCLUSIONS

Three-dimensional numerical flow modeling and analysis was performed for a meandering compound channel with varied emergent cylindrical floodplain vegetation densities. The models were first calibrated and validated with a smooth floodplain case based on flume experiments performed by the Shiono et al. research group (Chan, 2003; Shiono et al., 2008; Spooner, 2001). The three-dimensional numerical flow models showed that floodplain vegetation density and relative depth had notable influences on the stage-discharge relationships, average main channel streamwise velocities and boundary shear stresses, primary and secondary flow structures, and layer-averaged flow velocity fields.

As discharge and relative depth were increased above bankfull, the average main channel streamwise velocities and boundary shear stresses decreased to initial threshold minima at low overbank flow depths. As vegetation density increased, these minima in average main channel streamwise velocity and boundary shear stress occurred at higher relative depths and discharges. For the smooth floodplain scenario, the average main channel streamwise velocities and boundary shear stresses rose with increasing relative depth and discharge at a greater rate than those in the low floodplain vegetation density scenario. For the high floodplain vegetation density scenario, the average main channel streamwise velocity and boundary shear stress generally did not rise above the initial minima value. Secondary drops in the average main channel streamwise velocities and boundary shear stresses occurred for the low and high floodplain vegetation density scenarios at high relative depths. For the vegetated floodplain scenarios, the boundary shear stress fields had strong gradients and were patchy compared with the smooth floodplain scenarios. Primary and secondary flow structures in the main channel as well as patterns in the inbank and overbank depth-averaged flow layers were considerably affected by the emergent floodplain vegetation density as well. Connections were drawn between these flow patterns to explain trends in the average main channel streamwise velocities and boundary shear stresses affected by floodplain vegetation density and relative depth conditions. As vegetation density increased, the flow path of overbank flows deviated more from the valley-wise direction and cross stream flows plunged more steeply below the bankfull level as they returned to the main channel. This increased plunging of the overbank flow layer into the inbank flow layer indicates that greater interactions between flow layers occurred leading to greater energy losses. The link between energy losses and the strength of separation between inbank and overbank flow layers at the bankfull level horizontal plane helped to explain trends in the flow velocity and boundary shear stress fields between floodplain scenarios. Finally, improving the state of understanding on how floodplain vegetation density and relative depth affect hydrodynamics particularly in the main channel of meandering compound channels may be of use to river scientists and engineers for better predicting and understanding geomorphic change as well as protecting natural and built environments within systems in nature similar to those in the current study.

REFERENCES

Aberle, J., & Järvelä, J. (2013). Flow resistance of emergent rigid and flexible floodplain vegetation. *Journal of Hydraulic Research*, *51*(1), 33–45. https://doi.org/10.1080/00221686.2012.754795

Abril, J. B., & Knight, D. W. (2004). Stage-discharge prediction for rivers in flood applying a depth-averaged model. *Journal of Hydraulic Research*, *42*(6), 616–629. https://doi.org/10.1080/00221686.2004.9628315

Bottorff, R. L. (1974). Cottonwood Habitat for Birds in Colorado. *American Birds*, *28*(6 (December)), 975–979.

Brooks, A. P., & Brierley, G. J. (2002). Mediated equilibrium: The influence of riparian vegetation and wood on the long-term evolution and behaviour of a near-pristine river. *Earth Surface Processes and Landforms*, *27*(4), 343–367. https://doi.org/10.1002/esp.332

Bywater-Reyes, S., Wilcox, A. C., & Diehl, R. M. (2017). Multiscale influence of woody riparian vegetation on fluvial topography quantified with ground-based and airborne lidar. *Journal of Geophysical Research: Earth Surface*, *122*(6), 1218–1235. https://doi.org/10.1002/2016JF004058

Chan, T. L. (2003). *A study of sediment transport in two-stage meandering channel* [Thesis, Loughborough University]. /articles/thesis/A_study_of_sediment_transport_in_two-stage_meandering_channel/9454535/1

Choudhury, D. (1993). Calculation of turbulent separated flows using a renormalization group based κ-ε turbulence model. *ASME-FED*, *149*, 177.

Crosato, A., & Saleh, M. S. (2011). Numerical study on the effects of floodplain vegetation on river planform style. *Earth Surface Processes and Landforms*, *36*(6), 711–720. https://doi.org/10.1002/esp.2088

Decamps, H., Joachim, J., & Lauga, J. (1987). The importance for birds of the riparian woodlands within the alluvial corridor of the river garonne, S.W. France. *Regulated Rivers: Research & Management*, *1*(4), 301–316. https://doi.org/10.1002/rrr.3450010403

Dupuis, V., Proust, S., Berni, C., & Paquier, A. (2017). Compound channel flow with a longitudinal transition in hydraulic roughness over the floodplains. *Environmental Fluid Mechanics*, *17*(5), 903–928. https://doi.org/10.1007/s10652-017-9525-0

Ervine, D. A., Babaeyan-Koopaei, K., & Sellin, R. H. J. (2000). Two-Dimensional Solution for Straight and Meandering Overbank Flows. *Journal of Hydraulic Engineering*, *126*(9), 653–669. https://doi.org/10.1061/(ASCE)0733-9429(2000)126:9(653)

Ervine, D. A., & Jasem, H. K. (1995). Observations on flows in skewed compound channels. *Proceedings of the Institution of Civil Engineers - Water, Maritime and Energy*, *112*(3), 249–259. https://doi.org/10.1680/iwtme.1995.27887

Farzadkhoo, M., Keshavarzi, A., Hamidifar, H., & Javan, M. (2018). A comparative study of longitudinal dispersion models in rigid vegetated compound meandering channels. *Journal of Environmental Management*, *217*, 78–89. https://doi.org/10.1016/j.jenvman.2018.03.084

Farzadkhoo, M., Keshavarzi, A., Hamidifar, H., & Javan, M. (2019). Sudden pollutant discharge in vegetated compound meandering rivers. *CATENA*, *182*, 104155. https://doi.org/10.1016/j.catena.2019.104155

Fischer-Antze, T., Stoesser, T., Bates, P., & Olsen, N. R. B. (2001). 3D numerical modelling of open-channel flow with submerged vegetation. *Journal of Hydraulic Research*, *39*(3), 303–310. https://doi.org/10.1080/00221680109499833

Fukuoka, S. (n.d.). *Two Types of Flood Flow Depending on Relative Depth and Sinuosity in Doubly Meandering Compound Rivers Simple Meandering Flow and Compound Meandering Flow*. 6.

Ghani, U., Wormleaton, P., Hashhim, A., & Hashmi, N. (2010). Three Dimensional CFD Modeling of Flow Structure in Compound Channels. *Mehran University Research Journal of Engineering and Technology*, *29*.

Gurnell, A. M., Corenblit, D., Jalón, D. G. de, Tánago, M. G. del, Grabowski, R. C., O'Hare, M. T., & Szewczyk, M. (2016). A Conceptual Model of Vegetation–hydrogeomorphology Interactions Within River Corridors. *River Research and Applications*, *32*(2), 142–163. https://doi.org/10.1002/rra.2928

Helmiö, T. (2002). Unsteady 1D flow model of compound channel with vegetated floodplains. *Journal of Hydrology*, *269*(1), 89–99. https://doi.org/10.1016/S0022-1694(02)00197-X

Helton, A. M., Wright, M. S., Bernhardt, E. S., Poole, G. C., Cory, R. M., & Stanford, J. A. (2015). Dissolved organic carbon lability increases with water residence time in the alluvial aquifer of a river floodplain ecosystem: Aquifer dissolved organic carbon. *Journal of Geophysical Research: Biogeosciences*, *120*(4), 693–706. https://doi.org/10.1002/2014JG002832

Huai, W., Gao, M., Zeng, Y., & Li, D. (2009). Two-dimensional analytical solution for compound channel flows with vegetated floodplains. *Applied Mathematics and Mechanics*, *30*(9), 1121–1130. https://doi.org/10.1007/s10483-009-0906-z

Huai, W. X., Zeng, Y. H., Xu, Z. G., & Yang, Z. H. (2009). Three-layer model for vertical velocity distribution in open channel flow with submerged rigid vegetation. *Advances in Water Resources*, *32*(4), 487–492. https://doi.org/10.1016/j.advwatres.2008.11.014

Huai, W., Xu, Z., Yang, Z., & Zeng, Y. (2008). Two dimensional analytical solution for a partially vegetated compound channel flow. *Applied Mathematics and Mechanics*, *29*(8), 1077. https://doi.org/10.1007/s10483-008-0811-y

Ielpi, A., & Lapôtre, M. G. A. (2020). A tenfold slowdown in river meander migration driven by plant life. *Nature Geoscience*, *13*(1), 82–86. https://doi.org/10.1038/s41561-019-0491-7

James, C. S., & Wark, J. B. (1992). Conveyance estimation for meandering channels. *Undefined*. https://www.semanticscholar.org/paper/Conveyance-estimation-for-meandering-channels-James-Wark/463cdf4c760f5298b11cc47dc941e245515c6d72

Jing, H., Guo, Y., Li, C., & Zhang, J. (2009). Three-dimensional numerical simulation of compound meandering open channel flow by the Reynolds stress model. *International Journal for Numerical Methods in Fluids*, *59*(8), 927–943. https://doi.org/10.1002/fld.1855

Karamisheva, R. D., Lyness, J. F., Myers, W. R. C., & O’Sullivan, J. (2006). Sediment discharge prediction in meandering compound channels. *Journal of Hydraulic Research*, *44*(5), 603–613. https://doi.org/10.1080/00221686.2006.9521710

Klopstra, D., Barneveld, H., Noortwijk, J., & Velzen, E. (1997). Analytical model for hydraulic roughness of submerged vegetation. *Proceedings, Congress of the International Association of Hydraulic Research, IAHR*.

Kondolf, G. M., & Curry, R. R. (1986). Channel erosion along the Carmel river, Monterey county, California. *Earth Surface Processes and Landforms*, *11*(3), 307–319. https://doi.org/10.1002/esp.3290110308

Li, S. S., & Millar, R. G. (2011). A two-dimensional morphodynamic model of gravel-bed river with floodplain vegetation. *Earth Surface Processes and Landforms*, *36*(2), 190–202. https://doi.org/10.1002/esp.2033

Liébault, F., & Piégay, H. (2002). Causes of 20th century channel narrowing in mountain and piedmont rivers of southeastern France. *Earth Surface Processes and Landforms*, *27*(4), 425–444. https://doi.org/10.1002/esp.328

Liu, C., Shan, Y., Liu, X., Yang, K., & Liao, H. (2016). The effect of floodplain grass on the flow characteristics of meandering compound channels. *Journal of Hydrology*, *542*, 1–17. https://doi.org/10.1016/j.jhydrol.2016.07.037

López, F., & García, M. (1998). Open-channel flow through simulated vegetation: Suspended sediment transport modeling. *Water Resources Research*, *34*(9), 2341–2352. https://doi.org/10.1029/98WR01922

Loveless, J. H., Sellin, R. H. J., Bryant, T. B., Wormleaton, P. R., Catmur, S., & Hey, R. (2000). The Effect of Overbank Flow in a Meandering River on its Conveyance and the Transport of Graded Sediments. *Water and Environment Journal*, *14*(6), 447–455. https://doi.org/10.1111/j.1747-6593.2000.tb00293.x

Lyness, J. F., Myers, W. R. C., & O Sullivan, J. J. (1998). HYDRAULIC CHARACTERISTICS OF MEANDERING MOBILE BED COMPOUND CHANNELS. *Proceedings of the Institution of Civil Engineers - Water Maritime and Energy*, *130*(4), 179–188. https://doi.org/10.1680/iwtme.1998.31046

Martín-Vide, J. P. (2001). Restoration of an urban river in Barcelona, Spain. *Environmental Engineering Policy*, *2*, 113–119. https://doi.org/10.1007/s100220000030

Moncho-Esteve, I. J., García-Villalba, M., Muto, Y., Shiono, K., & Palau-Salvador, G. (2018). A numerical study of the complex flow structure in a compound meandering channel. *Advances in Water Resources*, *116*, 95–116. https://doi.org/10.1016/j.advwatres.2018.03.013

Naot, D., Nezu, I., & Nakagawa, H. (1996). Hydrodynamic Behavior of Partly Vegetated Open Channels. *Journal of Hydraulic Engineering*, *122*(11), 625–633. https://doi.org/10.1061/(ASCE)0733-9429(1996)122:11(625)

Nepf, H. M. (1999). Drag, turbulence, and diffusion in flow through emergent vegetation. *Water Resources Research*, *35*(2), 479–489. https://doi.org/10.1029/1998WR900069

Nepf, H. M., & Vivoni, E. R. (2000). Flow structure in depth-limited, vegetated flow. *Journal of Geophysical Research: Oceans*, *105*(C12), 28547–28557. https://doi.org/10.1029/2000JC900145

O'Sullivan, J., Myers, W. C., Lyness, J., & Lambert, M. (2003). *Discharge assessment in mobile-bed compound meandering channels*. https://doi.org/10.1680/WAME.2003.156.4.313

Pezzinga, G. (1994). Velocity Distribution in Compound Channel Flows by Numerical Modeling. *Journal of Hydraulic Engineering*, *120*(10), 1176–1198. https://doi.org/10.1061/(ASCE)0733-9429(1994)120:10(1176)

Pope, S. B. (2000). *Turbulent Flows*. Cambridge University Press. https://doi.org/10.1017/CBO9780511840531

Rameshwaran, P., & Shiono, K. (2007). Quasi two-dimensional model for straight overbank flows through emergent. *Journal of Hydraulic Research*, *45*(3), 302–315. https://doi.org/10.1080/00221686.2007.9521765

Raupach, M. R., & Shaw, R. H. (1982). Averaging procedures for flow within vegetation canopies. *Boundary-Layer Meteorology*, *22*(1), 79–90. https://doi.org/10.1007/BF00128057

Sellin, R. H. J., Ervine, D. A., & Willetts, B. B. (1993). Behaviour of meandering two-stage channels. *Proceedings of the Institution of Civil Engineers - Water, Maritime and Energy*, *101*(2), 99–111. https://doi.org/10.1680/iwtme.1993.23591

Shan, Y., Liu, X., Yang, K., & Liu, C. (2017). Analytical model for stage-discharge estimation in meandering compound channels with submerged flexible vegetation. *Advances in Water Resources*, *108*, 170–183. https://doi.org/10.1016/j.advwatres.2017.07.021

Shiono, K., Chan, T. L., Spooner, J., Rameshwaran, P., & Chandler, J. H. (2009). The effect of floodplain roughness on flow structures, bedforms and sediment transport rates in meandering channels with overbank flows: Part I. *Journal of Hydraulic Research*, *47*(1), 5–19. https://doi.org/10.3826/jhr.2009.2944-I

Shiono, K., & Muto, Y. (1998). Complex flow mechanisms in compound meandering channels with overbank flow. *Journal of Fluid Mechanics*, *376*, 221–261. https://doi.org/10.1017/S0022112098002869

Shiono, K., Spooner, J., Chan, T., Rameshwaran, P., & Chandler, J. (2008). Flow characteristics in meandering channels with non-mobile. *Journal of Hydraulic Research*, *46*(1), 113–132. https://doi.org/10.1080/00221686.2008.9521848

Shukla, D. R., & Shiono, K. (2008). CFD modelling of meandering channel during floods. *Proceedings of the Institution of Civil Engineers - Water Management*, *161*(1), 1–12. https://doi.org/10.1680/wama.2008.161.1.1

Smith, L. M., & Woodruff, S. L. (1997). *Renormalization-Group Analysis of Turbulence*. 36.

Spooner, J. (2001). *Flow structures in a compound meandering channel with flat and natural bedforms* [Thesis, Loughborough University]. /articles/thesis/Flow_structures_in_a_compound_meandering_channel_with_flat_and_natural_bedforms/9454931/1

Sullivan, J. C., Wan, Y., & Willis, R. A. (2020). Modeling Floodplain Inundation, Circulation, and Residence Time Under Changing Tide and Sea Levels. *Estuaries and Coasts*, *43*(4), 693–707. https://doi.org/10.1007/s12237-020-00709-0

Tanino, Y., & Nepf, H. M. (2008). Laboratory Investigation of Mean Drag in a Random Array of Rigid, Emergent Cylinders. *Journal of Hydraulic Engineering*, *134*(1), 34–41. https://doi.org/10.1061/(ASCE)0733-9429(2008)134:1(34)

Thornton, C. I., Abt, S. R., Morris, C. E., & Fischenich, J. C. (2000). Calculating Shear Stress at Channel-Overbank Interfaces in Straight Channels with Vegetated Floodplains. *Journal of Hydraulic Engineering*, *126*(12), 929–936. https://doi.org/10.1061/(ASCE)0733-9429(2000)126:12(929)

Toebes, G. H., & Sooky, A. A. (1967). Hydraulics of Meandering Rivers with Flood Plains. *Journal of the Waterways and Harbors Division*, *93*(2), 213–236.

Vargas-Luna, A., Crosato, A., Calvani, G., & Uijttewaal, W. S. J. (2016). Representing plants as rigid cylinders in experiments and models. *Advances in Water Resources*, *93*, 205–222. https://doi.org/10.1016/j.advwatres.2015.10.004

Wang, Y., Zhang, H., Yang, P., & Wang, Y. (2018). Experimental Study of Overland Flow through Rigid Emergent Vegetation with Different Densities and Location Arrangements. *Water*, *10*(11), 1638. https://doi.org/10.3390/w10111638

Waterways Experiment Station (U.S.) & United States. (1956). *Hydraulic capacity of meandering channels in straight floodways: Hydraulic model investigation, CWI item no. 807, hydraulic capacity of meandering channels.* U.S. Waterways Experiment Station. https://catalog.hathitrust.org/Record/100393751

Wiel, M. J. V. D., & Darby, S. E. (2007). A new model to analyse the impact of woody riparian vegetation on the geotechnical stability of riverbanks. *Earth Surface Processes and Landforms*, *32*(14), 2185–2198. https://doi.org/10.1002/esp.1522

Wolman, M. G., & Miller, J. P. (1960). Magnitude and Frequency of Forces in Geomorphic Processes. *The Journal of Geology*, *68*(1), 54–74.

Wormleaton, P. R., & Ewunetu, M. (2006a). Three-dimensional k–∊ numerical modelling of overbank flow in a mobile bed meandering channel with floodplains of different depth, roughness and planform. *Journal of Hydraulic Research*, *44*(1), 18–32. https://doi.org/10.1080/00221686.2006.9521658

Wormleaton, P. R., & Ewunetu, M. (2006b). Three-dimensional k–∊ numerical modelling of overbank flow in a mobile bed meandering channel with floodplains of different depth, roughness and planform. *Journal of Hydraulic Research*, *44*(1), 18–32. https://doi.org/10.1080/00221686.2006.9521658

Yakhot, V., & Orszag, S. A. (1986). Renormalization group analysis of turbulence. I. Basic theory. *Journal of Scientific Computing*, *1*(1), 3–51. https://doi.org/10.1007/BF01061452

Yang, S.-Q., Tan, S. K., & Wang, X.-K. (2012). Mechanism of secondary currents in open channel flows. *Journal of Geophysical Research: Earth Surface*, *117*(F4). https://doi.org/10.1029/2012JF002510

Zen, S., Zolezzi, G., Toffolon, M., & Gurnell, A. M. (2016). Biomorphodynamic modelling of inner bank advance in migrating meander bends. *Advances in Water Resources*, *93*, 166–181. https://doi.org/10.1016/j.advwatres.2015.11.017

Appendix A: Boundary shear stress contour plots

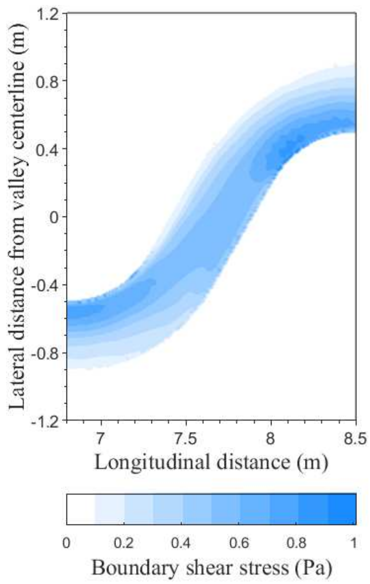

Figure A1. Relative depth case of 0 for smooth floodplain scenario

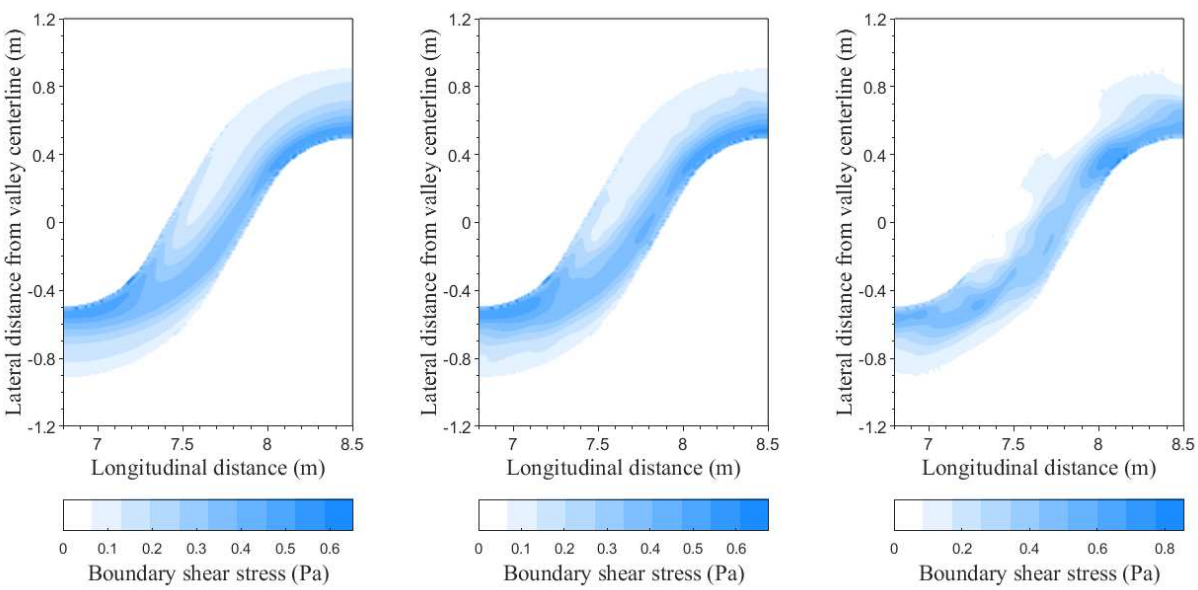

(a) (b) (c)

Figure A2. Relative depth cases of 0.13 for (a) smooth, (b) low density, and (c) high density floodplain scenarios

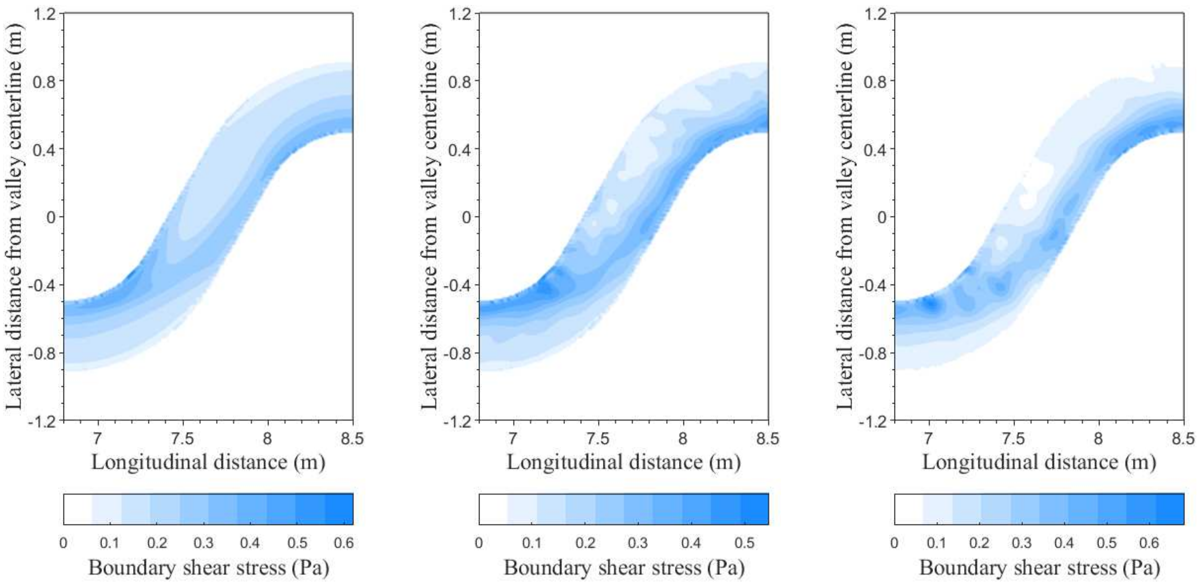

(a) (b) (c)

Figure A3. Relative depth cases of 0.20 for (a) smooth, (b) low density, and (c) high density floodplain scenarios

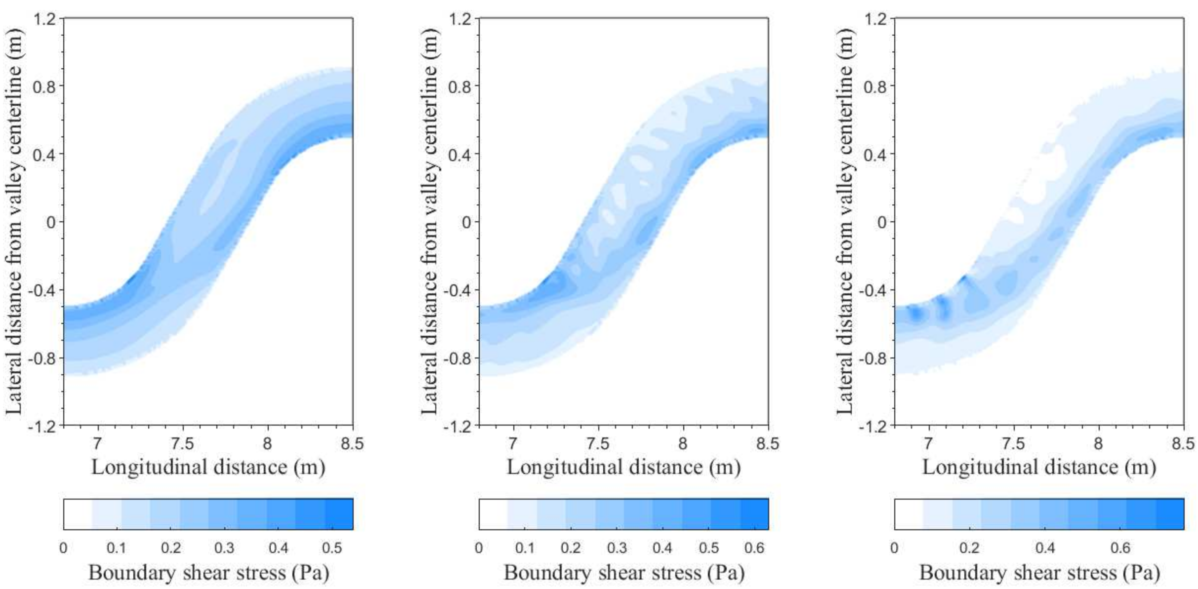

(a) (b) (c)

Figure A4. Relative depth cases of 0.25 for (a) smooth, (b) low density, and (c) high density floodplain scenarios

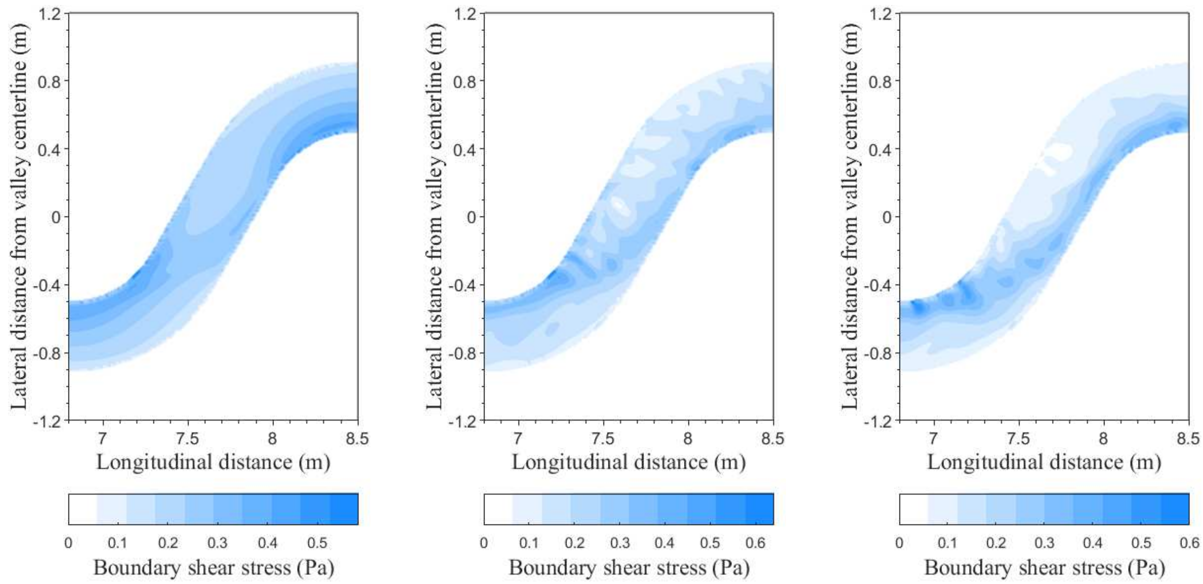

(a) (b) (c)

Figure A5. Relative depth cases of 0.29 for (a) smooth, (b) low density, and (c) high density floodplain scenarios

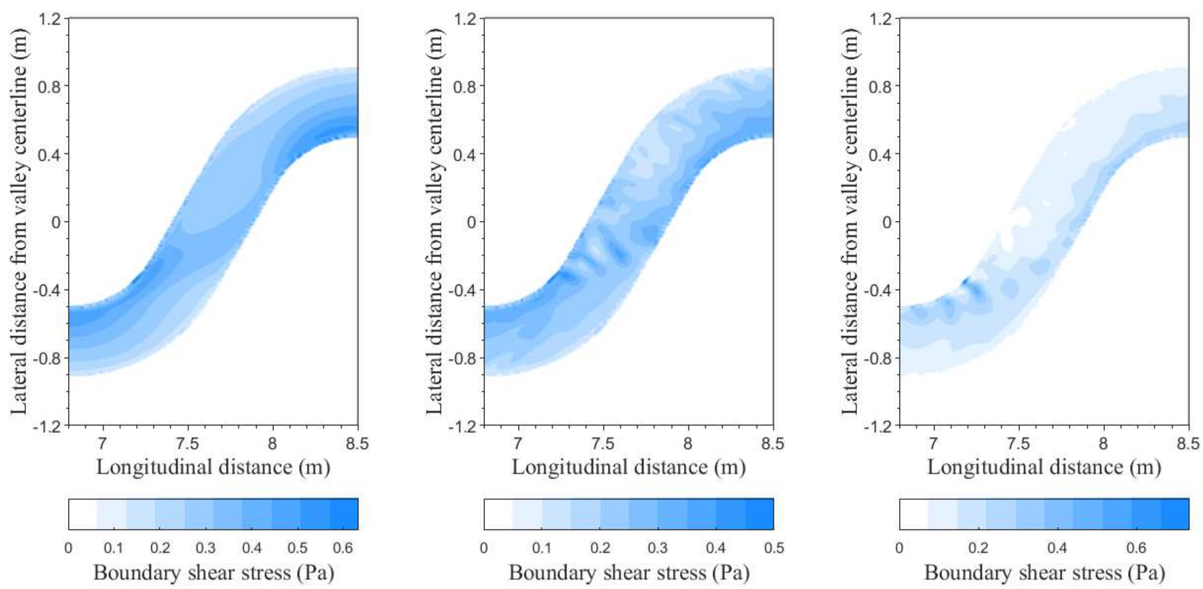

(a) (b) (c)

Figure A6. Relative depth cases of 0.35 for (a) smooth, (b) low density, and (c) high density floodplain scenarios

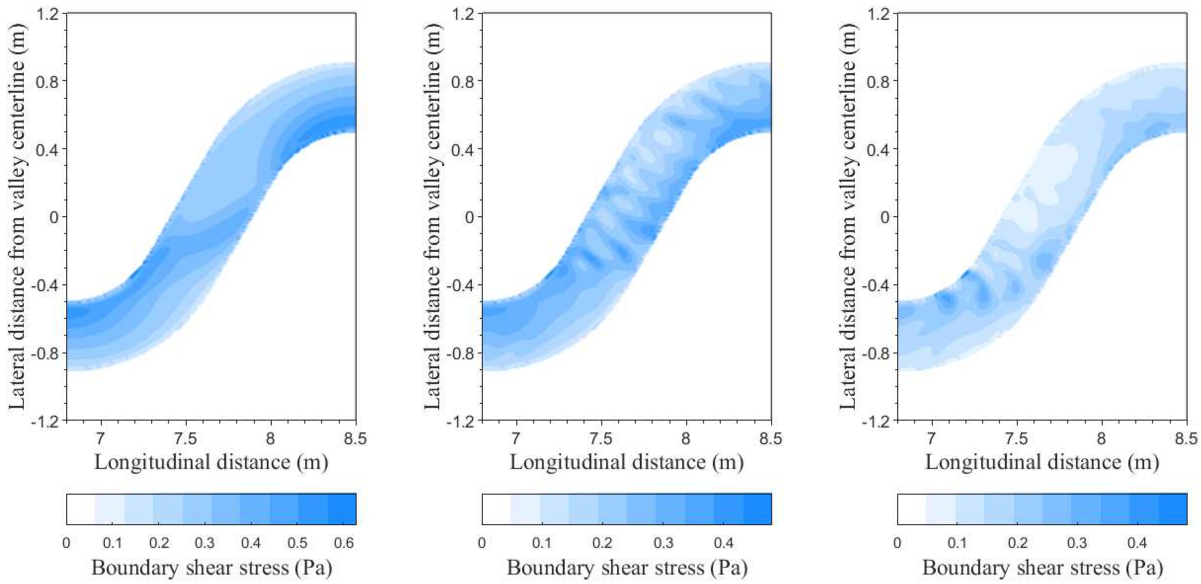

(a) (b) (c)

Figure A7. Relative depth cases of 0.40 for (a) smooth, (b) low density, and (c) high density floodplain scenarios

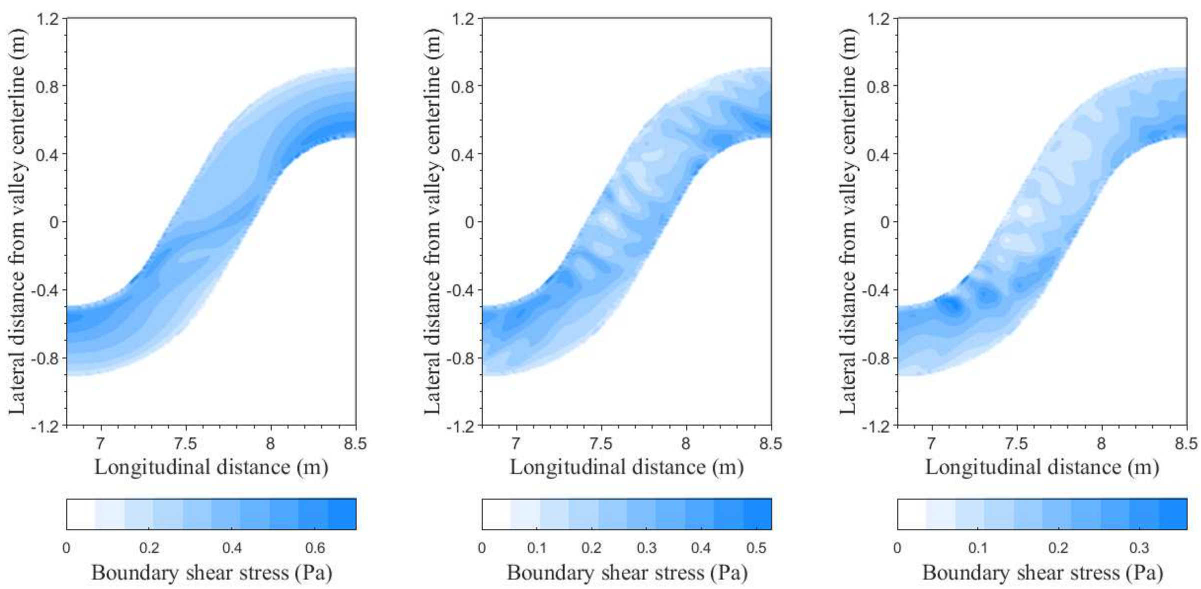

(a) (b) (c)

Figure A8. Relative depth cases of 0.46 for (a) smooth, (b) low density, and (c) high density floodplain scenarios

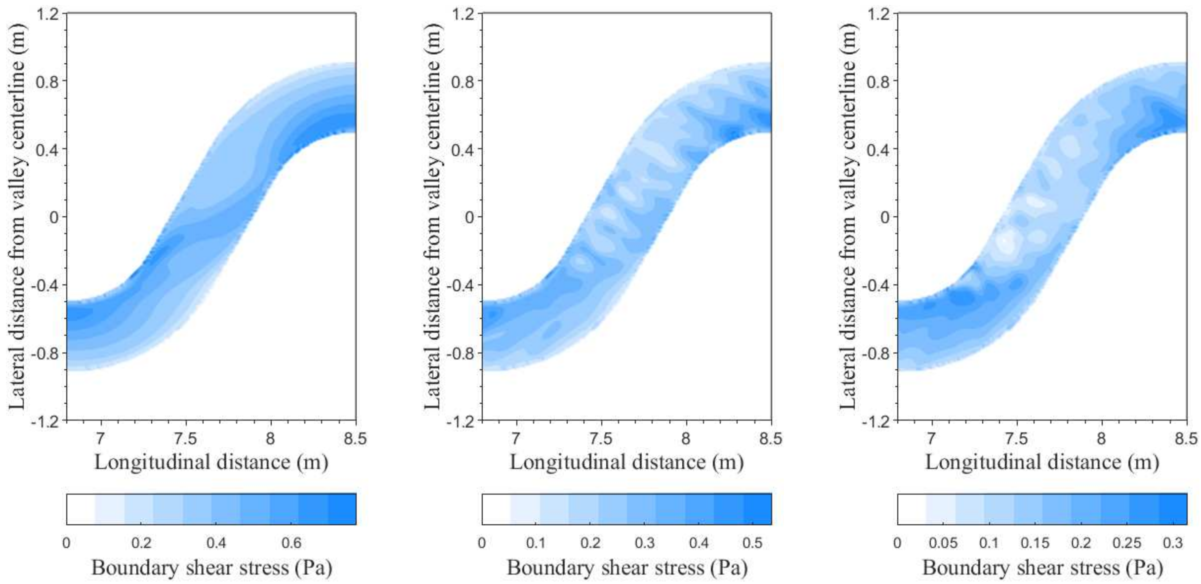

(a) (b) (c)

Figure A9. Relative depth cases of 0.50 for (a) smooth, (b) low density, and (c) high density floodplain scenarios

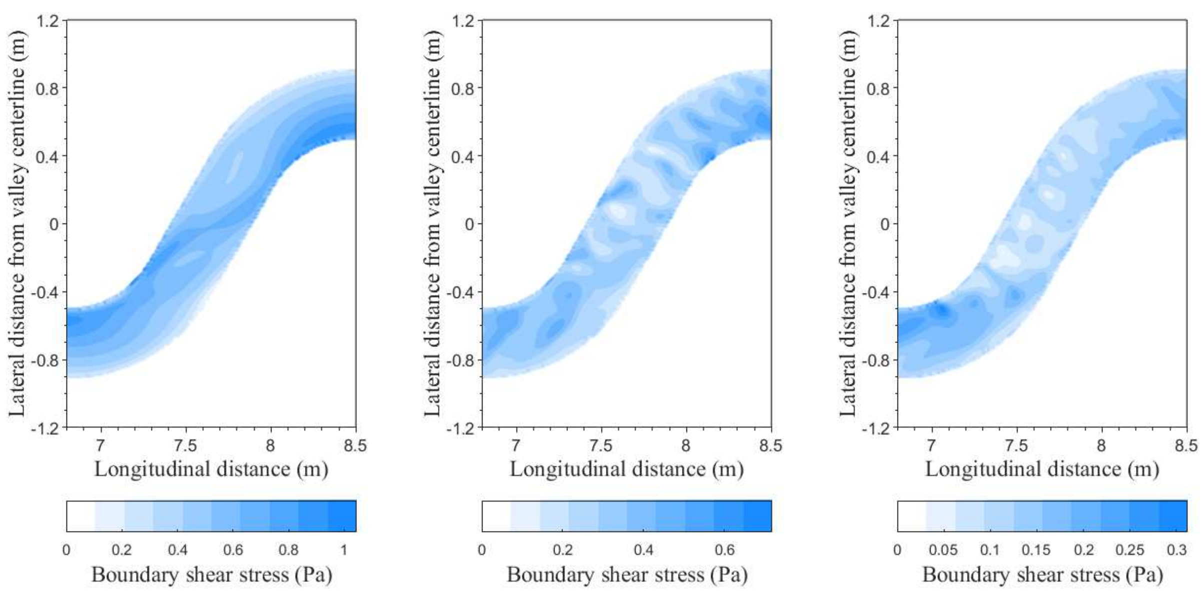

(a) (b) (c)

Figure A10. Relative depth cases of 0.60 for (a) smooth, (b) low density, and (c) high density floodplain scenarios

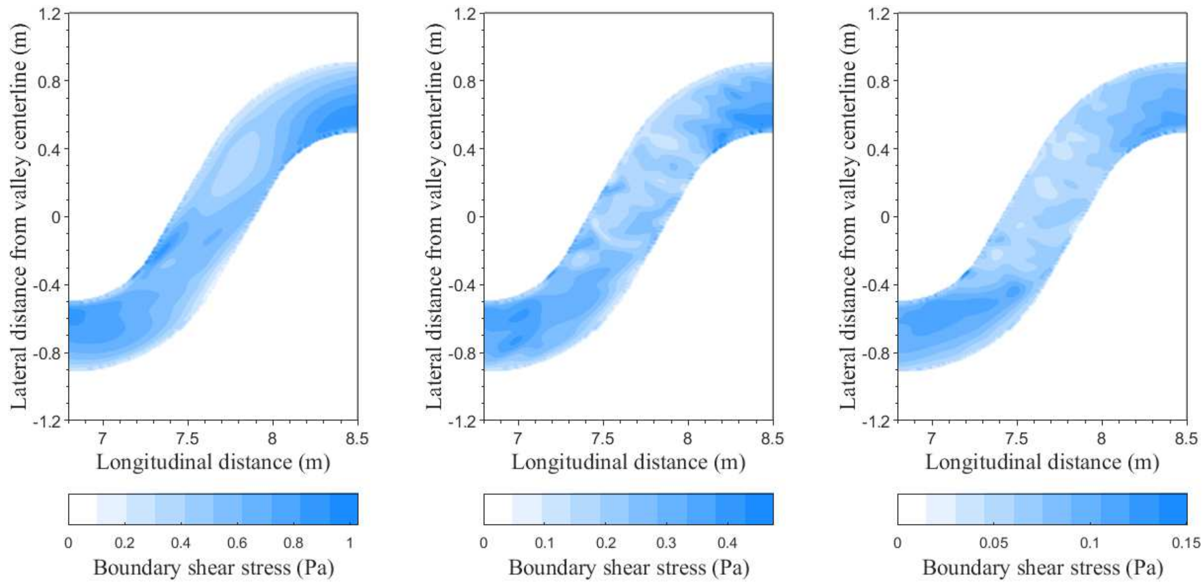

(a) (b) (c)

Figure A11. Relative depth cases of 0.80 for (a) smooth, (b) low density, and (c) high density floodplain scenarios

Appendix B: Boundary shear stress cross section plots

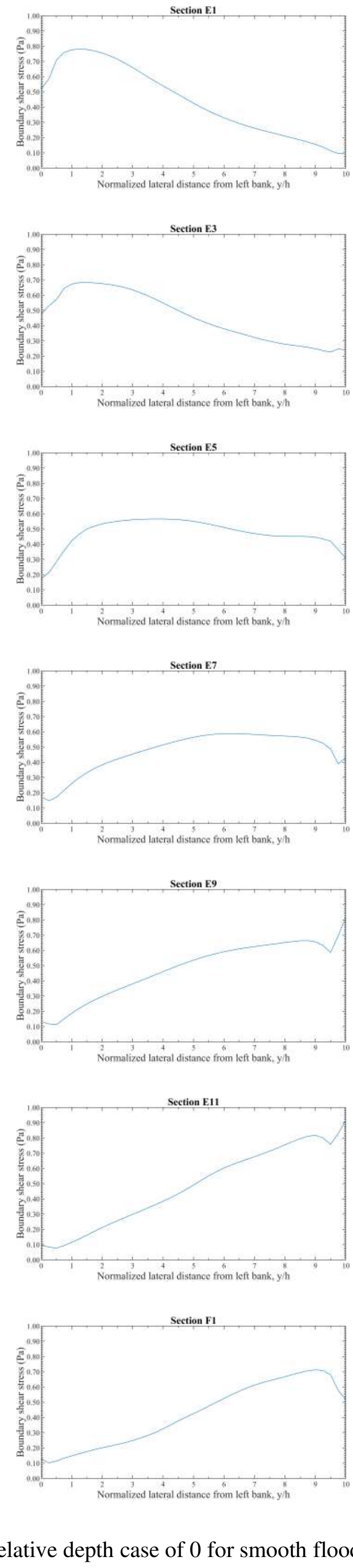

Figure B1. Relative depth case of 0 for smooth floodplain scenario

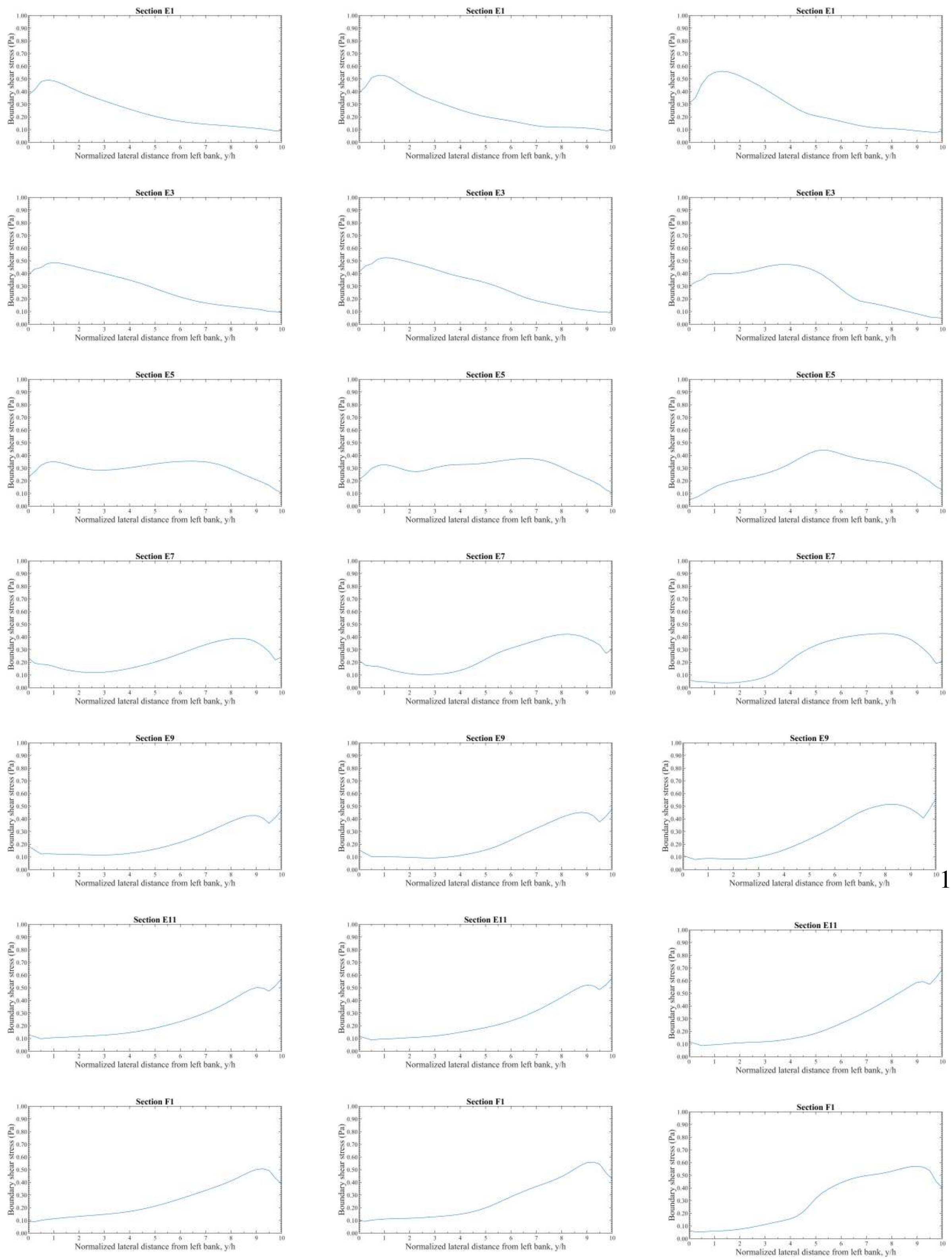

(a) (b) (c)

Figure B2. Relative depth cases of 0.13 for (a) smooth, (b) low density, and (c) high density floodplain scenarios

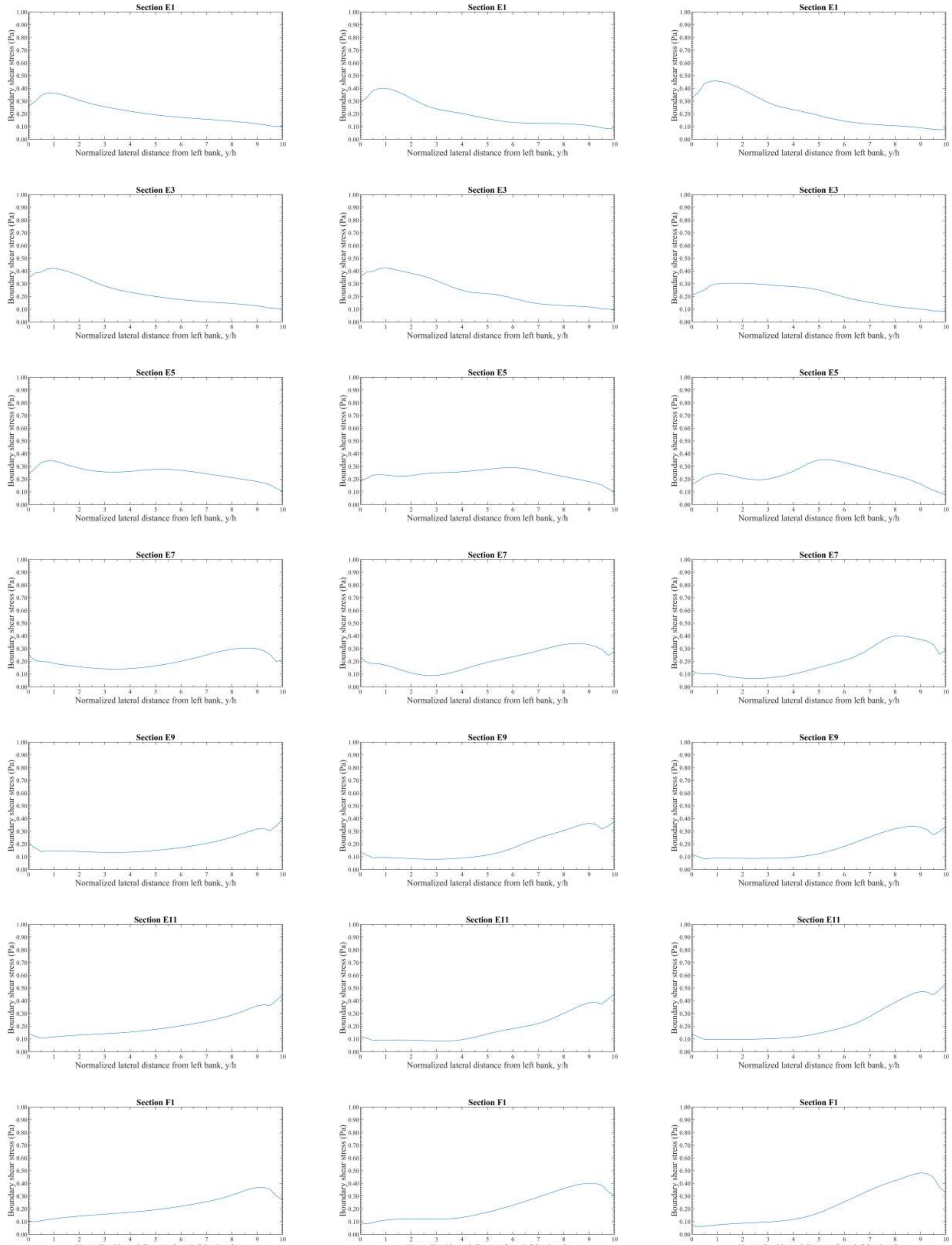

(a) (b) (c)

Figure B3. Relative depth cases of 0.20 for (a) smooth, (b) low density, and (c) high density floodplain scenarios

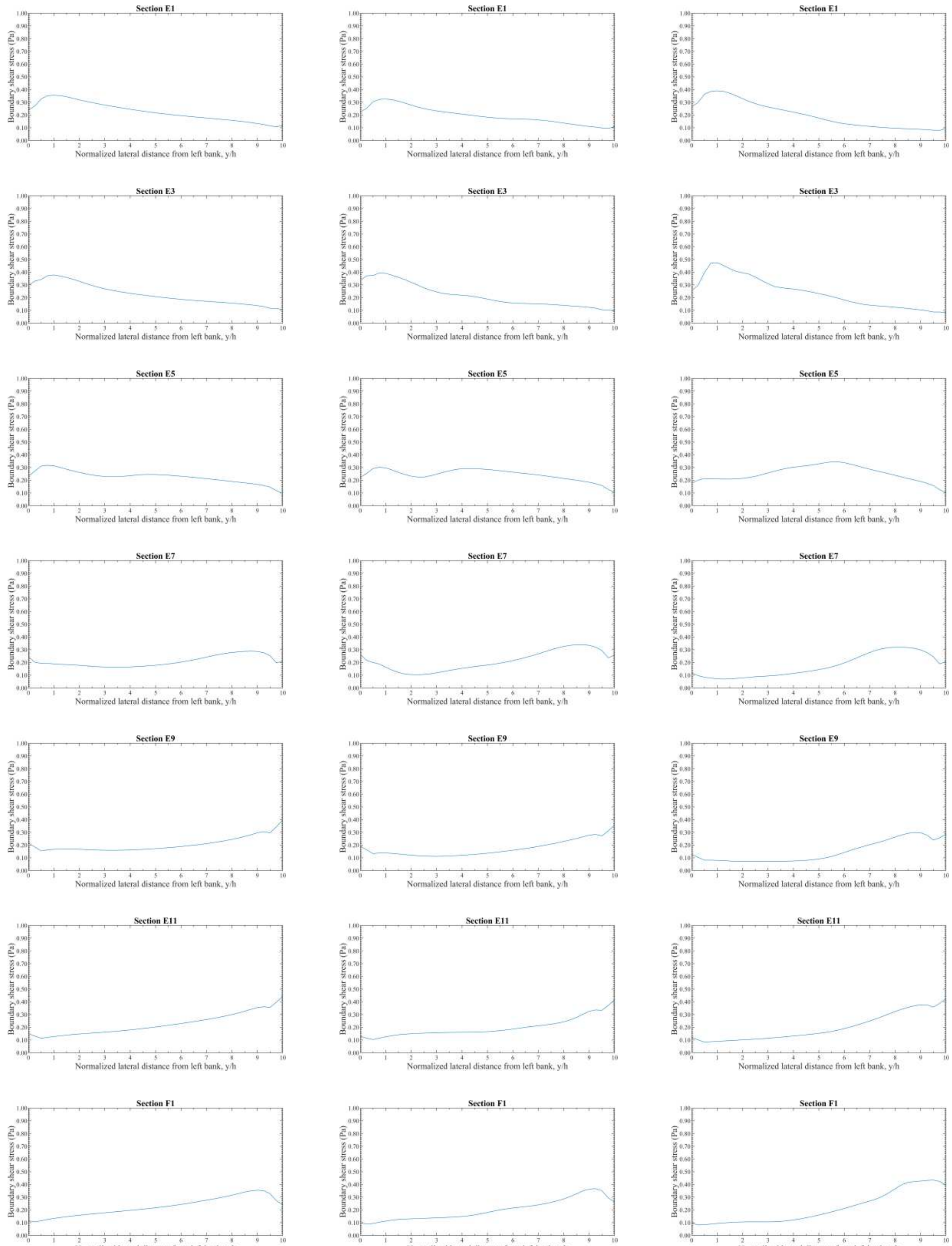

(a) (b) (c)

Figure B4. Relative depth cases of 0.25 for (a) smooth, (b) low density, and (c) high density floodplain scenarios

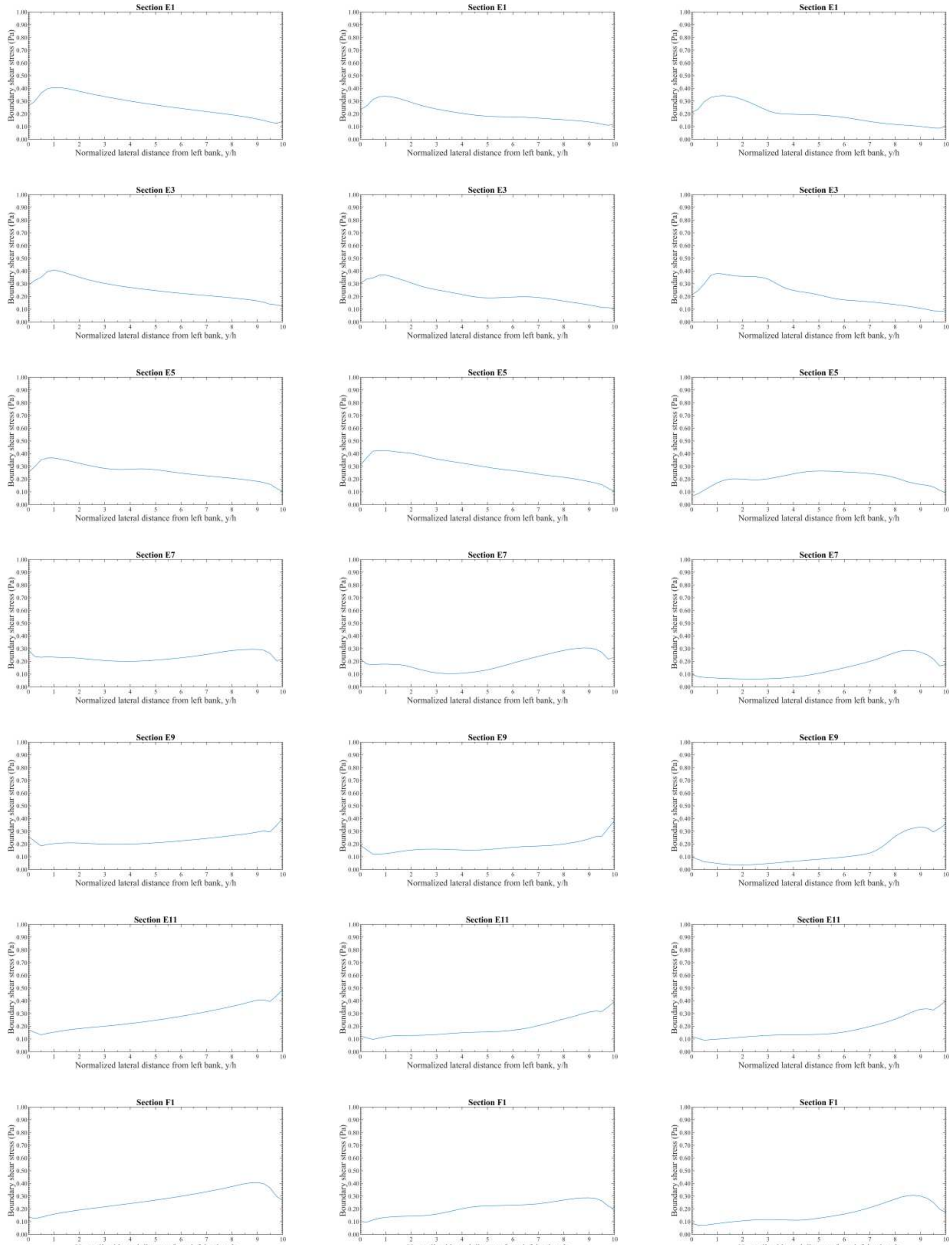

(a) (b) (c)

Figure B5. Relative depth cases of 0.29 for (a) smooth, (b) low density, and (c) high density floodplain scenarios

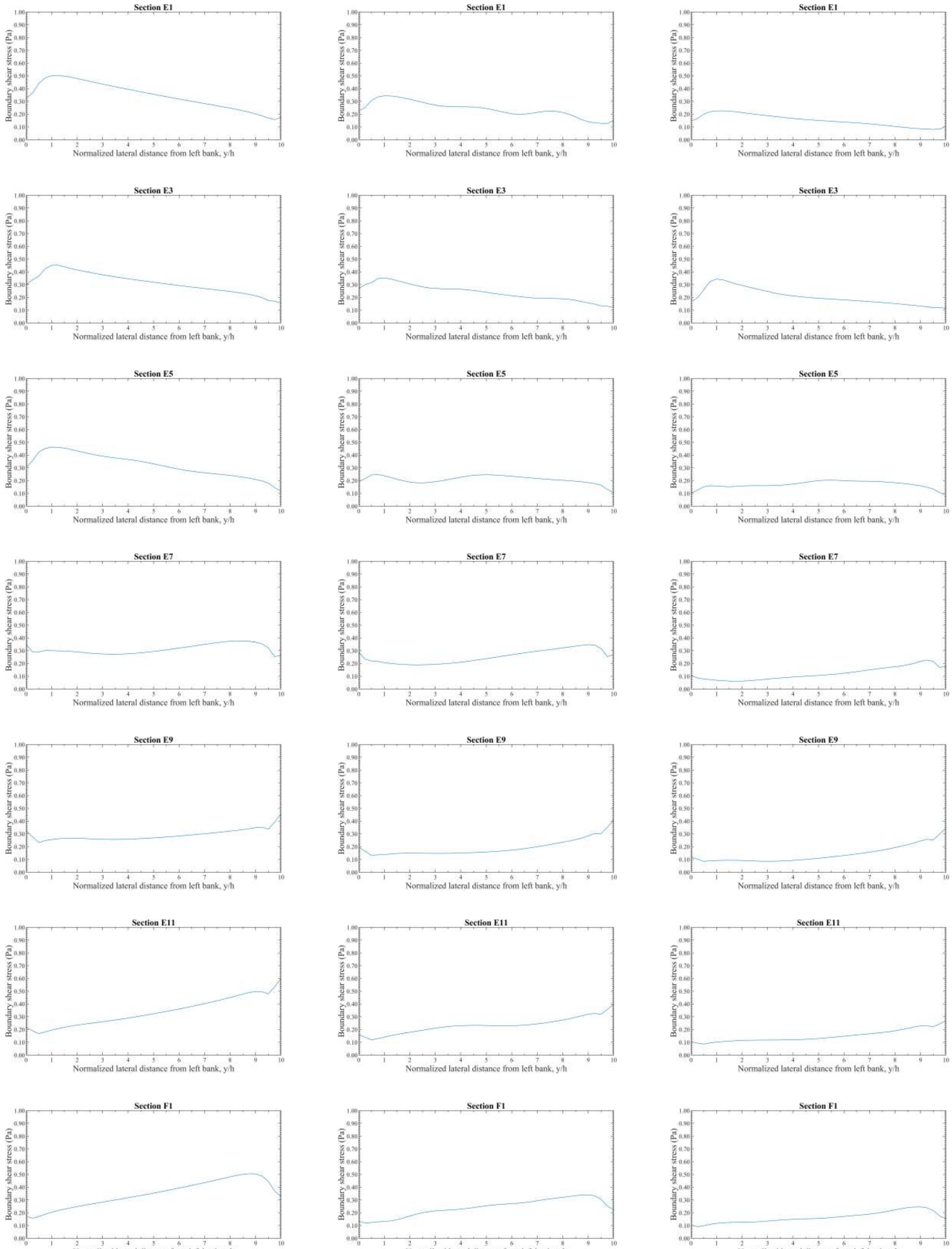

(a) (b) (c)

Figure B6. Relative depth cases of 0.35 for (a) smooth, (b) low density, and (c) high density floodplain scenarios

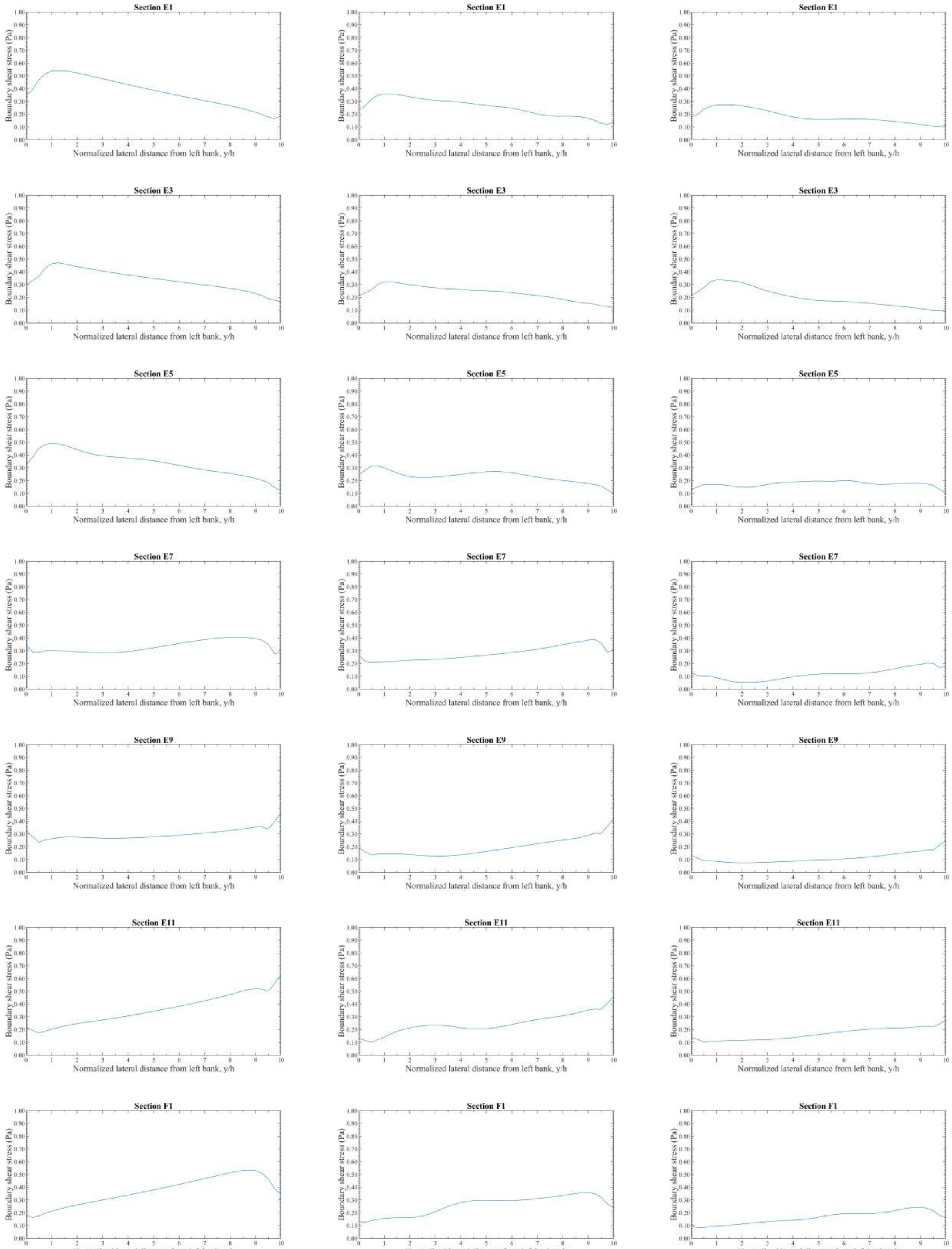

(a) (b) (c)

Figure B7. Relative depth cases of 0.40 for (a) smooth, (b) low density, and (c) high density floodplain scenarios

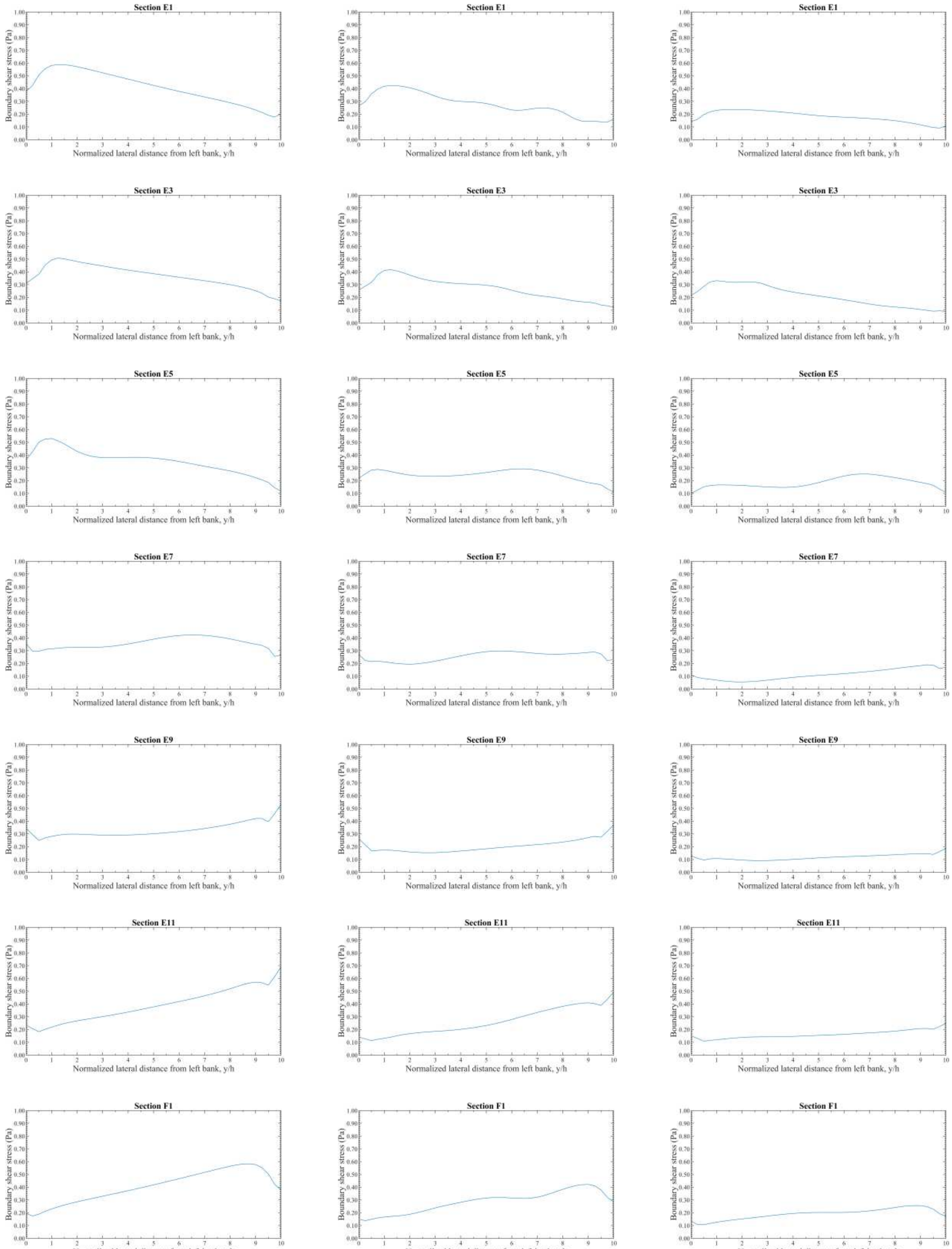

(a) (b) (c)

Figure B8. Relative depth cases of 0.46 for (a) smooth, (b) low density, and (c) high density floodplain scenarios

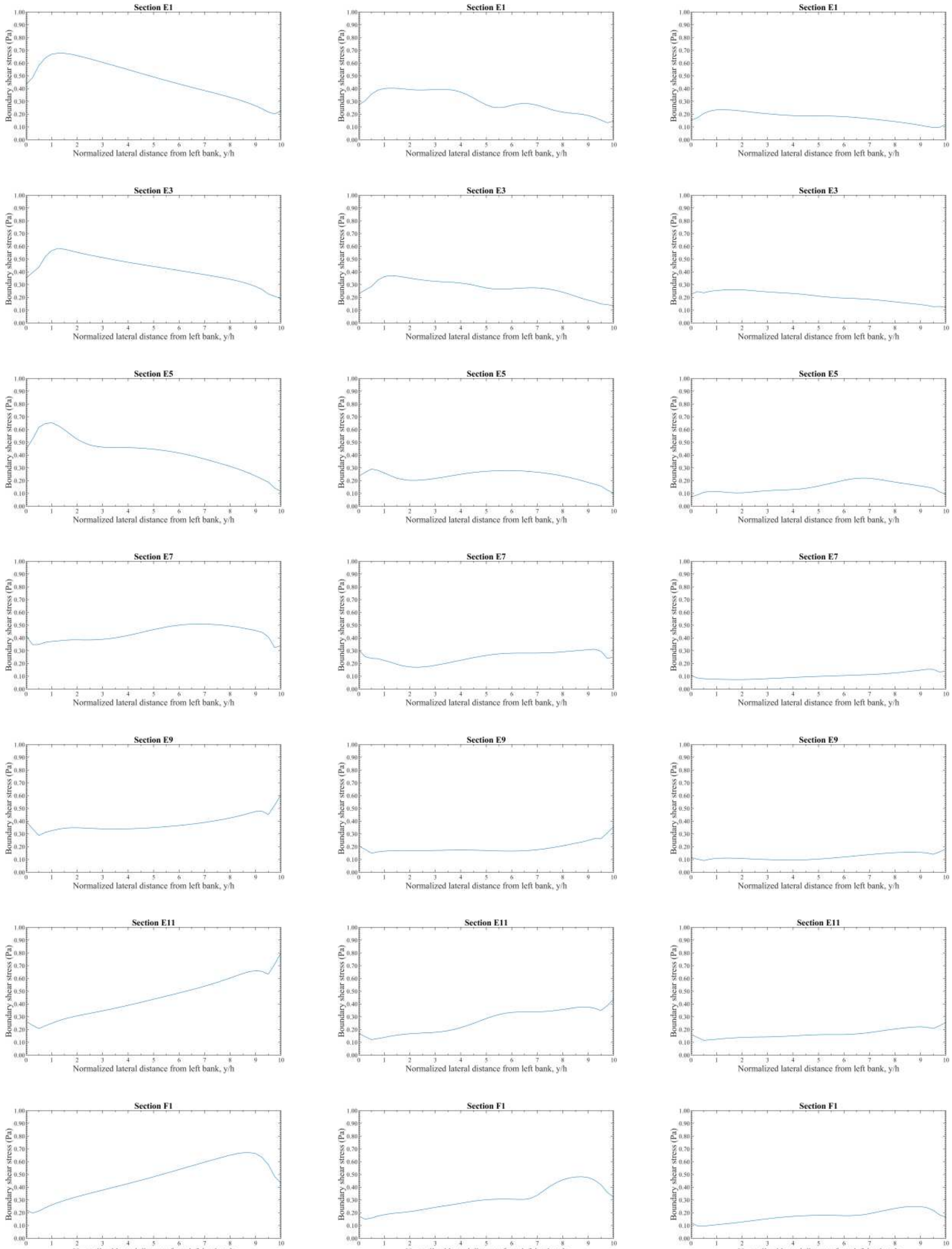

(a) (b) (c)

Figure B9. Relative depth cases of 0.50 for (a) smooth, (b) low density, and (c) high density floodplain scenarios

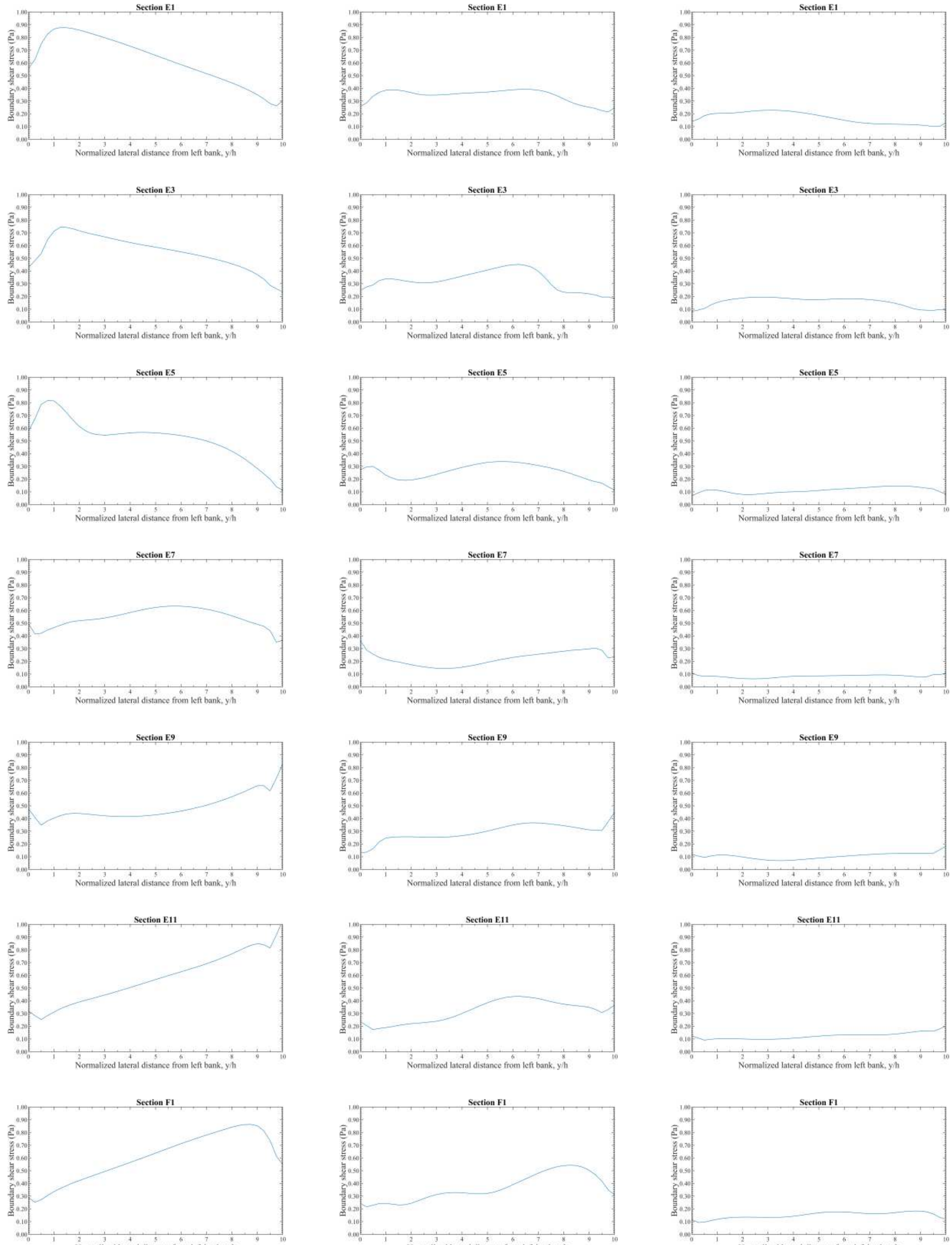

(a) (b) (c)

Figure B10. Relative depth cases of 0.60 for (a) smooth, (b) low density, and (c) high density floodplain scenarios

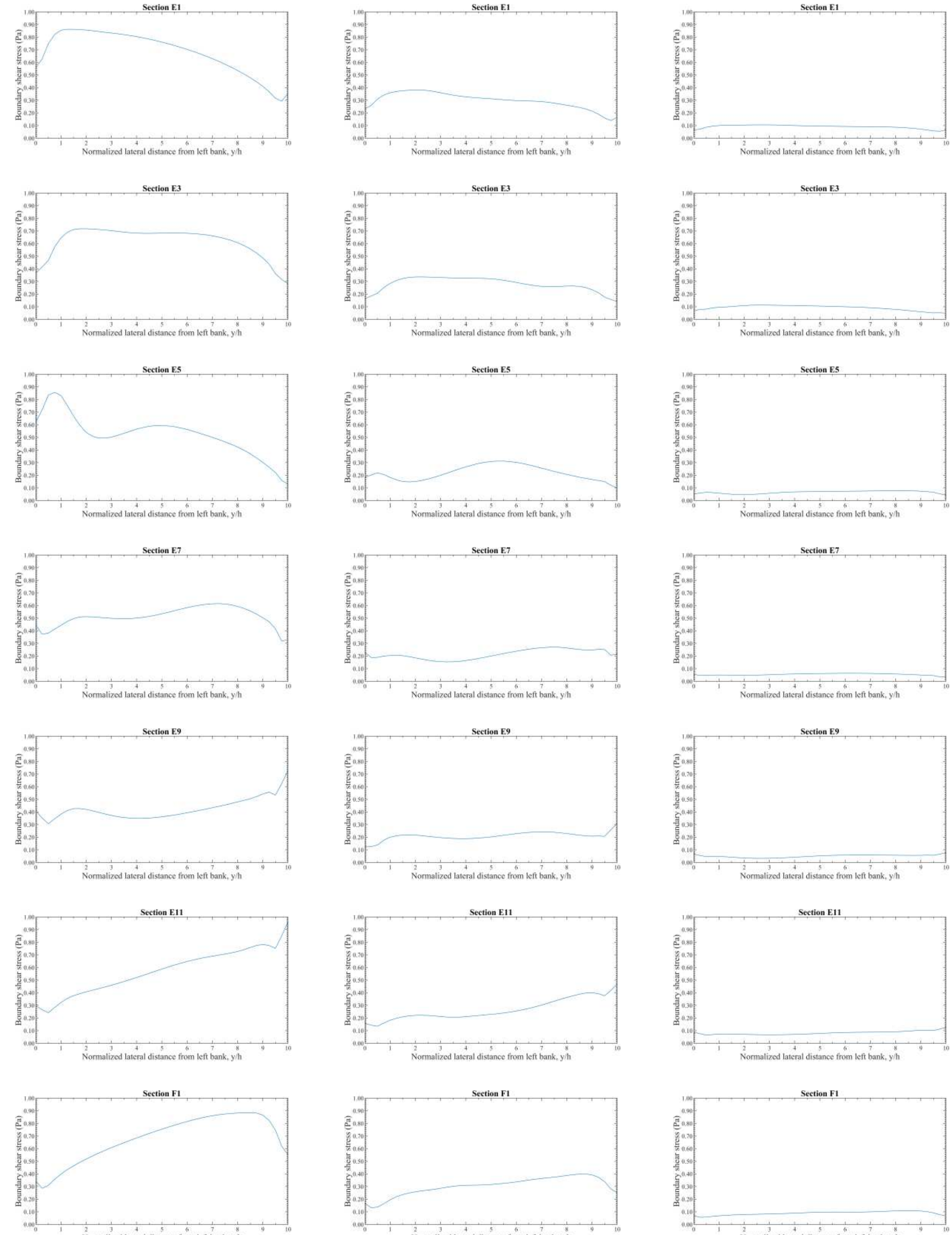

(a) (b) (c)

Figure B11. Relative depth cases of 0.80 for (a) smooth, (b) low density, and (c) high density floodplain scenarios

Appendix C: Main channel primary and secondary flow cross section plots

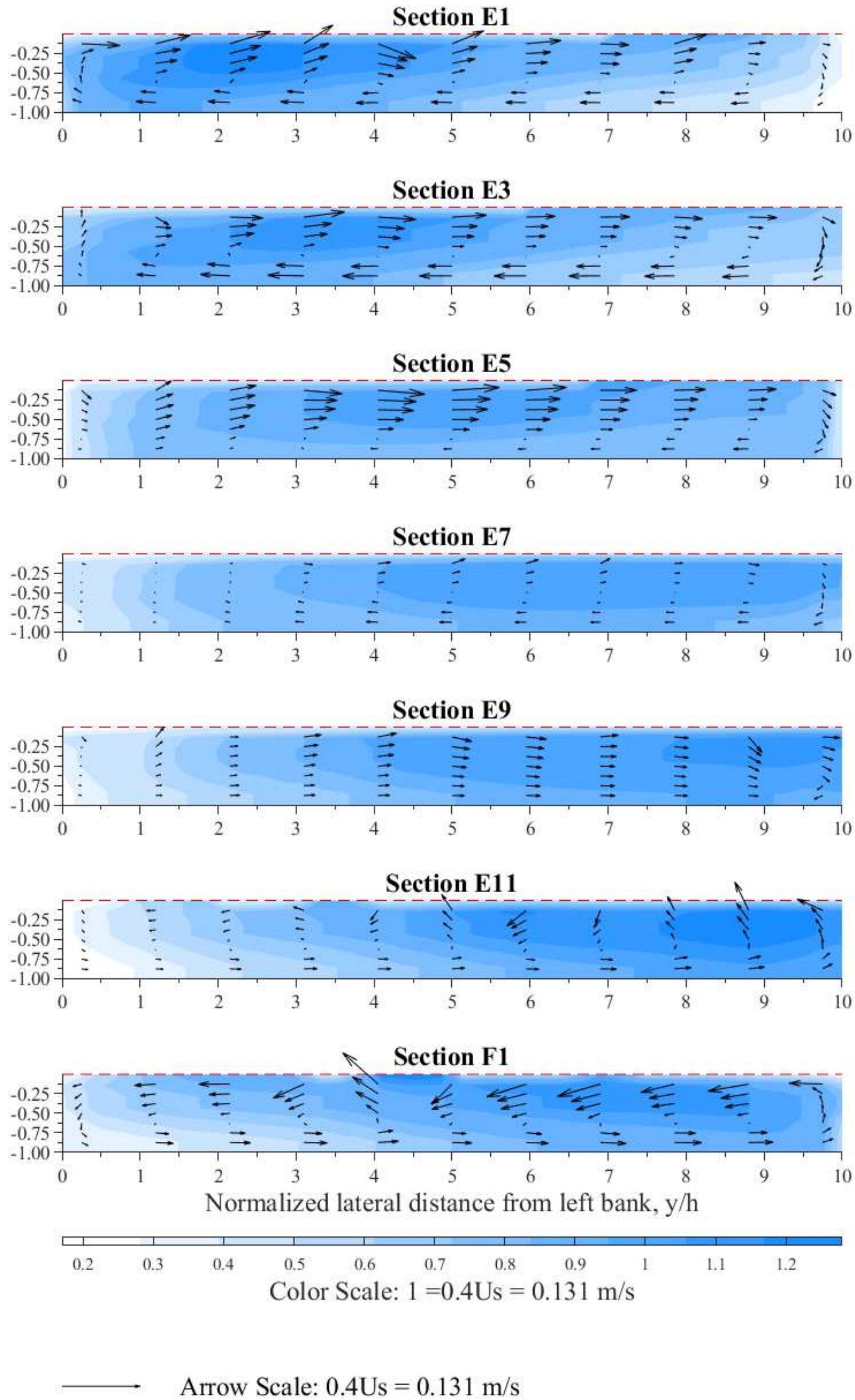

Figure C1. Relative depth case of 0 for smooth floodplain scenario

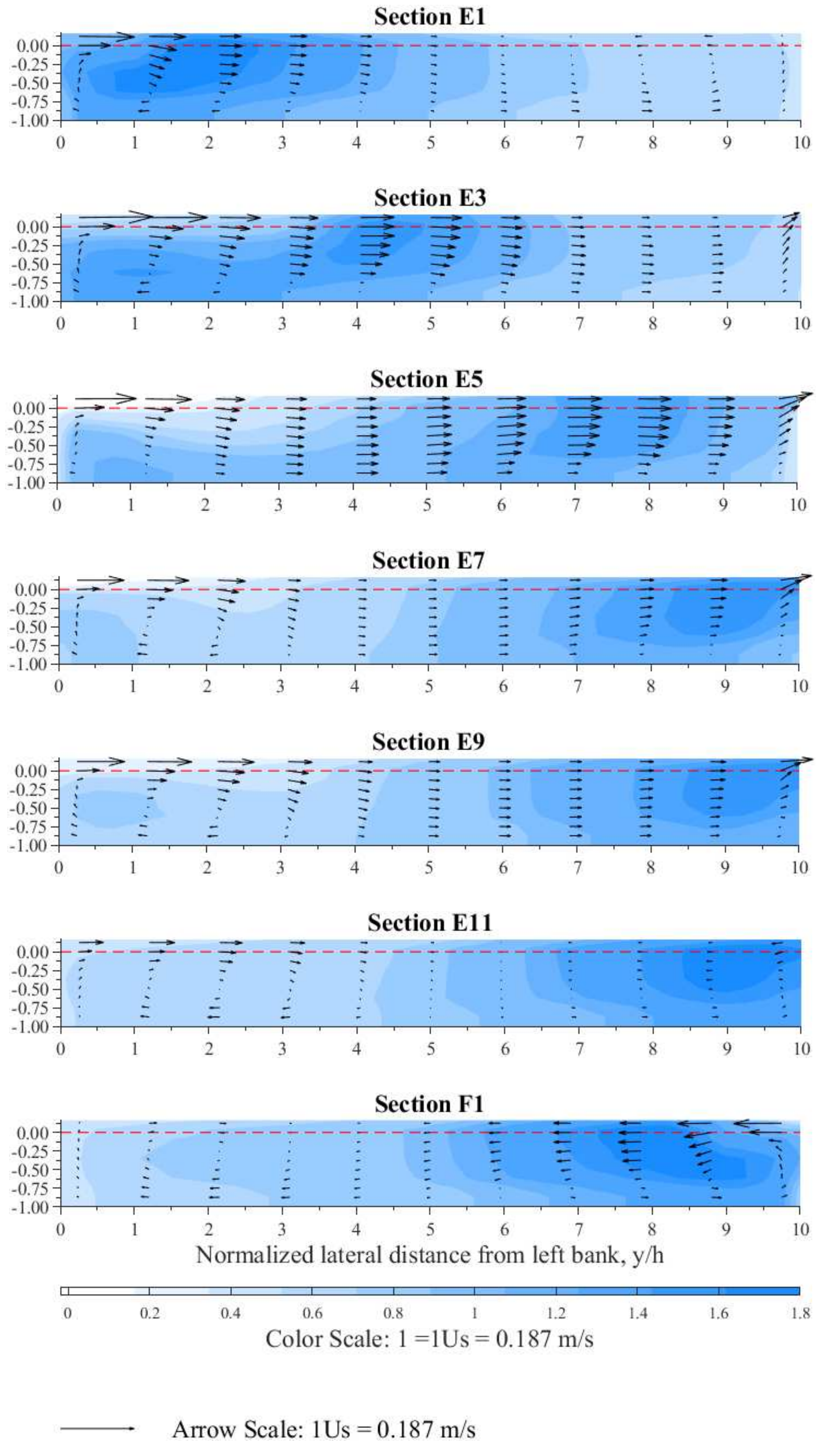

(a)

Figure C2. Relative depth cases of 0.13 for (a) smooth, (b) low density, and (c) high density floodplain scenarios

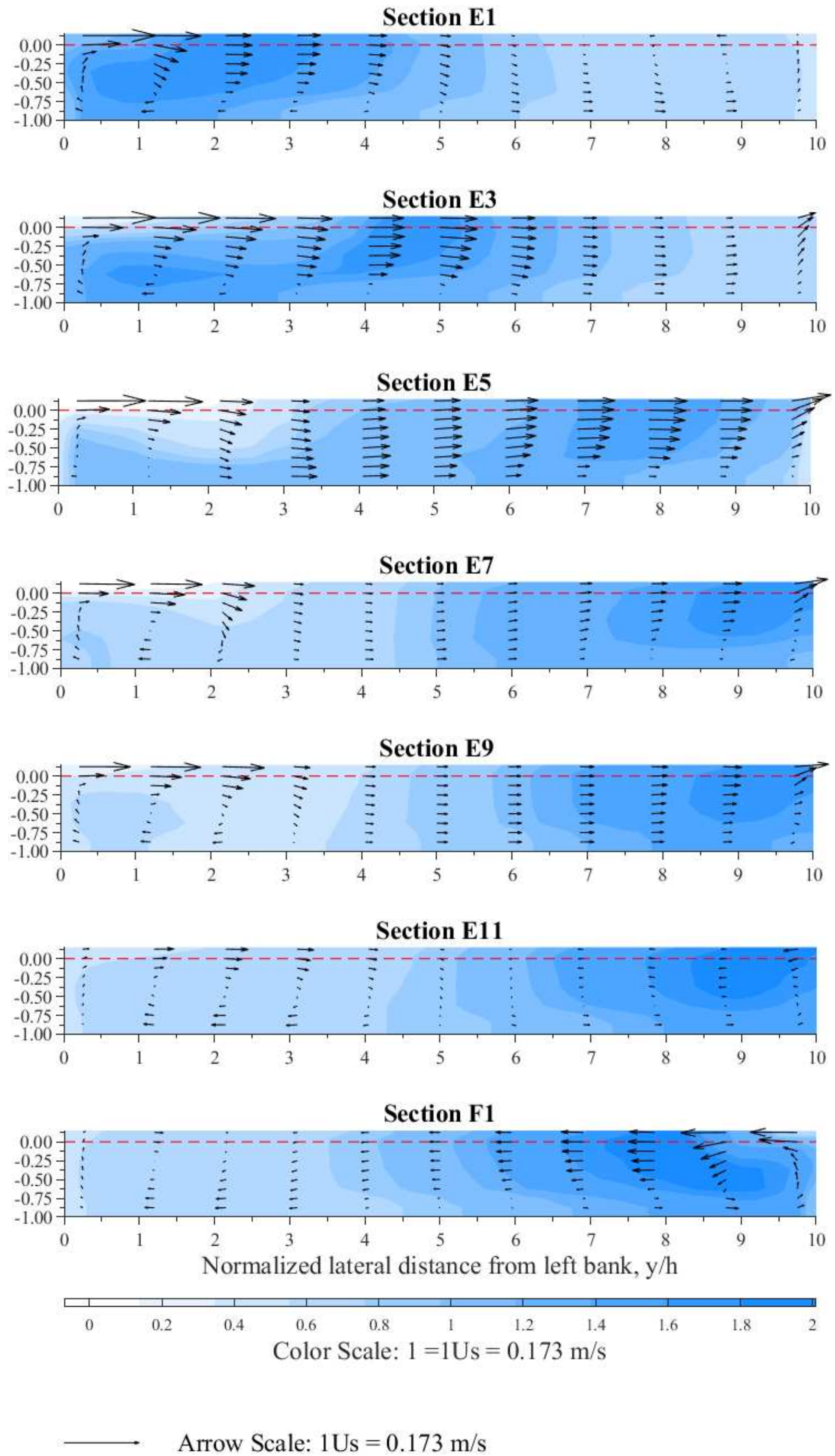

(b)

Figure C2. Relative depth cases of 0.13 for (a) smooth, (b) low density, and (c) high density floodplain scenarios

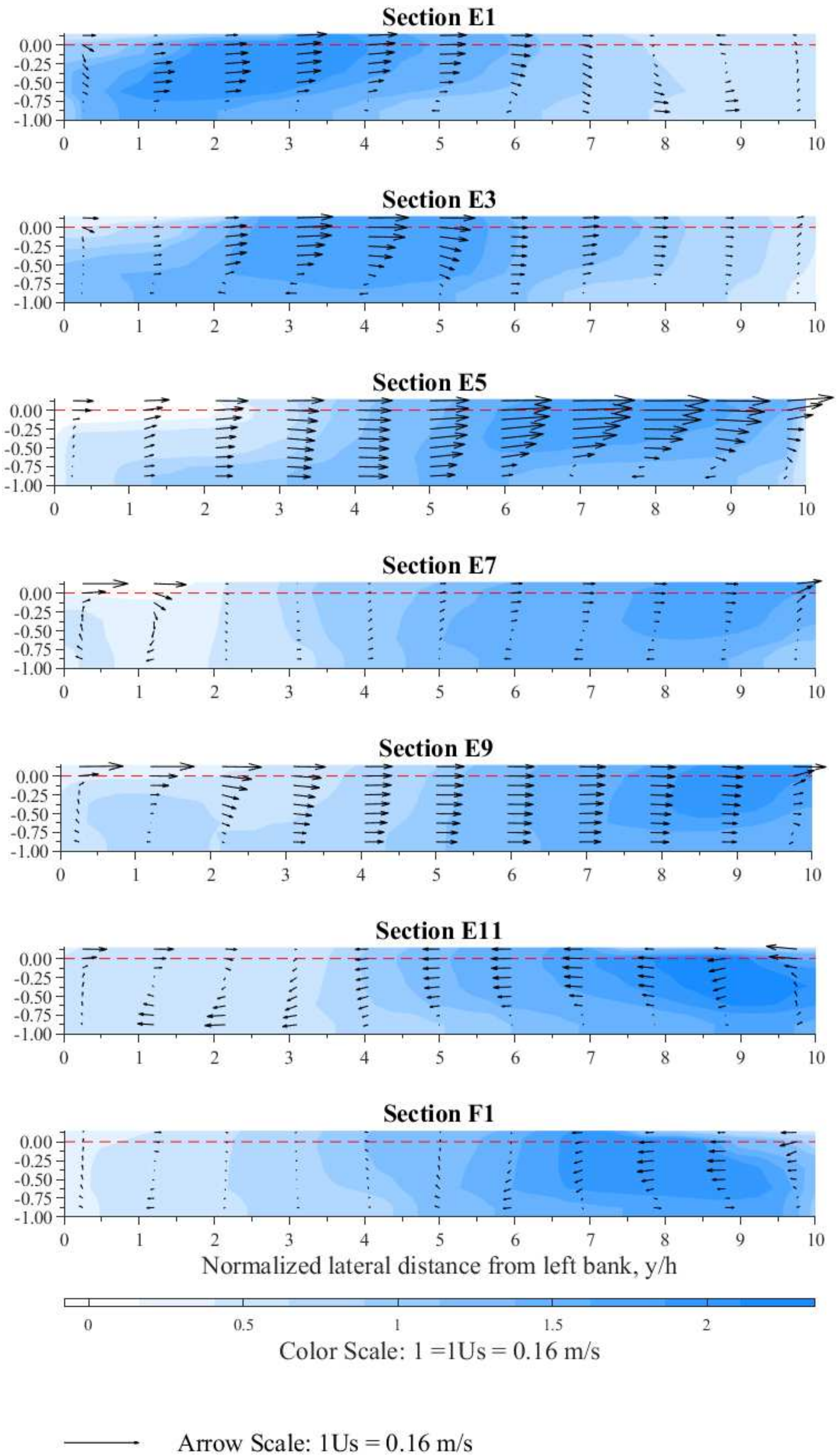

(c)

Figure C2. Relative depth cases of 0.13 for (a) smooth, (b) low density, and (c) high density floodplain scenarios

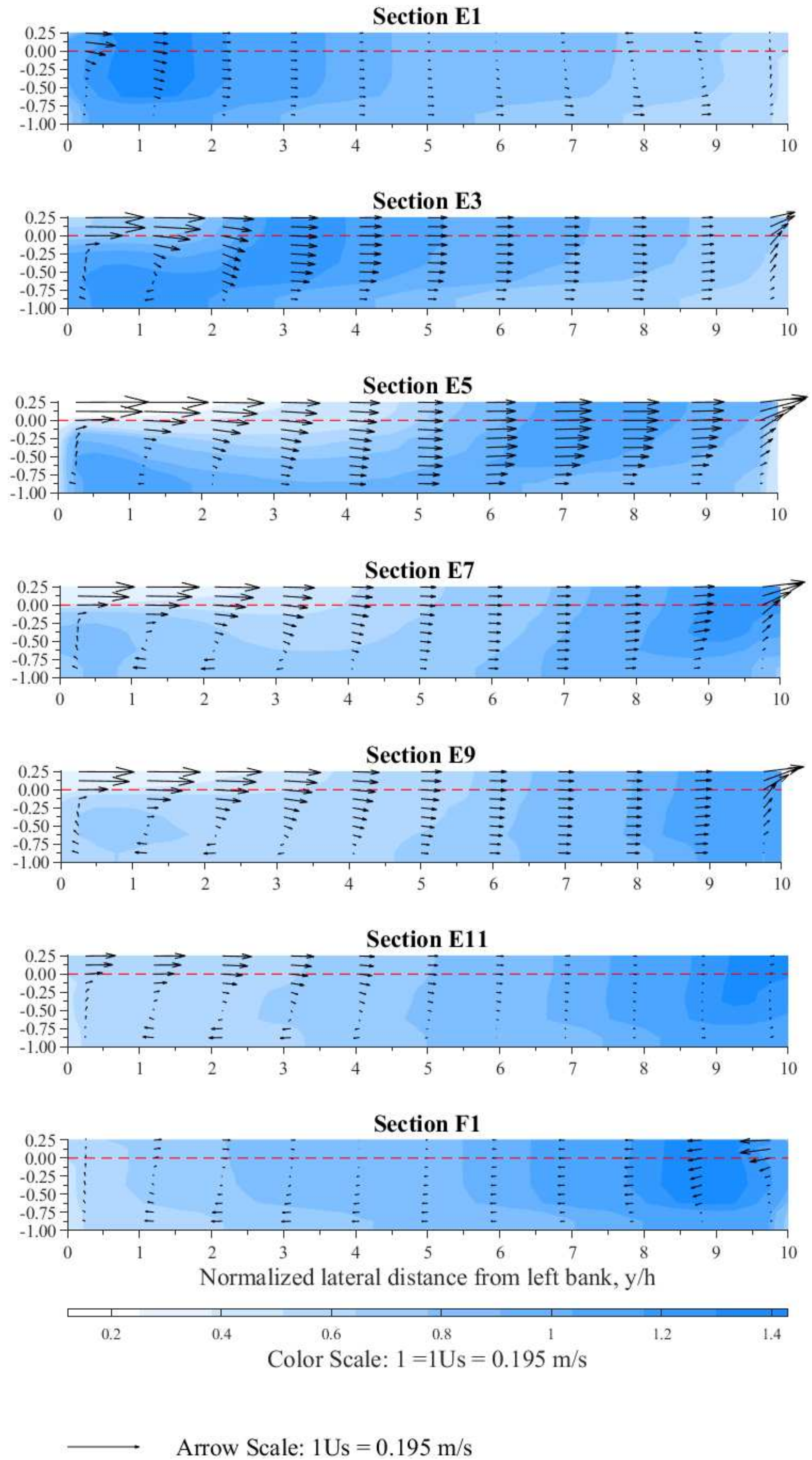

(a)

Figure C3. Relative depth cases of 0.20 for (a) smooth, (b) low density, and (c) high density floodplain scenarios

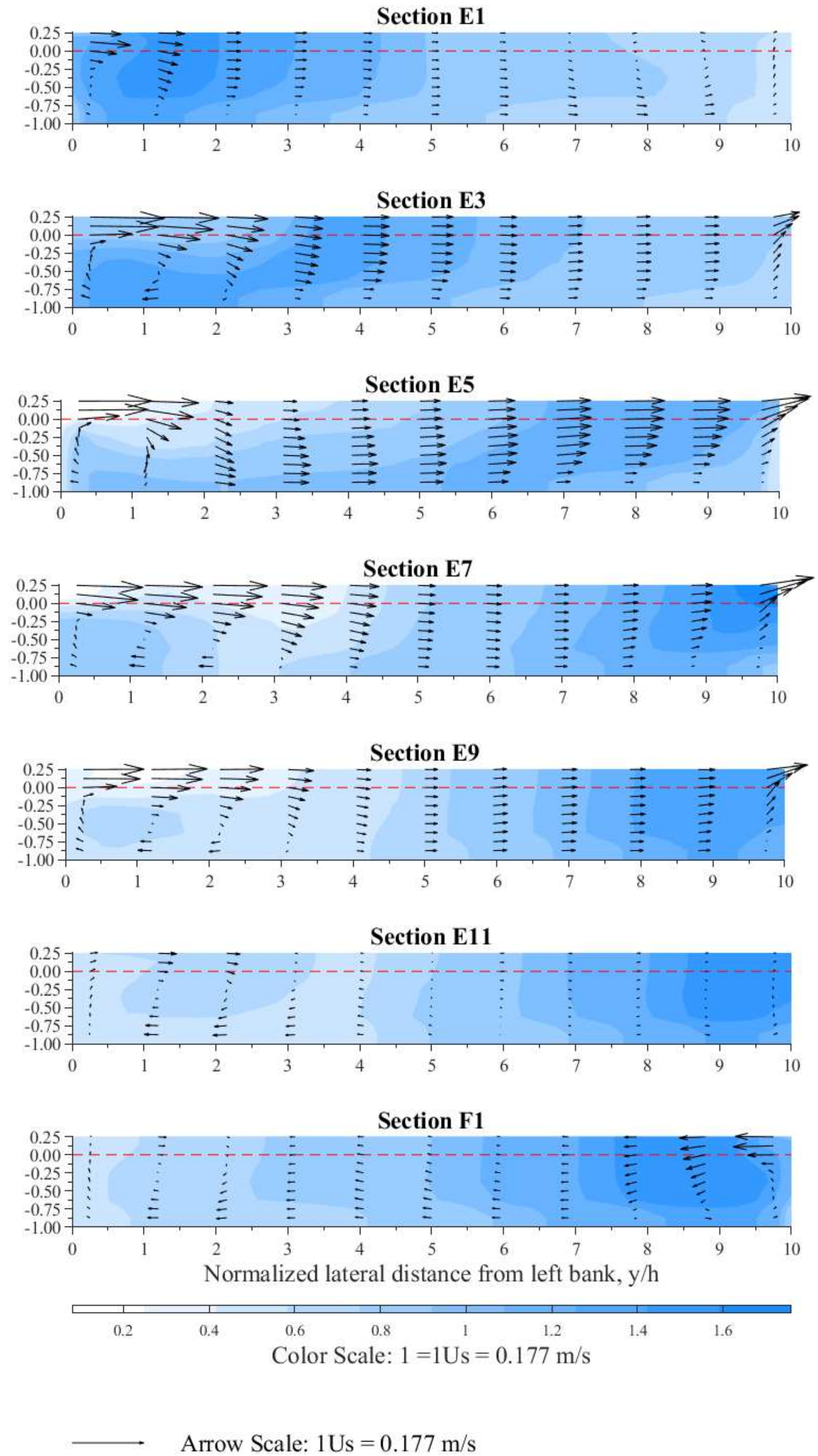

(b)

Figure C3. Relative depth cases of 0.20 for (a) smooth, (b) low density, and (c) high density floodplain scenarios

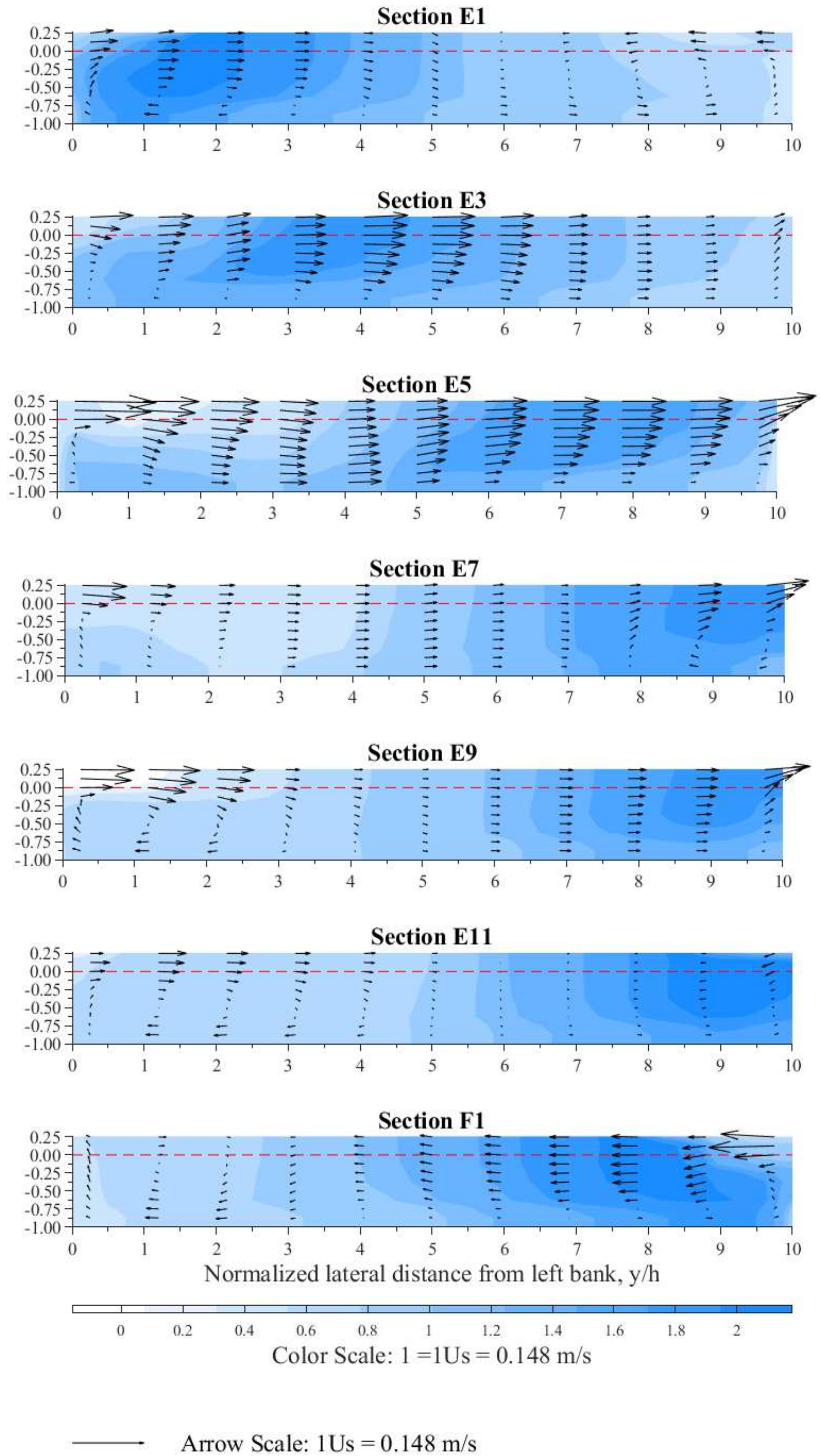

(c)

Figure C3. Relative depth cases of 0.20 for (a) smooth, (b) low density, and (c) high density floodplain scenarios

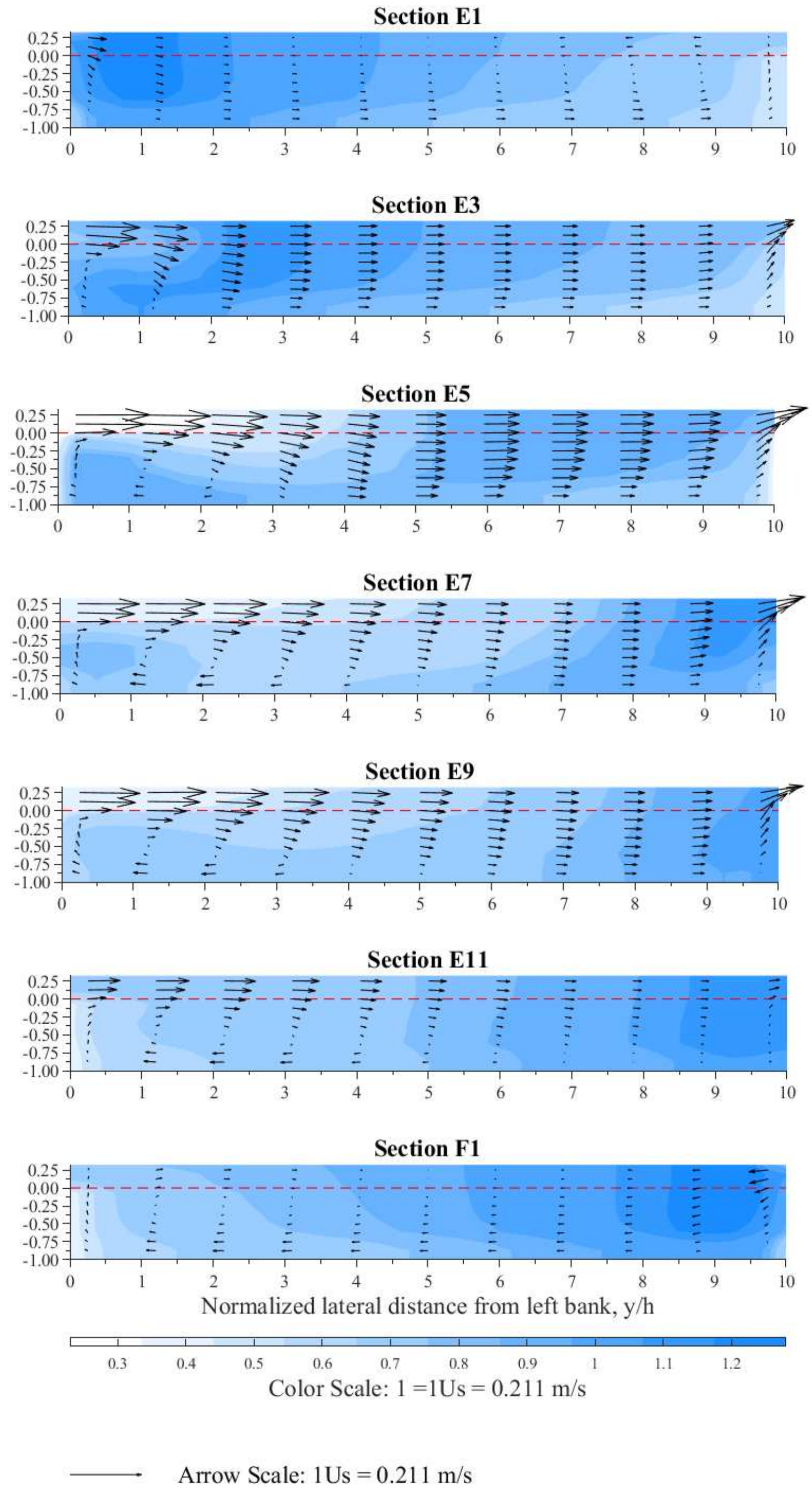

(a)

Figure C4. Relative depth cases of 0.25 for (a) smooth, (b) low density, and (c) high density floodplain scenarios

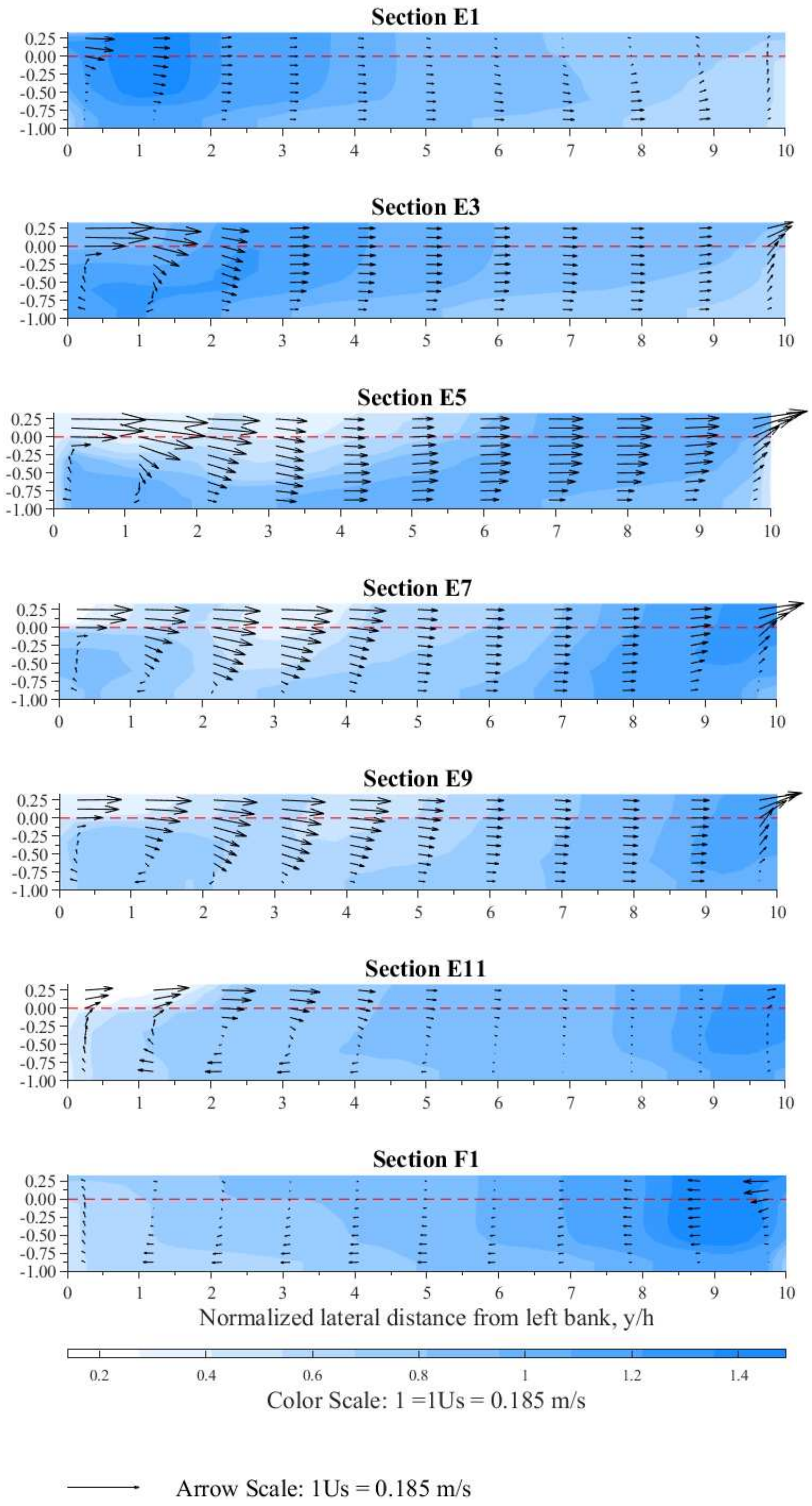

(b)

Figure C4. Relative depth cases of 0.25 for (a) smooth, (b) low density, and (c) high density floodplain scenarios

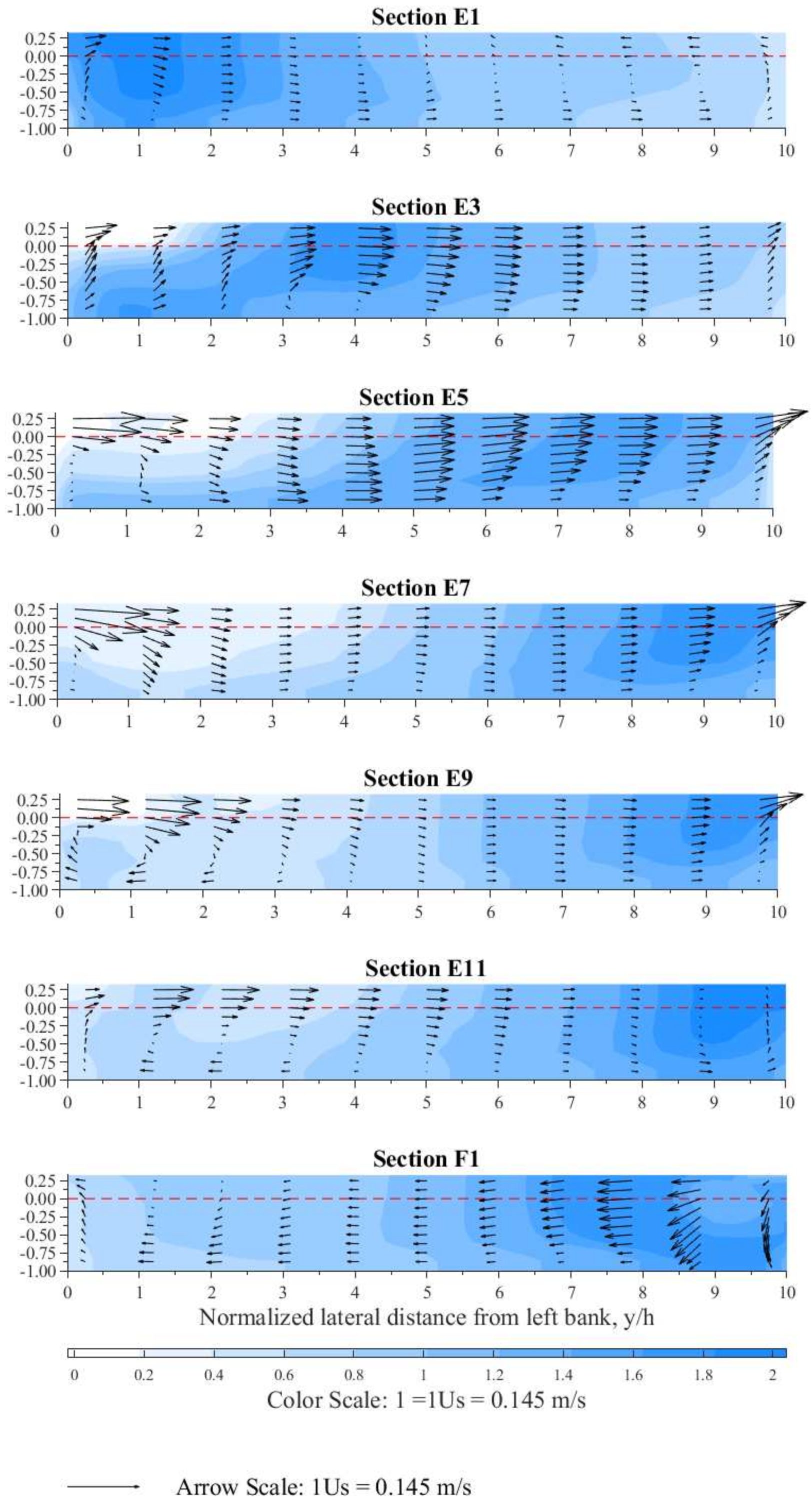

(c)

Figure C4. Relative depth cases of 0.25 for (a) smooth, (b) low density, and (c) high density floodplain scenarios

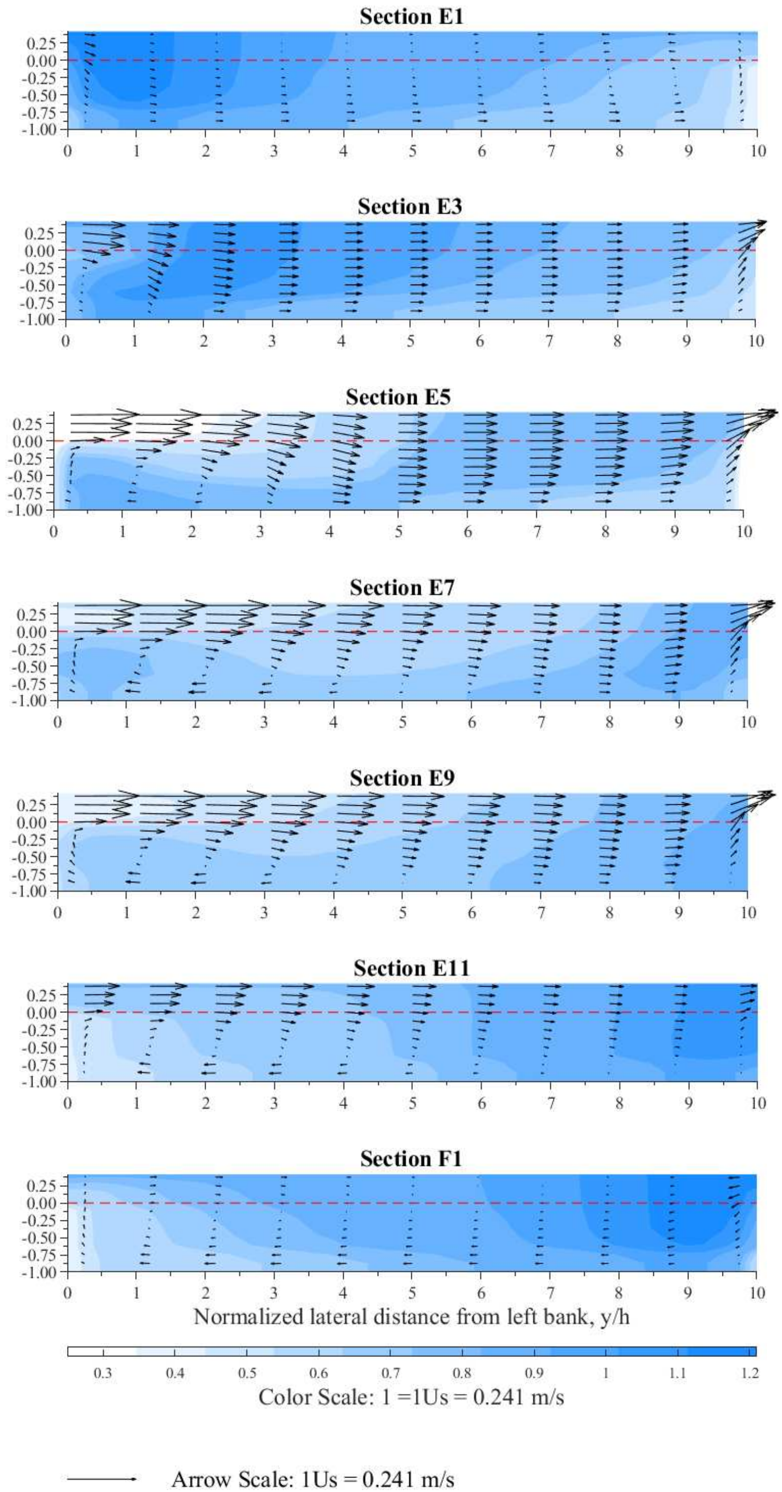

(a)

Figure C5. Relative depth cases of 0.29 for (a) smooth, (b) low density, and (c) high density floodplain scenarios

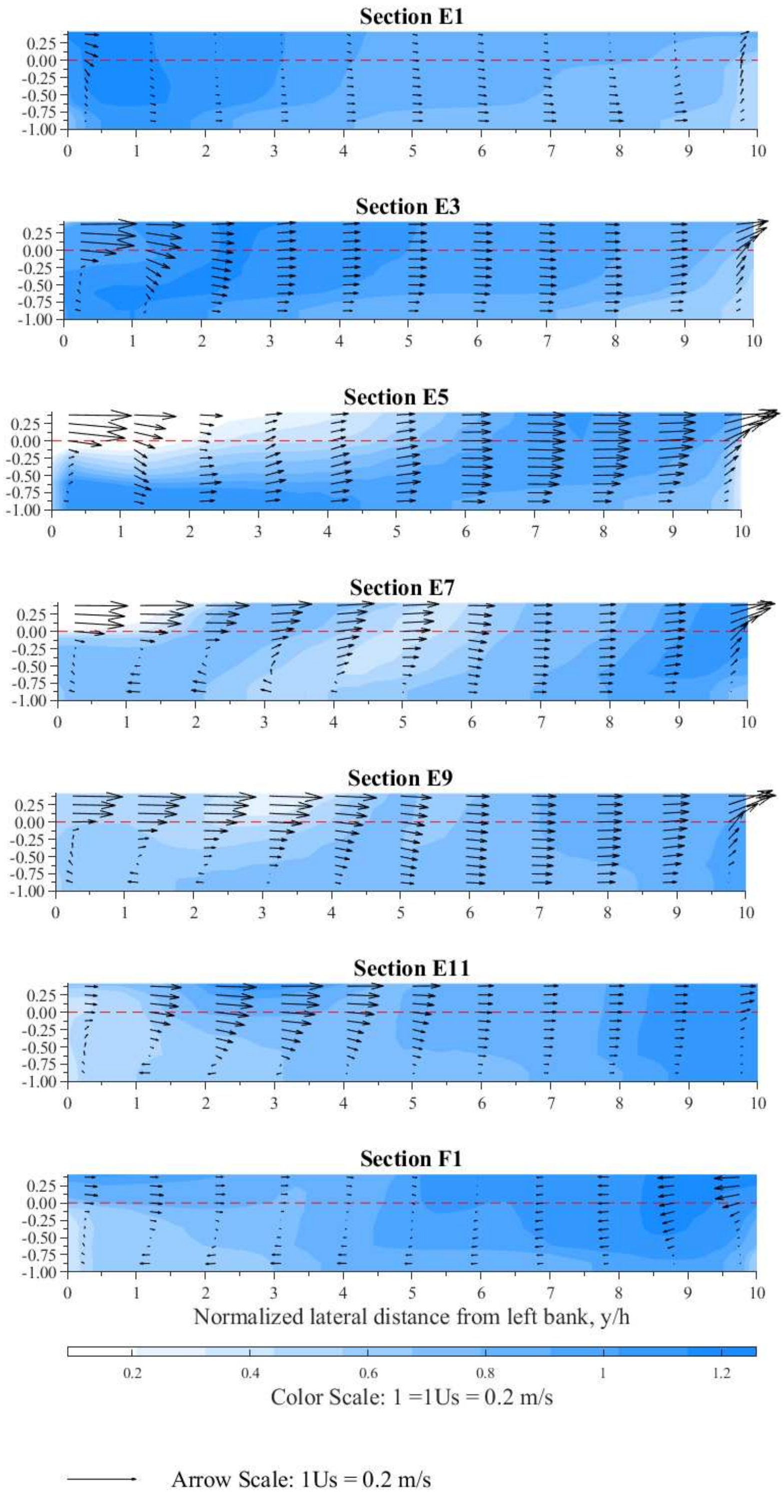

(b)

Figure C5. Relative depth cases of 0.29 for (a) smooth, (b) low density, and (c) high density floodplain scenarios

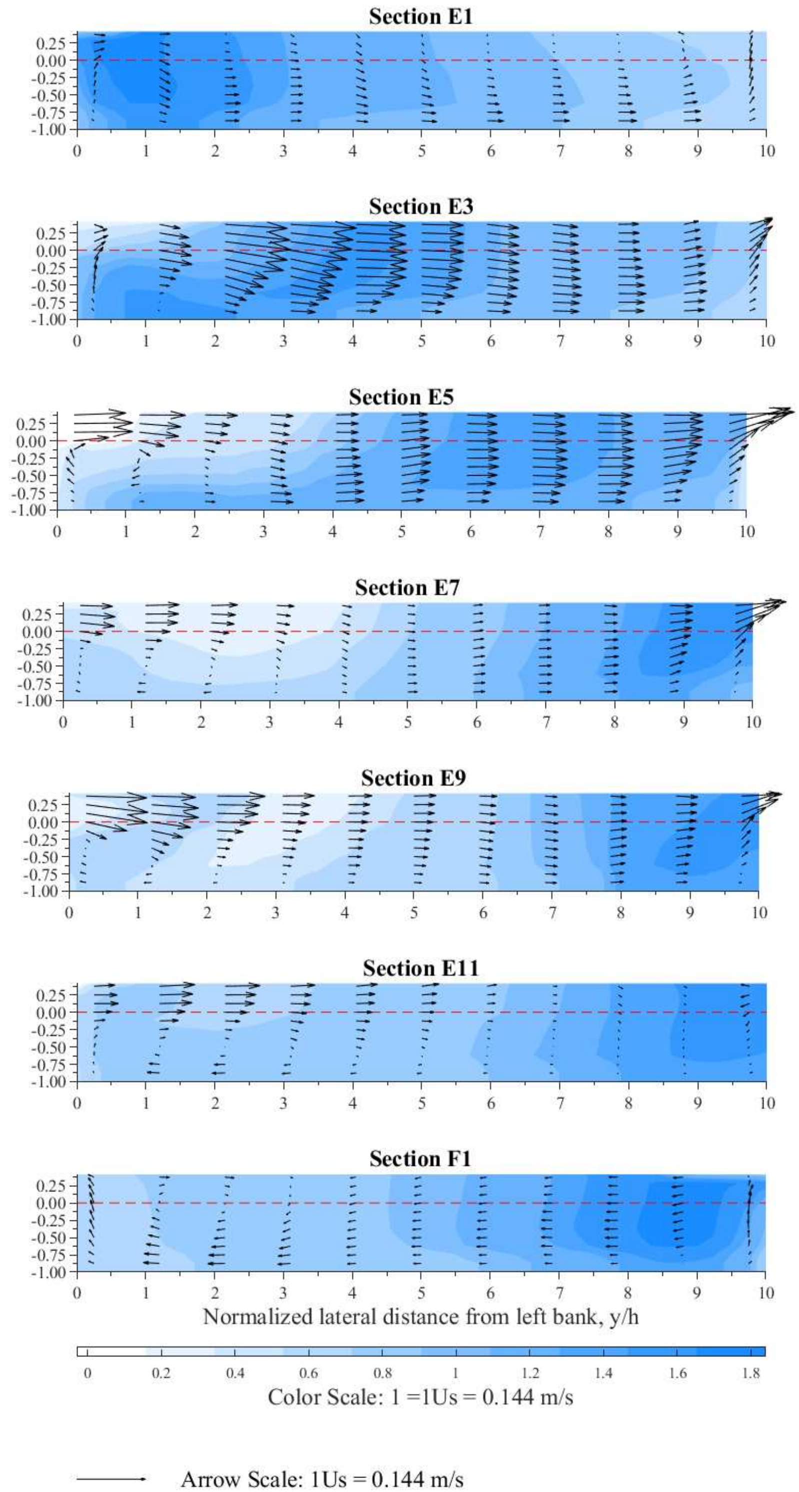

(c)

Figure C5. Relative depth cases of 0.29 for (a) smooth, (b) low density, and (c) high density floodplain scenarios

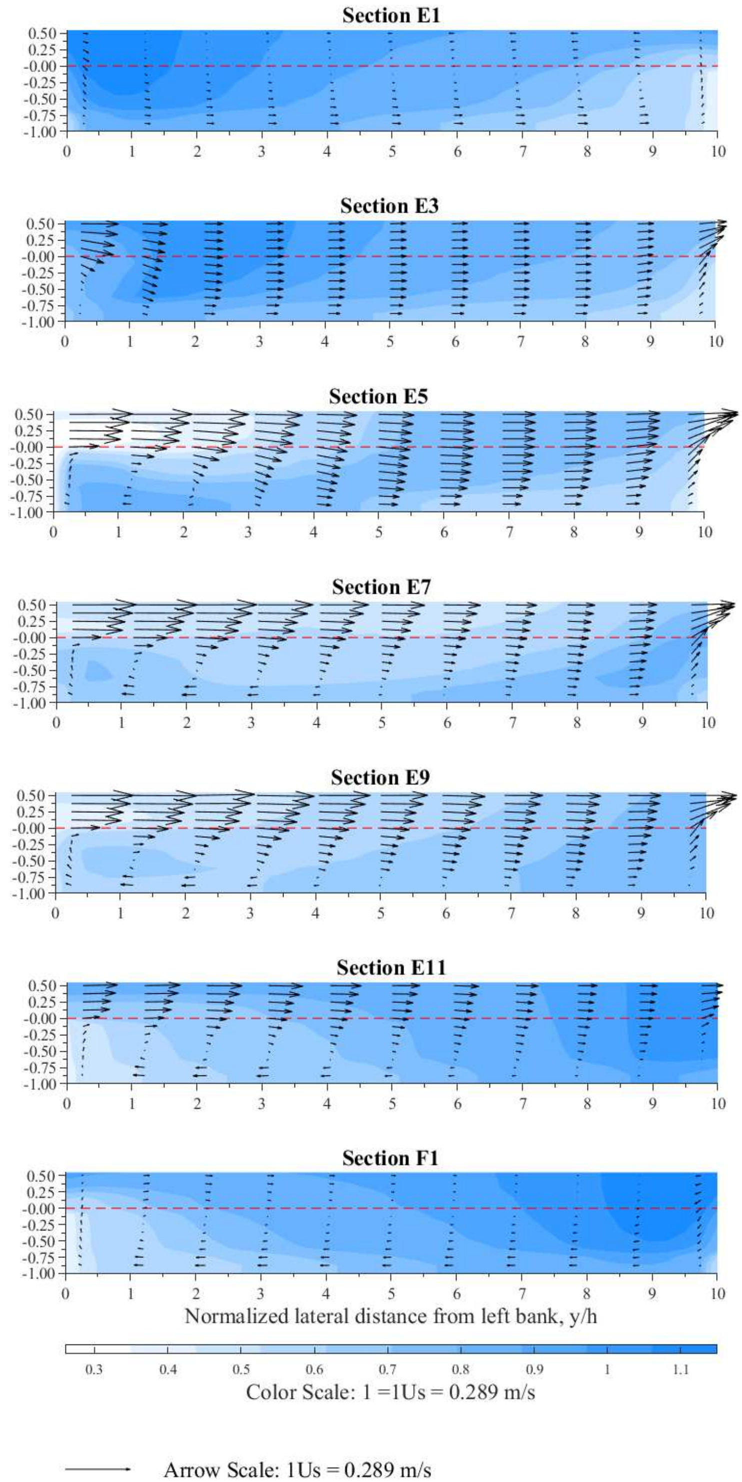

(a)

Figure C6. Relative depth cases of 0.35 for (a) smooth, (b) low density, and (c) high density floodplain scenarios

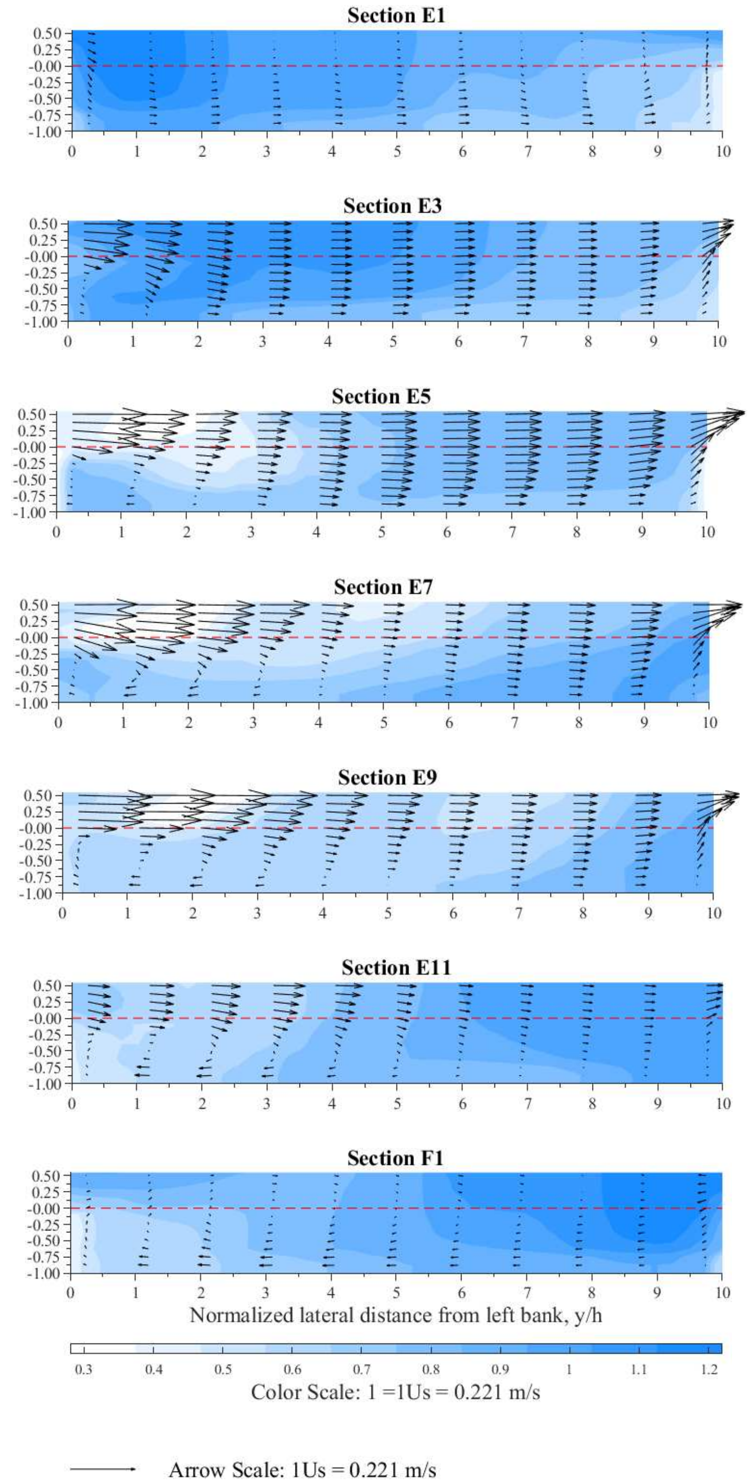

(b)

Figure C6. Relative depth cases of 0.35 for (a) smooth, (b) low density, and (c) high density floodplain scenarios

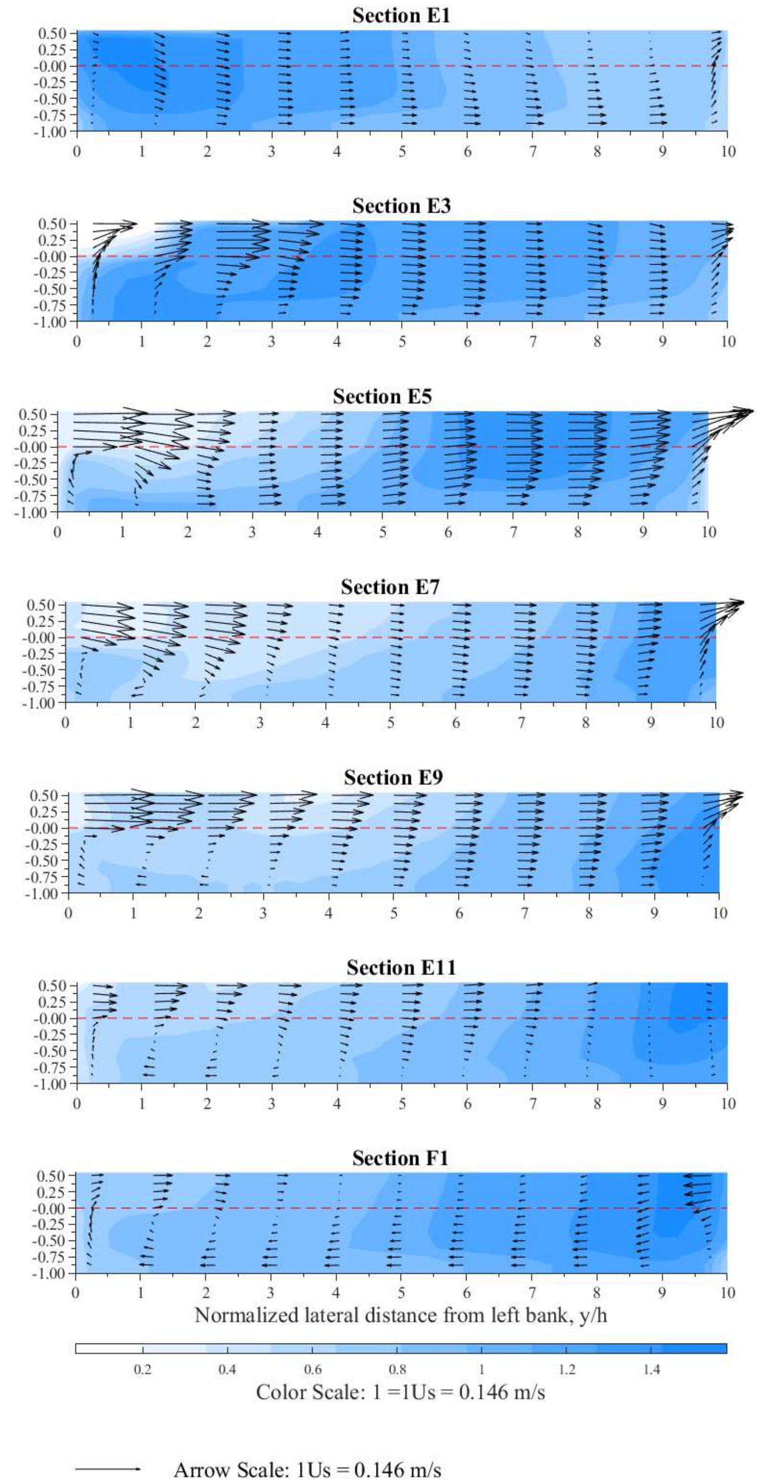

(c)

Figure C6. Relative depth cases of 0.35 for (a) smooth, (b) low density, and (c) high density floodplain scenarios

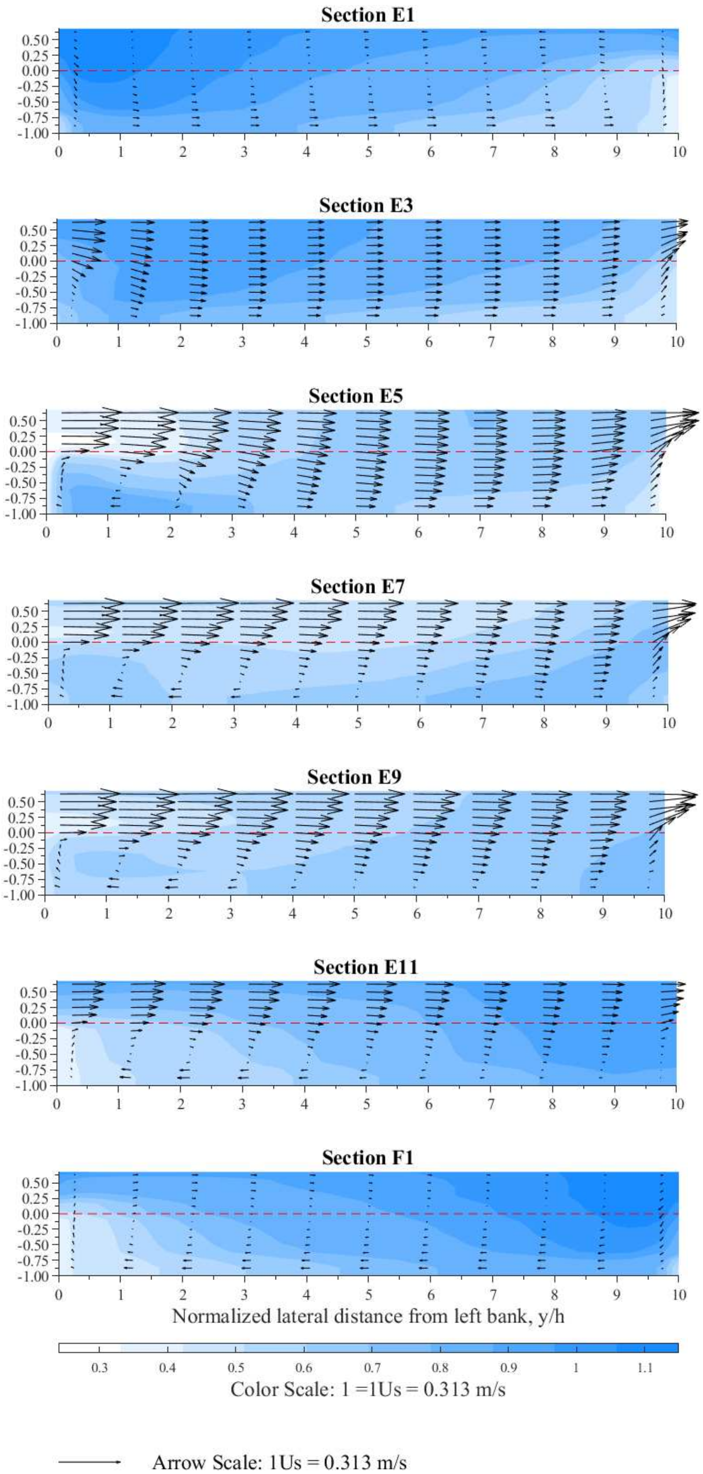

(a)

Figure C7. Relative depth cases of 0.40 for (a) smooth, (b) low density, and (c) high density floodplain scenarios

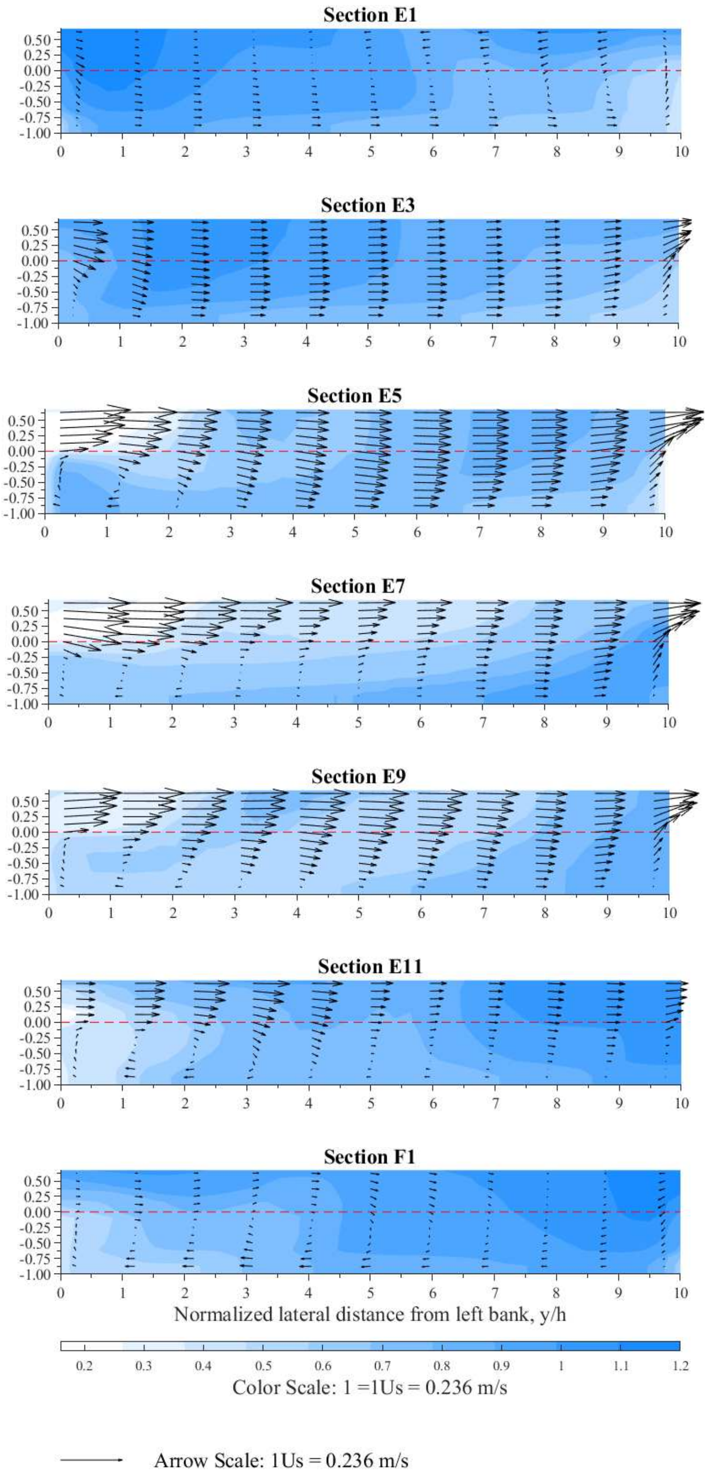

(b)

Figure C7. Relative depth cases of 0.40 for (a) smooth, (b) low density, and (c) high density floodplain scenarios

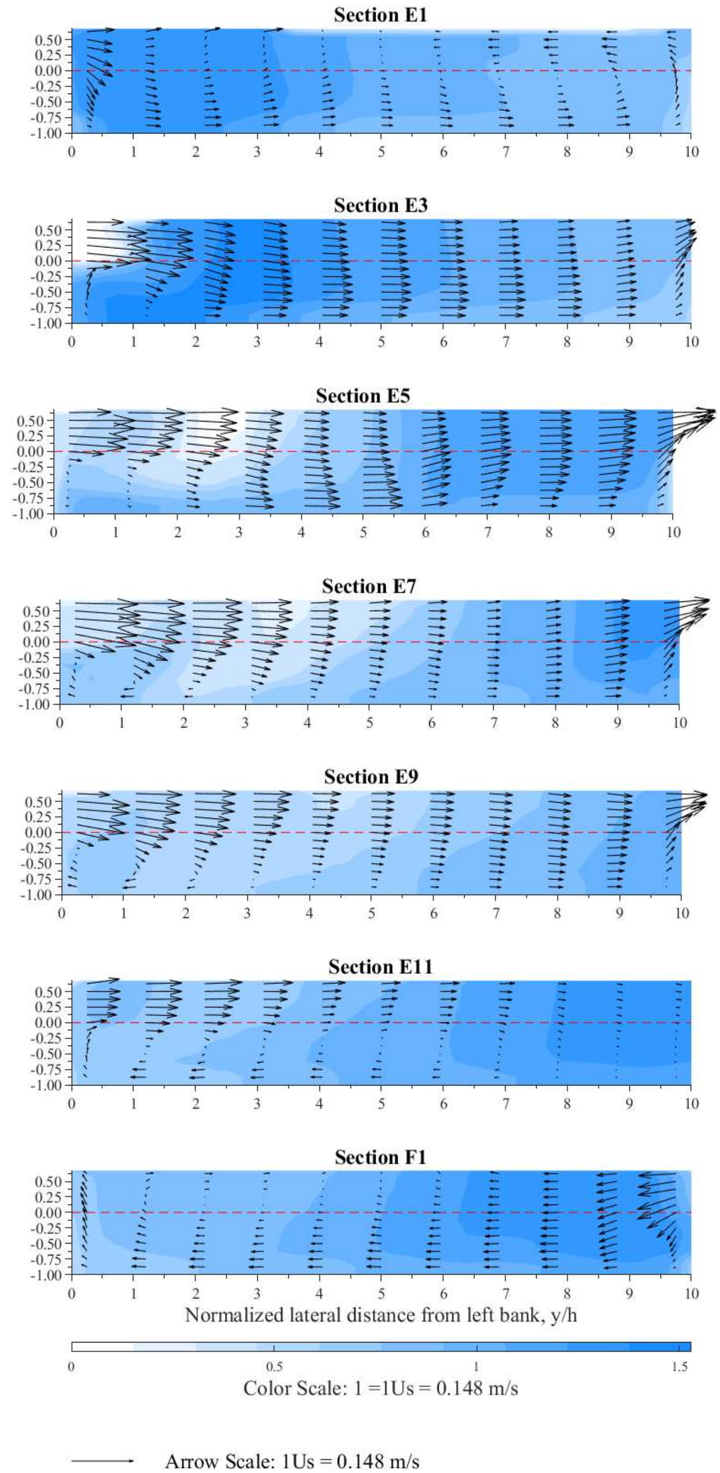

(c)

Figure C7. Relative depth cases of 0.40 for (a) smooth, (b) low density, and (c) high density floodplain scenarios

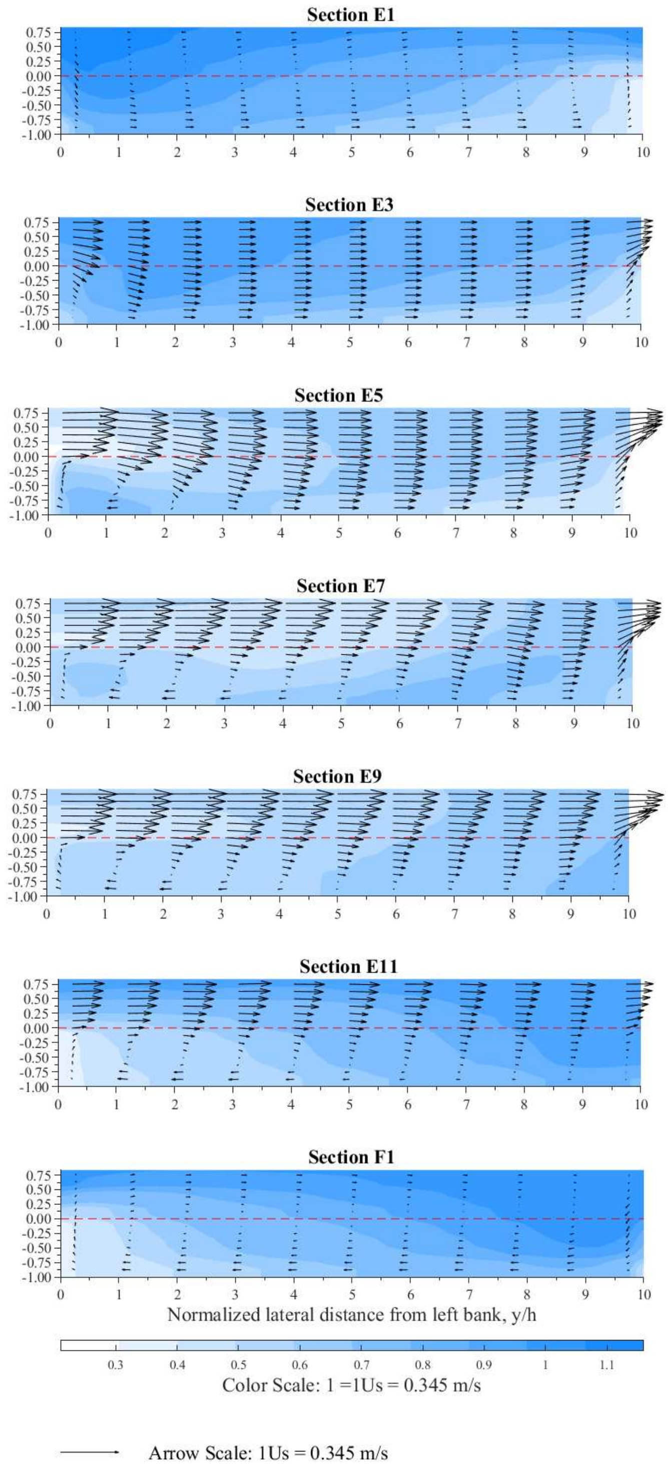

(a)

Figure C8. Relative depth cases of 0.46 for (a) smooth, (b) low density, and (c) high density floodplain scenarios

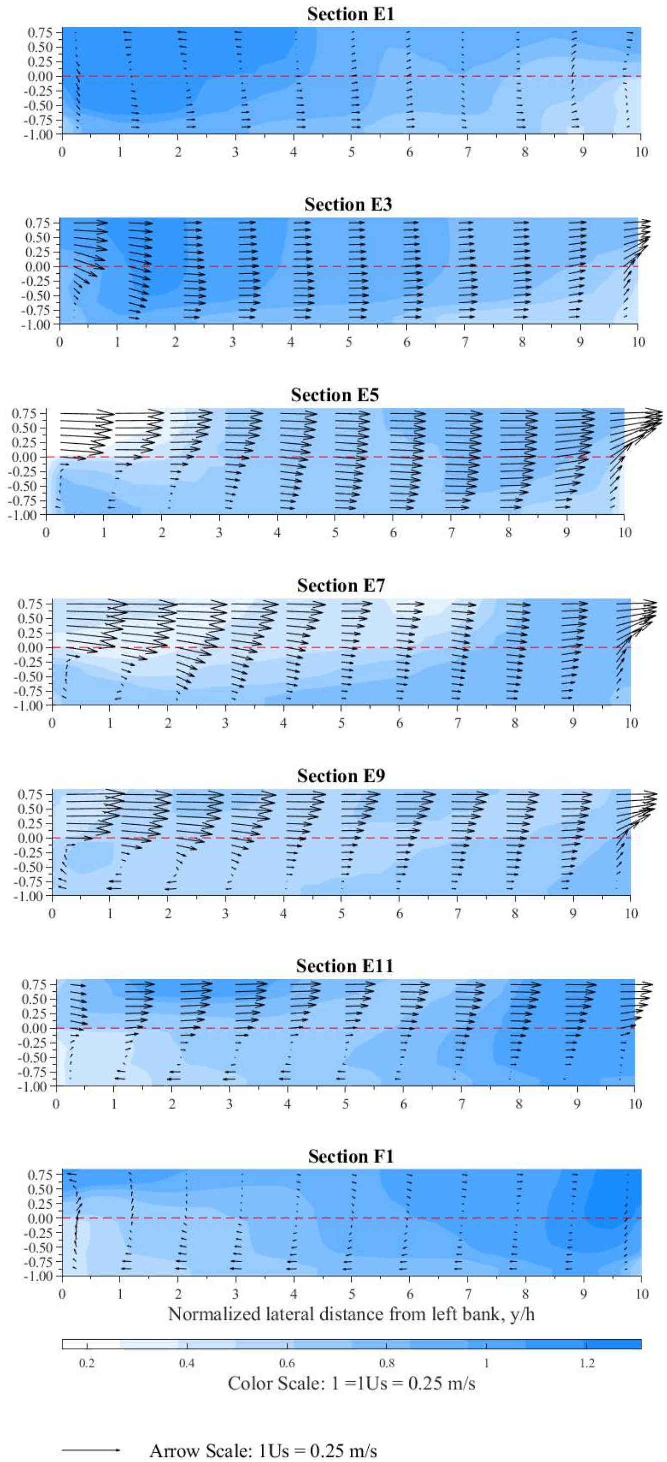

(b)

Figure C8. Relative depth cases of 0.46 for (a) smooth, (b) low density, and (c) high density floodplain scenarios

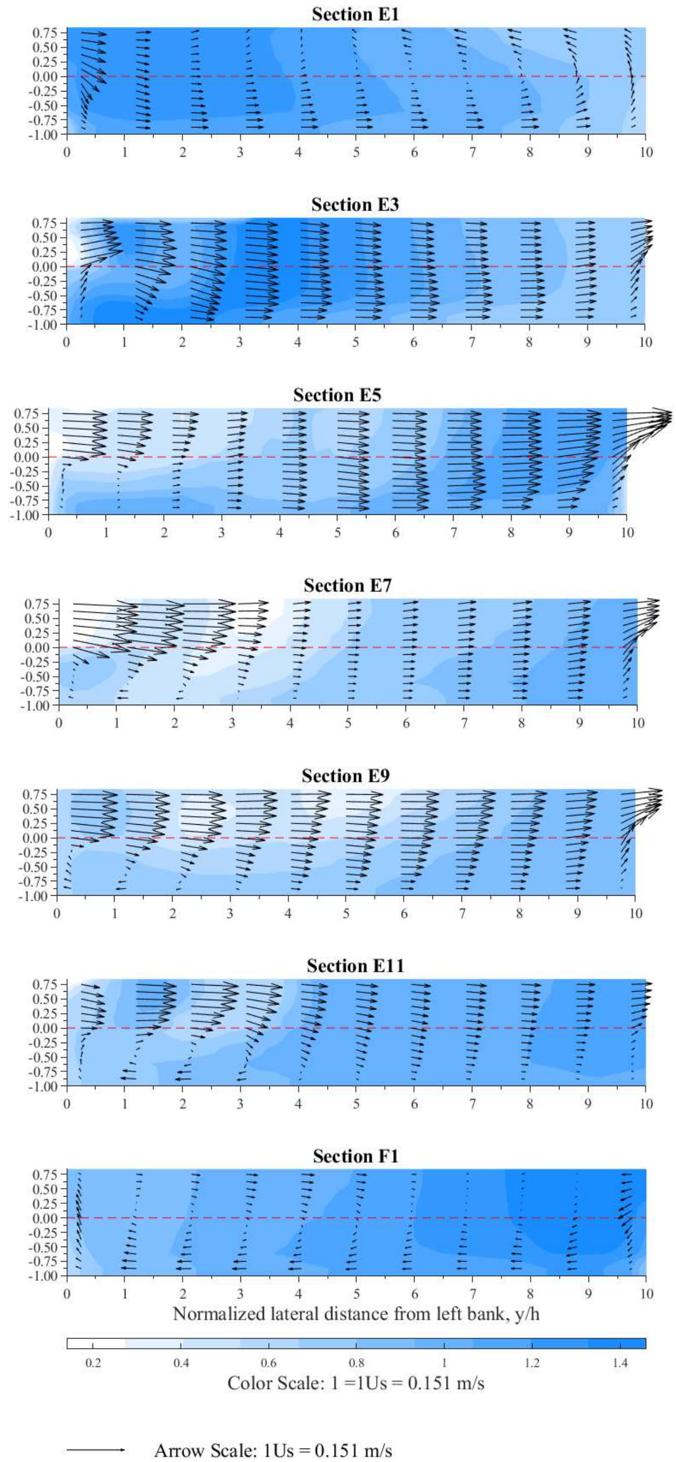

(c)

Figure C8. Relative depth cases of 0.46 for (a) smooth, (b) low density, and (c) high density floodplain scenarios

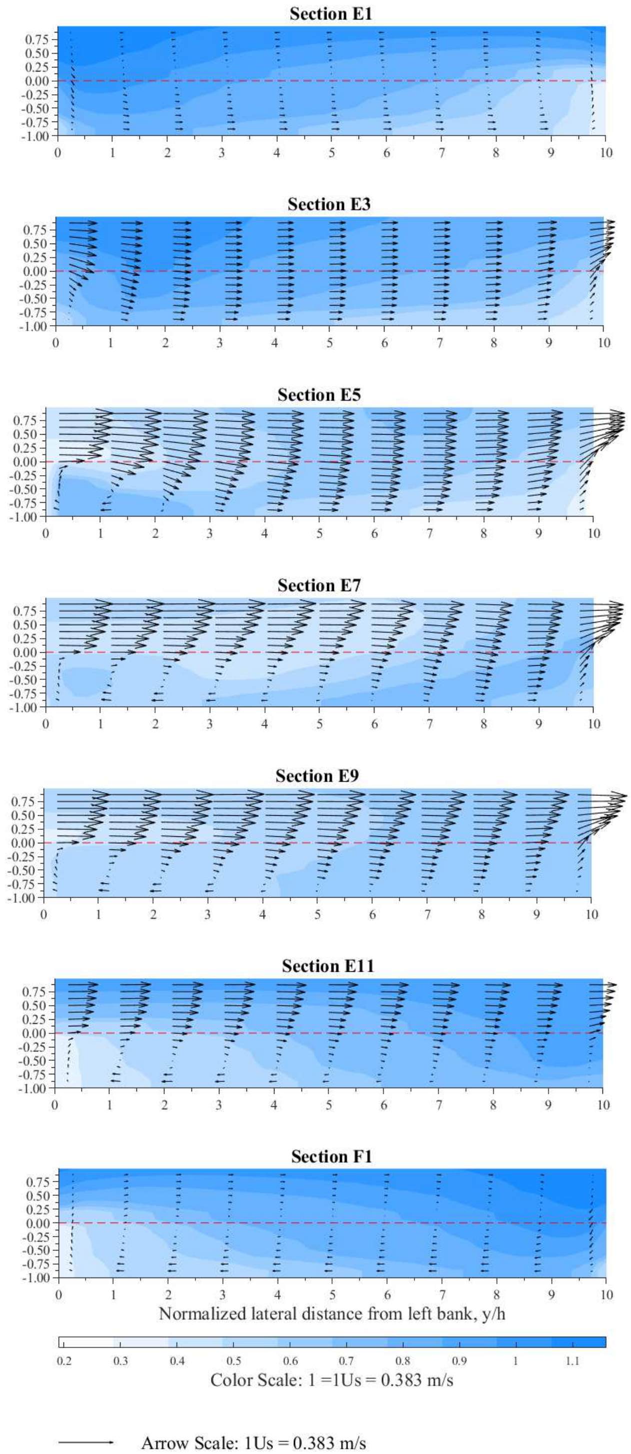

(a)

Figure C9. Relative depth cases of 0.50 for (a) smooth, (b) low density, and (c) high density floodplain scenarios

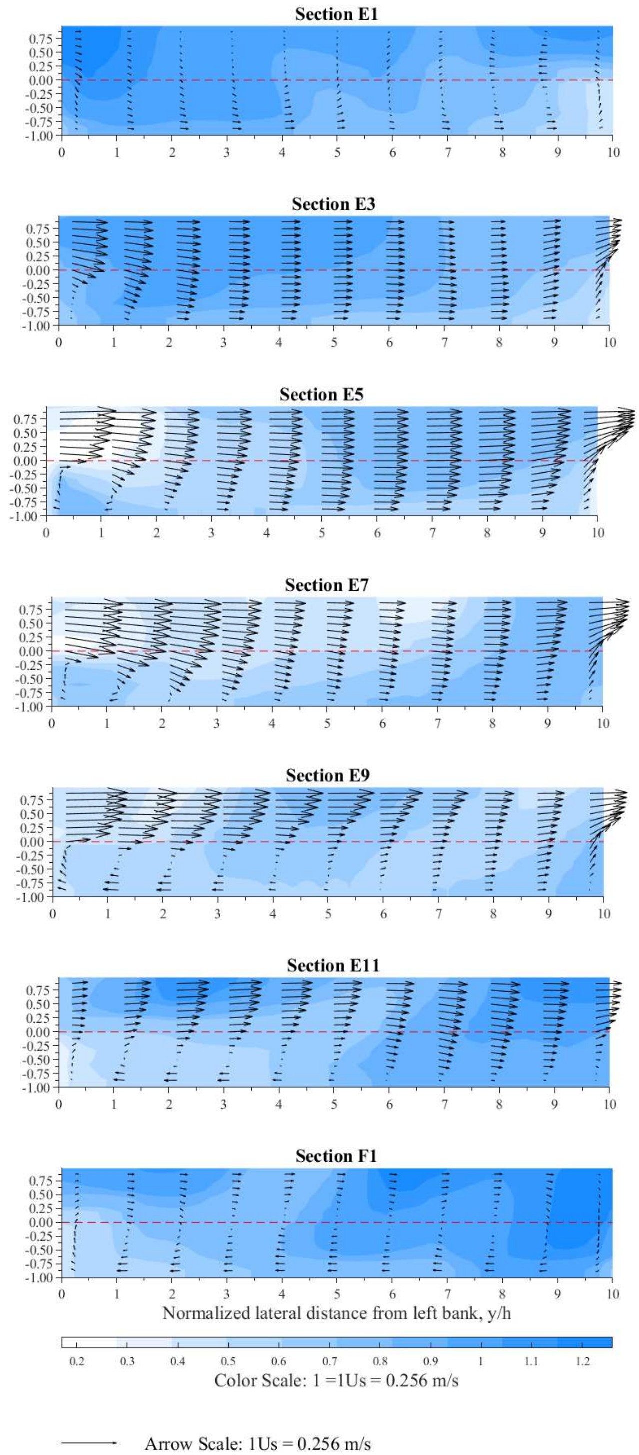

(b)

Figure C9. Relative depth cases of 0.50 for (a) smooth, (b) low density, and (c) high density floodplain scenarios

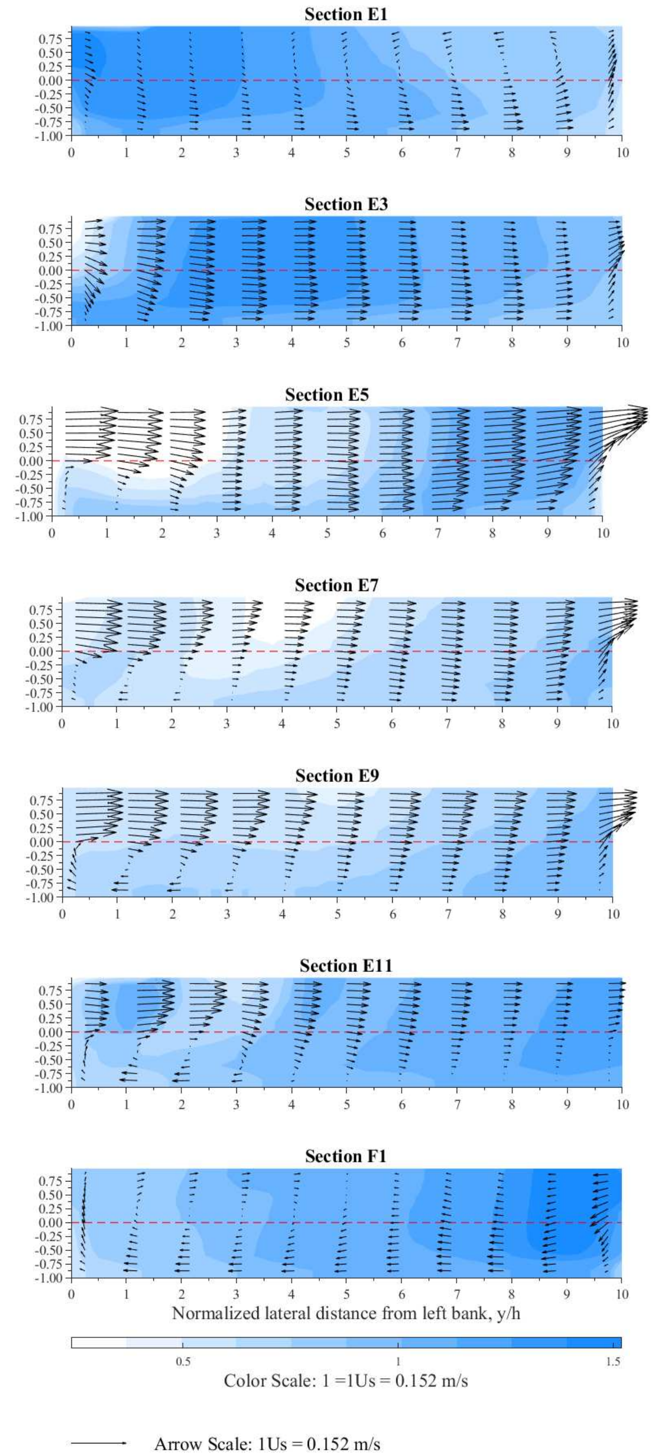

(c)

Figure C9. Relative depth cases of 0.50 for (a) smooth, (b) low density, and (c) high density floodplain scenarios

(a)

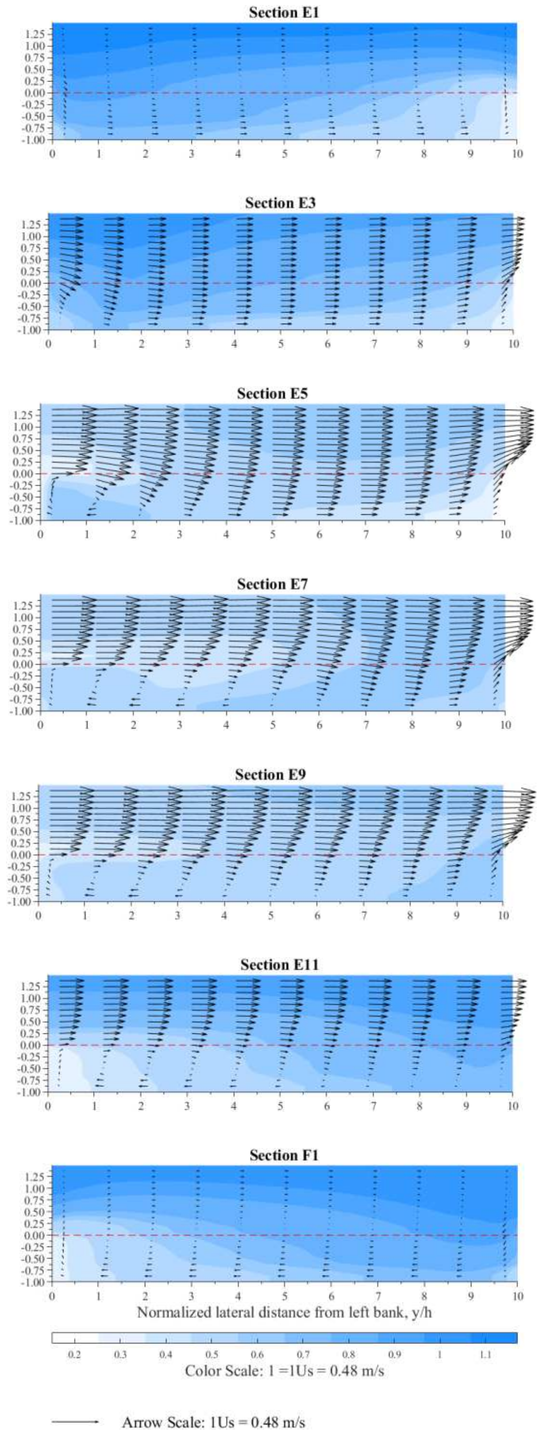

Figure C10. Relative depth cases of 0.60 for (a) smooth, (b) low density, and (c) high density floodplain scenarios

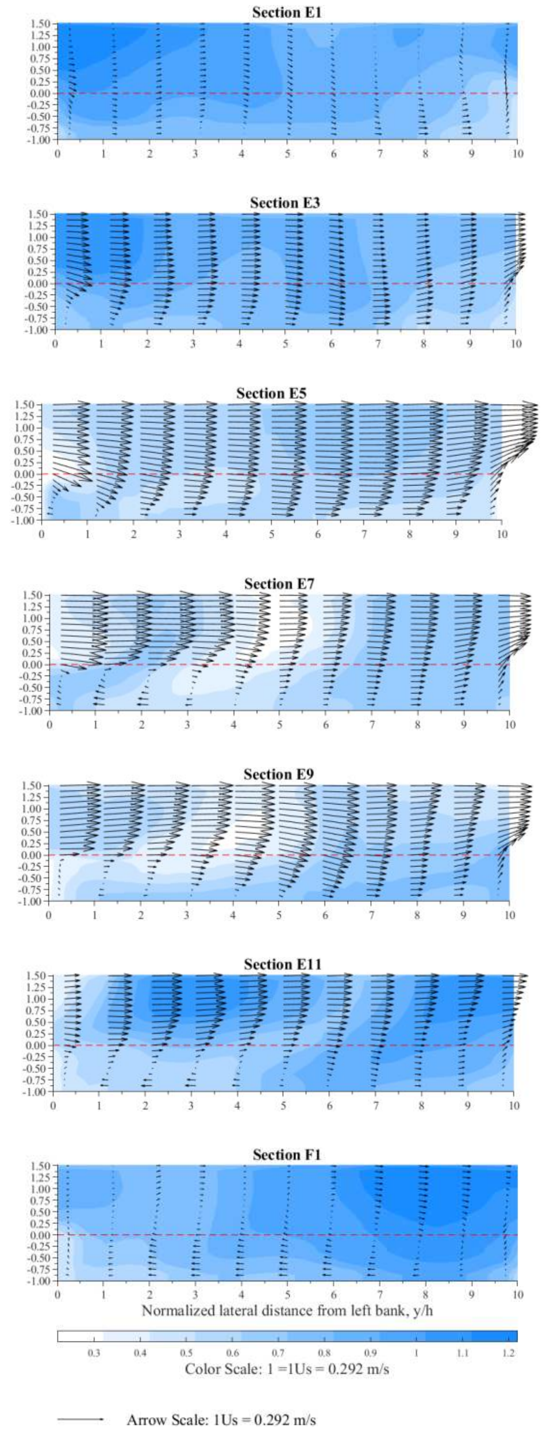

(b)

Figure C10. Relative depth cases of 0.60 for (a) smooth, (b) low density, and (c) high density floodplain scenarios

(c)

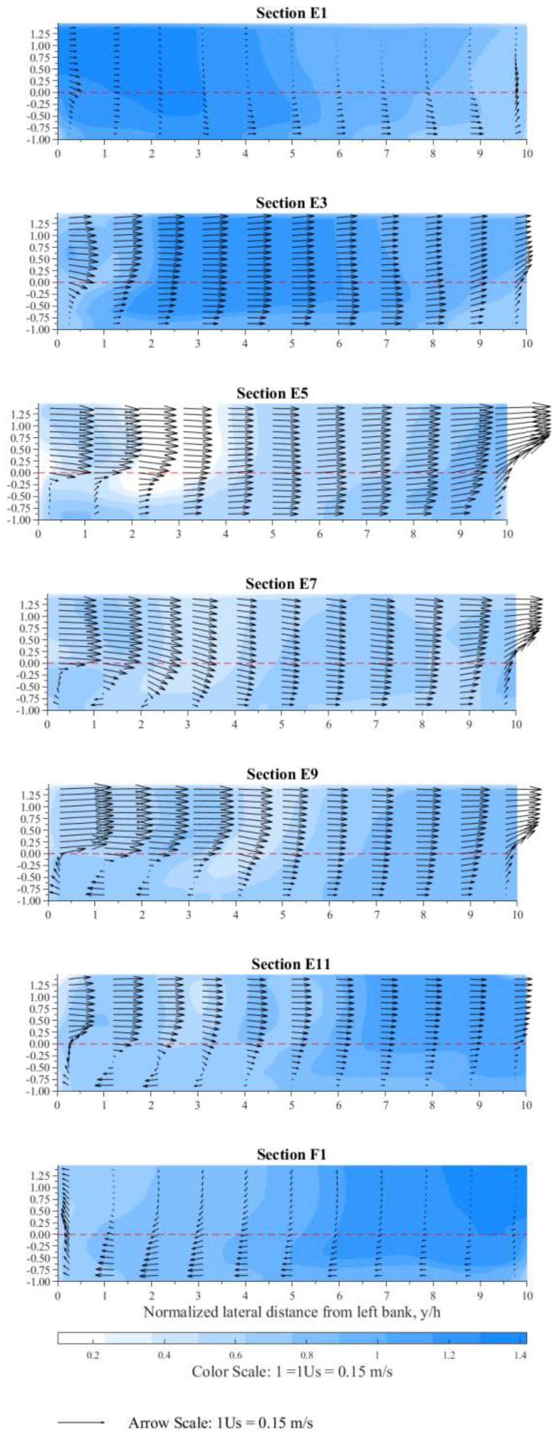

Figure C10. Relative depth cases of 0.60 for (a) smooth, (b) low density, and (c) high density floodplain scenarios

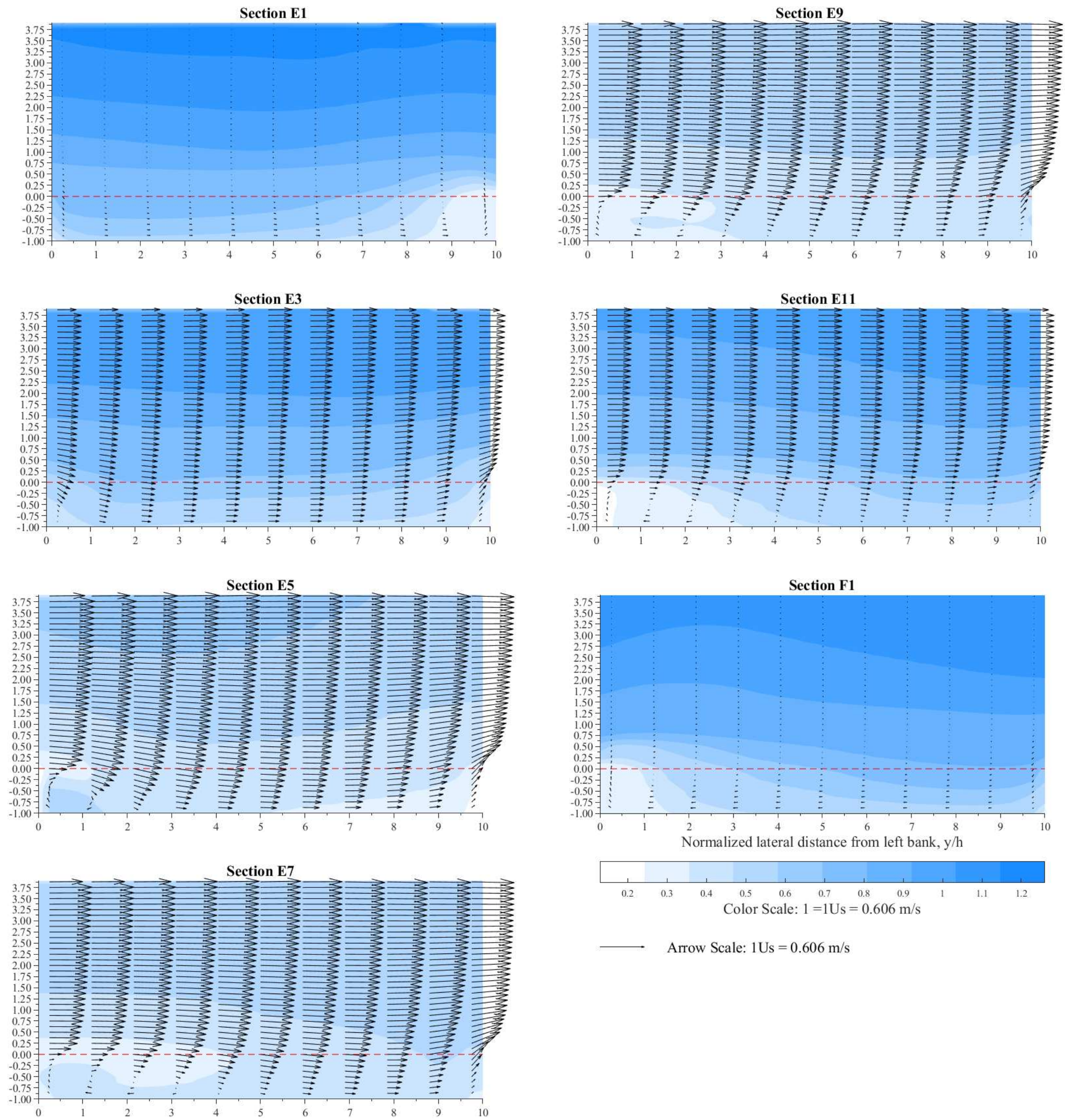

(a)

Figure C11. Relative depth cases of 0.80 for (a) smooth, (b) low density, and (c) high density floodplain scenarios

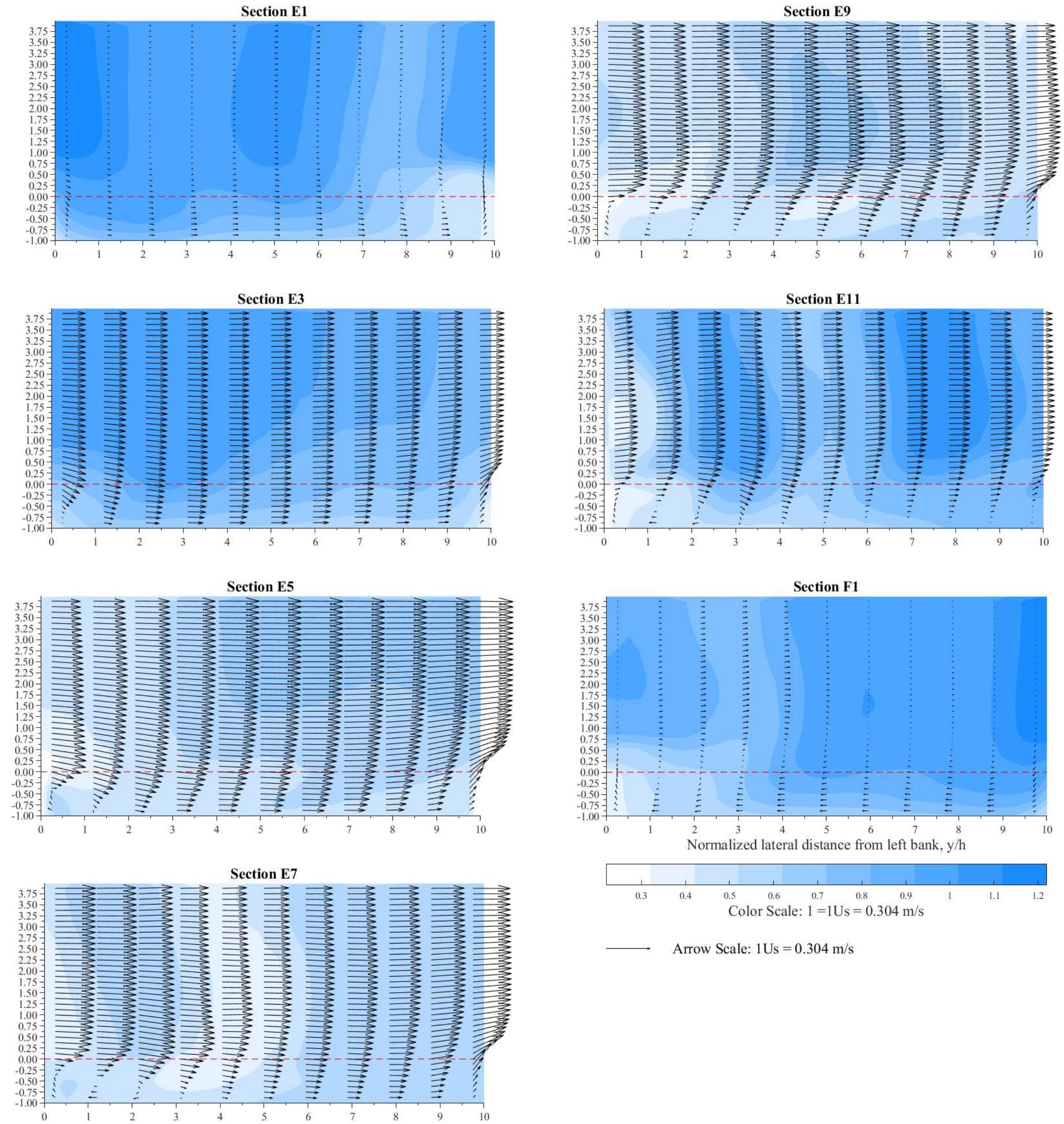

(b)

Figure C11. Relative depth cases of 0.80 for (a) smooth, (b) low density, and (c) high density floodplain scenarios

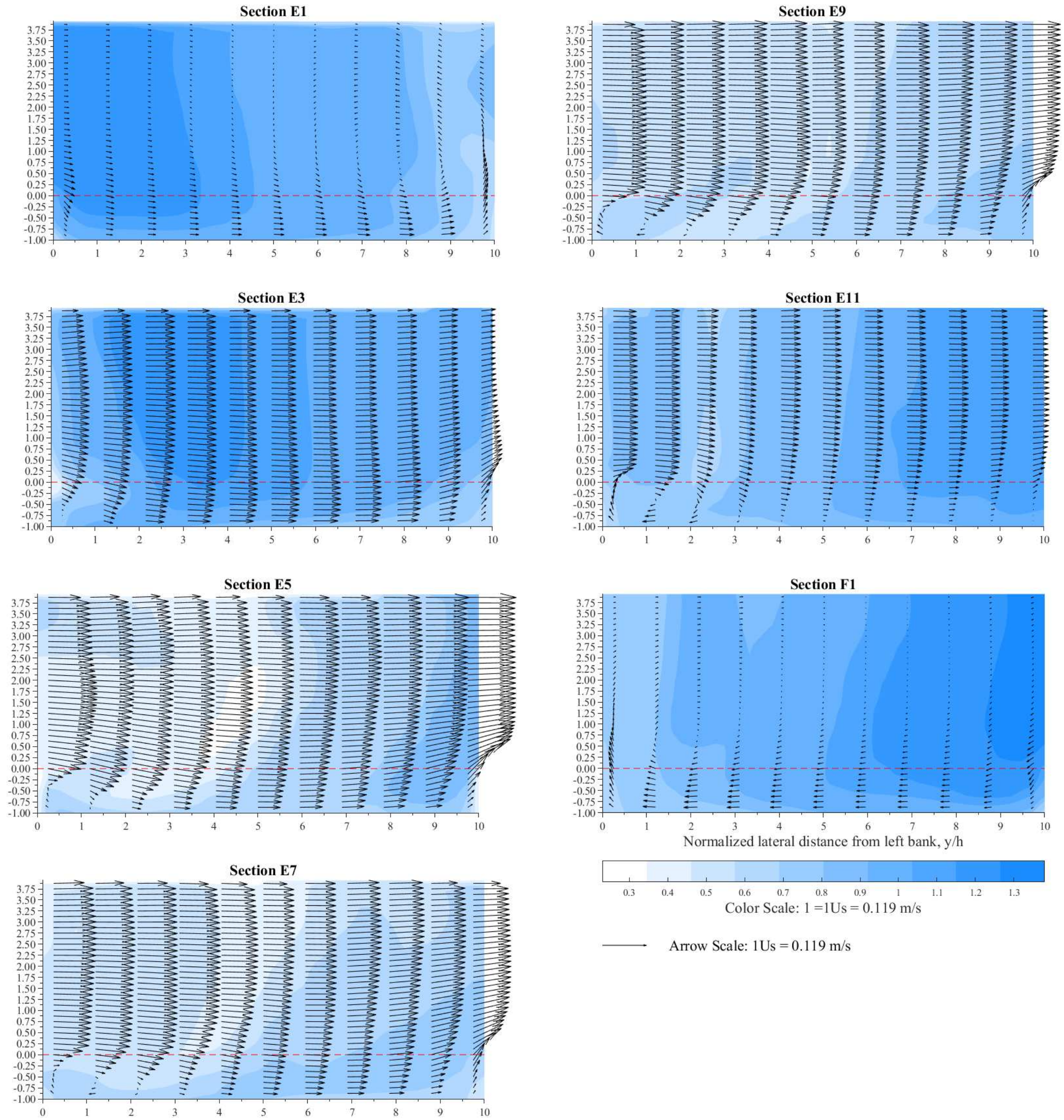

(c)

Figure C11. Relative depth cases of 0.80 for (a) smooth, (b) low density, and (c) high density floodplain scenarios

Appendix D: Layer-averaged flow velocity field planform plots

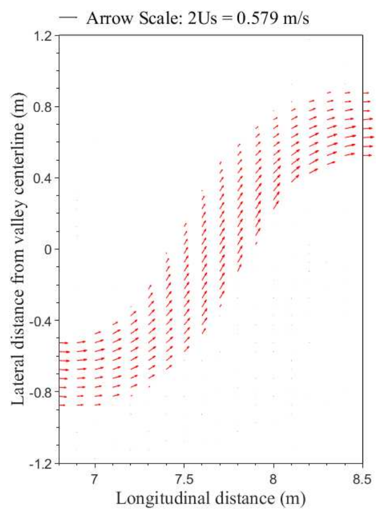

Figure D1. Relative depth case of 0 for smooth floodplain scenario

Dr = 0

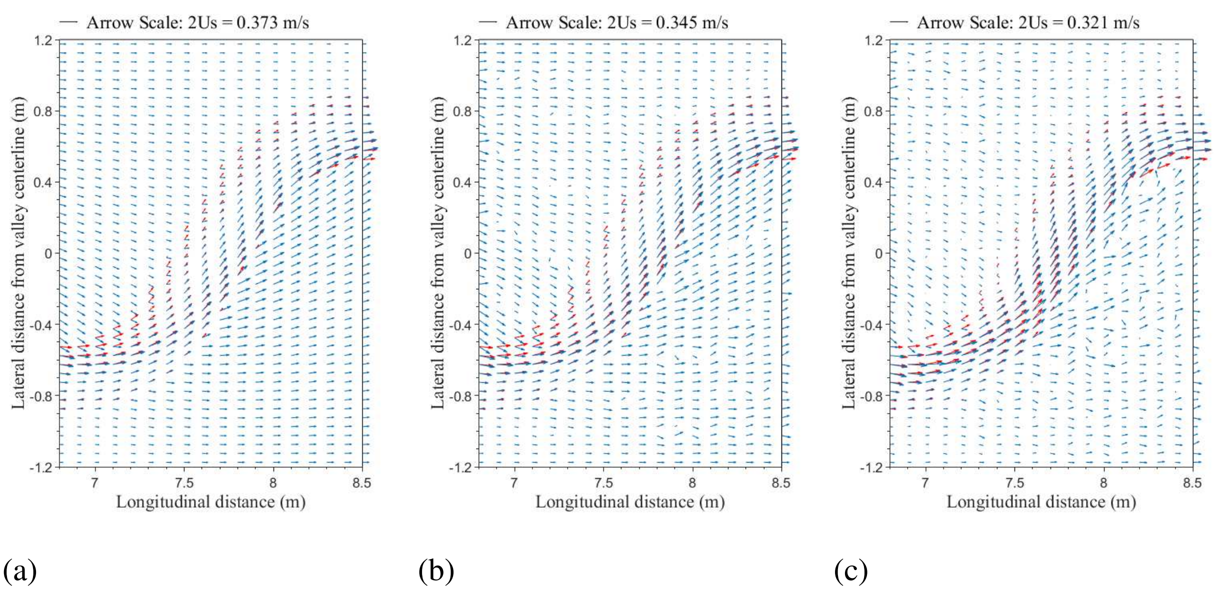

Figure D2. Relative depth cases of 0.13 for (a) smooth, (b) low density, and (c) high density floodplain scenarios

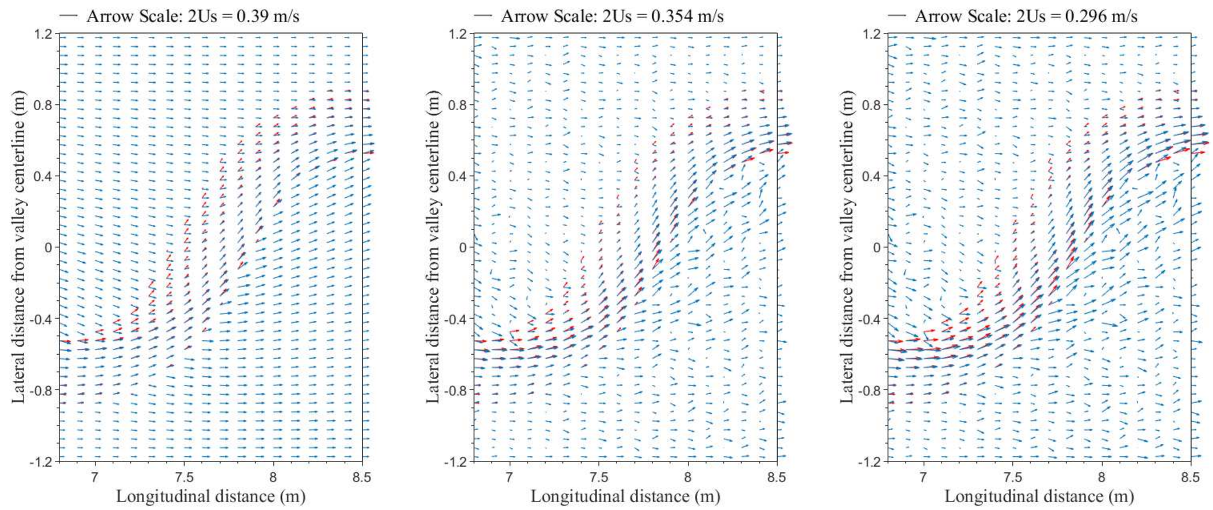

(a) (b) (c)

Figure D3. Relative depth cases of 0.20 for (a) smooth, (b) low density, and (c) high density floodplain scenarios

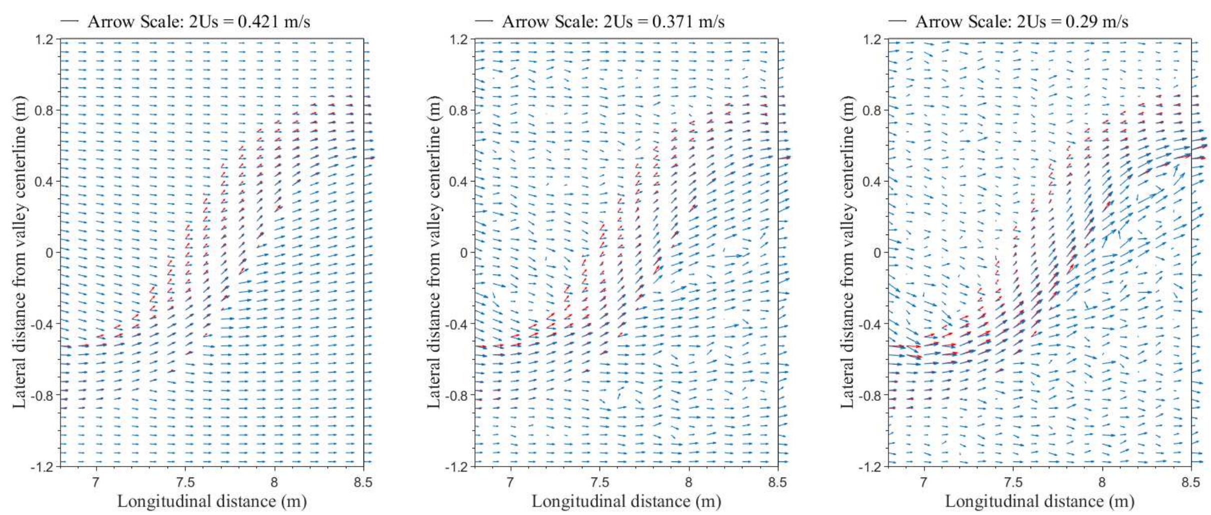

(a) (b) (c)

Figure D4. Relative depth cases of 0.25 for (a) smooth, (b) low density, and (c) high density floodplain scenarios

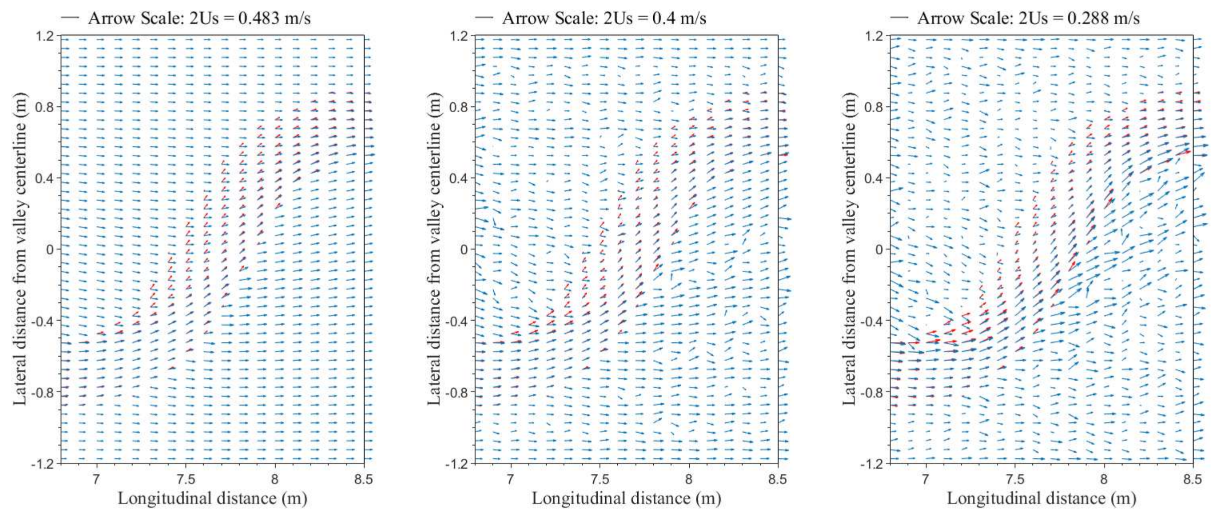

(a) (b) (c)

Figure D5. Relative depth cases of 0.29 for (a) smooth, (b) low density, and (c) high density floodplain scenarios

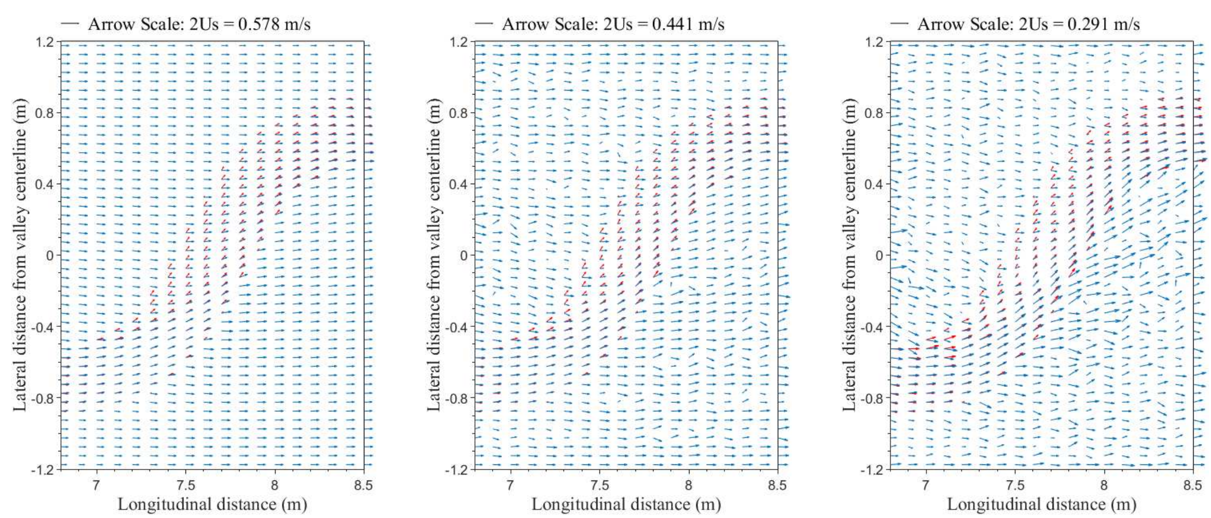

(a) (b) (c)

Figure D6. Relative depth cases of 0.35 for (a) smooth, (b) low density, and (c) high density floodplain scenarios

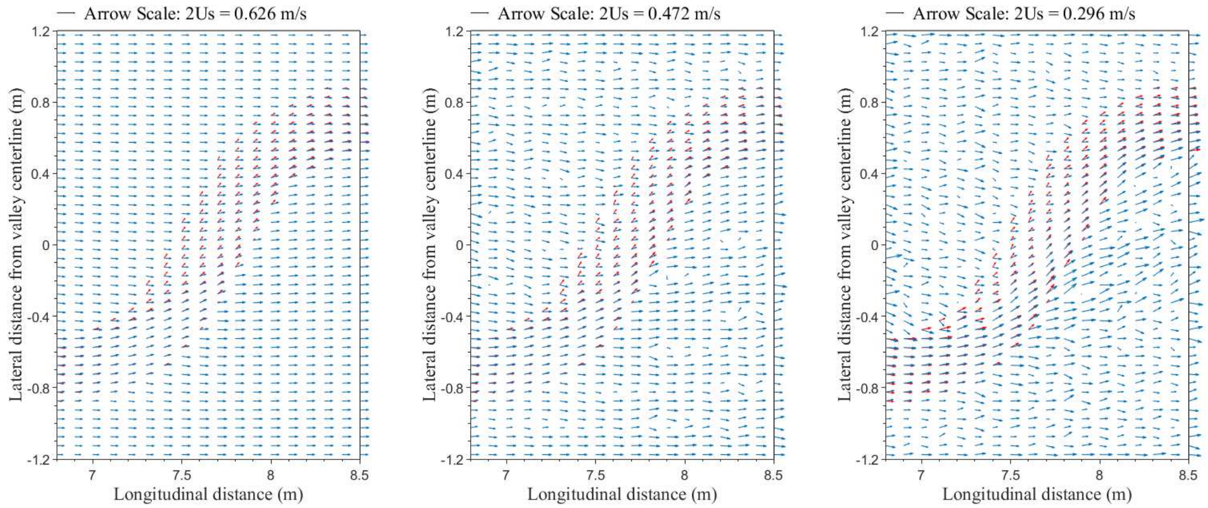

(a) (b) (c)

Figure D7. Relative depth cases of 0.40 for (a) smooth, (b) low density, and (c) high density floodplain scenarios

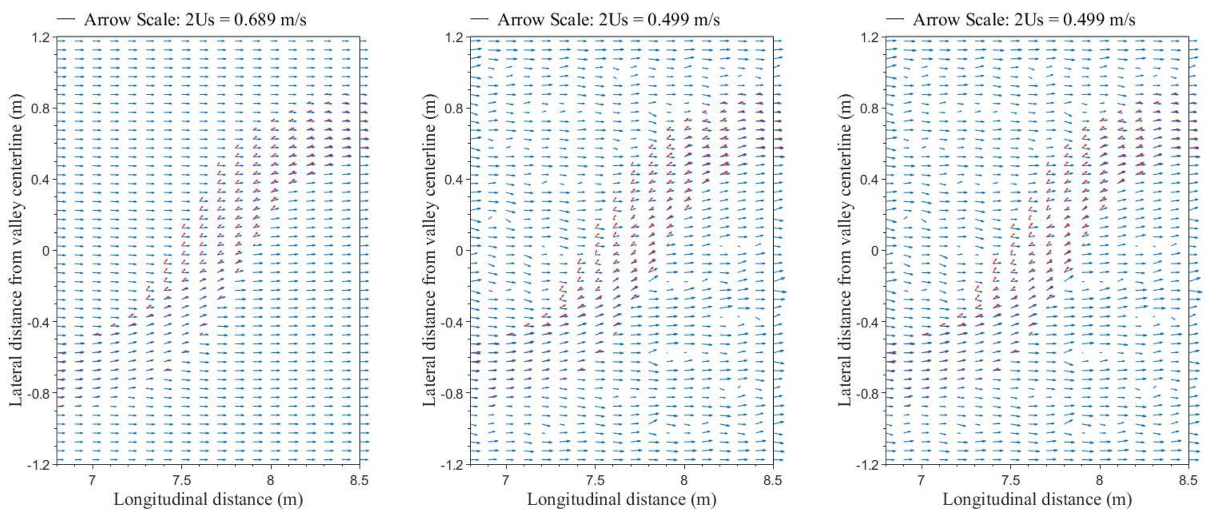

(a) (b) (c)

Figure D8. Relative depth cases of 0.46 for (a) smooth, (b) low density, and (c) high density floodplain scenarios

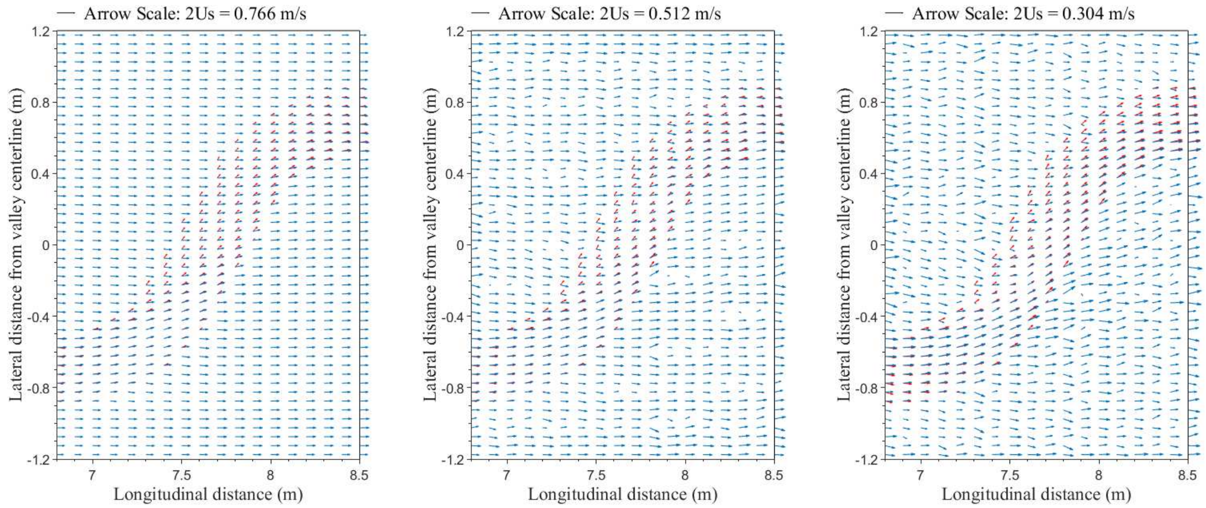

(a) (b) (c)

Figure D9. Relative depth cases of 0.50 for (a) smooth, (b) low density, and (c) high density floodplain scenarios

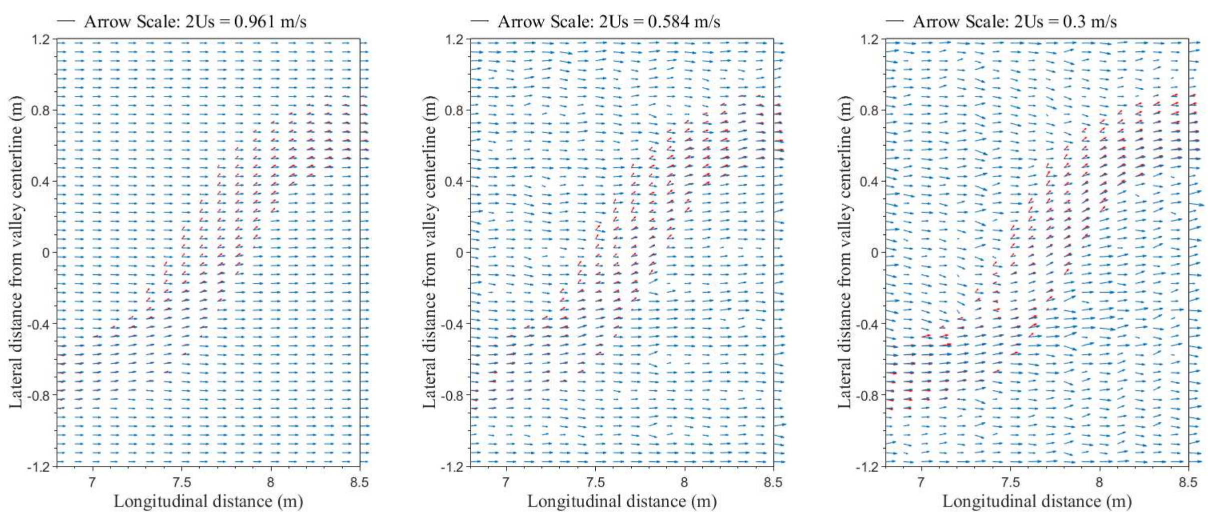

(a) (b) (c)

Figure D10. Relative depth cases of 0.60 for (a) smooth, (b) low density, and (c) high density floodplain scenarios

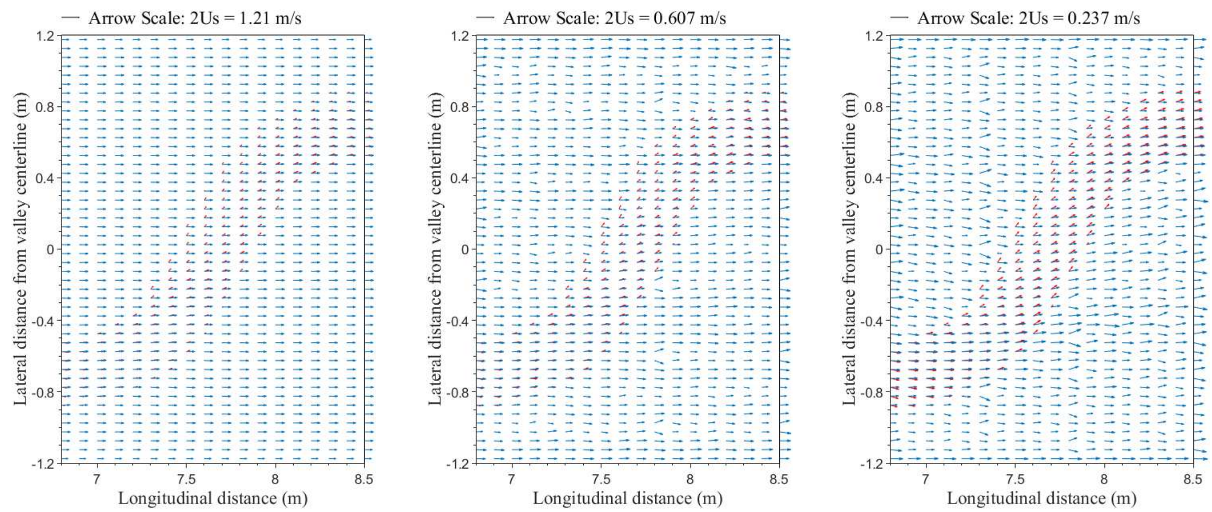

(a) (b) (c)

Figure D11. Relative depth cases of 0.80 for (a) smooth, (b) low density, and (c) high density floodplain scenarios